

Graph Neural Network Flavour Tagging and Boosted Higgs Measurements at the LHC

Samuel John Van Stroud
University College London

Submitted to University College London in fulfilment
of the requirements for the award of the
degree of **Doctor of Philosophy**

March 18, 2023

Declaration

I, Samuel John Van Stroud confirm that the work presented in this thesis is my own. Where information has been derived from other sources, I confirm that this has been indicated in the thesis.

Samuel Van Stroud

Abstract

This thesis presents investigations into the challenges of, potential improvements to, and the application of b -jet identification to study the Higgs boson at the ATLAS experiment at the Large Hadron Collider (LHC). A focus is placed on the high transverse momentum regime, which is a critical region in which to study the Standard Model, but within which successful b -jet identification becomes difficult.

As b -jet identification relies on the successful reconstruction of charged particle trajectories (tracks), the tracking performance is investigated and potential improvements are assessed. Track reconstruction becomes increasingly difficult at high transverse momentum due to the increased multiplicity and collimation of tracks, and also due to the presence of displaced tracks that may occur as the result of the decay of a long-flying b -hadron. The investigations revealed that the track quality selections applied during track reconstruction are suboptimal for tracks inside high transverse momentum b -jets, motivating future studies into the optimisation of these cuts.

To improve b -tagging performance two novel techniques are employed: the classification of the origin of tracks and the application of graph neural networks. An algorithm has been developed to classify the origin of tracks, which allows a more optimal collection of tracks to be selected for use in other algorithms. A graph neural network (GNN) jet flavour tagger has also been developed. This tagger requires only tracks and jet variables as inputs, making a break from previous algorithms, which relied on the outputs of several other

algorithms. This model is trained to simultaneously predict the jet flavour, track origins, and track-pair compatibility (i.e. vertexing), and demonstrates markedly improvements in b -tagging performance, both at low and high transverse momenta. The closely related task of c-jet identification also benefits from these methods.

Analysis of high transverse momentum $H \rightarrow b\bar{b}$ decays, where the Higgs boson is produced in association with a vector boson, was also performed using 139 fb^{-1} of 13 TeV proton-proton collision data from Run 2 of the LHC. The analysis is described, with a focus on the detailed modelling studies performed by the author. The analysis measured provided first measurements in this channel of the Higgs boson production in two high transverse momentum regions.

Impact Statement

This thesis details research in experimental particle physics. The primary contributions are on the improvement of the data analysis algorithms which are used to process proton-proton collisions induced within the ATLAS detector at the Large Hadron Collider (LHC), and the analysis of candidate Higgs boson events.

The primary outcome of the research is an advancement of knowledge about how the Universe works on the most fundamental level, encoded for example in the improved measurement of the fundamental constants for the Standard Model, or in the observation of previously unseen particles or interactions. Although this kind of knowledge doesn't always have an immediate and direct relevance for society, potential applications are impossible to rule out and could have a very large impact further in the future, as has been seen with previous advancements in fundamental science.

The research does find indirect application in the form of associated technological developments that have transferable application within different fields. The cutting-edge techniques developed at CERN for ATLAS and the LHC have found many spin-off applications elsewhere in society, for example the World Wide Web, high-field magnet technology in MRI, touch-screen technology and cloud computing. Fundamental physics, as a proposer of novel and difficult problems, can therefore be seen as a way to generate innovative technologies.

Working in the field also helps to train skilled researchers, which can be redeployed to other areas of society to tackle various problems. In this thesis advanced statistical and data science methods are

deployed. Such methods currently find wide and varied use in many fields. The training of such highly skilled individuals, has a sustained and significant positive economic impact.

Finally, the work carried at ATLAS and the LHC is widely publicised – support of and interest in fundamental physics research helps to generate excitement about science and technology, and educate people about how the Universe works. This in turn attracts people into the area, propagating the benefits described above.

Acknowledgements

Firstly I give thanks to my supervisor Tim Scanlon for all the guidance and support he has offered over the course of this doctorate. Tim has always been consistent with clear explanations and sound advice throughout the last four years. I would also like to thank everyone I've worked with at ATLAS and at UCL. In particular I have Jonathan Shlomi to thank for the fruitful collaboration on advancements in flavour tagging. I would also like to thank Brian Moser and Hannah Arnold for their patient support during the course of the VH , $H \rightarrow b\bar{b}$ analysis. I'm grateful to everyone I've worked with in the ATLAS Flavour Tagging and Tracking groups, in particular to Gabriel Facini, Valerio Dao, Bingxuan Liu and Francesco Di Bello for their guidance, and Dan Guest for his fastidious merge request reviews. This thesis was made in L^AT_EX 2 _{ε} using the “heptesis” class [1].

Contents

1	Introduction	12
2	Theoretical Framework	14
2.1	The Standard Model	14
2.1.1	Quantum Electrodynamics	15
2.1.2	Quantum Chromodynamics	17
2.1.3	The Electroweak Sector	18
2.2	The Higgs Mechanism	19
2.2.1	Electroweak Symmetry Breaking	20
2.2.2	Fermionic Yukawa Coupling	23
2.2.3	Higgs Sector Phenomenology	25
3	The Large Hadron Collider and the ATLAS Detector	28
3.1	The Large Hadron Collider	29
3.2	Coordinate System & Collider Definitions	30
3.2.1	ATLAS Coordinate System	31
3.2.2	Track Parameterisation	32
3.2.3	Hadron Collider Definitions	32
3.3	The ATLAS Detector	36
3.3.1	Inner Detector	37
3.3.2	Calorimeters	40
3.3.3	Muon Spectrometer	42
3.3.4	The Trigger	43
3.4	Reconstructed Physics Objects	44
3.4.1	Tracks	44
3.4.2	Vertices	48
3.4.3	Jets	49
3.4.4	Leptons	51

3.4.5	Missing Transverse Momentum	53
4	Tracking and Flavour Tagging	54
4.1	<i>b</i> -tagging Algorithms	55
4.2	<i>b</i> -hadron Reconstruction	56
4.2.1	Decay Topology	56
4.2.2	Challenges	58
4.3	Investigations into High p_T <i>b</i> -hadron Tracking	62
4.3.1	Shared Hits	62
4.3.2	Global χ^2 Fitter Outlier Removal	63
4.4	Conclusion	65
5	Track Classification MVA	68
5.1	Machine Learning Background	68
5.1.1	Neural Networks	70
5.1.2	Training with Gradient Descent	72
5.2	Track Truth Origin Labelling	72
5.3	Fake Track Identification Tool	73
5.3.1	Datasets	75
5.3.2	Model Inputs	76
5.3.3	Model Hyperparameters	78
5.3.4	Results	78
5.4	<i>b</i> -hadron Track Identification	80
5.5	Combined Approach	80
5.6	Conclusion	82
6	Graph Neural Network Flavour Tagger	84
6.1	Motivation	84
6.2	Graph Neural Network Theory	86
6.3	Experiemtal Setup	88
6.3.1	Datasets	88
6.4	Model Architecture	89
6.4.1	Model Inputs	89
6.4.2	Auxiliary Training Objectives	91
6.4.3	Architecture	92
6.4.4	Training	96

6.5	Results	97
6.5.1	b -tagging Performance	99
6.5.2	c -tagging Performance	100
6.5.3	Ablations	103
6.5.4	Inclusion of Low-Level Vertexing Algorithms	105
6.5.5	Jet Display Diagrams	107
6.5.6	Vertexing Performance	109
6.5.7	Track Classification Performance	113
6.5.8	Looser Track Selection	115
6.6	Other Implementations of GN1	116
6.6.1	High Level Trigger	116
6.6.2	High Luminosity LHC	116
6.7	Conclusion	119
7	Boosted VHbb Analysis	123
7.1	Analysis Overview	124
7.1.1	Data & Simulated Samples	126
7.1.2	Object Reconstruction	126
7.1.3	Selection Criteria	128
7.1.4	Control Regions	129
7.1.5	Background Composition	129
7.2	Systematic Uncertainties & Background Modelling	132
7.2.1	Implementation of Variations	133
7.2.2	Sources of Systematic Modelling Uncertainties	134
7.2.3	Sources of Experimental Uncertainties	136
7.2.4	Vector Boson + Jets Modelling	137
7.2.5	Diboson Modelling	141
7.2.6	$t\bar{t}$ and single-top Modelling	146
7.2.7	Signal Modelling	147
7.3	Statistical Treatment	148
7.3.1	Likelihood Function	148
7.3.2	Background Normalisations	151
7.3.3	Asimov Dataset & Expected Results	152
7.4	Results	152
7.4.1	Post-fit Distributions	153

7.4.2	Post-fit Yields	153
7.4.3	Observed Signal Strength & Significance	153
7.4.4	Impact of Systematics	159
7.4.5	STXS Interpretation	163
7.5	Conclusion	163
8	Conclusion	165
8.1	Summary	165
8.2	Future Work	166
Bibliography		168
List of figures		183
List of tables		195

² Chapter 1

³ Introduction

- ⁴ This thesis describes various efforts in improving the understanding of the Higgs
⁵ boson and its coupling to heavy flavour quarks, primarily through the improvement
⁶ of the algorithms used to reconstruct and analyse jets. The thesis is structured in
⁷ the following manner:
- ⁸ Chapter 2 describes the theoretical foundations of the work presented in the rest of
⁹ the thesis.
- ¹⁰ Chapter 3 describes the ATLAS detector and the CERN accelerator complex. Details
¹¹ of reconstructed physics objects are also provided.
- ¹² Chapter 4 provides an overview of the reconstruction of charged particle tracks
¹³ (tracking) and identification of jets containing b -hadrons (b -tagging) at ATLAS, and
¹⁴ studies into the challenges of high transverse momentum b -tagging.
- ¹⁵ Chapter 5 describes the development of an algorithm to predict the origins of tracks.
¹⁶ The tool is used to improve b -tagging performance by the identification and removal
¹⁷ of fake tracks before their input to the b -tagging algorithms.
- ¹⁸ Chapter 6 introduces a novel monolithic approach to b -tagging using graph neural
¹⁹ networks and auxiliary training objectives.
- ²⁰ Chapter 7 describes the measurement of the associated production of a Higgs boson
²¹ decaying into a pair of b -quarks at high transverse momentum.
- ²² Chapter 8 contains some concluding remarks.

²³ The author's contribution to the work presented in this thesis is as follows.

²⁴ **Tracking:** The author was an active member of the Cluster and Tracking in Dense
²⁵ Environments group throughout their PhD, starting with their qualification task
²⁶ on the understanding of tracking performance at high transverse momentum. The
²⁷ author played a key role in software r22 validation studies for the tracking group,
²⁸ including the validation of the quasi-stable particle interaction simulation and the
²⁹ radiation damage Monte-Carlo simulation. The author helped design and improve
³⁰ several tracking software frameworks, and contributed to heavy flavour tracking
³¹ efficiency studies in dense environments. The author developed a tool to identify
³² and reject fake-tracks, which is being investigated for use in the upcoming tracking
³³ paper.

³⁴ ***b*-tagging:** The author has been an active member of the Flavour Tagging group
³⁵ since September 2014. The author played a key role in investigating the performance
³⁶ of the low level taggers at high transverse momentum and led studies into the
³⁷ labelling and classification of track origins. Based on work by Jonathan Shlomi [2],
³⁸ the author helped develop a new flavour tagging algorithm which offers a large
³⁹ performance improvement with respect to the current state of the art. The author
⁴⁰ was the primary editor of a public note associated with this work [3], which will
⁴¹ also be further developed in an upcoming paper. The author also contributed to
⁴² the proliferation of the new algorithm to the trigger, High Luminosity LHC, and
⁴³ $X \rightarrow bb$ use cases. The author also played a key role in software r22 validation
⁴⁴ studies for the Flavour Tagging group, including the validation of the quasi-stable
⁴⁵ particle interaction simulation. The author maintains and contributes to various
⁴⁶ software frameworks used in the Flavour Tagging group, including as lead developer
⁴⁷ of three packages, to create training datasets, pre-process samples for algorithm
⁴⁸ studies and a framework for training graph neural networks, and contributes to group
⁴⁹ documentation.

⁵⁰ **Higgs:** The author was an active member of the Boosted VHbb analysis group. The
⁵¹ author performed various studies deriving systematic uncertainties for the $V+jets$
⁵² and diboson backgrounds. The author also produced and maintained samples, ran fit
⁵³ studies and cross checks, and gave the diboson unblinding approval talk to the Higgs
⁵⁴ group. The author also contributed to the development of the analysis software.

55 **Chapter 2**

56 **Theoretical Framework**

57 The Standard Model (SM) of particle physics is the theory describing all known
58 elementary particles and their interactions via three of the four fundamental forces.

59 Developed by merging the successful theories of quantum mechanics and relativity
60 in the second half of the 20th century, the SM's position today at the centre of our
61 understanding of the nature of the Universe is firmly established by an unparalleled
62 level of agreement between the model predictions and experimental results [4, 5].

63 The SM has predicted the discovery of the top and bottom quarks [6–8], the W
64 and Z bosons [9], and the tau neutrino [10]. The last missing piece of the SM to be
65 discovered was the Higgs boson, first theorised in the 1960s [11–13], and eventually
66 observed at the LHC in 2012 [14, 15]. After its discovery, much ongoing work has
67 been carried out performing detailed measurements of its mass and interactions with
68 other particles.

69 In this chapter, an overview of the SM is given in Section 2.1, and a more detailed
70 discussion of the Higgs sector and Higgs phenomenology is provided in Section 2.2.

71 **2.1 The Standard Model**

72 The SM is formulated in the language of Quantum Field Theory (QFT). In this
73 framework, particles are localised excitations of corresponding quantum fields, which
74 are operator-valued distributions across spacetime.

75 Central to QFT is the Lagrangian density which describes the kinematics and
 76 dynamics of a field. Observations of conserved quantities are linked, via Noether's
 77 theorem, to symmetries which are expressed by the Lagrangian. Alongside Global
 78 Poincaré symmetry, the SM Lagrangian observes a local non-Abelian $SU(3)_C \otimes$
 79 $SU(2)_L \otimes U(1)_Y$ gauge symmetry. Gauge symmetries leave observable properties of
 80 the system unchanged when the corresponding gauge transformations are applied
 81 to the fields. The full Lagrangian of the SM can be broken up into distinct terms
 82 corresponding to the different sectors, as in Eq. (2.1). An overview of each sector is
 83 given in the following chapters.

$$\mathcal{L}_{\text{SM}} = \mathcal{L}_{\text{EW}} + \mathcal{L}_{\text{QCD}} + \mathcal{L}_{\text{Higgs}} + \mathcal{L}_{\text{Yukawa}} \quad (2.1)$$

84 The SM provides a mathematical description of how three of the four fundamental
 85 forces interact with the matter content of the Universe. The particle content of the
 86 SM consists of spin-1/2 fermions, listed in Table 2.1, and integral spin bosons listed
 in Table 2.2.

Generation	Leptons			Quarks		
	Flavour	Mass [MeV]	Charge [e]	Flavour	Mass [MeV]	Charge [e]
First	e	0.511	-1	u	2.16	$2/3$
	ν_e	$< 1.1 \times 10^{-6}$	0	d	4.67	$-1/3$
Second	μ	105.7	-1	c	1.27×10^3	$2/3$
	ν_μ	< 0.19	0	s	93.4	$-1/3$
Third	τ	1776.9	-1	t	173×10^3	$2/3$
	ν_τ	< 18.2	0	b	4.18×10^3	$-1/3$

Table 2.1: The fermions of the SM [16]. Three generations of particles are present. Also present (unlisted) are the antiparticles, which are identical to the particles up to a reversed charge sign.

87

88 2.1.1 Quantum Electrodynamics

89 Quantum electrodynamics (QED) is the relativistic quantum theory which describes
 90 the interactions between the photon and charged matter. Consider a Dirac spinor
 91 field $\psi = \psi(x)$ and its adjoint $\bar{\psi} = \psi^\dagger \gamma^0$, where ψ^\dagger denotes the Hermitian conjugate

Name	Symbol	Mass [GeV]	Charge [e]	Spin
Photon	γ	$< 1 \times 10^{-27}$	$< 1 \times 10^{-46}$	1
Charged Weak boson	W^\pm	80.377 ± 0.012	± 1	1
Neutral Weak boson	Z	91.1876 ± 0.0021	0	1
Gluon	g	0	0	1
Higgs	H	125.25 ± 0.17	0	0

Table 2.2: The bosons of the SM [16]. The photon, weak bosons and gluons are gauge bosons arising from gauge symmetries, and carry the four fundamental forces of the SM. The recently discovered Higgs boson is the only fundamental scalar particle in the SM.

of ψ . The field ψ describes a fermionic spin-1/2 particle, for example an electron. The Dirac Lagrangian density is

$$\mathcal{L}_{\text{Dirac}} = \bar{\psi}(i\cancel{\partial} - m)\psi, \quad (2.2)$$

where $\cancel{\partial} = \gamma^\mu \partial_\mu$ denotes the contraction with the Dirac gamma matrices γ^μ (summation over up-down pairs of indices is assumed). Application of the Euler-Lagrange equation on Eq. (2.2) yields the Dirac equation

$$(i\cancel{\partial} - m)\psi = 0. \quad (2.3)$$

Suppose some fundamental symmetry that requires invariance under a local $U(1)$ gauge transformation

$$\psi \rightarrow \psi' = \psi e^{-iq\alpha(x)}, \quad (2.4)$$

where α varies over every spacetime point x . Under this transformation, the Dirac equation transforms as

$$(i\cancel{\partial} - m)\psi e^{-iq\alpha(x)} + q\cancel{\partial}\alpha(x)\psi e^{-iq\alpha(x)} = 0. \quad (2.5)$$

For the Dirac equation to remain invariant under the transformation in Eq. (2.4), a new field A_μ which transforms as $A_\mu \rightarrow A'_\mu = A_\mu + \partial_\mu\alpha(x)$ must be added. The transformed interaction term

$$-q\cancel{A}\psi \rightarrow -q\cancel{A}\psi e^{-iq\alpha(x)} - q\cancel{\partial}\alpha(x)\psi e^{-iq\alpha(x)} \quad (2.6)$$

104 will then cancel the asymmetric term in Eq. (2.5) as required. The $U(1)$ invariant
105 Lagrangain can therefore be constructed by adding an interaction between the ψ
106 and A_μ fields to Eq. (2.2). For completeness, the kinetic term for the the new field
107 A_μ is also added in terms of $F_{\mu\nu} = \partial_\mu A_\nu - \partial_\nu A_\mu$, which is trivially invariant under
108 the transformation in Eq. (2.4). The interaction term is typically absorbed into the
109 covariant derivative $D_\mu = \partial_\mu + iqA_\mu$, thus named as it transforms in the same way as
110 the field ψ . Collecting these modifications to Eq. (2.2) yields the QED Lagrangain

$$\mathcal{L}_{\text{QED}} = -\frac{1}{4}F_{\mu\nu}F^{\mu\nu} + \bar{\psi}(iD^\mu - m)\psi. \quad (2.7)$$

111 The quadratic term $A_\mu A^\mu$ is not invariant and therefore the the field A_μ must be
112 massless. Requiring invariance under local $U(1)$ gauge transformations necessitated
113 the addition of a new field A_μ , interpreted as the photon field, which interacts with
114 charged matter. In the SM, the QED Lagrangian is absorbed into the electroweak
115 sector, discussed in Section 2.1.3.

116 2.1.2 Quantum Chromodynamics

117 Quantum Chromodynamics (QCD) is the study of quarks, gluons and their interac-
118 tions. Quarks and gluons carry colour charge, which comes in three kinds, called
119 red, green and blue. While the $U(1)$ symmetry group in Section 2.1.1 was Abelian,
120 the QCD Lagrangian is specified by requiring invariance under transformations from
121 the non-Abelian $SU(3)$ group, making it a Yang-Mills theory [17] which requires the
122 addition of self-interacting gauge fields. The infinitesimal $SU(3)$ group generators
123 are given by $T_a = \lambda_a/2$, where λ_a are the eight Gell-Mann matrices. These span the
124 space of infinitesimal group transformations and do not commute with each other,
125 instead satisfying the commutation relation

$$[T_a, T_b] = if_{abc}T_c, \quad (2.8)$$

126 where f_{abc} are the group's structure constants. Consider the six quark fields $q_k = q_k(x)$.
127 Each flavour of quark q_k transforms in the fundamental triplet representation, in
128 which each component of the triplet corresponds to the colour quantum number
129 for red, green and blue colour charged respectively. $G_{\mu\nu}^a$ are the eight gluon field

¹³⁰ strength tensors, one for each generator T_a , defined as

$$G_{\mu\nu}^a = \partial_\mu A_\nu - \partial_\nu A_\mu - g_s f^{abc} A_\mu^b A_\nu^c, \quad (2.9)$$

¹³¹ where A_μ^a are the gluon fields and g_s is the strong coupling constant. The covariant
¹³² derivative is written as

$$D_\mu = \partial_\mu + ig_s T_a A_\mu^a. \quad (2.10)$$

¹³³ The full QCD Lagrangian is then given by

$$\mathcal{L}_{\text{QCD}} = -\frac{1}{4} G_{\mu\nu}^a G_a^{\mu\nu} + q_k (i \not{D} - m_k) q_k. \quad (2.11)$$

¹³⁴ Cubic and quartic terms of the gauge fields A_μ^a appear in the Lagrangian, leading to
¹³⁵ the gluon's self interaction.

¹³⁶ The QCD coupling constant g_s varies, or “runs”, with energy. At lower energy scales
¹³⁷ (and corresponding larger distance scales) the interaction is strong. This leads to
¹³⁸ quark confinement, whereby an attempt to isolate individual colour-charged quarks
¹³⁹ requires so much energy that additional quark-antiquark pairs are produced. At
¹⁴⁰ higher energy scales (and corresponding smaller distance scales), asymptotic freedom
¹⁴¹ occurs as the interactions become weaker, allowing perturbative calculations to be
¹⁴² performed. Hadrons are bound states of quarks. They are invariant under $SU(3)$
¹⁴³ gauge transformations (i.e. are colour-charge neutral, or *colourless*).

¹⁴⁴ 2.1.3 The Electroweak Sector

¹⁴⁵ The weak and electromagnetic forces are unified in the Glashow-Weinberg-Salam
¹⁴⁶ (GWS) model of electroweak interaction [18–20]. The Lagrangian is specified by
¹⁴⁷ requiring invariance under the symmetry group $SU(2)_L \otimes U(1)_Y$, as motivated by a
¹⁴⁸ large amount of experimental data. Here, $SU(2)_L$ is referred to as weak isospin and
¹⁴⁹ $U(1)_Y$ as weak hypercharge.

150 The generators of $SU(2)_L$ are $T_a = \sigma_a/2$, where σ_a are the three Pauli spin matrices
151 which satisfy the commutation relation

$$[T_a, T_b] = i\varepsilon_{abc}T_c. \quad (2.12)$$

152 The generator of $U(1)_Y$ is $Y = 1/2$. Each generator corresponds to a gauge field,
153 which, after symmetry breaking (discussed in Section 2.2), give rise to the massive
154 vector bosons, W^\pm and Z , and the massless photon. The massive vector bosons
155 are the carriers of the weak force. Due to the mass of the force carriers, the weak
156 force has a short range and so it appears weak even though its intrinsic strength is
157 comparable to that of QED.

158 The charge operator Q can be written as a combination of the third $SU(2)_L$ generator
159 and the $U(1)_Y$ generator as in

$$Q = T_3 + Y. \quad (2.13)$$

160 The weak force violates parity conservation [21–23], i.e. invariance under parity
161 transformations (mirror reflections). Only left handed fermions participate in the
162 weak interaction. Since there is no other force through which neutrinos interact with
163 other particles, there are no right handed neutrinos in the Standard Model.

164 2.2 The Higgs Mechanism

165 The Brout-Englert-Higgs mechanism (henceforth just the “Higgs mechanism”) is the
166 process through which the fundamental particles of the SM acquire mass [11–13].
167 Experimentally it was known that the weak force had a low effective strength, which
168 was suggestive of a massive mediating gauge particle. However, directly adding
169 mass to the weak gauge bosons violates the non-Abelian symmetry of the SM.
170 Instead, the gauge bosons gain mass through the interaction with a scalar Higgs
171 field which results from the spontaneous breakdown of symmetry as discussed in
172 Section 2.2.1. Similarly, the Higgs mechanism gives mass to the fermions, as discussed
173 in Section 2.2.2. Section 2.2.3 described some basic phenomenology of the Higgs
174 particle relevant to hadron colliders.

¹⁷⁵ 2.2.1 Electroweak Symmetry Breaking

¹⁷⁶ Spontaneous symmetry breaking (SSB) is a key part of the Higgs mechanism. It
¹⁷⁷ is the transition of a physical system from a state of manifest symmetry to a state
¹⁷⁸ of hidden, or *broken*, symmetry. In particular, this applies to physical systems
¹⁷⁹ where the Lagrangian observes some symmetry, but the lowest energy vacuum states
¹⁸⁰ do not exhibit that same symmetry. In other words, the symmetry is broken for
¹⁸¹ perturbations around the vacuum state.

¹⁸² Consider the case in which the gauge fields from the local $SU(2)_L \otimes U(1)_Y$ symmetry
¹⁸³ group (discussed in Section 2.1.3) are coupled to a complex scalar field $\phi = \phi(x)$,
¹⁸⁴ transforms as a weak isospin doublet. Omitting the kinetic term of the gauge fields,
¹⁸⁵ and writing $\phi^2 \equiv \phi^\dagger \phi$, the Lagrangain is

$$\mathcal{L}_{\text{Higgs}} = (D_\mu \phi)^\dagger (D^\mu \phi) - [\mu^2 \phi^2 + \lambda \phi^4], \quad (2.14)$$

¹⁸⁶ where the covariant derivative is given by

$$D_\mu = \partial_\mu + igA_\mu^a T^a + ig'B_\mu, \quad (2.15)$$

¹⁸⁷ and T^a are the generators of $SU(2)$. The potential term $V(\phi)$ is made up of a
¹⁸⁸ quadratic and quartic term in the scalar field ϕ , which each contain an arbitrary
¹⁸⁹ parameter, respectively λ and μ . The quartic term gives the field self-interaction, and
¹⁹⁰ cannot be negative as this would lead to a potential that was unbounded from below.
¹⁹¹ The quadratic term can be positive or negative. In the case where the quadratic term
¹⁹² is positive, it is interpreted as a mass term for the scalar field. By choosing $\mu^2 < 0$
¹⁹³ the field becomes unphysical due to its negative mass. The shape of the potential in
¹⁹⁴ this case is shown in Fig. 2.1. Note that in the case of the Standard Model, the scalar
¹⁹⁵ field ϕ is a complex doublet, and so the corresponding potential is 5-dimensional.
¹⁹⁶ In order to obtain a physical interpretation of the Lagrangain in Eq. (2.14) for the
¹⁹⁷ case where $\mu^2 < 0$, the field ϕ is expanded around the vacuum state. The vacuum
¹⁹⁸ expectation value (VEV) is the expected value of the field ϕ which minimises the
¹⁹⁹ potential $V(\phi)$ (equivalently the expected value of the field operator ϕ when the
²⁰⁰ system is in a vacuum state, $|\langle \phi \rangle_0|^2 \equiv |\langle 0 | \phi | 0 \rangle|^2 \equiv \phi_0^2$). Minimising the potential

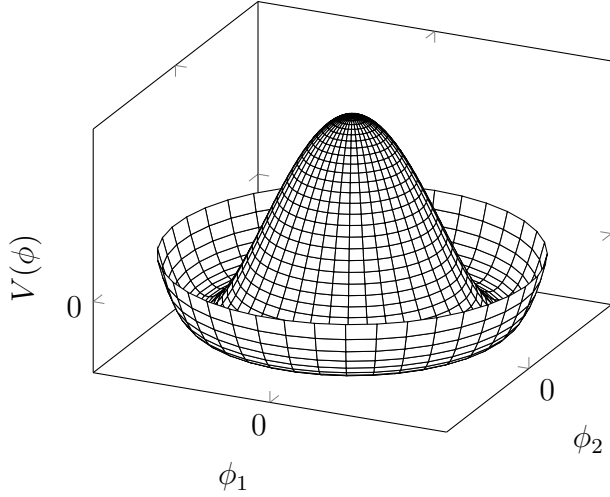


Figure 2.1: The Higgs potential $V(\phi)$ of the complex scalar field singlet $\phi = \phi_1 + i\phi_2$, with a choice of $\mu^2 < 0$ leading to a continuous degeneracy in the true vacuum states. A false vacuum is present at the origin.

201 gives a VEV of

$$\phi_0^2 = -\mu^2/\lambda = v^2. \quad (2.16)$$

202 Due to the shape of the potential in Fig. 2.1, there is a degeneracy in the direction
203 that the complex doublet ϕ points. As all the different vacuum states minimise
204 the potential and therefore yield identical physics, one can arbitrarily choose the
205 state to lie along the second component of the doublet. Application of Eq. (2.13)
206 shows this choice is manifestly invariant under the charge operator. This allows
207 the identification of the unbroken subgroup $U(1)_Q$, under which the ground state is
208 invariant. The generator of $U(1)_Q$ is the charge operator Q .

209 Adding the particle content back to the theory by expanding the field around the
210 vacuum state, and making a transformation to the unitary gauge to remove unphysical
211 Nambu-Goldstone modes (which arise in the context of global symmetries [24, 25]),
212 yields

$$\phi = \frac{1}{\sqrt{2}} \begin{bmatrix} 0 \\ v + H \end{bmatrix}, \quad (2.17)$$

where H is a real scalar field, the *true vacuum* Higgs field. Substituting this into Eq. (2.14) and identifying physical fields from the quadratic terms of linear combinations of unphysical fields, one can write the physical fields W_μ^\pm , Z_μ and A_μ in terms of the original fields A_μ^a and B_μ . This gives

$$W_\mu^\pm = \frac{1}{\sqrt{2}}(A_\mu^1 \mp iA_\mu^2) \quad \begin{bmatrix} A_\mu \\ Z_\mu \end{bmatrix} = \begin{bmatrix} \cos \theta_W & \sin \theta_W \\ -\sin \theta_W & \cos \theta_W \end{bmatrix} \begin{bmatrix} B_\mu \\ A_\mu^3 \end{bmatrix}. \quad (2.18)$$

where θ_W is the weak mixing angle defined by

$$\cos \theta_W = \frac{g}{\sqrt{g^2 + g'^2}}. \quad (2.19)$$

The corresponding masses of the now massive vector bosons can be read off as

$$m_W = \frac{1}{2}gv \quad m_Z = \frac{m_W}{\cos \theta_W}, \quad (2.20)$$

while the photon remains massless. The Higgs mass is $m_H = v\sqrt{\lambda} = \mu$.

This is the Higgs mechanism. It maintains the renormalisability and unitarity of the SM whilst allowing the weak vector bosons to acquire mass. In summary, an unphysical complex scalar field ϕ with a nonzero VEV leads to spontaneous symmetry breaking. Due to the non-Abelian symmetry breaking, would-be massless Nambu-Goldstone modes, which arise after expansion around the true vacuum state, are cancelled out by making a local gauge transformation to the unitary gauge, and instead are absorbed by the vector bosons, allowing them to acquire mass.

This sector of the SM contains four fundamental parameters that must be determined from experiment. These can be specified by the Lagrangian parameters g , g' , v and λ or the physically measurable parameters m_Z , $\sin \theta_W$, m_H and e . In the local neighbourhood around the true vacuum, the macroscopic symmetry of the system is not realised, and therefore the physical particles do not obey the original symmetry. However, information about the symmetry is retained through some additional constraints on the parameters of the theory. Prior to symmetry breaking, the potential contained two terms and two constants. After symmetry breaking there are three terms but still only two constants that relate these terms. This is the vestige of the original symmetry.

237 Spontaneous symmetry breaking has modified the original symmetry group of the SM
238 $SU(2)_L \times U(1)_Y \rightarrow SU(3)_C \otimes U(1)_Q$. Three broken generators from the symmetry
239 group $SU(2)_L \times U(1)_Y$ have been absorbed into the definition of the physical weak
240 vector bosons, giving them mass. The same methodology can be used to generate
241 the fermion masses, as shown in the next section.

242 2.2.2 Fermionic Yukawa Coupling

243 Adding the masses of the fermions by hand breaks the gauge invariance of the
244 theory. Instead, we can use a Yukawa coupling between the fermion fields and the
245 Higgs field in order to generate mass terms after spontaneous electroweak symmetry
246 breakdown [19]. In this way, the fermion masses are determined by both the respective
247 couplings to the Higgs field and the VEV of the Higgs field itself, which sets the
248 basic mass scale of the theory.

249 The Higgs field ϕ transforms as an $SU(2)$ doublet with $Y = 1/2$, as does the left-
250 handed fermion field ψ_L . The right-handed fermion field ψ_R transforms as an $SU(2)$
251 singlet.

252 Charged Lepton Masses

253 The renormalisable and gauge invariant coupling between a fermionic field ψ and a
254 scalar Higgs field ϕ can be written as

$$\mathcal{L}_{\text{Yukawa}} = -g_f(\bar{\psi}_L \phi \psi_R + \bar{\psi}_R \phi^\dagger \psi_L). \quad (2.21)$$

255 where $\psi_L = (\nu_L, e_L)$ and $\psi_R = e_R$ for the first generation leptons. After spontaneous
256 symmetry breaking (see Section 2.2.1), the scalar Higgs field in unitary gauge
257 Eq. (2.17) consists of a VEV and the true vacuum Higgs field H . Substituting this
258 in to Eq. (2.21) yields

$$\mathcal{L}_{\text{Yukawa}} = -\frac{v g_e}{\sqrt{2}} \bar{e} e - \frac{g_e}{\sqrt{2}} \bar{e} H e, \quad (2.22)$$

259 using $\bar{e} e = (\bar{e}_L + \bar{e}_R)(e_L + e_R) = \bar{e}_L e_R + \bar{e}_R e_L$. The VEV component of ϕ provides
260 the first term in Eq. (2.22) which is quadratic in the electron field, and can therefore

261 be identified as the electron mass term. An interaction term between the electron
 262 field e and the true vacuum Higgs field H is also present. Mass is generated for the
 263 other charged lepton generations in the same way.

264 **Quark Masses**

265 The down-type quarks acquire their mass analogous to the leptons, with $\psi_L = (u_L, d_L)$
 266 and $\psi_R = d_R$ for the first quark generation. Mass is generated for the up-type quarks
 267 using the conjugate field to ϕ which transforms under $SU(2)$ as a doublet with
 268 $Y = -1/2$. The conjugate field $\tilde{\phi}$ is constructed as

$$\tilde{\phi} = i\sigma_2 \phi^\dagger = \begin{bmatrix} 0 & 1 \\ -1 & 0 \end{bmatrix} \begin{bmatrix} \phi_1^\dagger \\ \phi_2^\dagger \end{bmatrix} = \frac{1}{\sqrt{2}} \begin{bmatrix} v + H \\ 0 \end{bmatrix}, \quad (2.23)$$

269 and transforms in the same way as ϕ . This field can be used to write an additional
 270 Yukawa coupling which provides mass for the up-type quarks in a similar way as
 271 before.

$$\mathcal{L}_{\text{Yukawa}}^{\text{up}} = -g_q (\bar{\psi}_L \tilde{\phi} \psi_R + \bar{\psi}_R \tilde{\phi}^\dagger \psi_L) \quad (2.24)$$

272 Considering the first generation of up-type quarks with $\psi_L = (u_L, d_L)$ and $\psi_R = u_R$,
 273 substitution into Eq. (2.24) yields

$$\mathcal{L}_{\text{Yukawa}}^{\text{up}} = -\frac{vg_u}{\sqrt{2}} \bar{u}u - \frac{g_u}{\sqrt{2}} \bar{u}Hu. \quad (2.25)$$

274 The Yukawa terms mix quarks of different generations. Physical particles are detected
 275 in their mass eigenstates q , which diagonalise the mass matrix, but interact via the
 276 weak interaction according to their weak eigenstates \tilde{q} , which are superpositions
 277 of the mass eigenstates. This feature of the weak sector leads to mixing between
 278 different generations of quarks. Quark mixing can be expressed using the Cabibbo-
 279 Kobayashi-Maskawa (CKM) matrix, which specifies the strength of flavour-changing
 280 weak currents. The entries in the matrix are enumerated as

$$\begin{bmatrix} \tilde{d} \\ \tilde{s} \\ \tilde{b} \end{bmatrix} = \begin{bmatrix} V_{ud} & V_{us} & V_{ub} \\ V_{cd} & V_{cs} & V_{cb} \\ V_{td} & V_{ts} & V_{tb} \end{bmatrix} \begin{bmatrix} d \\ s \\ b \end{bmatrix}, \quad (2.26)$$

281 where the size of the elements $|V_{pq}|^2$ measures the probability of a transition between
282 states p and q .

283 2.2.3 Higgs Sector Phenomenology

284 As previously discussed in this chapter, the Higgs field plays a key role in the SM
285 by giving mass to fundamental particles. The strength of the coupling between
286 the Higgs field and another particle is proportional to that particle's mass. This
287 fact dictates which production mechanisms and decay modes are dominant at the
288 LHC. The cross sections for different production mechanisms at a centre of mass
289 energy $\sqrt{s} = 13 \text{ TeV}$ are shown as a function of the Higgs mass m_H in Fig. 2.2. At
290 leading order in QCD, Higgs boson production occurs mainly through four modes,
291 shown in Fig. 2.3. The dominant production mode is gluon-gluon fusion ($pp \rightarrow H$),
292 which is predominantly mediated by a virtual top quark loop. Vector boson fusion
293 ($pp \rightarrow qqH$) is the second most likely production mechanism, in which a pair of
294 W or Z bosons fuse to produce a Higgs after being radiated by two quarks. Next
295 most common is the associated production of a Higgs boson and a vector boson
296 ($pp \rightarrow VH$), in which a pair of quarks fuse to produce a single W or Z boson which
297 radiates a Higgs. The final of the four leading production modes is top quark fusion,
298 in which two gluons each radiate a quark-antiquark pair, and a quark from each pair
299 fuses to produce a Higgs boson.

300 Although gluon-gluon fusion is the dominant production mode, for hadronic decays
301 of the Higgs boson the associated production with a vector boson has the advantage
302 of leading to a more distinct signature due to the likelihood of the vector bosons
303 decaying leptons. Leptons provide a clean signals to detect and trigger on.

304 Since the Higgs boson couples proportional to mass, decays to heavier particles are
305 favoured. The branching ratios of different Higgs boson decay modes are shown
306 as a function of m_H in Fig. 2.4. Approximately 58% of the time the Higgs boson
307 decays to a pair of b -quarks, the dominant decay mode. The next most likely decay
308 mode is to a pair of W bosons, which occurs approximately 20% of the time. After
309 the b -quark, the next heaviest fermions are the tau lepton and the c -quark, decays
310 to pairs of these particles happen approximately an order of magnitude less often.
311 Decays to pairs of vector bosons are via a virtual off shell Higgs boson only. While
312 the $H \rightarrow \gamma\gamma$ and $H \rightarrow ZZ$ branching ratios are small compared with fermionic decay

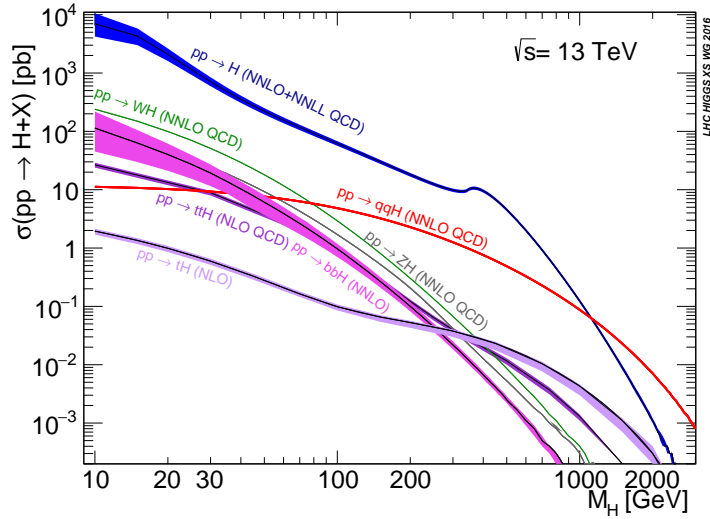


Figure 2.2: Higgs boson production cross sections as a function of Higgs mass (m_H) at $\sqrt{s} = 13 \text{ TeV}$ [26]. Uncertainties are shown in the shaded bands. At $m_H = 125 \text{ GeV}$, Higgs boson production is dominated by gluon-gluon fusion, vector boson fusion, associated production with vector bosons, and top quark fusion.

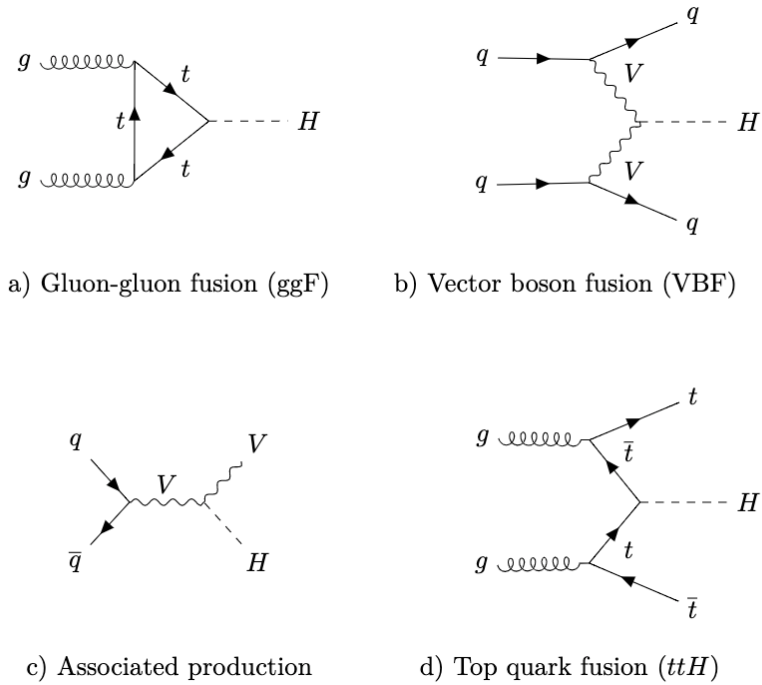


Figure 2.3: Diagrams for the four main Higgs boson production modes at the LHC for a Higgs mass $m_H = 125 \text{ GeV}$ at a centre of mass energy $\sqrt{s} = 13 \text{ TeV}$.

³¹³ modes (around 0.2% for $H \rightarrow \gamma\gamma$), these decay channels were instrumental in the
³¹⁴ initial discovery of the Higgs due to the low level of background processes which
³¹⁵ mimic the final state [14, 15].

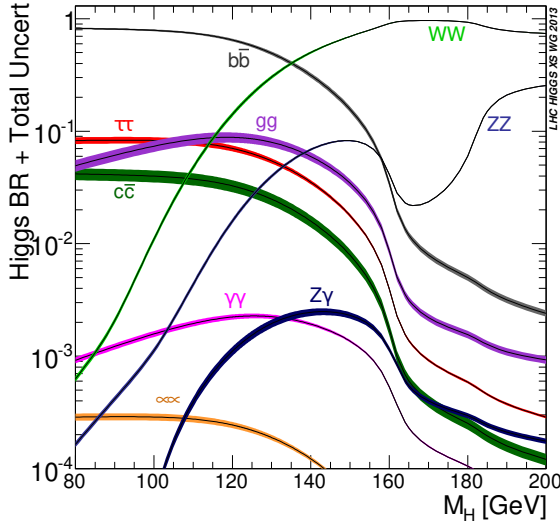


Figure 2.4: Higgs boson branching ratios as a function of Higgs mass (m_H) at $\sqrt{s} = 13$ TeV [26]. Uncertainties are shown in the shaded bands. At $m_H = 125$ GeV, the Higgs predominantly decays to a pair of b -quarks, around 58% of the time. The leading subdominant decay mode is to a pair of W bosons.

³¹⁶ This thesis presents a measurement of the Higgs bosons production rate using events
³¹⁷ with a Higgs boson produced in association with vector boson and decaying to a pair
³¹⁸ of b -quarks, i.e. $pp \rightarrow VH(b\bar{b})$. The $H \rightarrow b\bar{b}$ decay mode directly probes the Higgs
³¹⁹ coupling to fermions, and more specifically to the bottom quark. This coupling was
³²⁰ first observed in 2018 [27, 28]. Ongoing work measuring the coupling strengths, in
³²¹ particular in the high energy regime, is the focus of the analysis presented in this
³²² thesis in Chapter 7.

323 Chapter 3

324 The Large Hadron Collider and the
325 ATLAS Detector

326 Since the completion of its construction in 2008, the Large Hadron Collider (LHC) [29]
327 at CERN has extended the frontiers of particle physics through significant increases
328 in centre of mass energy and luminosity compared with previous collider experiments.
329 The LHC accelerates bunches of protons around a 27 km ring until they are travelling
330 just 3 m s^{-1} slower than the speed of light, at which point they are made to
331 collide. The proton bunches travel round the ring 11,000 times per second in two
332 concentric beams, which are guided by superconducting magnets cooled using liquid
333 helium to -271.3°C (1.9 K). The beams travel in opposite directions around the
334 ring and are crossed at four locations so that collisions between protons can take
335 place. Around these collision points four specialised detectors, ALICE [30], CMS [31],
336 LHCb [32] and ATLAS [33], are located to capture information about the products
337 of the collisions.

338 In this chapter, a brief overview of the LHC and the accelerator complex at CERN
339 is given in Section 3.1. The coordinate system used at the ATLAS detector and
340 other common definitions are introduced in Section 3.2. An overview of the different
341 detector systems is provided in Section 3.3, and finally descriptions of various
342 commonly used reconstructed objects is given in Section 3.4.

³⁴³ 3.1 The Large Hadron Collider

³⁴⁴ The LHC is operated in multi-year *runs* during which beams of protons are circulated
³⁴⁵ and collided. Between runs there are periods of shutdown while the accelerator and
³⁴⁶ detector machinery is maintained and upgraded. Run 1 began in 2010 when the LHC
³⁴⁷ collided proton bunches, each containing more than 10^{11} particles, 20 million times
³⁴⁸ per second, providing 7 TeV proton-proton collisions at instantaneous luminosities
³⁴⁹ of up to $2.1 \times 10^{32} \text{ cm}^{-2} \text{ s}^{-1}$. The centre-of-mass energy was increased to 8 TeV
³⁵⁰ in 2012. Over the course of Run 1, 26.4 fb^{-1} of usable integrated luminosity was
³⁵¹ recorded. Run 2, which spanned 2015–2018, further increased the the proton-proton
³⁵² collision energy to 13 TeV. During Run 2 the bunch spacing was reduced, leading
³⁵³ to a collision rate of 40 MHz. Over the course of Run 2 a total usable integrated
³⁵⁴ luminosity of 139 fb^{-1} was recorded. 2022 marked the beginning of Run 3 which,
³⁵⁵ with a higher center of mass energy and peak luminosity, is expected to culminate in
³⁵⁶ an approximate tripling of the dataset size. A summary of key information about
³⁵⁷ each run is listed in Table 3.1.

Period	Year	\sqrt{s} [TeV]	$\langle \mu \rangle$	Bunch spacing [ns]	Luminosity [$\text{cm}^{-2} \text{ s}^{-1}$]
Run 1	2010–2012	7–8	18	50–150	8×10^{33}
Run 2	2015–2018	13	34	25	$1\text{--}2 \times 10^{34}$
Run 3	2022–2025	13.6	50	25	2×10^{34}

Table 3.1: Overview of the different LHC runs [34,35]. The average number of interactions per bunch-crossing is denoted as $\langle \mu \rangle$ (see Section 3.2.3), and is here averaged over the entire run. The luminosity is the peak instantaneous luminosity. Numbers for Run 3 are preliminary and are only provided to give an indication of expected performance.

³⁵⁸ An overview of the accelerator complex at CERN is shown in Fig. 3.1. The LHC is
³⁵⁹ at the final stage of a chain of accelerators which incrementally step-up the energy
³⁶⁰ of incoming protons. The first accelerator is Linac2 (which has been replaced by
³⁶¹ Linac4 in 2020), a linear accelerator which accelerates negative hydrogen ions to an
³⁶² energy of 160 MeV. Upon leaving Linac4, the ions are stripped of both electrons
³⁶³ and the resulting protons are fed into the Proton Synchrotron Booster (PSB), which
³⁶⁴ increases the energy of the protons to 2 GeV. The protons leaving the PSB are passed
³⁶⁵ to the Proton Synchrotron (PS), which increases the energy to 26 GeV, and then
³⁶⁶ from the PS to the Super Proton Synchrotron (SPS) which further increases the

367 energy to 450 GeV. Finally, the proton beams are injected in the LHC where they
 368 are accelerated to their final energy of 6.5 TeV (for Run 2).

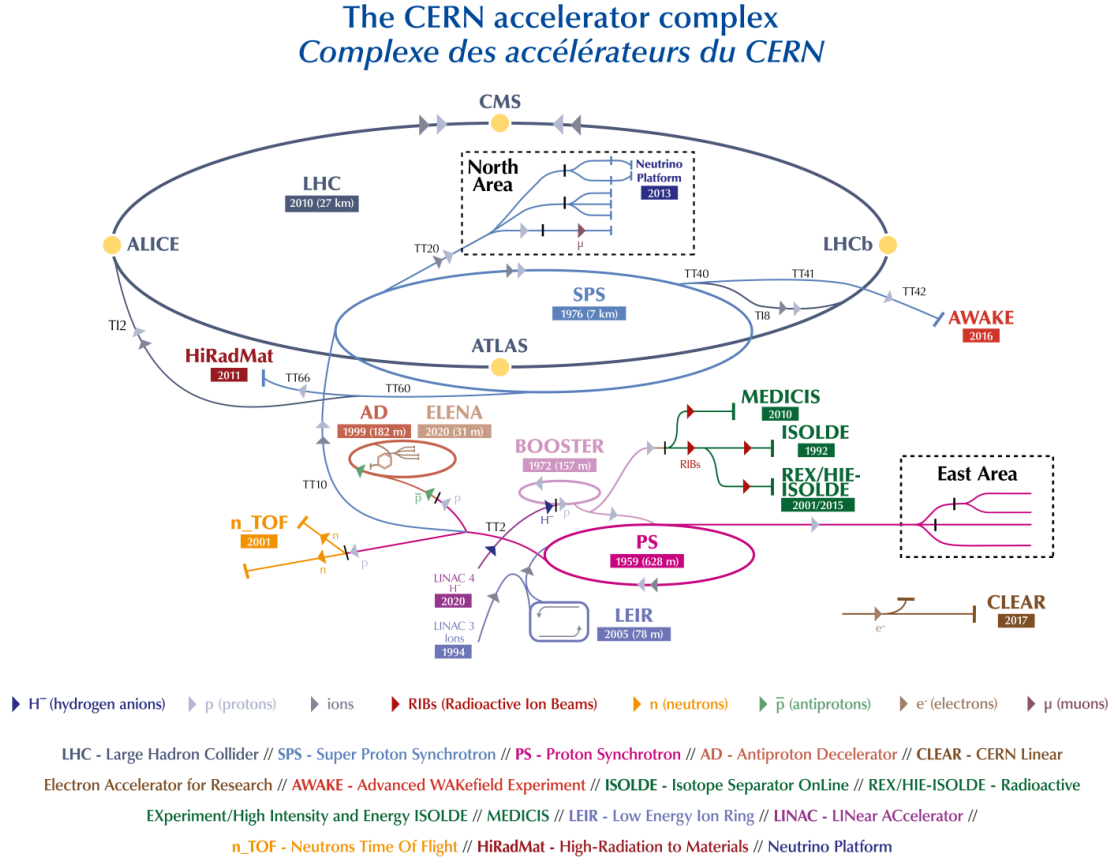


Figure 3.1: An overview of the CERN accelerator complex [36]. The LHC is fed by a series of accelerators starting with Linac2 (or Linac4 from 2020). Next are the Proton Synchrotron Booster, the Proton Synchrotron, and finally the Super Proton Synchrotron which injects protons into the LHC.

369 3.2 Coordinate System & Collider Definitions

370 In Section 3.2.1, the coordinate system used at ATLAS is introduced. The parame-
 371 terisation used for specifying the trajectory of charged particle tracks is described in
 372 Section 3.2.2, and definitions for some frequently occurring concepts and quantities
 373 is provided in Section 3.2.3.

³⁷⁴ 3.2.1 ATLAS Coordinate System

³⁷⁵ The origin of the coordinate system used by ATLAS is the nominal interaction point
³⁷⁶ in the centre of the detector. As shown in Fig. 3.2, the z -axis points along the
³⁷⁷ direction of the beam pipe, while the x -axis points from the interaction point to the
³⁷⁸ centre of the LHC ring, and the y -axis points upwards. The transverse plane lies
³⁷⁹ in x - y while the longitudinal plane lies along the z -axis. A cylindrical coordinate
³⁸⁰ system with coordinates (r, ϕ) is used in the transverse plane, where r is the radius
³⁸¹ from the origin and ϕ is the azimuthal angle around the z -axis.

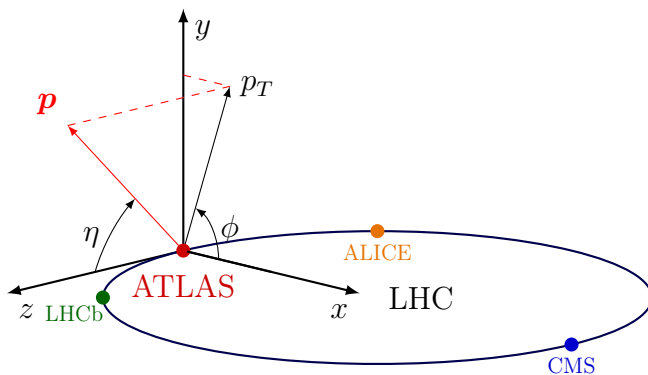


Figure 3.2: The coordinate system used at the ATLAS detector, showing the locations of the four main experiments located at various points around the LHC. The 3-vector momentum $\mathbf{p} = (p_x, p_y, p_z)$ is shown by the red arrow. Reproduced from Ref. [37].

³⁸² The polar angle θ is commonly specified in terms of the pseudorapidity η , defined as

$$\eta = -\ln \left[\tan \left(\frac{\theta}{2} \right) \right]. \quad (3.1)$$

³⁸³ The pseudorapidity is a convenient quantity to work with as differences in η are
³⁸⁴ invariant under Lorentz boosts.

³⁸⁵ The transverse momentum p_T of an object is the sum in quadrature of the momenta
³⁸⁶ in the transverse plane

$$p_T = \sqrt{p_x^2 + p_y^2}. \quad (3.2)$$

387 Angular distance between two objects is measured in units of ΔR and is defined as

$$\Delta R = \sqrt{(\Delta\eta)^2 + (\Delta\phi)^2}, \quad (3.3)$$

388 where $\Delta\eta$ and $\Delta\phi$ are the differences in pseudorapidity and azimuthal angle between
389 the two objects.

390 3.2.2 Track Parameterisation

391 The trajectories of charged particle tracks are parameterised as a helix which is fully
392 specified using five parameters: $(d_0, z_0, \phi, \theta, q/p)$. The transverse and longitudinal
393 impact parameters (IP) d_0 and z_0 specify the closest approach of the trajectory of a
394 particle to an given origin, where the hard scatter primary vertex (see Section 3.4.2)
395 is used in this thesis. ϕ and θ are the azimuthal and polar angles respectively, and
396 q/p is the measured charge on the track¹ divided by the scalar 3-momentum. Fig. 3.3
397 shows each of these parameters diagrammatically.

398 Impact parameter significances are defined as the IP divided by its corresponding
399 uncertainty, $s(d_0) = d_0/\sigma(d_0)$ and $s(z_0) = z_0/\sigma(z_0)$. When used in flavour tagging
400 (see Chapter 4), track IP significances are lifetime signed according to the track's
401 direction with respect to the jet axis and the primary vertex [39]. The signed IP
402 significances is positive if the track crosses the jet axis in front of the primary vertex
403 and negative if the crossing is behind the primary vertex.

404 3.2.3 Hadron Collider Definitions

405 Cross Section

406 The cross section σ is closely related to the probability of an interaction between
407 two colliding particles, and is analogous to an effective cross-sectional area of the
408 particles. The cross section of a process depends on the transition matrix element
409 and a phase space integral. At hadron colliders such as the LHC, the proton-proton

¹Reconstructed charged particles are assumed to have a charge of ± 1 .

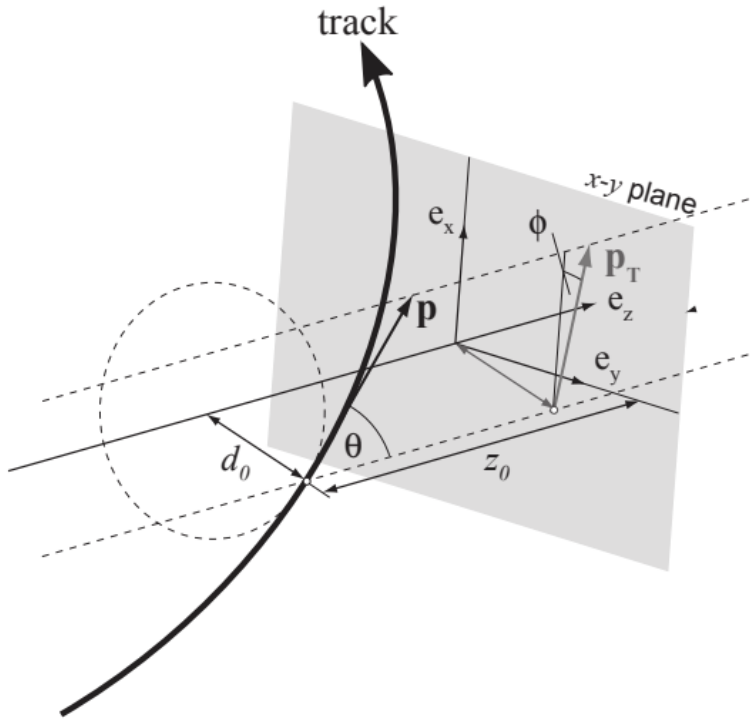


Figure 3.3: The track parameterisation used at the ATLAS detector. Five coordinates ($d_0, z_0, \phi, \theta, q/p$) are specified, defined at the track's point of closest approach to the nominal interaction point at the origin of the coordinate system. The figure shows the three-momentum \mathbf{p} and the transverse momentum p_T (defined in Eq. (3.2)). The basis vectors e_x, e_y and e_z are also shown. Reproduced from Ref. [38].

⁴¹⁰ cross section can be factorised as

$$\sigma(pp \rightarrow X) \approx \text{PDFs} \cdot \text{partonic cross section.} \quad (3.4)$$

⁴¹¹ The partonic cross section can be calculated at high energies such as those found at
⁴¹² the LHC, while the parton distribution functions (PDFs) have to be extracted from
⁴¹³ experimental results.

⁴¹⁴ Luminosity

⁴¹⁵ The total number of proton-proton collisions N is related to the total pp cross σ
⁴¹⁶ section by the integrated luminosity L , as in

$$N = \sigma L = \sigma \int \mathcal{L} dt. \quad (3.5)$$

⁴¹⁷ The instantaneous luminosity \mathcal{L} relates the cross section to the number of collisions
⁴¹⁸ per unit time. For two colliding bunched proton beams, it is defined as

$$\mathcal{L} = \frac{1}{\sigma} \frac{dN}{dt} = \frac{fn_1 n_2}{4\pi \sigma_x \sigma_y}, \quad (3.6)$$

⁴¹⁹ where n_1 and n_2 are the number of protons in the colliding bunches, f is the bunch
⁴²⁰ crossing frequency, and σ_x and σ_y are the rms width of the beam in the horizontal
⁴²¹ and vertical directions.

⁴²² The total luminosity recorded over the course of Run 2 is shown in Fig. 3.4. In
⁴²³ total, 139 fb^{-1} of usable physics data was collected over the three-year run. The
⁴²⁴ uncertainty on the total integrated luminosity is 1.7% [40].

⁴²⁵ Pile-up

⁴²⁶ At the centre of the ATLAS detector, bunches of more than 10^{11} protons are collided.
⁴²⁷ Each bunch-crossing is called an *event*. There is generally one hard proton-proton
⁴²⁸ scatter per event. Additional interactions are typically relatively soft ($low-p_T$) and
⁴²⁹ are known as *pile-up*. Pile-up from interactions within the same bunch-crossing is
⁴³⁰ known as *in-time* pile-up while residual signatures from previous bunch-crossings
⁴³¹ is known as *out-of-time* pile-up. The number of pile-up interactions is denoted μ ,

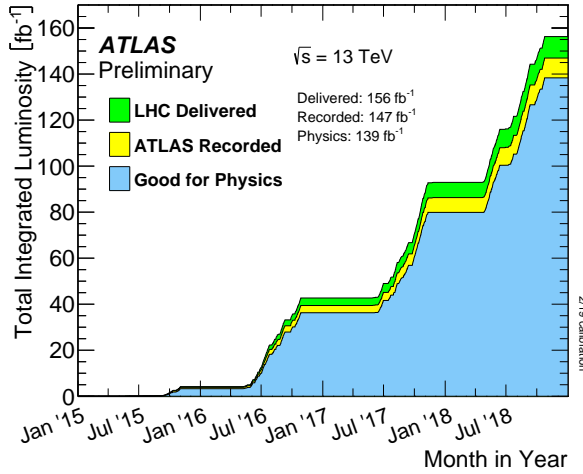


Figure 3.4: Delivered, recorded, and usable integrated luminosity as a function of time over the course of Run 2 [35]. A total of 139 fb^{-1} of collision data is labelled as good for physics, meaning all sub-detector systems were operating nominally.

432 which is often given as a time-averaged value $\langle \mu \rangle$. Histograms showing the number of pile-up interactions over the course of Run 2 are shown in Fig. 3.5.

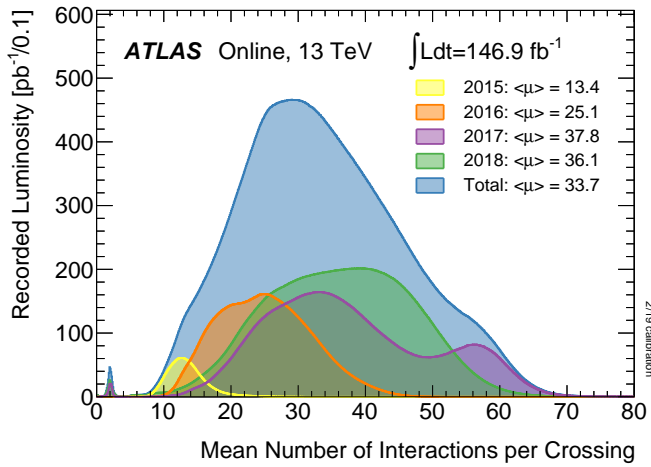


Figure 3.5: Average pile-up profiles measured by ATLAS during Run 2 [35].

⁴³⁴ 3.3 The ATLAS Detector

⁴³⁵ The ATLAS² detector is made up of several specialised sub-detectors which are
⁴³⁶ arranged concentrically around the nominal interaction point at the centre of the
⁴³⁷ detector, as shown in Fig. 3.6. The detector is designed to cover nearly the entire solid
⁴³⁸ angle around the collision point. In this section a brief overview of each sub-detector
⁴³⁹ is given, in order of increasing radial distance from the point of collision. The inner
⁴⁴⁰ tracking detector is described in Section 3.3.1, the electromagnetic and hadronic
⁴⁴¹ calorimeters in Section 3.3.2, the muon spectrometer in Section 3.3.3, and finally the
⁴⁴² trigger is described in Section 3.3.4. More complete information on the detector can
⁴⁴³ be found in Ref. [33], while an overview of physics performance is given in [41].

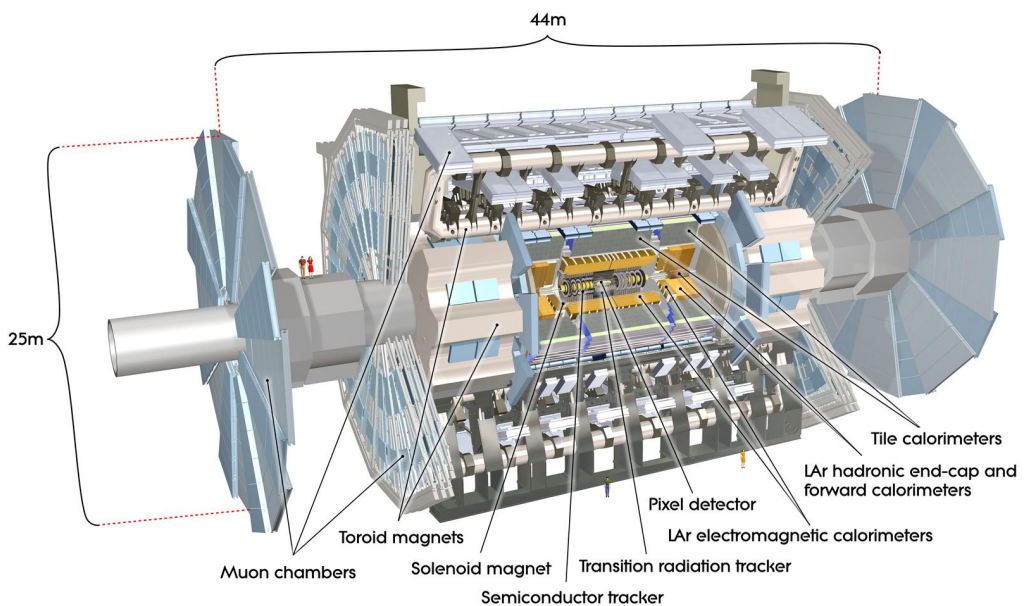


Figure 3.6: A 3D model of the entire ATLAS detector [42]. Cutouts to the centre of the detector reveal the different subdetectors which are arranged in concentric layers around the nominal interaction point.

²A Toroidal LHC ApparatuS.

⁴⁴⁴ 3.3.1 Inner Detector

⁴⁴⁵ The inner-detector system (ID) provides high-resolution charged particle trajectory
⁴⁴⁶ tracking in the range $|\eta| < 2.5$. The ID is immersed in a 2 T axial magnetic field,
⁴⁴⁷ produced by a superconducting solenoidal magnet, which enables the measurement
⁴⁴⁸ of particle momentum and charge. After Run 3, the ID will be replaced by the
⁴⁴⁹ ITk [43, 44].

⁴⁵⁰ The inner detector is made up of several sub-systems, shown in Figs. 3.7 and 3.8. The
⁴⁵¹ high-granularity silicon pixel detector covers the innermost region and typically pro-
⁴⁵² vides four spacepoint measurements per track. It is followed by the silicon microstrip
⁴⁵³ tracker (SCT), which usually provides a further four spacepoint measurements (8
⁴⁵⁴ hits) per track. These silicon detectors are complemented by the Transition Radiation
⁴⁵⁵ Tracker (TRT), which enables radially extended track reconstruction up to $|\eta| = 2.0$
⁴⁵⁶ and typically provides 33 (38) additional hits in the barrel (endcap).

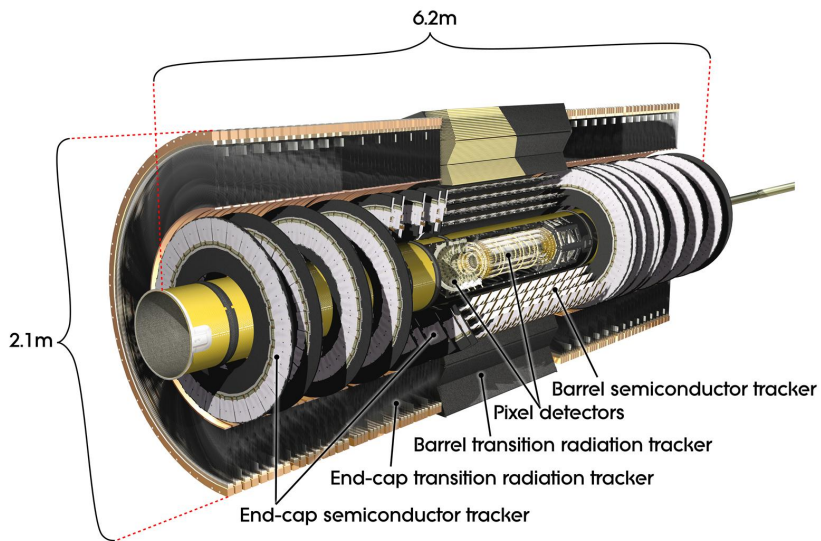


Figure 3.7: A 3D model of the ATLAS ID showing the pixel, SCT and TRT subdetectors [45].

⁴⁵⁷ The target inverse momentum resolution for the combined ID measurement is
⁴⁵⁸ parameterised as a function of the track transverse momentum and polar angle [41].

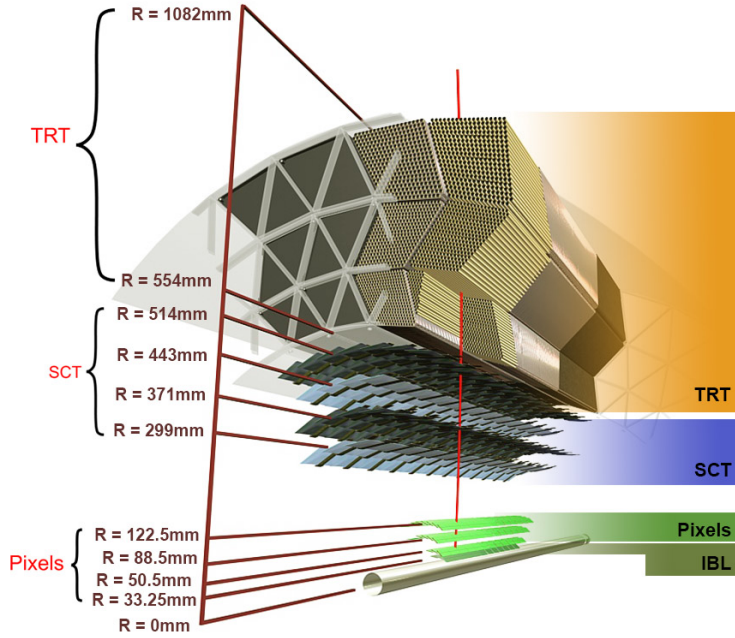


Figure 3.8: A cross-sectional view of the ATLAS ID, with the radii of the different barrel layers shown [38].

⁴⁵⁹ The parameterisation is given by

$$\sigma(1/p_T) = 0.36 \oplus \frac{13}{p_T \sin \theta} \text{ TeV}^{-1}, \quad (3.7)$$

⁴⁶⁰ where \oplus denotes a sum in quadrature. For low- p_T tracks (e.g. $p_T \approx 500 \text{ MeV}$) in the
⁴⁶¹ central region this corresponds to a relative error of approximately 0.01%. Meanwhile
⁴⁶² for high- p_T tracks (e.g. $p_T \approx 100 \text{ GeV}$) in the central region this corresponds to
⁴⁶³ a relative error of approximately 4%. The momentum resolution generally good
⁴⁶⁴ enough to correctly identify the sign of the charge on particles up to the highest
⁴⁶⁵ energies expected at the LHC. The transverse impact parameter resolution $\sigma(d_0)$ is
⁴⁶⁶ parameterised similarly as

$$\sigma(d_0) = 11 \oplus \frac{115}{p_T \sin \theta} \mu\text{m}. \quad (3.8)$$

⁴⁶⁷ Typical uncertainties for the transverse IP resolution are 230 μm and 11 μm for low
⁴⁶⁸ and high- p_T tracks in the central region, respectively.

⁴⁶⁹ Pixel Detector

⁴⁷⁰ The silicon pixel detector is comprised of four cylindrical barrels at increasing radii
⁴⁷¹ from the beamline, and four disks on each side. The innermost barrel layer is the
⁴⁷² insertable B-layer (IBL), shown in Fig. 3.9. The IBL was installed before Run 2 [46,47]
⁴⁷³ and lies approximately just 33 mm from the beam axis. The second-to-innermost layer
⁴⁷⁴ is often referred to as the B-layer. The specification of the pixel detector determines
⁴⁷⁵ the impact parameter resolution and the ability to reconstruct primary and secondary
⁴⁷⁶ vertices. The detector is required to have a high granularity (i.e. resolution) to
⁴⁷⁷ maintain the low occupancy required to resolve nearby particles. Individual pixels
⁴⁷⁸ are 50 μm in the transverse direction $R\phi$ and 400 μm in the longitudinal z direction
⁴⁷⁹ (250 μm for the IBL). Cluster positions have a resolution of approximately 10 μm in
⁴⁸⁰ $R\phi$ and 100 μm in z .

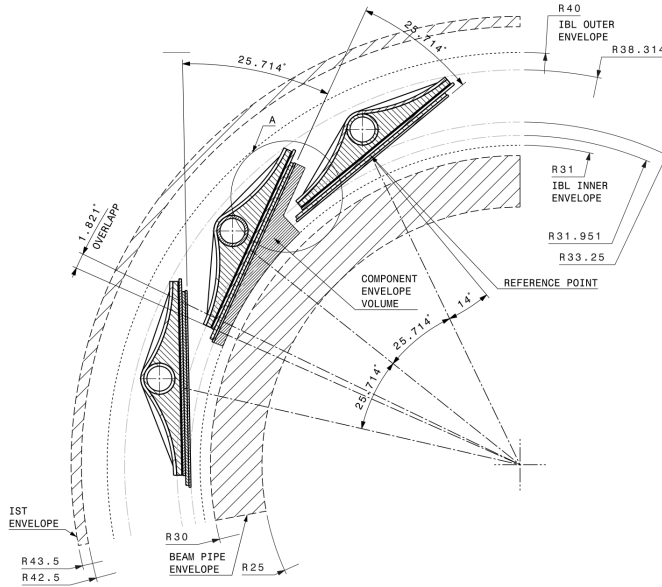


Figure 3.9: A schematic cross-sectional view of the ATLAS IBL [46].

⁴⁸¹ Semi-Conductor Tracker (SCT)

⁴⁸² The SCT is made up of four concentric barrel layers in the central region, and nine
⁴⁸³ disks in each end-cap. Each layer is itself made of a pair of silicon microstrip layers,
⁴⁸⁴ with a small stereo angle (20 mrad) between the two layers enabling the z -coordinate

485 to be measured from a pair of strip measurements. The SCT typically provides four
486 precision spacepoint measurements (eight strip measurements) per track in the barrel
487 region. These have intrinsic uncertainties of $17\text{ }\mu\text{m}$ in the transverse direction $R\phi$, and
488 $580\text{ }\mu\text{m}$ in the longitudinal direction z [48]. The measurements provide a contribution
489 to the measurement of charged particle momentum and impact parameter.

490 **Transition Radiation Tracker (TRT)**

491 The TRT is a straw-tube tracker which complements the higher-resolution silicon-
492 based tracks by offering a larger number of hits per track (typically more than 30)
493 and a long lever arm, which aids the accurate measurement of particle momentum.
494 It is made up of approximately 300 000 drift tubes with a diameter of 4 mm which
495 are filled with an argon/xenon gas mixture. The walls of each tube are electrically
496 charged, and a thin conducting wire runs along the center. When a charged particle
497 traverses a tube, it ionises the gas and the resulting liberated electrons drift along
498 the electric field to the wire, where an associated charge is registered. In the barrel
499 the straws run parallel to the z -axis and therefore the TRT only provides tracking
500 information in $R\phi$. Straws are arranged radially in the end-caps. The resulting
501 two-dimensional spacepoints have a resolution of approximately $120\text{ }\mu\text{m}$. The spaces
502 between the straws are filled with a polymer which encourages the emission of
503 transition radiation, aiding electron identification.

504 **3.3.2 Calorimeters**

505 The calorimeter system measures the energy of incident particles over the range
506 $|\eta| < 4.9$. There are two main sub-systems: the electromagnetic calorimeter (ECal),
507 which focuses on the measurement of electrons and photons, and the hadronic
508 calorimeter (HCal), which measures the energy of hadrons. A schematic view of the
509 calorimeter system is shown in Fig. 3.10. Upon entering the calorimeter, incident
510 particles will interact with the detector material to produce a shower of secondary
511 particles with reduced energies. The charge deposited in this process is measured to
512 reconstruct the energy of the initial incident particle. The two calorimeter sub-systems
513 must provide strong containment of showering particles to prevent punch-through of
514 EM and hadronic particles to the HCal and muon systems respectively.

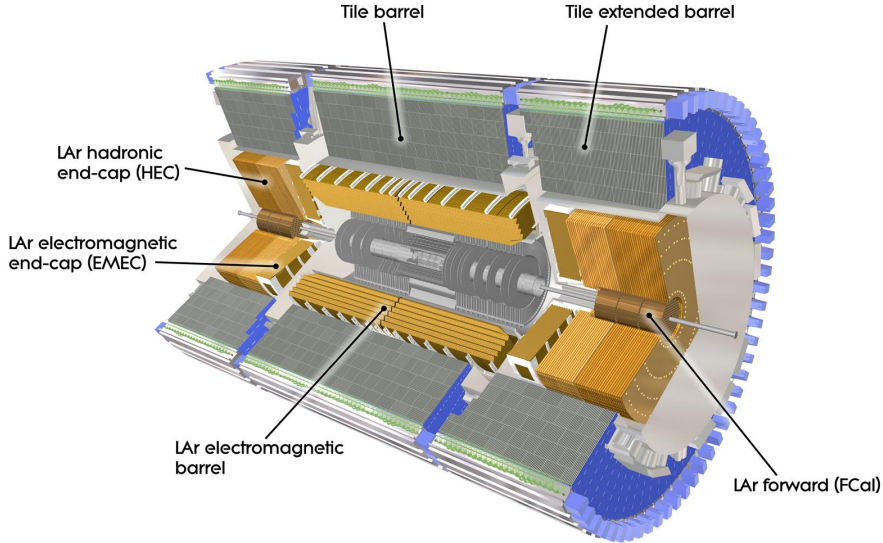


Figure 3.10: The ATLAS calorimeters [49]. The ECal uses LAr-based detectors, while the HCal uses mainly scintillating tile detectors. In the forward region the HCal also includes the LAr hadronic endcaps.

515 Liquid Argon (LAr) Electromagnetic Calorimeter

516 The more granular lead/liquid-argon ECal covers the region $|\eta| < 3.2$ and is split
 517 into barrel (covering $|\eta| < 1.475$) and end-cap (covering $1.375 < |\eta| < 3.2$) regions.
 518 EM calorimetry works by encouraging electrons and photons to interact with electric-
 519 ically charged particles in detector material via bremsstrahlung ($e \rightarrow e\gamma$) and pair
 520 production ($\gamma \rightarrow e^+e^-$). The EM calorimeter uses lead absorber plates to initiate
 521 EM showers, resulting in secondary particles which ionise the surrounding liquid
 522 argon. The charge is collected on copper electrodes and read out. The accordion
 523 geometry of the ECal allows for a full coverage in ϕ without any azimuthal cracks.

524 The energy resolution of the LAr calorimeter is made up of a sampling and a constant
 525 term, which are summed in quadrature to produce the overall energy resolution. The
 526 sampling term contributes approximately $10\%/\sqrt{E}$, while the constant term adds an
 527 additional 0.7%. Photons with moderate transverse energy $E_T \approx 50 \text{ GeV}$ have an
 528 overall energy resolution of at most 1.6% over most of the pseudorapidity range. At
 529 lower $E_T \approx 10 \text{ GeV}$, the resolution is degraded to approximately 5%. The resolution
 530 measurements are obtained from test beam data [41].

531 **Hadronic Tile Calorimeter**

532 In the central barrel region with $|\eta| < 1.7$, the HCal uses a tile calorimeter with
533 steel as an absorbing material, and scintillating tiles as the active material. Two
534 copper/liquid-argon calorimeter end-caps are also used. Incident hadrons interact
535 via the strong and electromagnetic forces with the absorber material, mainly loosing
536 energy due to multiple inelastic nuclear collisions. The active material captures the
537 resulting electrons and photons to measure the energy of the incident hadron.

538 The hadronic energy resolution of the HCal is parameterised as a function of the
539 hadron's transverse energy

$$\sigma(E_T)/E_T = 50\%/\sqrt{E_T} \oplus 3\%, \quad (3.9)$$

540 corresponding to a energy resolution of 11% (6.5%) for a hadron with E_T of approxi-
541 mately 10 GeV (50 GeV) [50].

542 **3.3.3 Muon Spectrometer**

543 Due to their higher mass, muons easily pass unimpeded through the ID and calorime-
544 ters and therefore require specialised detectors for their measurement. The Muon
545 Spectrometer (MS) is made up of dedicated tracking and triggering hardware, as
546 shown in Fig. 3.11. The precision tracking system uses three layers of monitored drift
547 tubes with a barrel region covering $|\eta| < 1.2$ and end-caps covering $1 < |\eta| < 2.7$.
548 The inner layers of the end-caps use cathode strip chambers to better cope with the
549 high occupancy in the forward region. The trigger system is comprised of resistive
550 plate chambers in the barrel region covering $|\eta| < 1.0$ and thin gap chambers in
551 the end-cap regions covering $1 < |\eta| < 2.4$. A set of three superconducting air-core
552 toroidal magnets, each made up of eight coils, is used in each of the barrel and
553 end-caps to deflect the muons as they pass through the MS, allowing their momentum
554 and charge to be measured from the direction and magnitude of curvature. The
555 toroidal magnets generate a field which is largely orthogonal to the muon trajec-
556 tories which allows for maximum deflection. The transverse momentum resolution
557 (measured for combined ID and muon tracks, see Section 3.4.4) has been measured

558 to be approximately 1.7% in the central region for low- p_T muons, increasing to 4% for high- p_T muons in the forward regions [51].

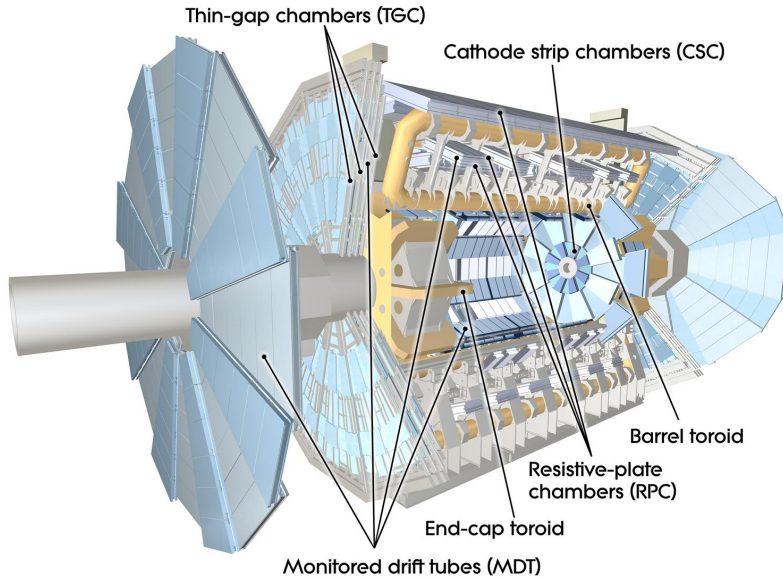


Figure 3.11: The ATLAS muon spectrometer [52].

559

560 3.3.4 The Trigger

561 The 25 ns bunch spacing used over the course of Run 2 corresponds to a bunch-
 562 crossing or event rate of 40 MHz (see Table 3.1). If the full information for the
 563 detector was written out for each event, this would correspond to the generation
 564 of 60 TB of data each second. This is more than can be feasibly read out from the
 565 hardware, processed and stored, requiring the use of a trigger system which quickly
 566 makes a decision about whether or not an event is potentially interesting and should
 567 be kept for further analysis. The trigger system is comprised of two levels which
 568 aim to identify various signatures, such as electrons, muons, taus, photons, and jets
 569 (including b -jets), as well as events with large total or missing transverse energy. The
 570 hardware-based Level-1 (L1) trigger uses coarse information from the calorimeters
 571 and MS to accept events at an average rate of 100 kHz approximately 2.5 μ s after the
 572 event. After the L1 trigger, the software-based High Level Trigger (HLT) makes use
 573 of 40 000 CPU cores to make a final selection on surviving events in approximately a
 574 few hundred milliseconds. The final event read-out rate is approximately 1.2 kHz,

575 corresponding to 1.2 GB s^{-1} of permanent data storage. More information is provided
576 in [53].

577 3.4 Reconstructed Physics Objects

578 Event reconstruction is the process of analysing the output from the detector to
579 determine the type and properties of particles present in an event. The reconstructed
580 event provides information about the underlying physics process that led to these
581 observable final state particles. Events passing the trigger selection (described in
582 Section 3.3.4) undergo offline reconstruction, which makes use of the full information
583 from the detector. Reconstruction and analysis of events relies on the extensive
584 ATLAS software stack, see Ref. [54] for more information.

585 Several different reconstructed objects are used for physics analyses. Objects relevant
586 to this thesis are described below.

587 3.4.1 Tracks

588 The reconstructed trajectories of charged particles are referred to as *tracks*. Tracks
589 are reconstructed from the energy depositions (called *hits*) left by the particles as
590 they traverse the inner detector. Tracks are used in the reconstruction of other
591 objects, including vertices and jets, so their accurate reconstruction is a critical
592 task. A comprehensive introduction to ATLAS tracking is available in Ref. [55],
593 while specific optimisations for dense environments are detailed in Refs. [56, 57]. An
594 overview of track reconstruction is given below.

595 Space-point Formation (Clustering)

596 When a charged particle traverses a silicon layer, charge can be collected in more
597 than one pixel or strip. This is due to the incident angle of the particles with respect
598 to the sensor, and also the drift of electrons between sensors caused by the magnetic
599 field. Clusters (also called *hits* or *space-points*) are formed by clustering neighbouring
600 pixels or strips and estimating locations of space-points using the shape and energy
601 distribution of the clusters.

602 Track Finding

603 Space-points are used to build track seeds. These are groups of three hits which
604 are geometrically compatible with being part of a track segment. A combinatorial
605 Kalman filter (KF) is used to build track candidates by extending track seeds. The
606 filter can create multiple track candidates per seed, with bifurcations along the track
607 occurring when more than one compatible space-point exists on a given layer. In
608 this way, the KF creates an excess of *track candidates*, which are only required to
609 satisfy basic quality requirements. Track candidates are allowed to reuse or *share*
610 hits freely (a single hit may be used by multiple track candidates). Typically, the
611 presence of shared hits is a predictor of a bad track due to the high granularity of
612 the ATLAS tracking detectors. At this stage, there can also be a large number of
613 incorrect hits assigned to otherwise good tracks, and additionally large numbers of
614 *fake* tracks, which are comprised of a majority of wrong hits and do not correspond
615 to the trajectory of any one physical particle (fake tracks are defined as those where
616 the majority of associated hits do not originate from one single truth particle, see
617 Eq. (5.5)). The low quality of tracks at this stage necessitates an ambiguity solving
618 step, in which candidates are cleaned, and the highest quality track are selected.

619 Ambiguity Solving

620 Ambiguity solving was introduced as part of the ATLAS New Tracking effort [55],
621 which was intended to improve track reconstruction performance in dense envi-
622 ronments. In the ambiguity solver, track candidates are processed individually in
623 descending order of a track score. The track score quantifies the likelihood of the
624 track corresponding to the trajectory of a real particle. Scoring uses a number of
625 variables, including the number and positions of hits (preferring hits in more precise
626 regions of the detector), the transverse momentum of the track and the track fit
627 quality. The track fit quality describes the quality of the track as the χ^2 divided
628 by the number degrees of freedom on the track. A preference for high transverse
629 momentum tracks promotes the successful reconstruction of the more physically
630 interesting energetic particles, and suppresses the large number of wrong hits assigned
631 to low momentum tracks. The ambiguity solver also penalises tracks with missing
632 hits on the innermost detector layers.

During the processing of a track candidate, the track is cleaned (whereby problematic hits are removed), and, if the resulting track satisfies the quality selection criteria, a high precision fit of the track parameters using the surviving hits is performed. The high precision fit makes full use of all available information, and uses an updated position and uncertainty estimate for each cluster obtained from a Neural Network (NN) [58]. If the track has reached this stage without being rejected by passing various quality requirements, it is re-scored and returned to the list of track candidates. If the same track is then processed again without requiring modification, it is added to the final track collection. Track candidates that fall below certain quality threshold are rejected. This selection does allow for the possibility of a track having small number of shared hits, as detailed in Table 3.2.

Parameter	Selection
p_T	$> 500 \text{ MeV}$
$ \eta $	< 2.5
$ d_0 $	$< 3.5 \text{ mm}$
$ z_0 \sin \theta $	$< 5 \text{ mm}$
Silicon hits	≥ 8
Shared silicon hits	< 2
Silicon holes	< 3
Pixel holes	< 2

Table 3.2: Quality selections applied to tracks, where d_0 is the transverse IP of the track, z_0 is the longitudinal IP with respect to the PV and θ is the track polar angle (see Section 3.2.2 for the IP definitions). Silicon hits are hits on the pixel and SCT layers. Shared hits are hits used on multiple tracks which have not been classified as split by the cluster-splitting neural networks [57]. A hole is a missing hit, where one is expected, on a layer between two other hits on a track.

644 Neural Network Cluster Splitting

As part of track cleaning, shared hits are classified by a NN to determine if they are compatible with the characteristic features of a merged cluster [56, 58]. A merged cluster is one made up of a combination of energy deposits from more than one particle, which have become merged due to the closeness of the associated particles and the limited resolution of the detector. It is common for clusters to become

merged in dense environments, as discussed in Section 4.2. If the cluster is predicted to be merged it is labelled as being freely shareable, or *split*. Hits not compatible with the merged hypothesis can still be shared by a limited number of tracks, but come with a penalty for the track which may hinder its acceptance into the final track collection.

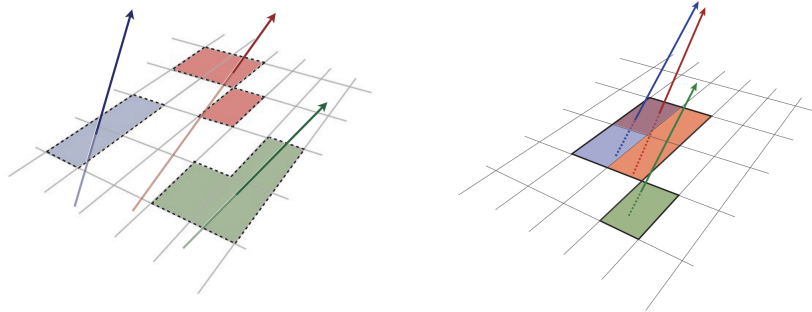


Figure 3.12: Particles (left) which have enough separation will leave charge depositions which are resolved into separate clusters. Sufficiently close particles (right) can lead to merged clusters. Their combined energy deposits are reconstructed as a single merged cluster [57].

654

655 Pseudotracking

Pseudotracking uses Monte Carlo truth information to group together all the hits left by each truth particle. Each collection of hits which, as a unit, satisfies basic quality requirements is directly used in a full resolution track fit. If the track fit is successful, a “pseudotrack” track is created and stored. If the track fit fails, or the collection of hits does not pass the basic quality requirements (for example because of a lack of hits) then the particle is said to be un-reconstructable. In this way, pseudotracking performance represents the ideal reconstruction performance given the ATLAS detector, with perfect hit-to-track association and track reconstruction efficiency. The approach was introduced in Ref. [59] as a way to obtain a fast approximation of tracking reconstruction for simulated data, however the technique has become a useful tool for studying tracking performance in general [56].

667 3.4.2 Vertices

668 Groups of reconstructed tracks can be examined to determine whether the particles
669 originated from a common spatial point of origin. This occurs when proton-proton
670 collisions take place (primary vertices), when a particle decays or radiates, and also
671 as a result of interaction with the detector material (secondary vertices). Vertex
672 reconstruction is made up of two stages. First, vertex finding takes place, which
673 is the process of grouping tracks into compatible vertices. Second, vertex fitting
674 combines information from compatible tracks to reconstruct the physical properties
675 of the vertex, such as mass and position.

676 Primary Vertices

677 Each proton-proton interaction happens at a *primary vertex* (PV). Primary vertices
678 are iteratively reconstructed with tracks using the iterative vertex finder (IVF) [60].
679 The *hard scatter vertex* of an event is chosen as the primary vertex whose associated
680 tracks have the largest sum of transverse momentum squared, $\Sigma(p_T^2)$.

681 Secondary Vertices

682 Secondary vertices (SV) occur when a particle radiates or decays at a sufficient
683 distance from the primary vertex to be resolved from the primary vertex (see
684 Section 4.2.1). Two widely used secondary vertexing tools are used within ATLAS:
685 SV1 and JetFitter [61]. Each attempts to reconstruct secondary vertices inside a jet
686 using the tracks associated to that jet (see Section 3.4.3 for more information about
687 track association). SV1 by design attempts to reconstruct only a single inclusive
688 vertex per jet. This inclusive vertex groups all b -hadron decay products, including
689 tracks from the b -hadron decay itself and tracks from $b \rightarrow c$ decays. The second tool,
690 JetFitter attempts to resolve each displaced vertex inside the jet, such that secondary
691 vertices from b -hadron decays are reconstructed separately to tertiary vertices from
692 $b \rightarrow c$ decay chains.

693 3.4.3 Jets

694 Jets are an aggregate reconstructed object corresponding to a collection of collimated
 695 stable particles which results from the presence of a quark or gluon. Jets are built
 696 by clustering constituent objects (e.g. tracks or calorimeter clusters) using a jet
 697 finding algorithm, for example the anti- k_t algorithm [62], which is implemented in
 698 FASTJET [63].

699 Objects can be associated to jets in one of two ways. The first is via a geometrical
 700 matching in ΔR (see) The second is via a ghost association [64], where the object is
 701 assigned a negligible momentum and re-clustered into the jet after its formation.

702 Jets from pile-up interactions are suppressed using [65]

703 EMTopo Jets

704 EMTopo jets are reconstructed from noise-suppressed topological clusters (topoclus-
 705 ters) of calorimeter energy depositions [66]. The clustering uses the energy significance
 706 of each cell, defined as

$$S_{\text{cell}} = \frac{E_{\text{cell}}}{\sigma_{\text{noise, cell}}}, \quad (3.10)$$

707 where E_{cell} is the energy measured in a given calorimeter cell, and $\sigma_{\text{noise, cell}}$ is the
 708 expected level of noise on the cell (e.g. from pile-up interactions). Topoclusters are
 709 formed from a seed cell with a large S_{cell} , and expanded by iteratively adding neigh-
 710 bouring cells with a sufficiently large energy significance. Collections of topoclusters
 711 are then clustered into a jet using the anti- k_t algorithm with a radius parameter of
 712 0.4 (small- R jets) or 1.0 (large- R jets). More information, including information on
 713 the calibration of the topocluster jet energy scale, is available in Ref. [66].

714 Particle Flow Jets

715 Particle-flow (PFlow) jets are reconstructed from particle-flow objects [67] using
 716 the anti- k_t algorithm with a radius parameter of 0.4. Particle-flow objects integrate
 717 information from both the ID and the calorimeters, improving the energy resolution

718 at high transverse momenta and reducing pile-up contamination. The PFlow jet
719 energy scale is calibrated according to Ref. [68].

720 **Large- R Jets**

721 Large- R jets have a radius parameter $R = 1.0$ and are built by clustering topological
722 calorimeter clusters using the anti- k_t algorithm [69]. The large radius parameter
723 is especially useful for containing the decay products of a boosted Higgs boson, as
724 discussed in Chapter 7. Due to their large size, large- R jets benefit from a grooming
725 procedure called trimming which remove soft contaminants inside the jet [70, 71].
726 Trimming aims to remove jet constituents from pile-up and the underlying event,
727 which helps to improve the jet mass resolution and its robustness to varying levels
728 of pile-up. The jet mass is computed using a combination of information from the
729 calorimeters and ID, and a calibration to data is applied [72].

730 **Track-jets**

731 Track-jets are built by clustering tracks using the anti- k_t clustering algorithm. They
732 are associated to large- R jets as sub-jets and used to identify large- R jets containing
733 b -hadrons. The radius parameter is allowed to vary with transverse momentum such
734 that a broader cone (up to $R = 0.4$) is used for low- p_T track-jets and a narrower
735 cone (down to $R = 0.02$) for high- p_T track-jets [73, 74]. The narrower cone is better
736 suited to clustering highly collimated jet constituents at high- p_T .

737 **Jet Flavour Labels**

738 Jet flavour labels are assigned to small- R jets according to the presence of a truth
739 hadron within $\Delta R(\text{hadron}, \text{jet}) < 0.3$ of the jet axis. If a b -hadron is found the jet is
740 labelled a b -jet. In the absence of a b -hadron, if a c -hadron is found the jet is called
741 a c -jet. If no b - or c -hadrons are found, but a τ is found in the jet, it is labelled as a
742 τ -jet, else it is labelled as a light-jet.

743 PFlow jets are used to train the algorithms discussed in Chapter 5 and Chapter 6.

744 Jet Track Association

745 Tracks are associated to small- R jets using a ΔR association cone, the width of which
 746 decreases as a function of jet p_T , with a maximum cone size of $\Delta R \approx 0.45$ for jets
 747 with $p_T = 20$ GeV and minimum cone size of $\Delta R \approx 0.25$ for jets with $p_T > 200$ GeV.
 748 If a track is within the association cones of more than one jet, it is assigned to the
 749 jet which has a smaller $\Delta R(\text{track}, \text{jet})$.

750 3.4.4 Leptons

751 Electrons and muons leave characteristic signatures that are picked up in the ECal
 752 and MS respectively. The reconstruction of both types of charged lepton is briefly
 753 outlined below.

754 Electrons

755 A diagrammatic view of electron reconstruction is shown in Fig. 3.13. Electrons
 756 candidates are reconstructed by matching PV-compatible³ inner detector tracks
 757 to topological calorimeter clusters. The track-cluster matching criteria takes into
 758 account the significant energy loss of the electron due to bremsstrahlung. If a match
 759 is found, a refit of the track is performed using the Gaussian Sum Filter (GSF) [75],
 760 which better handles trajectory reconstruction in the presence of bremsstrahlung.
 761 Various identification criteria are then applied to the candidates using a likelihood-
 762 based (LH) method to improve purity. These include requirements on the track
 763 quality and cluster matching, the shape of electromagnetic shower in the ECal,
 764 leakage into the HCal, and the amount of transition radiation detected in the TRT.
 765 Isolation criteria with respect to other nearby ID tracks and calorimeter clusters may
 766 also be applied. A full description can be obtained from Ref. [76].

767 Muons

768 Muon reconstruction makes use of the dedicated MS (see Section 3.3.3), the tracks
 769 from the ID, and the presence of characteristic signatures in the calorimeters. Muon

³The ID track associated with the electron is required to satisfy $d_0/s(d_0) < 5$ and $z_0 \sin \theta < 0.5$ mm.

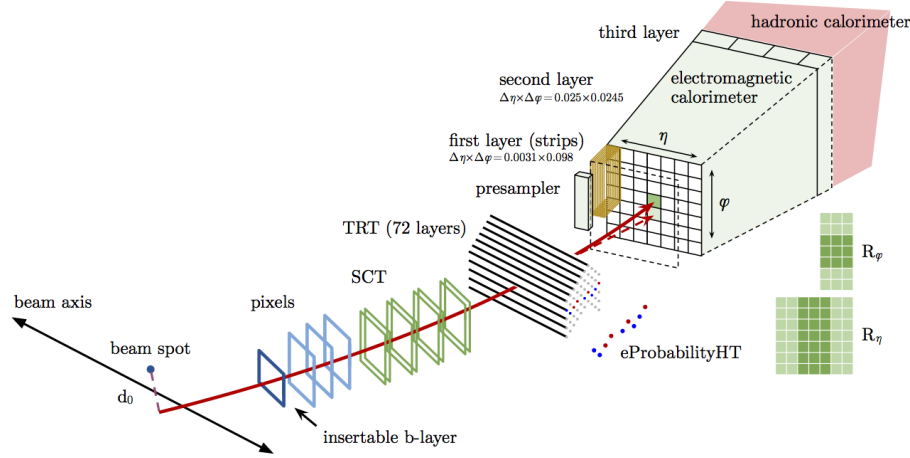


Figure 3.13: A sketch of electron reconstruction using the ATLAS detector [76]. Electron reconstruction makes use of the entire ID and the calorimeters.

770 tracks (i.e. a track reconstructed in the MS) are reconstructed by connecting straight-
 771 line track segments, which are identified via a Hough transform, and combined into
 772 a approximately parabolic trajectory. Finally, a global χ^2 fit is performed, taking
 773 into account possible interactions between the muon and the detector material. A
 774 reconstructed muon is called *combined* if it can be matched successfully to an to
 775 an ID track. Combined muons undergo a further fit with the combined ID and MS
 776 hits, with the energy loss due to the traversal of the calorimeters being taking into
 777 account.

778 After reconstruction, candidate undergo an identification processes which helps to
 779 efficiently identify prompt muons whilst rejecting background signals (e.g. non-
 780 prompt muons from pion and kaon decays, the punch-through of a hadron from the
 781 calorimeter, or the semi-leptonic decay of a heavy flavour hadron). Combined muon
 782 identification takes into account discrepancies in the p_T and charge measurements
 783 in the MS and ID, and the χ^2 of the combined track fit. Selections on the number
 784 of hits in the ID and MS are also applied. At the medium identification working
 785 point, approximately 96% of prompt muons with $20 \text{ GeV} < p_T < 100 \text{ GeV}$ are
 786 successfully identified. On top of the identification requirements, a number of
 787 isolation requirements can also be applied to further suppress background signals.

788 More information on muon reconstruction, identification and isolation can be found
 789 in Ref. [77].

790 3.4.5 Missing Transverse Momentum

791 An imbalance in the final state transverse momentum can occur as a result of
792 incomplete measurement of the final state particles. In particular, neutrinos are
793 not measured by the detector and contribute to the missing transverse momentum
794 $\mathbf{E}_T^{\text{miss}}$. Incomplete detector acceptance and inaccuracies in the reconstruction of the
795 final state can also contribute to the missing transverse momentum of an event. In
796 order to calculate the missing transverse momentum, the negative vector sum of
797 the momentum of all photons, leptons and small- R jets with $p_T > 20 \text{ GeV}$ is taken.
798 The momenta of tracks associated to the primary vertex are also taken into account.
799 The magnitude of $\mathbf{E}_T^{\text{miss}}$ is written E_T^{miss} . More information about missing transverse
800 momentum reconstruction is provided in [78].

801 **Chapter 4**

802 **Tracking and Flavour Tagging**

803 Many ATLAS analyses rely on flavour tagging, which is the identification of jets
804 containing heavy-flavour hadrons (b -hadrons and c -hadrons) as opposed to those
805 containing only light-flavour hadrons or gluons. In particular, b -tagging is the
806 identification of jets originating only from b -hadrons (i.e. b -jets).

807 Flavour tagging is a critical component of the physics programme of the ATLAS
808 experiment. It is of crucial importance for the study of the Standard Model (SM)
809 Higgs boson and the top quark, which decay preferentially to b -quarks [79, 80], and
810 additionally for several Beyond the Standard Model (BSM) resonances that readily
811 decay to heavy flavour quarks [81].

812 The various b -jet identification algorithms (also called *taggers*) used in ATLAS
813 are described in Section 4.1. These work by identifying the unique signatures of
814 b -jets, which are outlined in Section 4.2. Ultimately, the tagging algorithms use
815 input information about the reconstructed jet and its associated tracks. Successful
816 b -tagging relies therefore on the efficient and accurate reconstruction of tracks, and
817 especially those tracks corresponding to the products of b -hadron decays. A summary
818 of the challenges facing tracking and b -tagging at high transverse momentum is given
819 in Section 4.2.2. Some preliminary investigations into improving tracking in the
820 high- p_T regime are investigated in Section 4.3. In Section 4.4 the conclusions of this
821 chapter are summarised.

4.1 *b*-tagging Algorithms

The current ATLAS flavour tagger, DL1r [82], is a deep neural network which accepts as inputs the outputs of a number of independently optimised *low-level* algorithms [61], as shown in Fig. 4.1. Correspondingly, DL1r is referred to as a *high-level* tagger (i.e. one that uses a multivariate approach to combine outputs of the low-level taggers). Each of these low-level algorithms reconstructs distinct features of the experimental signature of heavy flavour jets using the tracks associated to the jet. The low-level algorithms are a combination of manually optimised reconstruction algorithms for example the SV1 and JetFitter algorithms which reconstruct displaced decay vertices [61, 83], and trained taggers such as RNNIP and DIPS which use IP and hit information from a variable number of tracks [84, 85].

In addition to DL1r, another widely used high-level tagger is the MV2c10 algorithm [61, 82, 86]. This tagger is used in the analysis described in Chapter 7. Similar to DL1r the MV2c10 algorithm takes inputs from the outputs of a number of low-level algorithms (IPxD, SV1 and JetFitter). The outputs of the low-level algorithms are provided as inputs to a boosted decision tree. The working point is tuned to achieve an average *b*-jet efficiency of 70% on simulated $t\bar{t}$ events. At this efficiency working point, rejection factors for *c*-jets and light-jets are approximately 9 and 304 respectively.

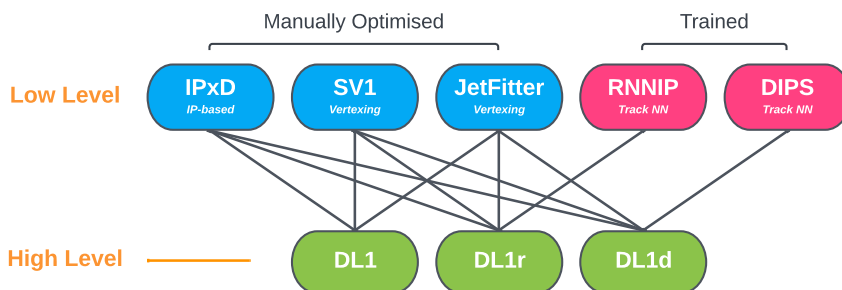


Figure 4.1: An overview of different high and low level level taggers used in ATLAS. The low level taggers are IPxD, SV1 and JetFitter, and RNNIP and DIPS [61, 83–85]. The outputs of these taggers are fed into the high level taggers DL1, DL1r and DL1d [82, 87].

841 4.2 b -hadron Reconstruction

842 This section outlines the typical detector signature of a b -hadron in Section 4.2.1
 843 and discusses some associated reconstruction difficulties in Section 4.2.2.

844 4.2.1 Decay Topology

845 b -hadrons are quasi-stable bound states of a bottom quark and one or more lighter
 846 quarks. Collectively, these are the B -mesons (e.g. $B^+ = u\bar{b}$, $B^0 = d\bar{b}$) and baryons
 847 (e.g. $\Lambda_b^0 = udb$). After a b -quark is produced as the result of a proton-proton collision,
 848 they quickly hadronise. The hadronisation process is hard – around 70-80% of
 849 the b -quark’s momentum is passed to the b -hadron, with the rest being radiated
 850 as prompt hadronisation or fragmentation particles. See Ref. [88] for a more in
 851 depth discussion on hadronisation and the closely related process of fragmentation.
 852 Henceforth the combined hadronisation and fragmentation products will be referred
 853 to collectively as fragmentation.

854 b -hadrons are interesting objects of study due to their relatively long proper lifetimes
 855 $\tau \approx 1.5$ ps [89]. This lifetime corresponds to a proper decay length $c\tau \approx 450$ μm . In
 856 the rest frame of the detector, the typical b -hadron travels a distance

$$d = \gamma\beta c\tau \approx \gamma c\tau \quad (4.1)$$

857 before decaying, where in the high energy limit $\gamma = E_b/m_b$ and $\beta = v/c = 1$.

858 For a 50 GeV b -hadron, this gives $d \approx 4.5$ mm, which is displaced enough to be
 859 resolved from the primary vertex. Meanwhile for a 1 TeV b -hadron, $d \approx 90$ mm –
 860 well beyond the radius of the first pixel layer (the IBL) which is situated at a radius
 861 of approximately 33 mm from the center of the detector (the distance varies due
 862 to the interleaved structure) Fig. 4.2 shows how the mean decay radius varies as a
 863 function of b -hadron p_T . This significant displacement is characteristic of b -jets and
 864 makes it possible to reconstruct secondary vertices at the b -hadron decay point.

865 b -hadrons decay weakly to on average four or five collimated stable particles [90].
 866 These particles, along with any other fragmentation particles, are reconstructed in
 867 the detector as a jet. A b -jet has several characteristic features which differentiate it

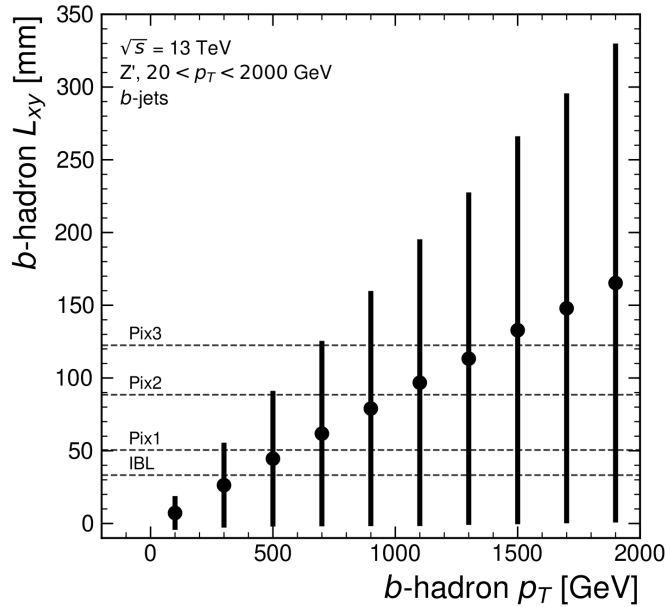


Figure 4.2: The truth b -hadron decay radius L_{xy} as a function of truth transverse momentum p_T for reconstructed b -jets in Z' events. Error bars show the standard deviation. The pixel layers are shown in dashed horizontal lines.

from light-jets. The primary feature is the presence of a high mass secondary vertex that is significantly displaced from the primary vertex. Reconstruction of these vertices from tracks with common points of spatial origin is a common approach used in the identification of b -jets.

Additional signatures of b -hadrons are as follows. Associated tracks and SVs can have a large transverse impact parameter d_0 as a result of the b -hadron displacement (as shown in Fig. 4.3). Since it is common for the b -hadron to decay to a c -hadron with non-negligible lifetime, tertiary vertices can be found within b -jets resulting from $b \rightarrow c$ decay chains. The b - or c -hadron also decays semileptonically in approximately 40% of cases [16]. The presence of a reconstructed electron or muon inside a jet can also be a key indicator that the jet was instantiated by a b -hadron.

These signatures are primarily identified using tracks associated to jets, or using reconstructed electrons or muons, which also rely on tracks as discussed in Section 3.4.4. As such, efficient and accurate track reconstruction is essential for high performance flavour tagging.

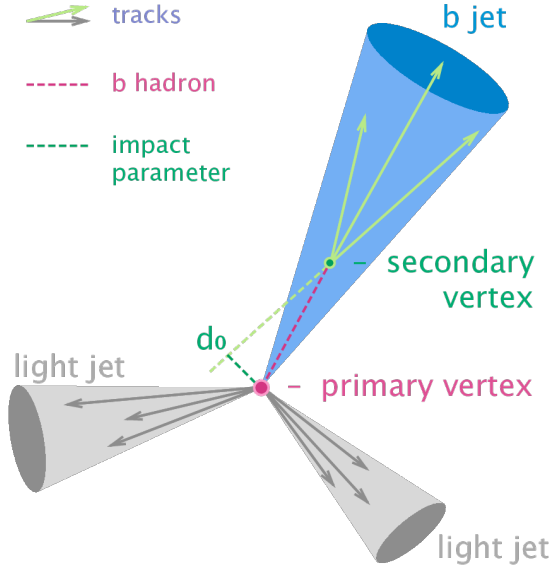


Figure 4.3: Diagram of a typical b -jet (blue) which has been produced in an event alongside two light jets (grey) [91]. The b -hadron has travelled a significant distance (pink dashed line) from the primary interaction point (pink dot) before its decay. The large transverse impact parameter d_0 is a characteristic property of the trajectories of b -hadron decay products.

883 In cores of high- p_T jets, track density is high due to the increased multiplicity and
 884 collimation of tracks (see Chapter 4). As a result, the separation between tracks
 885 can be of the same order as the active sensor dimensions, resulting in an increase
 886 in merged clusters and tracks which share hits [57]. Due to the relatively long
 887 lifetimes of b -hadrons and c -hadrons, which can traverse several layers of the ID
 888 before decaying and have highly collimated decay products, the presence of shared
 889 or missing hits is a critical signature of heavy flavour jets.

890 4.2.2 Challenges

891 As discussed, a necessary requirement for successful b -tagging is the efficient and
 892 accurate reconstruction of the charged particle trajectories in the jet. For high p_T
 893 jets ($p_T > 200$ GeV) this task becomes difficult due to a combination of effects. As
 894 the b -jet energy increases, the multiplicity of the fragmentation products inside the
 895 jet increases, while the multiplicity of the products of the weak decay is unaffected.
 896 The “signal” tracks (those from the weak decay of the b -hadron) therefore become
 897 significantly outnumbered. Both fragmentation and b -hadron weak decay products

898 also become increasingly collimated as their inherited transverse momentum increases.
 899 At high energies, the increased decay length of b -hadrons (and c -hadrons) means
 900 that decay products have less of an opportunity to diverge before reaching the
 901 first tracking layers of the detector (shown in Fig. 4.4). If the weak decay of the
 902 b -hadron takes place close enough to a detector layer, or if the particles are otherwise
 903 sufficiently collimated, charge deposits left by nearby particles may not be resolved
 904 individually, instead being reconstructed as merged clusters.

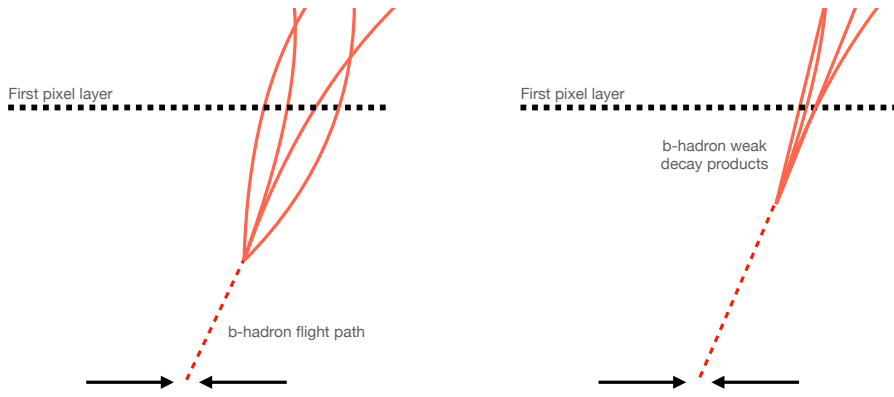


Figure 4.4: At lower p_T (left) the decay length of the b -hadron is on average reduced, and the decay tracks are less collimated. At higher p_T (right) the b -hadron decay length increases and the resulting decay tracks are more collimated and have less distance over which to diverge before reaching detector elements. As a result, the ID may be unable to resolve charged depositions from different particles, resulting merged clusters.

905 As discussed in Section 3.4.1, merged clusters are generally rare, and so shared
 906 hits generally predict bad tracks and are correspondingly penalised during track
 907 reconstruction. However, in the core of high p_T b -jets the density of particles is high
 908 enough that the probability of cluster merging increases dramatically. Successful
 909 reconstruction of such tracks requires the presence of shared hits to be effectively
 910 dealt with but in the standard reconstruction the presence of these can end up
 911 impairing the successfully reconstruction of the track. Furthermore, decays may also
 912 take place inside the tracking detectors themselves, which at best leads to missing
 913 measurements on the most sensitive detector layers, and at worst can lead to wrong
 914 inner layer hits being added to displaced tracks, since the reconstruction process
 915 penalises tracks without inner layer hits.

916 The above effects create two related, but distinct problems for b -tagging. The first
 917 part is a drop in track reconstruction efficiency. The presence of shared and missing
 918 hits reduces a track's score in the ambiguity solver meaning that higher ranking, but
 919 potentially worse, track candidates are processed first and take ownership of the hits.
 920 This can make it difficult for otherwise reasonable b -hadron decay tracks to meet
 921 the ambiguity solver's stringent track quality requirements, leading to their rejection
 922 at this stage and an overall decrease in the b -hadron decay track reconstruction
 923 efficiency. As shown in Fig. 4.5, this can result in a large drop in reconstruction
 924 efficiency for b -hadron decay products of up to 50% for at $p_T = 2 \text{ TeV}$.

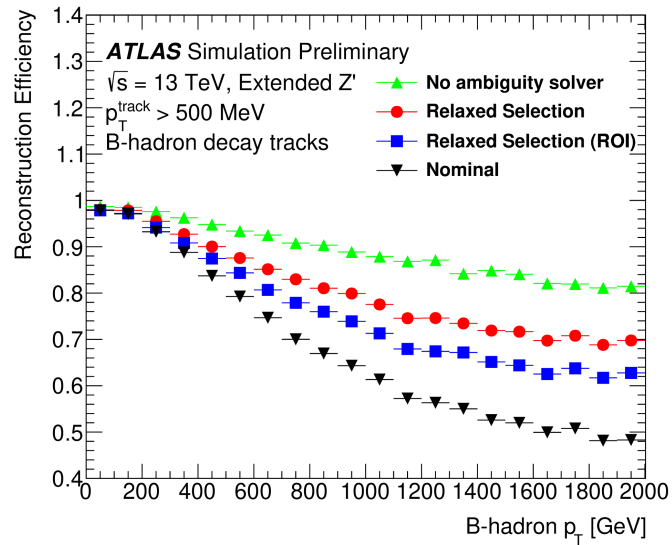


Figure 4.5: b -hadron decay track reconstruction efficiency as a function of truth b -hadron p_T [92]. Nominal track reconstruction is shown in black, while the track reconstruction efficiency for track candidates (i.e. the pre-ambiguity solver efficiency) is shown in green. For high- p_T b -hadrons, the ambiguity solver is overly aggressive in its removal of b -hadron decay tracks. Suggestions for the improvement of the track reconstruction efficiency in this regime by the loosening of cuts in the ambiguity solver are shown in blue and red.

925 The second part of the problem is that, due to the high multiplicity of clusters
 926 available for assignment in the vicinity of the typical high- p_T b -hadron decay track,
 927 and also given the strong positive bias of the ambiguity solver towards those tracks
 928 with pixel measurements in each layer (especially the innermost IBL measurement),
 929 many b -hadron decay tracks are assigned incorrect inner layer hits. This is only a
 930 problem for those decay products which were produced within the pixel detector
 931 as a result of a significantly displaced b -hadron decay, and so do not have a correct

hit available for assignment. Fig. 4.6 shows the number of hits as a function of the reconstructed track p_T for fragmentation tracks and tracks from the weak decay of the b -hadron. The baseline tracks represent the standard reconstruction setup, while the pseudotracks represent the ideal tracking setup as outlined in Section 3.4.1. Hit multiplicities on the pseudotracks decrease at high p_T due to the flight of the b -hadron before its decay. The baseline tracks have more hits than the pseudotracks, indicating that they are being incorrectly assigned additional hits on the inner layers of the detector.

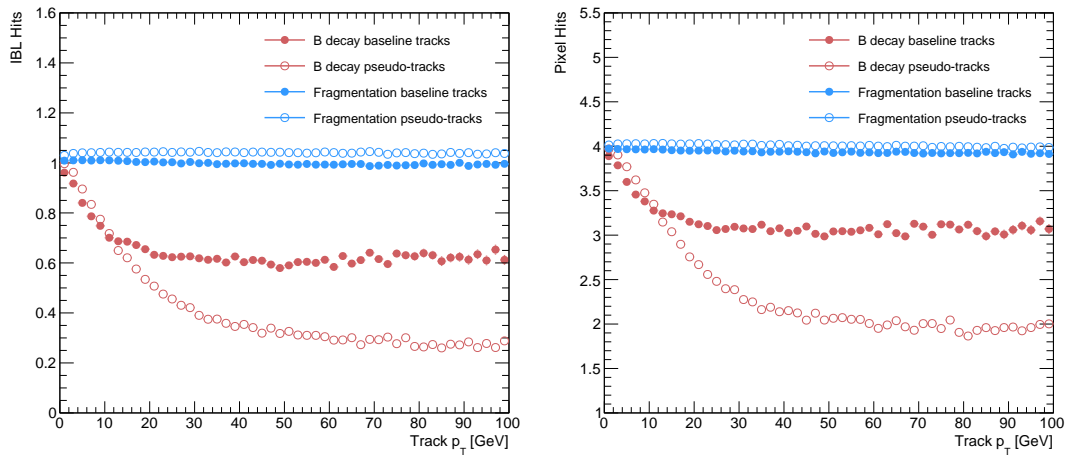


Figure 4.6: Hit multiplicities on the IBL (left) and the pixel layers (right) as a function of the p_T of the reconstructed track for tracks in jets in a Z' sample at $\sqrt{s} = 13$ TeV. Tracks from the weak decay of the b -hadron are shown in red, while fragmentation tracks (which are prompt) are in blue. Baseline tracks are those produced in the standard reconstruction described in Section 3.4.1, while pseudotracks represent the ideal performance of the ATLAS detector and are described in Section 3.4.1.

These incorrect hits may skew the parameters of the track, which can in turn lower the performance of the downstream b -tagging algorithms. In particular, b -tagging algorithms rely heavily on the transverse impact parameter significance $s(d_0)$ of the track (see Section 3.2.2). The quality of this measurement is expected to be adversely affected by wrong inner-layer hits on the track. Furthermore, multiple tracks sharing an incorrect hit can lead to the creation of spurious secondary vertices, which can cause further problems for the b -tagging algorithms.

The combination of the effects described makes reconstructing tracks in the core of high p_T b -jets particularly challenging. The reduced reconstruction efficiency of b -hadron decay tracks and incorrectly assigned hits is thought to be the primary

cause of the observed drop in b -tagging efficiency at high energies, however further study is required to determine which effect may dominate.

4.3 Investigations into High p_{T} b -hadron Tracking

In Section 4.3.1 pseudotracks, a key tool for studying the ideal tracking performance of the ATLAS detector, are used to study the shared hit requirements on tracks in the dense cores of high- p_{T} b -jets. Section 4.3.2 details a study which investigated modifying the global track fitter to improve reconstruction performance in this regime.

4.3.1 Shared Hits

The ambiguity solver is not run for pseudotracks. However, if the standard track collection is produced alongside the pseudotracks, then cluster splitting neural networks will be run for the standard tracks, and the resulting classification of clusters will be propagated to hits on pseudotracks. This quirk allows one to study the inefficiencies of the cluster splitting process, and relatedly to determine whether shared hit cuts in the ambiguity solver are too loose or too tight. The fraction of hits that are shared for the IBL and the B-layer is shown in Fig. 4.7. The shared hits on pseudotracks represent correctly assigned hits from merged clusters that were not able to be classified as split by the cluster splitting neural networks. As such, these represent the number of shared hits the ambiguity solver should aim to allow given the current performance of the cluster splitting algorithm. For shared hits on the IBL for particles produced before the IBL, the baseline selection appears to be successful in disallowing excessive numbers of shared hits. However, the ambiguity solver fails to limit shared hits for those particles produced after the IBL, reflecting the previously discussed problem of displaced tracks picking up incorrect hits. Meanwhile, it is clear that for the B-layer, the ambiguity solver is being overly aggressive in its rejection of shared hits.

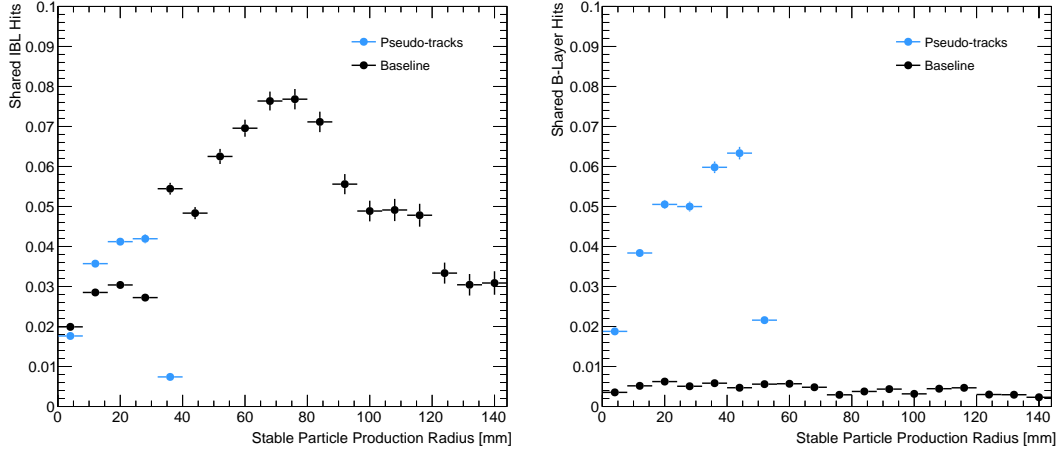


Figure 4.7: The fraction of IBL (left) and B-layer (right) hits which are shared on b -hadron decay tracks as a function of the production radius of the b -hadron decay product for tracks in jets in a Z' sample at $\sqrt{s} = 13$ TeV. Pseudotrack represent the ideal performance given the ATLAS detector, see Section 3.4.1.

976 4.3.2 Global χ^2 Fitter Outlier Removal

977 This section documents ongoing studies into improving hit-to-track assignment by
 978 using the Global χ^2 Fitter (GX2F) to identify and prevent incorrect hits from
 979 being assigned to tracks during the track fit. This is in contrast to a previously
 980 investigated approach [93] which attempted to identify and remove incorrect hits
 981 after the reconstruction of the track. As part of the track fit, an outlier removal
 982 procedure is run, in which suspicious hits are identified and removed.

983 The GX2F code, as a relatively low-level component of track reconstruction, has
 984 not undergone significant modification for several years, and was originally only
 985 optimised in the context of prompt, isolated tracks. During this time, a new tracking
 986 sub-detector, the IBL, was installed. The motivation for looking at the GX2F is that
 987 these changes may require re-optimisation of the GX2F code, and in particular the
 988 outlier removal procedures. Further motivation for this approach comes from the
 989 low rate of labelled outliers in baseline tracking, in contrast to the relatively higher
 990 rate of tracks with an incorrect IBL hit.

991 Implementation

992 The outlier removal procedure for the pixel detector is described in this section.
 993 The hits on the track are looped over in order of increasing radial distance to the
 994 beam pipe. For each hit, errors $\sigma(m_i)$ on the measurement of the transverse and
 995 longitudinal coordinates are calculated. These errors are dependent on the sub-
 996 detector which recorded the measurement (some sub-detectors are more precise than
 997 others). Additionally, a residual displacement $r_i = m_i - x_i$ between the predicted
 998 position of the track x_i (inclusive of the current measurement), and the position of
 999 the hit itself, m_i , is calculated. The pull p_i on the track state due to the current
 1000 measurement is calculated according to

$$1001 p_i = \frac{m_i - x_i}{\sqrt{\sigma(m_i)^2 - \sigma(x_i)^2}} \quad (4.2)$$

1002 This pull is computed for the transverse and longitudinal coordinates of the mea-
 1003 surement, and the maximum of the two is selected and checked to see if it exceeds
 1004 a certain selection threshold. If it does, the hit will be removed if the track also
 1005 exceeds a threshold on the total χ^2/n , where n is the number of degrees of freedom
 1006 on the track. The results of varying the outlier selection and χ^2/n thresholds are
 described below.

1007 Selection Optimisation

1008 A systematic variation of the outlier selection and χ^2/n thresholds has been carried
 1009 out. Both thresholds were reduced in fixed step sizes of 0.25 for the outlier selection
 1010 threshold and 1 for the χ^2/n threshold. The results for the best performing selections
 1011 are discussed below. The value of the outlier selection threshold was reduced from 4
 1012 down to 1.75, a change which affects the silicon layers (the TRT has separate outlier
 1013 removal logic). Furthermore, a specific cut for the IBL was introduced, and after
 1014 optimisation is set to 1.25. The second threshold on the track χ^2/n was also reduced
 1015 from 7 to 4. Finally, instead of taking the maximum of the pulls in the longitudinal
 1016 and transverse directions, a quadrature sum is taken of these two values and used.
 1017 This variation is labelled “Mod GX2F” and was found to improve performance.

1018 The results are shown in Fig. 4.8 and demonstrate a reduction in wrong hit assignment
 1019 whilst also improving slightly the rate at which good hits are assigned to tracks. For
 1020 a 1 TeV track, the rate to assign good hits to the track increases by approximately
 1021 10%, while the rate to assign incorrect hits decreases by approximately 16%. The
 1022 improvements are also observed when looking inclusively in all tracks, which avoids
 1023 the need for a specific b -jet region-of-interest selection.

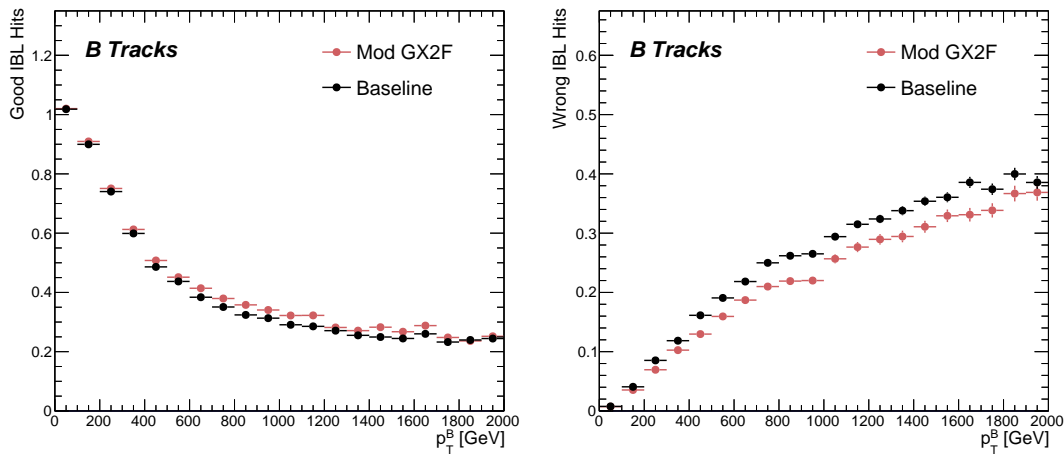


Figure 4.8: The average number of good (left) and wrong (right) IBL hits as a function of b -hadron p_T for tracks using baseline tracking (black) and the modified version of the outlier removal procedure (red).

1024 An improvement, though modest, of all track parameter resolutions and pulls is
 1025 observed. The improvement for the transverse impact parameter pull is shown in
 1026 Fig. 4.9. The results demonstrate an improvement in hit assignment, unchanged
 1027 reconstruction efficiency, and modest improvement in track parameter resolutions
 1028 and pulls. In addition, the truth match probability of tracks is unchanged, suggesting
 1029 that there is no increase in fake track rates. The changes are expected to have a
 1030 negligible impact on computational resources.

1031 4.4 Conclusion

1032 In this section, the difficulties facing efficient and accurate track reconstruction,
 1033 and hence performant b -tagging, have been outlined. The ambiguity solver, which
 1034 attempts to clean or reject tracks which have an excessive number of shared hits,

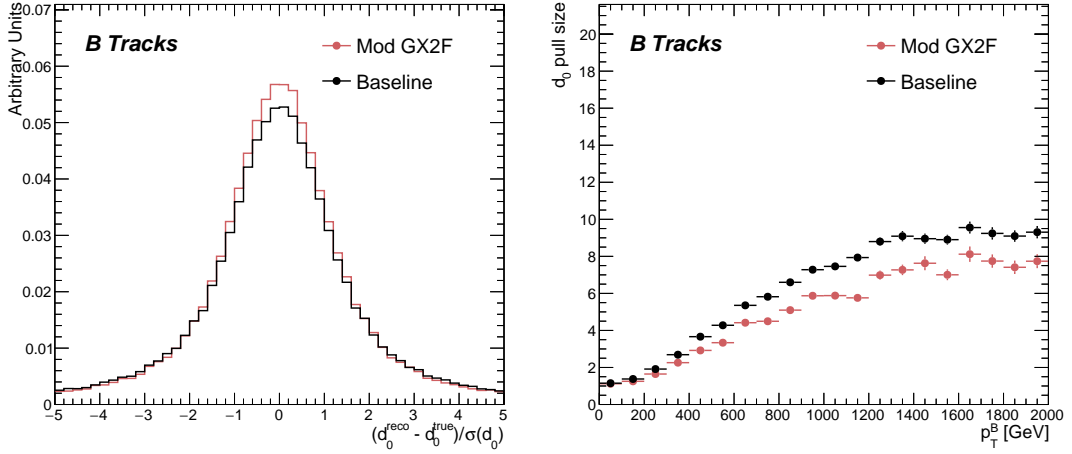


Figure 4.9: (left) b -hadron decay track d_0 pulls ($d_0/s(d_0)$) for baseline and modified GX2F tracks. (right) The absolute value of the d_0 pull as a function of the truth b -hadron transverse momentum.

is shown to be overly aggressive in the removal of b -hadron decay product track candidates. The ambiguity solving process relies on a complicated pre-defined selection which has not been optimised for high transverse momentum b -hadron track reconstruction. These conclusions have motivated further ongoing studies into the improvement of the track reconstruction in dense environments and the high- p_T regime, such as those in Ref. [92].

An optimisation of the outlier removal process in the global χ^2 fitter was carried out. The results of the optimisation show that more aggressive removal of outlier hits can lead to fewer wrong hits being assigned to tracks, and improvements in the pulls of the track parameters.

Future Work

The studies were carried out in Release 21 of the ATLAS software, and need to be reproduced using the newer Release 22 to confirm the results against other changes in the baseline tracking configuration. It is also necessary to study the impact of the improved outlier removal on the downstream b -tagging algorithms. Thanks to the all-in-one flavour tagging approach described in Chapter 6, this will in future be easier to study.

1052 As there are some known data-MC discrepancies, fine tuned optimisation such as the
1053 work presented here presents an opportunity to over-optimise the tracking algorithms
1054 on MC. As such, further studies validating the improved outlier removal procedure
1055 on data are required.

1056 **Chapter 5**

1057 **Track Classification MVA**

1058 This chapter details work on implementing a multivariate algorithm (MVA) to predict
1059 the truth origin of reconstructed tracks. An introduction to formalisms of machine
1060 learning is given in Section 5.1. In Section 5.2, the truth origin label is defined,
1061 and in Section 5.3 these labels are used to train a machine learning model that can
1062 effectively discriminate between good and fake tracks. Several studies motivated this
1063 work by demonstrating that at high p_T , b -tagging performance was degraded by the
1064 presence of large numbers of poorly reconstructed or fake tracks. If an algorithm
1065 could be trained to detect fake tracks, these could be removed before their input to
1066 the b -tagging algorithms with the aim of improving performance. In addition, other
1067 groups that are sensitive to the presence of fake tracks would also benefit from this
1068 work.

1069 **5.1 Machine Learning Background**

1070 Over the past few decades, machine learning (ML) techniques have become increas-
1071 ingly popular in High Energy Physics experiments due the increased volumes of
1072 high-dimensional data and improvements in the techniques used (in particular deep
1073 learning). Machine learning is the process by which a computer program uses data
1074 to learn suitable parameters for a predictive model. This is opposed to explicitly
1075 providing instructions on how to perform a task. A subfield known as *supervised*
1076 *learning* is used in this work, and consists of exposing a model to a large number of
1077 labelled examples in order to extract relationships between the input data and their

1078 labels. These relationships are often complex, and explicitly programmed rules can
1079 fail to fully capture the relationships between inputs and outputs.

1080 In the simplest case, a set of m labelled training examples $S = \{(x_1, y_1), \dots, (x_m, y_m)\}$
1081 is collected. Each element (x_i, y_i) consists of a input vector $x_i \in \mathbb{R}^{\text{input}}$, and the
1082 corresponding label y_i . In classification problems, these labels are integer *class*
1083 *labels* $y_i \in \{0, \dots, N - 1\}$, where N is the number of classes, which specify which
1084 of a pre-determined set of categorical classes the training example belongs to. The
1085 rest of the discussion in this chapter is limited to binary classification problems
1086 ($N = 2$). The two classes are often referred to as signal ($y_i = 1$) and background
1087 ($y_i = 0$), which need to be separated. Collecting sufficient and suitable data is one
1088 of the primary challenges of machine learning, as such data is not always readily
1089 available. Fortunately, sophisticated tools to simulate particle collisions have already
1090 been developed by the scientific community [94, 95]. These tools play a key role in
1091 generating a suitably large amount of labelled data which is used to train algorithms.
1092 More detail on the input datasets is given in Section 5.3.1.

1093 After obtaining suitable training data, the next step is to define a model. Given an
1094 input domain $\mathbb{R}^{\text{input}}$ and an output domain $(0, 1)$, the model $f_\theta : \mathbb{R}^{\text{input}} \rightarrow (0, 1)$ is a
1095 parameterised functional mapping from input space to output space. Given an input
1096 example x_i and a set of parameters θ , the model outputs a prediction $\hat{y}_i \in (0, 1)$ for
1097 the true label y_i , as in

$$f_\theta(x_i) = \hat{y}_i. \quad (5.1)$$

1098 The output \hat{y}_i is in the interval $(0, 1)$ so as to be interpreted as the probability that
1099 the input example x_i belongs to the signal class. The parameters θ of the model are
1100 randomly initialised, and the model is designed to be expressive enough to correctly
1101 map the inputs x_i to the outputs y_i given a reasonable optimisation of the parameters.
1102 To perform this optimisation, the model is then trained, which amounts to showing
1103 the model a series of labelled training examples and modifying the parameters of the
1104 model based on its ability to correctly predict the labels.

5.1.1 Neural Networks

Neural networks (NNs) are a common choice for the machine learning model f since they have the ability to approximate any function [96] and are easy to train via backpropagation [97].

Artificial Neurons

The basic functional component of a NN is the *artificial neuron* or node, which is loosely inspired by a mathematical model of a biological neuron [98, 99]. A diagram of an artificial neuron is shown in Fig. 5.1. Each neuron is defined by its parameters or *weights* θ and a choice of activation function. Each neuron takes a fixed number of inputs and computes the dot product of the input and weight vectors $x^T\theta$ and additionally adds a constant bias term θ_0 . This term plays the role of a trainable constant value that is independent of the inputs.

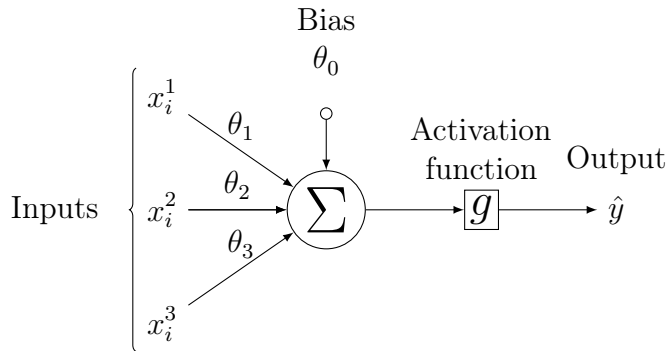


Figure 5.1: A diagram displaying the logical flow of a single neuron with three inputs x_i^j . Each input is multiplied by a weight θ_j , and the resulting values are summed. A bias term θ_0 is added, and the result z is passed to an activation function. Each neuron can be thought of as a logistic regression model.

The output of the dot product and bias term z is fed into an activation function $g(z)$. The activation function has several uses, most notably acting as a source of non-linearity and bounding the output of the neuron. Some common activation functions (sigmod, tanh, ReLU and SiLU) [100, 101] are shown in Fig. 5.2. The choice of activation function can have implications for the performance and convergence of the network, since the gradient of $g(z)$ is used to compute the weight updates during

1123 training. This is also why input data is typically normalised to have zero mean and
1124 unity variance [102].

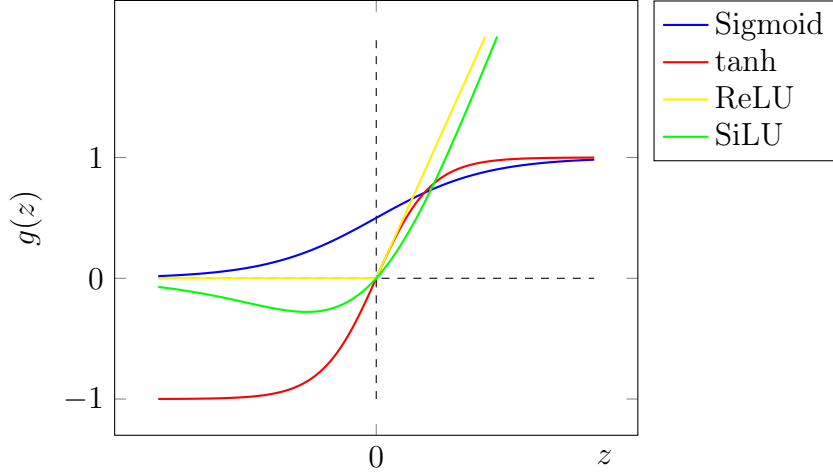


Figure 5.2: The output of several common choices for the activation function $g(z)$ of an artificial neuron. The input z is the output of the dot product between the activation and the weights, plus a bias term.

1125 **Networks**

1126 Several neurons are linked together in layers to form a neural network. The inputs
1127 are propagated layer-by-layer through the network until reaching the final output
1128 layer. The number of layers and neurons per layer are important hyperparameters
1129 (those parameters which are not optimised as part of the training process) which
1130 influence the performance of the model. In the case of binary classification, the final
1131 output layer generally consists of a single neuron with a sigmoid activation

$$g(z) = \frac{1}{1 + e^{-z}}, \quad (5.2)$$

1132 where z is the output from the dot product of the inputs and the weights, plus the
1133 bias term. This value is bounded between zero and one allowing the final output to
1134 be interpreted as the probability that the input sample belongs to the signal class.
1135 NNs have the crucial property of being differentiable functions, which facilitates the
1136 training process described in the next section.

1137 5.1.2 Training with Gradient Descent

1138 A training algorithm is used to optimise the weights and biases of a NN after
1139 exposure to the training data. The training algorithm works by minimising a loss
1140 function L , which quantifies the error in the model's predictions. NNs are commonly
1141 trained using backpropagation in combination with a variant of the stochastic gradient
1142 descent algorithm to iteratively update the model parameters. In binary classification
1143 problems, the binary cross entropy given in Eq. (5.3) loss if often used.

$$L(x_i, \theta) = y_i \ln[f_\theta(x_i)] + (1 - y_i) \ln[1 - f_\theta(x_i)] \quad (5.3)$$

1144 Since the model f is differentiable, a correction for each parameter θ_i can be computed
1145 by taking the partial derivative of L with respect to the parameter. Updated
1146 parameters θ'_i are calculated by updating the original parameter in the direction
1147 which reduces the loss.

$$\theta'_i = \theta_i - \alpha \frac{\partial L}{\partial \theta_i} \quad (5.4)$$

1148 The hyperparameter α is known as the *learning rate* and dictates the size of the
1149 step taken in the direction of the slope. The errors for each parameter are efficiently
1150 calculated using the backpropagation algorithm [97]. The process of updating weights
1151 is repeated until the weights are judged to have converged, which means the network
1152 is trained. In practice, small batches of the input data are shown to the network at
1153 a time. For each batch the average loss is calculated and the network's weights are
1154 updated. There are many extensions and variations of the gradient descent algorithm.
1155 This work uses the Adam optimiser which adds momentum to the weight updates
1156 (dampening oscillations) and an adaptive per-parameter learning rate [103].

1157 5.2 Track Truth Origin Labelling

1158 Crucial to supervised learning techniques are the ground truth class labels which the
1159 machine learning model is trained to predict. A set of track truth labels which a
1160 high degree of granularity have been implemented in the ATLAS software stack, and
1161 are listed in Table 5.1. The labelling scheme has been designed to be useful beyond
1162 the classification of good and fake tracks. The origins are determined by analysing

the simulated record to determine the physical process that led to the creation of the truth (i.e. simulated) particle which is associated with each reconstructed track. Tracks are associated with truth particles by selecting the particle with the highest *truth-matching probability* (TMP), defined in Eq. (5.5). For a given truth particle, the TMP is a weighted sum of the number of hits on a reconstructed track which are matched to the truth particle N^{match} , divided the total number of hits on the track N^{total} . The weights are subdetector-dependent and are designed to account for the varying importance of the different ID subdetectors (based upon their precision) in the reconstruction of a track.

$$\text{TMP} = \frac{10N_{\text{Pix}}^{\text{match}} + 5N_{\text{SCT}}^{\text{match}} + N_{\text{TRT}}^{\text{match}}}{10N_{\text{Pix}}^{\text{total}} + 5N_{\text{SCT}}^{\text{total}} + N_{\text{TRT}}^{\text{total}}} \quad (5.5)$$

For the fake track classification tool, the track truth origins in Table 5.1 are used to construct a binary label by assigning all fake tracks to the background category, and all other tracks as signal. The fake track classifier is then trained to distinguish between these two categories of tracks. Fake tracks are defined using the TMP, with a $\text{TMP} < 0.75$ ¹ giving a track the label of fake. Fake tracks are made up of combinatorial fakes, which are tracks which do not correspond to the trajectory of any truth particle, and poorly reconstructed tracks, which may somewhat resemble the trajectory of a truth particle but due to the presence of some wrong hits on the track will not accurately reproduce the true trajectory. In such cases the fake track can still be identified as having an origin: it is for example possible to have a fake track which is from the decay of a b -hadron.

5.3 Fake Track Identification Tool

The rate of fake tracks increases at high transverse momentum as shown in Fig. 5.3 due to the difficulties in track reconstruction outlined in Section 4.2.2. The performance of b -tagging algorithms is reduced as a direct result of the presence of these tracks as shown for SV1 (see Section 3.4.2) in Fig. 5.4, where the efficiency to mistag a light-jet decreases by up to 35% at a b -jet efficiency of 35% if such tracks are removed.

¹An alternative definition of a fake track as one with $\text{TMP} < 0.5$ is also in use within ATLAS, but 0.75 was used for this study.

Truth Origin	Description
Pile-up	From a pp collision other than the primary interaction
Fake	Created from the hits of multiple particles
Primary	Does not originate from any secondary decay
fromB	From the decay of a b -hadron
fromBC	From a c -hadron decay which itself is from the decay of a b -hadron
fromC	From the decay of a c -hadron which is not from the decay of a b -hadron
OtherSecondary	From other secondary interactions and decays

Table 5.1: Truth origins which are used to categorise the physical process that led to the production of a track. Tracks are matched to charged particles using the truth-matching probability [57]. A truth-matching probability of less than 0.75 indicates that reconstructed track parameters are likely to be mismeasured and may not correspond to the trajectory of a single charged particle. The “OtherSecondary” origin includes tracks from photon conversions, K_S^0 and Λ^0 decays, and hadronic interactions.

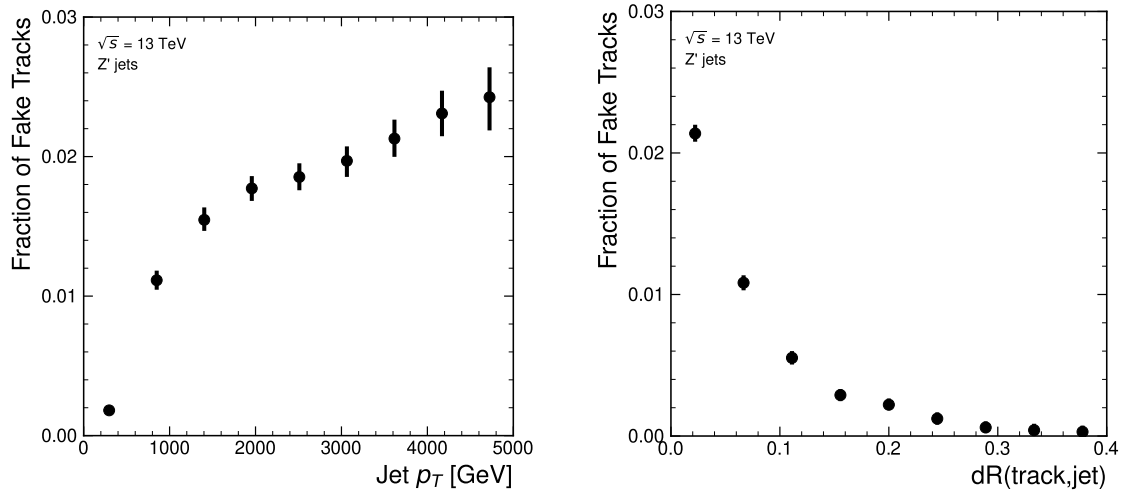


Figure 5.3: Rate of fake tracks as a function of jet transverse momentum (left) and $\Delta R(\text{track}, \text{jet})$ (right) for jets in the Z' sample. The rate of fake tracks increases significantly as a function of p_T , and also increases as the distance to the jet axis decreases.

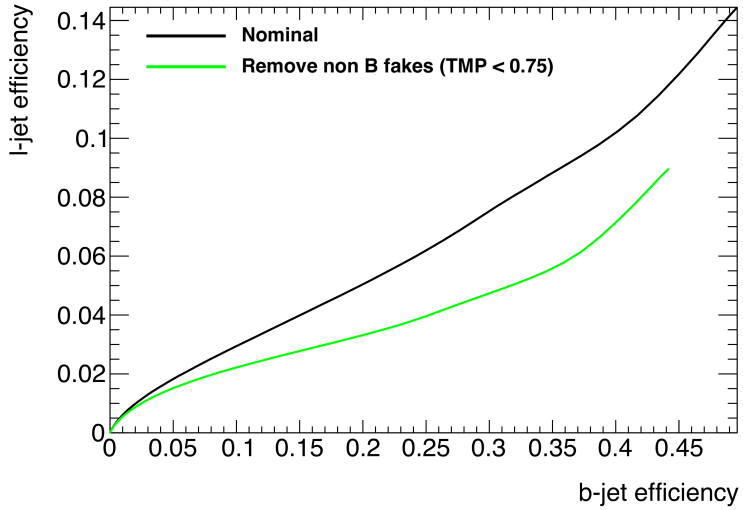


Figure 5.4: The light-jet efficiency of the low level tagger SV1 for jets in the Z' sample with $250 < p_T < 5000$ GeV, as a function of b -jet efficiency. The nominal tracking setup (black) is shown alongside the case where fake tracks which are not from the decay of a b -hadron are removed. The light-jet efficiency is decreased, demonstrating that the presence of fake tracks is detrimental to the algorithm performance.

1189 To identify and remove fake tracks, a NN classification tool was trained with all
 1190 non-fake tracks as the signal class and fake tracks as the background class. Inputs to
 1191 the model are described in Section 5.3.2, while fake track removal performance is
 1192 given in Section 5.3.4.

1193 5.3.1 Datasets

1194 To train and evaluate the model, simulated SM $t\bar{t}$ and BSM Z' events initiated by
 1195 proton-proton collisions at a center of mass energy $\sqrt{s} = 13$ TeV were used. The Z'
 1196 sample is constructed in such a manner that it has a relatively flat jet p_T spectrum
 1197 up to 5 TeV and decays democratically to equal numbers of b -, c - and light-jets.
 1198 The generation of the simulated event samples includes the effect of multiple pp
 1199 interactions per bunch crossing with an average pile-up of $\langle \mu \rangle = 40$, which includes
 1200 the effect on the detector response due to interactions from bunch crossings before
 1201 or after the one containing the hard interaction.

1202 The $t\bar{t}$ events are generated using the PowhegBox v2 generator [104–107] at
 1203 next-to-leading order with the NNPDF3.0NLO [108] set of parton distribution

functions (PDFs). The h_{damp} parameter² is set to 1.5 times the mass of the top-quark (m_{top}) [109], with $m_{\text{top}} = 172.5 \text{ GeV}$. The events are interfaced to PYTHIA 8.230 [110] to model the parton shower, hadronisation, and underlying event, with parameters set according to the A14 tune [111] and using the NNPDF2.3LO set of PDFs [112]. Z' events are generated with PYTHIA 8.2.12 with the same tune and PDF set. The decays of b - and c -hadrons are performed by EVTGEN v1.6.0 [113]. Particles are passed through the ATLAS detector simulation [114] based on GEANT4 [115].

Jets are required to have a pseudorapidity $|\eta| < 2.5$ and $p_{\text{T}} > 20 \text{ GeV}$. Additionally, a standard selection using the Jet Vertex Tagger (JVT) algorithm (see Section 3.4.3) at the tight working point is applied to jets with $p_{\text{T}} < 60 \text{ GeV}$ and $|\eta| < 2.4$ in order to suppress pile-up contamination [65].

5.3.2 Model Inputs

The fake track MVA is given two jet variables and 20 tracking related variables for each track fed into the network. The jet transverse momentum and signed pseudorapidity constitute the jet-level inputs, with the track-level inputs listed in Table 5.2.

The track parameters and hit pattern are key indicators of whether or not a track is fake. The FracRank variable is the ordered index of the tracks that pass the ambiguity solver’s selection divided by the total number of successfully reconstructed tracks in the event. The ambiguity solver processes track candidates iteratively in order of an internal score (see Section 3.4.1), and the order in which tracks are accepted is preserved. Since tracks with shared hits have lower scores, tracks which do not require the removal of shared hits are likely to be processed and accepted earlier on, whereas tracks with shared hits will be processed later and potentially have their shared hits removed. Hence the FracRank variable gives an indication of the track quality and how likely it is that hits would have been removed (tracks processed later on are more likely to have hits removed).

²The h_{damp} parameter is a resummation damping factor and one of the parameters that controls the matching of POWHEG matrix elements to the parton shower and thus effectively regulates the high- p_{T} radiation against which the $t\bar{t}$ system recoils.

Jet Input	Description
p_T	Jet transverse momentum
η	Signed jet pseudorapidity
Track Input	Description
p_T	Track transverse momentum
ΔR	Angular distance between the track and jet
d_0	Closest distance from the track to the PV in the longitudinal plane
z_0	Closest distance from the track to the PV in the transverse plane
nIBLHits	Number of IBL hits
nPixHits	Number of pixel hits
nSCTHits	Number of SCT hits
nTRTHits	Number of TRT hits
nBLHits	Number of B-layer hits
nIBLShared	Number of shared IBL hits
nIBLSplit	Number of split IBL hits
nPixShared	Number of shared pixel hits
nPixSplit	Number of split pixel hits
nSCTShared	Number of shared SCT hits
r_{first}	Radius of first hit
nDOF	Number of degrees of freedom on the track
FracRank	Ambiguity solver ordering variable

Table 5.2: Input features to the fake track classification NN. Basic jet kinematics, along with information about the reconstructed track parameters and constituent hits are used. Shared hits, are hits used on multiple tracks which have not been classified as split by the cluster-splitting neural networks [57], while split hits are hits used by multiple tracks which have been identified as merged, and therefore split.

1231 Track selection follows the loose selection described in Ref. [85] and outlined in
 1232 Table 3.2, which was found to improve the performance compared to previous tighter
 1233 selections, whilst ensuring good resolution of the track's parameters and a low fake
 1234 rate [57]. Inputs are scaled to have a central value of zero and a variance of unity
 1235 before training and evaluation.

1236 5.3.3 Model Hyperparameters

1237 Due to the imbalance between the two classes (with fake tracks being relatively
 1238 uncommon), a weight was added to the loss function for the background class to
 1239 balance their relative weights. The NN was made up of two hidden layers with
 1240 220 nodes per layer. The ReLU activation function was used in conjunction with
 1241 the Adam optimiser with a learning rate of $1e-3$. Optimisation of the networks
 1242 architecture was carried out to ensure optimal performance with a relatively small
 1243 number of learnable parameters – 54,000. The model was trained using 40 million
 1244 tracks with a further 4 million tracks each used for validation and testing. A full list
 1245 of the model hyperparameters is given in Table 5.3.

Hyperparameter	Value
Batch size	2048
Activation	ReLU
Optimiser	Adam
Initial learning rate	$1e-3$
Training epochs	20
Training tracks	40m
Validation tracks	4m
Testing tracks	4m

Table 5.3: Hyperparameter for the track classification model

1246 5.3.4 Results

1247 In order to evaluate the fake track classification tool, a orthogonal test sample of 4
 1248 million tracks in jets in the combined $t\bar{t}$ and Z' samples was used. The continuous

scalar output from the NN model is interpreted as the probability that a given track is a signal track (i.e. not fake). Fig. 5.5 shows the performance of the fake track classification MVA. The signal and background classes are well separated in the output of the tool. Also shown is a receiver operating characteristic (ROC) curve, which plots the rate of true positives against the rate of false positives over a scan of cut points on the NN output ranging from zero to one. The area under the curve (AUC) gives a summary of the aggregate classification power of the model. The fake track classification tool achieves an AUC of 0.935 for all tracks, which is indicative of a well-performing model. Considering only tracks from b -hadron decays, this value drops slightly to 0.928.

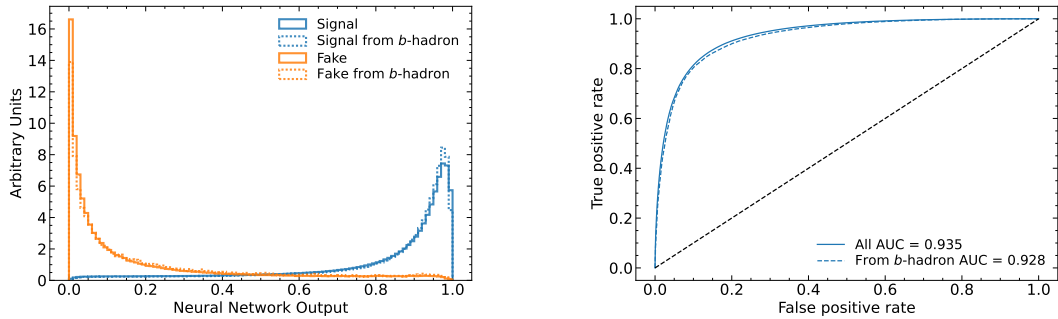


Figure 5.5: (left) Normalised histograms of the fake track classification model output separated for signal and fake tracks, and further separated by those tracks which are from the decay of a b -hadron. (right) The ROC curve for all tracks (solid line) and tracks from the decay of a b -hadron (dashed line). The plots show tracks in the combined $t\bar{t}$ and Z' testing sample. The model is able to successfully discriminate between signal and fake tracks, and shows a very similar performance when looking specifically at tracks from the decay of a b -hadron.

Signal and fake track efficiencies at two different NN output cut points are shown in Table 5.4. The results demonstrate that the tool is effective in retaining 98.8% of signal tracks, while correctly identifying (and therefore enabling the removal of) 45.6% of fake tracks. Table 5.4 also shows that a significant amount of tracks which are labelled as both fake and from the decay of a b -hadron are also removed. This can happen because fake tracks with $\text{TMP} < 0.75$ are still matched to a truth particle, which can be the decay product of a b -hadron.

MVA Output Cut	Signal Track Efficiency		Fake Track Efficiency	
	All	From b	All	From b
0.06	98.8%	98.9%	45.6%	39.8%
0.12	97.3%	97.5%	59.4%	53.6%

Table 5.4: Good and fake track selection efficiencies for the combined $t\bar{t}$ and Z' samples. Two working points are defined, cutting on the NN output at 0.06 and 0.12.

5.4 b -hadron Track Identification

After initial tests and investigation, it was found that fake tracks which were the result of b -hadron decays actually aided b -tagging performance, as demonstrated in Fig. 5.7. The application of a single tool which removed all fake tracks was therefore not optimal. A second tool was therefore trained in the same manner as the first, this one was designed to distinguish between those tracks which were from the decay of a b -hadron (FromB and FromBC in Table 5.1) and those which were not (all other truth origins). Fake tracks which were from the decay of a b -hadron were included in the signal class. The b -hadron decay track MVA was trained using the same setup as described above, with the same tracks, input variables, and training procedure. The performance of the model to separate b -hadron decay tracks from other tracks is shown in Fig. 5.6. Using a selection WP of 0.1, the model can retain 98.5% of b -hadron tracks and reject 46.2% of tracks not from the decay of a b -hadron. In Section 5.5, this model is used in conjunction with the fake track identification MVA to identify and remove fake tracks which are not from the decay of a b -hadron.

5.5 Combined Approach

A 2-dimensional cut was then used to only reject those tracks that had a high probability of being fake, and also a low probability of being a b -hadron decay track. The results of the combined approach are provided in Table 5.5, which shows that for the working point “A”, 98.6% of b -hadron decay tracks (both good and fake) are retained, while 50.7% of fake tracks which are not from b -hadron decays are rejected.

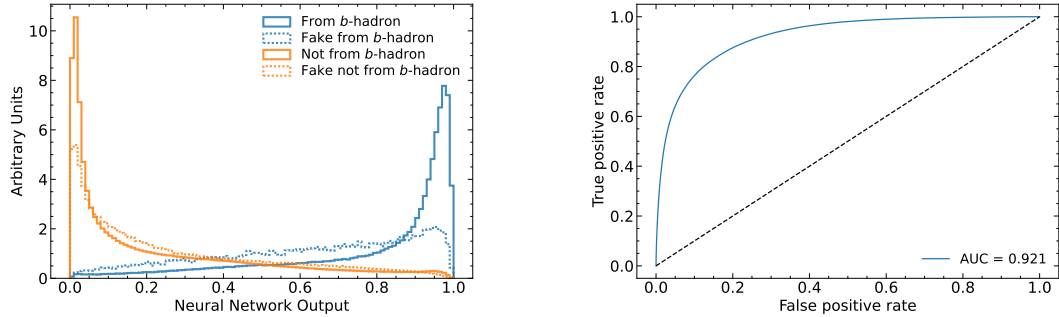


Figure 5.6: (left) Normalised histogram of the b -hadron track identification model output separated for tracks from the decay of a b -hadron and tracks from other sources. The two groups are further separated into those tracks which are fake. (right) The ROC curve for all tracks (solid line). The plots show tracks in the combined $t\bar{t}$ and Z' testing sample.

WP	Fake MVA Cut	b -hadron Decay MVA Cut	Retained b -hadron Tracks	Fake non- b -hadron Tracks Rejected
A	0.5	0.4	98.6%	50.7%
B	0.6	0.5	97.5%	62.0%

Table 5.5: Cut values for the fake and b -hadron decay track MVAs for the two defined working points. Working point “B” cuts more aggressively on the MVA outputs than WP “A”, removing more fake tracks but resulting in an increased loss of signal tracks (which here are all b -hadron decay tracks).

1287 The light-jet efficiency of SV1 is successfully reduced when using the combined tools
 1288 to remove fake tracks that are not from a b -hadron decay, as shown in Fig. 5.7. At a
 1289 b -jet efficiency of 70%, the light-jet mistag rate for jets with $250 < p_T < 400 \text{ GeV}$
 1290 is reduced from 0.054 to 0.044, a relative improvement of approximately 20%. For
 1291 jets with $400 < p_T < 1000 \text{ GeV}$ the mistage rate drops from 0.1 to 0.08 for a similar
 1292 relative improvement of 20%. The performance of the fake track removal approach
 1293 was also tested for the other low level vertexing algorithm – JetFitter. A similar level
 1294 of improvement in the light-jet mistag rate was observed with a reduction of up to a
 1295 20% reduction for both low- and high- p_T jets in the Z' sample achieved. Together,
 1296 these results demonstrate that by identifying and removing fake tracks which are not
 1297 the result of the weak decay of a b -hadron, the performance of the low level tagging
 1298 algorithms can be improved by an amount which is comparable to the improvement
 1299 that would be observed if the tracks were selected at truth level1.

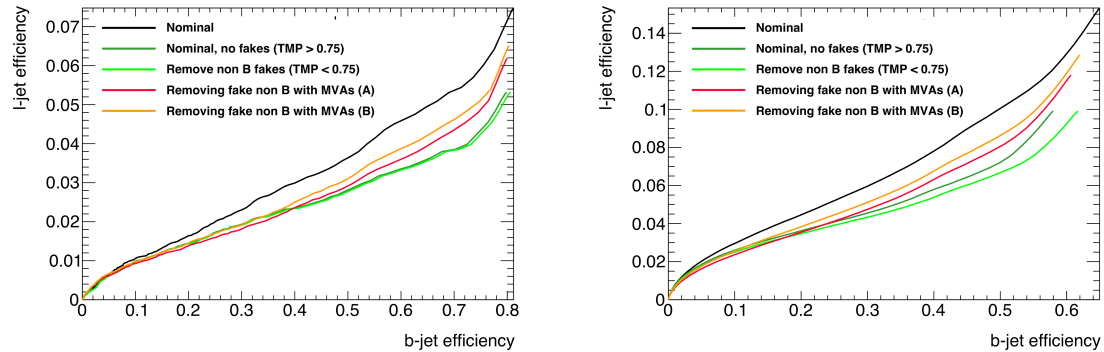


Figure 5.7: The effect of applying the fake track identification algorithm together with the b -hadron decay track identification on the jet tagging performance of SV1 for jets in the Z' sample with $250 \text{ GeV} < p_T < 400 \text{ GeV}$ (left) and $400 \text{ GeV} < p_T < 1 \text{ TeV}$ (right). The nominal SV1 light-jet rejection (black) is compared to two working points of fake track removal, labelled “A” (red) and “B” (orange), which represent two different 2D working points of the track classification tools. Removal of fake tracks based on truth information is shown by the green curves.

1300 5.6 Conclusion

1301 Fake tracks, which are prevalent in the core of high p_T jets, have an adverse impact
 1302 on b -tagging performance. A ML tool to identify fake tracks has been developed,
 1303 which can be used to limit the number of fake tracks being input to the b -tagging

algorithms. An advantage of the approach is that the continuous output of the model allows for the tuning of good and fake track identification efficiencies. Since it was found that b -hadron decay tracks can also be poorly reconstructed and thus marked as fake, it was deemed necessary also to train a second algorithm to detect b -hadron decay tracks so that the removal of these tracks could be avoided. Removing fake and non- b decay tracks in this way was found to improve the light-jet mistagging rate of SV1 and JetFitter by up to 20% at high transverse momentum. The improvement achieved using the classification tools was in general comparable with that achieved when using the truth information to remove the fake tracks not from the decay of a b -hadron.

Future Work

While removing tracks prior to their input to the low level tagging algorithms is shown here to be beneficial, a more performant alternative might be to keep these tracks but label them as being fake (for example using the output of the classification tool), and allow the tagging algorithms to take this into consideration. This is not straightforward with manually optimised taggers such as SV1 and JetFitter, but is possible with more advanced taggers as described in Chapter 6.

Tools which identify the origin of a given track have other potential uses. One application is to isolate a relatively pure sample of fake tracks which can be used to estimate the fake track rate in data, which would be useful for estimating the uncertainty on fake track modelling. Another application is to use the b -hadron track identification tool to improve the track-to-jet association. Both applications are currently under investigation.

The approach here works on a track-by-track basis, but a more sophisticated approach would consider the correlations between the tracks inside a jet. Also left for future work is to simultaneously train a single tool which discriminates between all the truth origins listed in Table 5.1. Such a tool would be useful as a general purpose multiclass classifier. An algorithm which takes both these aspects into consideration is discussed in Chapter 6.

₁₃₃₃ **Chapter 6**

₁₃₃₄ **Graph Neural Network Flavour
Tagger**

₁₃₃₆ This chapter introduces GN1, a novel ML-based flavour tagging algorithm based on
₁₃₃₇ graph neural networks (GNNs). In Section 6.1, an overview of the approach used
₁₃₃₈ for GN1 is given. An introduction to the theory of GNNs is provided in Section 6.2.
₁₃₃₉ Details of the experimental setup are provided in Section 6.3, while the architecture
₁₃₄₀ of GN1 is specified in Section 6.4.3. In Section 6.4.4, the training procedure is
₁₃₄₁ described, and in Section 6.5 the results are shown.

₁₃₄₂ **6.1 Motivation**

₁₃₄₃ GN1 is a monolithic approach to flavour tagging as illustrated in Fig. 6.1. As opposed
₁₃₄₄ to the existing approach to flavour tagging described in Chapter 4, which relies
₁₃₄₅ on a two tiered approach requiring the use of both low- and high-level algorithms,
₁₃₄₆ GN1 takes as inputs information directly from an unordered variable number of
₁₃₄₇ tracks as input, and predicts the jet flavour without requiring outputs from the
₁₃₄₈ intermediate low-level algorithms. In addition to predicting the flavour of the jet, the
₁₃₄₉ model predicts which physical processes produced the various tracks, and groups the
₁₃₅₀ tracks into vertices. These auxiliary training objectives provide valuable additional
₁₃₅₁ information about the contents of the jet and enhance the performance of the primary
₁₃₅₂ flavour prediction task. The use of GNNs offers a natural way to classify jets with

1353 variable numbers of unordered associated tracks (see Section 6.2), while allowing for
1354 the inclusion of auxiliary training objectives [2, 116].

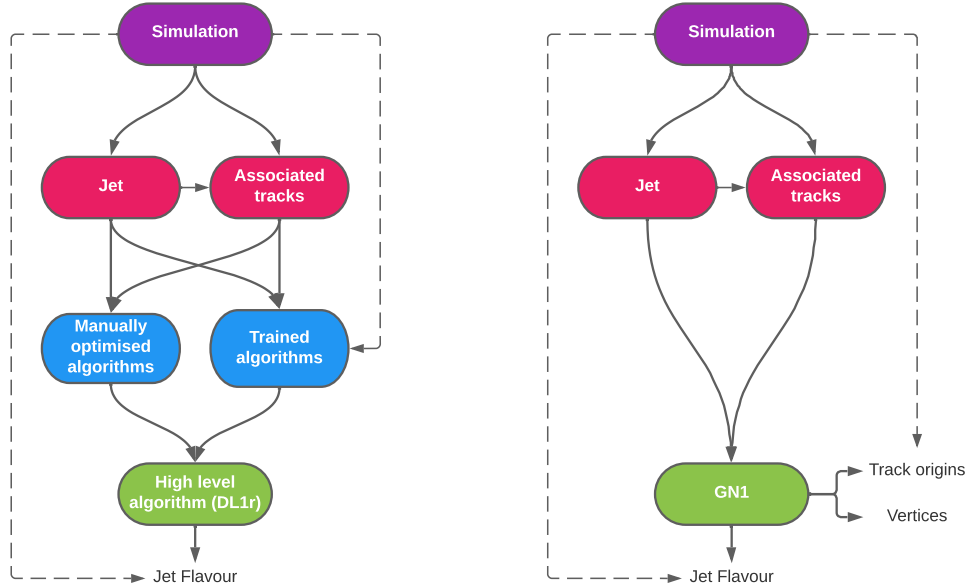


Figure 6.1: Comparison of the existing flavour tagging scheme (left) and GN1 (right). The existing approach utilises low-level algorithms (shown in blue), the outputs of which are fed into a high-level algorithm (DL1r). Instead of being used to guide the design of the manually optimised algorithms, additional truth information from the simulation is now being used as auxiliary training targets for GN1. The solid lines represent reconstructed information, whereas the dashed lines represent truth information [3].

1355 The current flavour tagging algorithms utilise a two-tired approach, with five low
1356 level algorithms feeding intermediate features into the high-level tagger DL1r, which
1357 outputs variables which discriminate between the different jet flavours. In contrast
1358 GN1 consists of only a single neural network, which takes the tracks as inputs along
1359 with some kinematic information about the jet. As a result, it does not depend on
1360 the outputs of any other flavour tagging algorithm. A simple training of the model
1361 fully optimises its parameters, representing a significant simplification with respect to
1362 the optimisation procedure for DL1r. This is particularly important when optimising
1363 the tagger for new regions of phase space (e.g. c -tagging or high- p_T b -tagging), or
1364 when the detector is upgraded or the charged particle reconstruction or selection
1365 algorithms are re-optimised.

1366 GN1 is trained to learn about the internal structure of the jet through the use of two
1367 auxiliary training objectives: the prediction of the underlying physics process from
1368 which each track originated, and the grouping of tracks originating from a common
1369 spatial position (i.e. a common vertex). These auxiliary objectives are meant to
1370 guide the neural network towards a more complete understanding of the underlying
1371 physics inside the jet, thereby removing the need for the low-level algorithms, which
1372 previously contained information about the underlying physics in their design. The
1373 training targets for the primary and auxiliary objectives are extracted from truth
1374 information, as opposed to reconstructed quantities available in both collision data
1375 and simulation.

1376 In this chapter, the following advantages of the GN1 approach will be demonstrated:

- 1377 1. GN1 boasts improved performance with respect to the current ATLAS flavour
1378 tagging algorithms, with significantly larger background rejection rates for a
1379 given signal efficiency. Alternatively the rejection rates can be kept fixed for a
1380 substantial increase in signal efficiency, in particular at high- p_T .
- 1381 2. The same network architecture can be easily optimised for a wider variety of
1382 use cases (e.g. c -jet tagging and high- p_T jet tagging) since there are no low-level
1383 algorithms to retune.
- 1384 3. There are fewer algorithms to maintain.
- 1385 4. Alongside the network’s prediction of the jet flavour, the auxiliary vertex and
1386 track origin predictions provide more information on why a jet was (mis)tagged
1387 or not. This information can also have uses in other applications, for instance
1388 to explicitly reconstruct displaced decay vertices or to remove fake tracks.¹

1389 6.2 Graph Neural Network Theory

1390 Graph neural networks are a more sophisticated neural network model (see Sec-
1391 tion 5.1.1) that are designed to operate on graph structured data. A brief introduction
1392 to GNNs is provided in this section following the formalism in Ref. [117].

¹A fake track is defined in this chapter as a track with a truth-matching probability less than 0.5, where the truth-matching probability is defined in Ref. [57].

1393 A graph \mathcal{G} consists of a set of N^n nodes $\mathcal{N} = \{h_i\}_{i=1:N^n}$, a set of N^e edges $\mathcal{E} =$
 1394 $\{e_i\}_{i=1:N^e}$, and a global representation u . Each node represents an individual object,
 1395 and edges are directed connections between two nodes, called the *sender* and *receiver*
 1396 nodes. The connectivity of the graph therefore encodes information about the
 1397 relationships between objects that exist in the graph.

1398 A single graph network layer consists of three separate update functions ϕ^e , ϕ^h and
 1399 ϕ^u one for each of the nodes, edges, and global graph representation, and similarly
 1400 three aggregation functions $\rho^{e \rightarrow h}$, $\rho^{e \rightarrow u}$ and $\rho^{h \rightarrow u}$. The aggregation functions combine
 1401 information across different edges or nodes for input into the update functions,
 1402 which produce new representations for the nodes, edges and global objects based on
 1403 the information in the previous layer and the aggregated information. The update
 1404 functions are typically each implemented as a dense feedforward neural network (as
 1405 described in Section 5.1.1). The edges e_i are updated by a edge network ϕ^e as in

$$e'_i = \phi^e(e_i, h_s, h_r, u), \quad (6.1)$$

1406 where h_s and h_r are the sender and receiver nodes respectively. The nodes are
 1407 updated with a node network ϕ^h as in

$$h'_i = \phi^h(\bar{e}'_i, h_i, u), \quad (6.2)$$

1408 where $\bar{e}'_i = \rho^{e \rightarrow h}(E'_i)$, and E'_i is the set of sender nodes for receiver node h_i . $\rho^{e \rightarrow h}$ is
 1409 referred to as the edge aggregation function. The global representation is updated
 1410 using the global network ϕ^u as in

$$u' = \phi^u(\bar{e}', \bar{h}', u), \quad (6.3)$$

1411 where \bar{e}' is the aggregation $\rho^{e \rightarrow u}$ over all updated edges e'_i and \bar{h}' is the aggregation
 1412 $\rho^{h \rightarrow u}$ over all updated nodes h'_i .

1413 The graph network layer performs a graph convolution, in an analogous way to a
 1414 convolutional neural network operating on a grid of pixels. The above description
 1415 is general, and not all concrete implementations of GNNs need to implement every
 1416 aspect. For example, the global graph representation need not be present, and
 1417 it is also possible that no dedicated edge features are present. In such cases the
 1418 corresponding update and aggregation functions are not needed. Fig. 6.2 shows two

1419 possible graph network update layers. The layer used in the GN1 model is specified
1420 in more detail in Section 6.4.3.

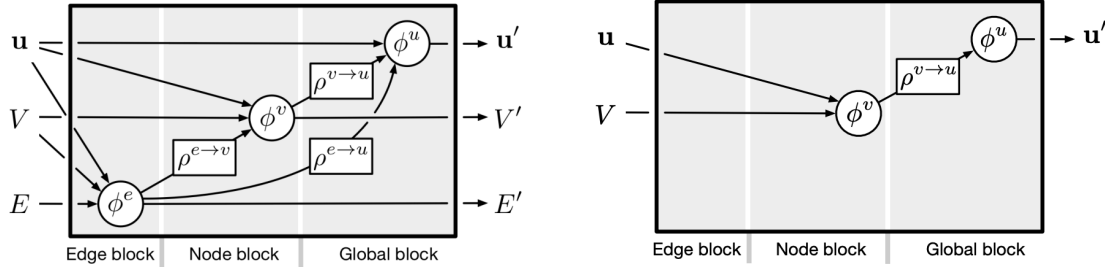


Figure 6.2: The flow of information through a graph neural network layer for (left) a full implementation of the layer and (right) a deep sets model [118]. Reproduced from Ref. [117].

1421 6.3 Experimental Setup

1422 6.3.1 Datasets

1423 The datasets used to train the GN1 tagger are the same as described in Section 5.3.1.
1424 The training dataset contains 30 million jets, 60% of which are $t\bar{t}$ jets and 40% of
1425 which are Z' jets. In order to evaluate the performance of the model during training,
1426 a statistically independent validation set of 500k jets from both the $t\bar{t}$ and Z' samples
1427 are used. For the testing of the model and the creation of the performance plots,
1428 a further 1 million independent testing jets from each of the $t\bar{t}$ and Z' samples are
1429 used. Before being fed into the model, the track- and jet-level inputs are normalised
1430 to have a mean of zero and a variance of unity. The jet flavour labels are assigned
1431 as described in Section 3.4.3. Truth labelled b -, c - and light-jets are kinematically
1432 re-sampled in p_T and η to ensure identical distributions in these variables.

1433 6.4 Model Architecture

1434 6.4.1 Model Inputs

1435 As inputs, GN1 is fed two kinematic jet variables and an unordered set of up to 40
1436 tracks which have been associated to the jet. If more than 40 tracks are associated
1437 to a given jet, only the first 40 tracks with the largest transverse IP significance $s(d_0)$
1438 (see Section 3.2.2) are fed into the model as inputs. Each track is characterised by 21
1439 variables as detailed in Table 6.1. The kinematic jet variables are the jet transverse
1440 momentum and signed pseudorapidity. For each track, variables containing the
1441 track parameters and uncertainties, and detailed information on the hit content are
1442 provided as inputs to the model.

1443 Dependence of the model on the absolute value of the azimuthal jet angle ϕ is
1444 explicitly removed by providing only the azimuthal angle of tracks relative to the jet
1445 axis. The track pseudorapidity is also provided relative to the jet axis.

1446 Since heavy flavour hadrons can decay semileptonically approximately 40% of the time,
1447 the presence of a reconstructed lepton in the jet carries discriminating information
1448 about the jet flavour. To exploit this, a variant of GN1 called GN1Lep is trained in
1449 addition to the baseline model. The GN1Lep variant is identical to the baseline model,
1450 except for the inclusion an additional track-level input, leptonID, which indicates
1451 if the track was used in the reconstruction of an electron, a muon or neither. The
1452 variable is signed by the charge of the reconstructed lepton. The leptons used in the
1453 definition of the leptonID variable are required to satisfy basic quality requirements.
1454 The muons are required to be combined [119], and the electrons are required to pass
1455 the *VeryLoose* likelihood-based identification working point [120].

1456 The selections applied to the tracks, outlined in Table 3.2, is the same as that used
1457 for the fake track classification MVA described in Chapter 5. However, Section 6.5.8
1458 demonstrates that further relaxation of the track selection requirements may be
1459 warranted.

Jet Input	Description
p_T	Jet transverse momentum
η	Signed jet pseudorapidity
Track Input	Description
q/p	Track charge divided by momentum
$d\eta$	Pseudorapidity of the track, relative to the jet η
$d\phi$	Azimuthal angle of the track, relative to the jet ϕ
d_0	Closest distance from the track to the PV in the longitudinal plane
$z_0 \sin \theta$	Closest distance from the track to the PV in the transverse plane
$\sigma(q/p)$	Uncertainty on q/p
$\sigma(\theta)$	Uncertainty on track polar angle θ
$\sigma(\phi)$	Uncertainty on track azimuthal angle ϕ
$s(d_0)$	Lifetime signed transverse IP significance
$s(z_0)$	Lifetime signed longitudinal IP significance
nPixHits	Number of pixel hits
nSCTHits	Number of SCT hits
nIBLHits	Number of IBL hits
nBLHits	Number of B-layer hits
nIBLShared	Number of shared IBL hits
nIBLSplit	Number of split IBL hits
nPixShared	Number of shared pixel hits
nPixSplit	Number of split pixel hits
nSCTShared	Number of shared SCT hits
nPixHoles	Number of pixel holes
nSCTHoles	Number of SCT holes
leptonID	Indicates if track was used to reconstruct an electron or muon

Table 6.1: Input features to the GN1 model. Basic jet kinematics, along with information about the reconstructed track parameters and constituent hits are used. Shared hits, are hits used on multiple tracks which have not been classified as split by the cluster-splitting neural networks [57], while split hits are hits used on multiple tracks which have been identified as merged. A hole is a missing hit, where one is expected, on a layer between two other hits on a track. The track leptonID is an additional input to the GN1Lep model [3].

1460 6.4.2 Auxiliary Training Objectives

1461 In addition to the jet flavour classification, two auxiliary training objectives are
1462 defined. The first auxiliary objective is the prediction of the physical process that
1463 gave rise to each track within the jet (i.e. the track origin), while the second is the
1464 prediction of track-pair vertex compatibility. Each auxiliary training objective comes
1465 with a training target which, similar to the jet flavour label, is a truth labels derived
1466 from the simulation. The presence of the auxiliary training objectives improves the
1467 jet classification performance as demonstrated in Section 6.5.3.

1468 For the track origin prediction objective, each track is labelled with one of the
1469 exclusive categories defined in Table 5.1 of Section 5.2 after analysing the particle
1470 interaction (or lack thereof) which led to its formation. Since the presence of different
1471 track origins is strongly related to the flavour of the jet, training GN1 to recognise
1472 the origin of the tracks provides an additional handle on the classification of the
1473 jet flavour. This task may also aid the jet flavour prediction by acting as a form of
1474 supervised attention [121] - in detecting tracks from heavy flavour decays the model
1475 may learn to pay more attention to these tracks.

1476 The vertexing auxiliary objective makes use of the fact that displaced decays of b -
1477 and c -hadrons lead to secondary and tertiary vertices inside the jet, as described
1478 in Section 4.2.1. The presence of displaced secondary vertices is not a completely
1479 clean signal of a heavy flavour jet, as displaced secondary vertices can also occur
1480 in light-jets as a result of material interactions, conversions, and long-lived particle
1481 decays (e.g. K_S^0 and Λ^0). For the auxiliary object, GN1 predicts a binary label
1482 for each pair of tracks in the jet. The label has a value of 1 if the truth particles
1483 associated with the two tracks in the pair originated from the same spatial point, and
1484 0 otherwise. To derive the corresponding truth labels for training, truth production
1485 vertices within 0.1 mm are merged. Track-pairs where one or both of the tracks in
1486 the pair have an origin label of either Pile-up or Fake are assigned a label of 0.
1487 Using the pairwise predictions from the model, groups of tracks that have common
1488 compatibility can be formed, resulting in the identification of vertices. Two existing
1489 low-level tagging algorithms, SV1 and JetFitter (introduced in Section 3.4.2), are
1490 currently used to find and reconstruct vertices inside jets and are used as inputs to
1491 the existing jet flavour tagger DL1r. The addition of this auxiliary training objective
1492 removes the need for inputs from a dedicated secondary vertexing algorithm.

1493 Both of the auxiliary training objectives described here can be considered as “stepping
1494 stones” on the way to classifying the flavour of the jet. By requiring the model to
1495 predict the truth origin of each track and the vertex compatibility of each track-pair,
1496 the model is guided to learn representations of the jet which are connected to the
1497 underlying physics and therefore relevant for classifying the jet flavour.

1498 **6.4.3 Architecture**

1499 A coarse optimisation of the network architecture hyperparameters (for example
1500 number of layers and number of neurons per layer) has been carried out in order
1501 to maximise the flavour tagging performance, but it is likely that further dedicated
1502 optimisation studies could lead to further performance improvements.

1503 The model architecture builds on a previous implementation of a GNN-based jet
1504 tagger [116]. The previous approach was comprised of two separate graph neural
1505 networks with the auxiliary tasks being performed at an intermediate stage after the
1506 first and before the second. This two stage approach was found to be unnecessary and
1507 as such GN1 simplifies the architecture into a single graph neural network with the
1508 auxiliary tasks being performed at the end, alongside the primary jet classification
1509 task. GN1 makes use of a more sophisticated graph neural network layer [122],
1510 which is described in more detail below. The changes significantly improved tagging
1511 performance and also led to a significant reduction in training time.

1512 As inputs, the model takes information about the jet and a number of associated
1513 tracks, as detailed in Section 6.4.1. The jet variables are concatenated with the
1514 variables for each track as shown in Fig. 6.3. The combined jet-track input vectors
1515 are then fed into a per-track initialisation network with three hidden layers, each
1516 containing 64 neurons, and an output layer with a size of 64, as shown in Fig. 6.4. The
1517 track initialisation network is similar to a deep sets model [118], but does not include
1518 a reduction operation (mean or summation) over the output track representations.
1519 The initialisation network allows for initial per-track input processing without the
1520 associated parameter count cost of the graph convolutional layers described below.

1521 The outputs of the track initialisation network are used to populate the nodes of a
1522 fully connected graph, such that each node in the graph neighbours every other node.
1523 Each node h_i in the graph corresponds to a single track in the jet, and is characterised

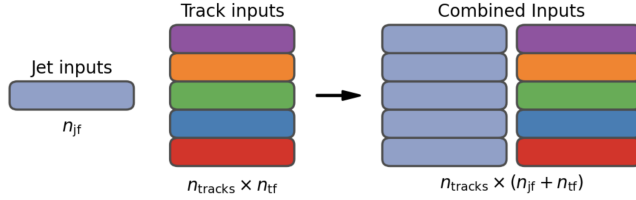


Figure 6.3: The inputs to GN1 are the two jet features ($n_{jf} = 2$), and an array of n_{tracks} , where each track is described by 21 track features ($n_{tf} = 21$). The jet features are copied for each of the tracks, and the combined jet-track vectors of length 23 form the inputs of GN1 [3].

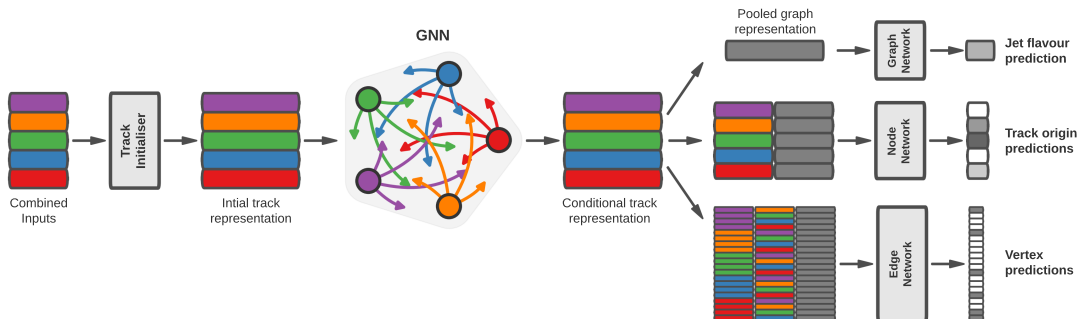


Figure 6.4: The network architecture of GN1. Inputs are fed into a per-track initialisation network, which outputs an initial latent representation of each track. These representations are then used to populate the node features of a fully connected graph network. After the graph network, the resulting node representations are used to predict the jet flavour, the track origins, and the track-pair vertex compatibility [3].

1524 by a feature vector, also called a representation. The per-track output representations
 1525 from the initialisation networks are used as the initial feature vectors of each node
 1526 in the graph. In each layer of the graph network, output node representations h'_i
 1527 are computed by aggregating the features of h_i and neighbouring nodes \mathcal{N}_i using
 1528 a multi-head attention mechanism ($n = 2$) as described in Ref. [122, 123]. First,
 1529 the feature vectors of receiver and sender nodes are fed into two fully connected
 1530 linear layers \mathbf{W}_r and \mathbf{W}_s , to produce an updated representation for each sender and
 1531 receiver node $\mathbf{W}_r h_i$ and $\mathbf{W}_s h_j$. These updated feature vectors are used to compute
 1532 edge scores $e(h_i, h_j)$ for each node pair, as in

$$e(h_i, h_j) = \mathbf{a} \cdot \theta [\mathbf{W}_r h_i + \mathbf{W}_s h_j], \quad (6.4)$$

1533 where, θ is a non-linear activation function, and \mathbf{a} is a learned vector. These edge
 1534 scores are then used to calculate attention weights a_{ij} for each pair of nodes using
 1535 the softmax function over the edge scores

$$a_{ij} = \text{softmax}_j [e(h_i, h_j)]. \quad (6.5)$$

1536 Finally, the updated representations for the receiver nodes h'_i are computed by taking
 1537 the weighted sum over each updated node representation $\mathbf{W}_r h_i$, with weights a_{ij}

$$h'_i = \sigma \left[\sum_{j \in \mathcal{N}_i} a_{ij} \cdot \mathbf{W}_r h_j \right]. \quad (6.6)$$

1538 The set of operations described above constitute a single graph network layer. Three
 1539 such layers are stacked to construct the graph network, representing a balance
 1540 between achieving good performance in a reasonable time and avoiding overtraining
 1541 due to inflation of the parameter count of the model. The final output from the graph
 1542 neural network is a set of per-node (i.e. per-track) feature vectors that are conditional
 1543 representations of each track given the other tracks in the jet. In order to perform

the jet flavour prediction, a flattened global representation of the jet is needed. To produce this, the output track representations are combined using a weighted sum, where the weights are learned during training and therefore act as a form of attention over the different tracks. The flattened outputs from the sum are then fed into a fully connected feedforward neural network with four layers and three outputs, one for each jet flavour. Two other separate fully connected feedforward neural networks are then also used to independently perform the auxiliary classification objectives of GN1. A summary of the different classification networks used for the various training objectives is shown in Table 6.2.

Network	Hidden layers	Output size	Label
Node classification network	128, 64, 32	7	Track origin
Edge classification network	128, 64, 32	1	Track-pair compatibility
Graph classification network	128, 64, 32, 16	3	Jet flavour

Table 6.2: A summary of GN1’s different classification networks used for the various training objectives, adapted from Ref. [3]. The hidden layers column contains a list specifying the number of neurons in each layer. ReLU activation is used through the network [100].

The node classification network predicts the track truth origin as defined in Table 5.1. This network takes as inputs the features from a single output node from the graph network and the global representation of the jet. The node network has three hidden layers containing 128, 64 and 32 neurons respectively, and an output size of seven, corresponding to the seven different truth origins defined in Table 5.1.

The edge classification network is used to predict whether the tracks in the track-pair belong to a common vertex. This network takes as inputs the concatenated representations from each pair of tracks and the global jet representation. Similar to the node network, the edge network has three hidden layers containing 128, 64 and 32 neurons respectively, and a single output, which is used to perform binary classification of the track-pair compatibility. The output predictions for the two auxiliary networks are used for the auxiliary training objectives discussed in Section 6.4.2.

Finally, the graph classification network is used to predict the jet flavour. This network takes only the global jet representation as input. The graph classification

1568 network is comprised of four fully connected hidden layers with 128, 64, 32 and 16
1569 neurons respectively, and has three outputs corresponding to the b -, c - and light-
1570 jet classes. To obtain probability outputs for each task, the outputs from each
1571 classification network are passed through a softmax function.

1572 6.4.4 Training

1573 The full GN1 training procedure minimises the total loss function L_{total} , defined as

$$L_{\text{total}} = L_{\text{jet}} + \alpha L_{\text{vertex}} + \beta L_{\text{track}}. \quad (6.7)$$

1574 This loss is composed of three terms: L_{jet} , the categorical cross entropy loss over the
1575 different jet flavours; L_{vertex} , the binary track-pair compatibility cross entropy loss;
1576 and L_{track} , the categorical cross entropy loss for the track origin prediction. L_{vertex} is
1577 computed via a weighted average over all intra-jet track-pairs in the batch, and L_{track}
1578 is computed by a weighted average over all tracks in the batch, where the weights
1579 are described below.

1580 The different losses converge to different values during training, reflecting differences
1581 in the relative difficulty of the various training objectives. The values of L_{vertex} and
1582 L_{track} are weighted by $\alpha = 1.5$ and $\beta = 0.5$ respectively to ensure they converge to
1583 similar values, giving them an equal weighting towards L_{total} . The values of α and
1584 β are chosen to ensure that L_{jet} converges to a larger value than either L_{vertex} and
1585 L_{track} , which reflects the primary importance of the jet classification objective. It
1586 was found that in practice the overall performance of the model was not sensitive
1587 to modest changes in the loss weights α and β . Pre-training using L_{total} (i.e. on
1588 all tasks) and fine tuning on only the jet classification task also did not improve
1589 performance versus the standard setup, indicating that the auxiliary tasks are not
1590 in direct competition with the jet classification task. As there was a large variation
1591 in the relative abundance of tracks of the different origins, the contribution of each
1592 origin to L_{track} was weighted by the inverse of the frequency of their occurrence. In
1593 vertexing loss L_{vertex} , the class weight for track-pairs where both tracks are from
1594 either a b - or c -hadron was increased by a factor of two as compared with other

1595 track-pairs, to encourage the network to focus on correctly classifying heavy flavour
1596 vertices.

1597 GN1 can be trained with either the node or edge networks (and their corresponding
1598 auxiliary tasks), or both, removed, as discussed in Section 6.5.3. In such cases,
1599 the corresponding losses L_{vertex} and L_{track} are also removed from the calculation
1600 of the overall loss L_{total} . The performance of the resulting models provides a
1601 useful indication of the benefit of including the auxiliary tasks to the primary jet
1602 classification objective.

1603 GN1 was trained for 100 epochs on 4 NVIDIA V100 GPUs. Each epoch takes
1604 approximately 25 mins to complete over the training sample of 30 million jets. The
1605 Adam optimiser [124] with an initial learning rate of $1e-3$, and a batch size of 4000
1606 jets (spread across the 4 GPUs) was used. Typically the validation loss, calculated
1607 on 500k jets, became stable after around 60 epochs. The epoch that minimized the
1608 validation loss was used for evaluation. GN1 has been integrated into the ATLAS
1609 software [54] using ONNX [125]. The test sample jet flavour predictions scores are
1610 computed using the ATLAS software stack as a verification of this process.

1611 6.5 Results

1612 The GN1 tagger is evaluated both as a b -tagging and c -tagging algorithm in Sec-
1613 tion 6.5.1 and Section 6.5.2 respectively. Evaluation is performed separately on
1614 jets in the $t\bar{t}$ sample with $20 < p_{\text{T}} < 250 \text{ GeV}$ and jets in the Z' sample with
1615 $250 < p_{\text{T}} < 5000 \text{ GeV}$. The performance of the model is compared to the DL1r
1616 tagger [82, 87], which has been retrained on 75 million jets from the same samples as
1617 GN1. The input RNNIP tagger [84] to DL1r has not been retrained. As discussed,
1618 each tagger predicts the probability that a jet belongs to the b -, c - and light-classes.
1619 To use the model for b -tagging, these probabilities are combined into a single score
1620 D_b , which is defined as

$$D_b = \log \frac{p_b}{(1 - f_c)p_l + f_c p_c}, \quad (6.8)$$

where f_c is a free parameter that determines the relative weight of p_c to p_l in the score D_b , controlling the trade-off between c - and light-jet rejection performance. The choice of f_c is arbitrary, and is optimised based upon the desired light- vs c -jet rejection performance. This parameter is set to a value of $f_c = 0.018$ for the DL1r model, obtained through an optimisation procedure described in Ref. [82]. Based on a similar optimisation procedure, a value of $f_c = 0.05$ is used for the GN1 models. A fixed-cut working point (WP) defines the corresponding selection applied to the tagging discriminant D_b in order to achieve a given efficiency on the inclusive $t\bar{t}$ sample.

A comparison of the b -tagging discriminant D_b between DL1r and GN1 is shown in Fig. 6.5. The shapes of the D_b distributions are generally similar for b -, c - and light-jets between both models, however, GN1 shifts the b -jet distribution to higher values of D_b in the regions with the greatest discrimination. The GN1 c -jet distribution is also shifted to lower values of D_b when compared with DL1r, enhancing the separation and indicating that GN1 is improving c -jet rejection when compared with DL1r.

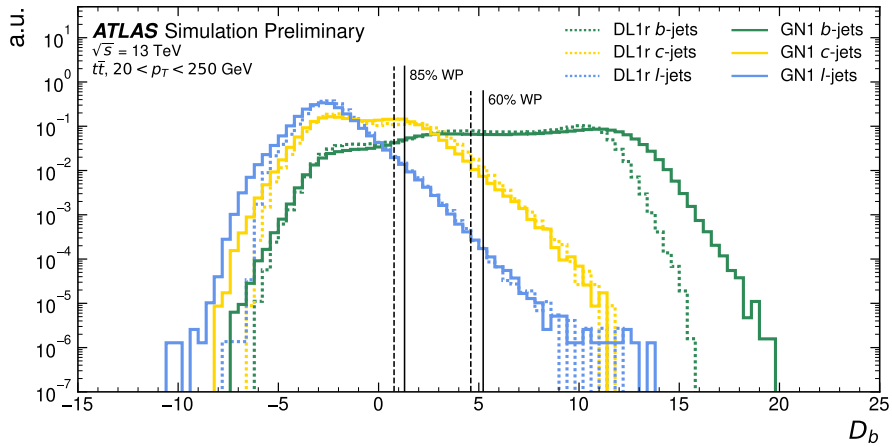


Figure 6.5: Comparison between the DL1r and GN1 b -tagging discriminant D_b for jets in the $t\bar{t}$ sample. The 85% WP and the 60% WP are marked by the solid (dashed) lines for GN1 (DL1r), representing respectively the loosest and tightest WPs typically used by analyses. A value of $f_c = 0.018$ is used in the calculation of D_b for DL1r and $f_c = 0.05$ is used for GN1. The distributions of the different jet flavours have been normalised to unity area [3].

6.5.1 b -tagging Performance

The performance of b -tagging algorithms is quantified by their ability to reject c - and light-jets for a given b -jet selection efficiency WP. In order to compare the b -tagging performance of the different taggers for the b -jet tagging efficiencies in the range typically used by analyses, the corresponding c - and light-jet rejection rates are displayed in Figs. 6.6 and 6.7 for jets in the $t\bar{t}$ and Z' samples respectively. Four standard WPs are defined with b -jet tagging efficiencies of 60%, 70%, 77% and 85% respectively. These WPs are commonly used by physics analyses depending on their specific signal and background requirements. The WPs are defined based on jets in the $t\bar{t}$ sample only. Due to the much higher jet p_T range in the Z' sample, and the increased difficulty in tagging jets at high- p_T (see Chapter 4), the corresponding b -jet tagging efficiencies for jets in the Z' sample are lower than the corresponding WPs calculated in the $t\bar{t}$ sample. For instance the WP cut value computed to provide a 70% b -jet tagging efficiency on the $t\bar{t}$ sample results in a b -jet tagging efficiency of just $\sim 30\%$ on the Z' sample. In order to account for this, the range of b -jet tagging efficiencies displayed for plots showing the performance for jets in the Z' sample (for example Fig. 6.7) is chosen to span the lower efficiencies achieved in the Z' sample at high- p_T .

For jets in the $t\bar{t}$ sample with $20 < p_T < 250 \text{ GeV}$, GN1 demonstrates considerably better c - and light-jet rejection when compared with DL1r across the full range of b -jet tagging efficiencies studied. The relative improvement is strongly dependent on the b -jet tagging efficiency under study. The largest improvements are found at lower b -jet tagging efficiencies. At a b -jet tagging efficiency of 70%, the c -jet rejection improves by a factor of ~ 2.1 while the light-jet rejection improves by a factor of ~ 1.8 with respect to DL1r. For high- p_T jets in the Z' sample with $250 < p_T < 5000 \text{ GeV}$, GN1 also brings a significant performance improvement with respect to DL1r across the range of b -jet tagging efficiencies studied. Again, the largest relative improvement in performance comes at the lower b -jet tagging efficiencies. At a b -jet efficiency of 30%, GN1 improves the c -jet rejection with respect to DL1r by a factor of ~ 2.8 and the light-jet rejection by a factor of ~ 6 . The performance comparison at lower b -jet tagging efficiencies is made more difficult due to the increased statistical uncertainties which result from the high rejection of background.

1668 The GN1Lep variant of GN1 demonstrates further improved performance with respect
1669 to the baseline model. This demonstrates the additional jet flavour discrimination
1670 power provided by the leptonID track input. For jets in the $t\bar{t}$ sample, the relative c -
1671 jet rejection improvement with respect to GN1 at the 70% b -jet WP is approximately
1672 25%. The improvement in light-jet rejection also increases by 40% at the same WP.
1673 For jets in the Z' sample, the relative c -jet rejection (light-jet rejection) performance
1674 with respect to GN1 improves by approximately 10% (25%) at a b -jet tagging
1675 efficiency of 30%.

1676 In general, the performance of all the taggers is strongly dependent on jet p_T , due
1677 to the increased multiplicity and collimation of tracks, and the displaced decays
1678 that result from within the heavy flavour jets (see Chapter 4). Together, they
1679 contribute to a reduced reconstruction efficiency for heavy flavour tracks, and a
1680 general degradation in quality of tracks inside the core of a jet, which in turn reduces
1681 the jet tagging performance. In order to study how the tagging performance changes
1682 as a function of the jet p_T , the b -jet tagging efficiency as a function of p_T for a fixed
1683 light-jet rejection of 100 in each bin is shown in Fig. 6.8. For jets in the $t\bar{t}$ sample,
1684 at a fixed light-jet rejection of 100, GN1 improves the b -jet tagging efficiency by
1685 approximately 4% across all the jet p_T bins. Meanwhile, GN1Lep again demonstrates
1686 improved performance with respect to GN1, in particular at lower p_T . The relative
1687 increase in the b -jet tagging efficiency increases from 4% to 8% with respect to DL1r.
1688 For jets in the Z' sample, GN1 again outperforms DL1r across the entire jet p_T range
1689 studied. The largest relative improvement in performance is found at the highest
1690 transverse momenta of jet $p_T > 2 \text{ TeV}$, and corresponds to an approximate factor of
1691 2 improvement in efficiency with respect to DL1r.

1692 The performance of the model was also evaluated as a function of the average
1693 number of pile-up interactions in the event. No significant dependence of the tagging
1694 performance was observed.

1695 6.5.2 c -tagging Performance

1696 As discussed previously, GN1 does not rely on any inputs from manually optimised
1697 low-level tagging algorithms. Since these algorithms were originally designed and
1698 tuned with the aim of b -tagging, and not c -tagging, the low level tagging algorithms
1699 may perform suboptimally for c -tagging purposes. The tagging of c -jets therefore

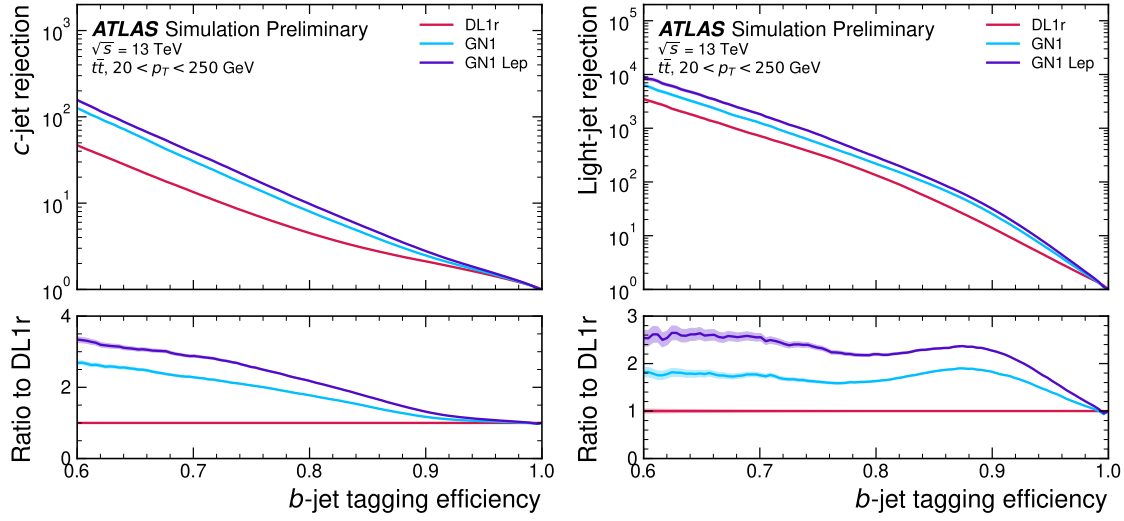


Figure 6.6: The c -jet (left) and light-jet (right) rejections as a function of the b -jet tagging efficiency for jets in the $t\bar{t}$ sample with $20 < p_T < 250 \text{ GeV}$. The ratio with respect to the performance of the DL1r algorithm is shown in the bottom panels. A value of $f_c = 0.018$ is used in the calculation of D_b for DL1r and $f_c = 0.05$ is used for GN1 and GN1Lep. Binomial error bands are denoted by the shaded regions. The x -axis range is chosen to display the b -jet tagging efficiencies usually probed in these regions of phase space [3].

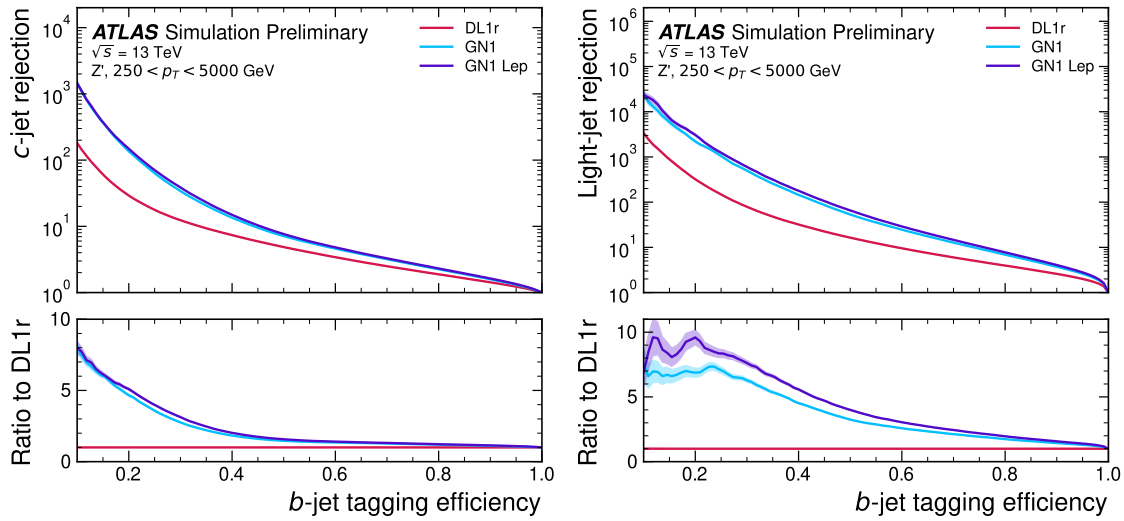


Figure 6.7: The c -jet (left) and light-jet (right) rejections as a function of the b -jet tagging efficiency for jets in the Z' sample with $250 < p_T < 5000 \text{ GeV}$. The ratio with respect to the performance of the DL1r algorithm is shown in the bottom panels. A value of $f_c = 0.018$ is used in the calculation of D_b for DL1r and $f_c = 0.05$ is used for GN1 and GN1Lep. Binomial error bands are denoted by the shaded regions. The x -axis range is chosen to display the b -jet tagging efficiencies usually probed in these regions of phase space [3].

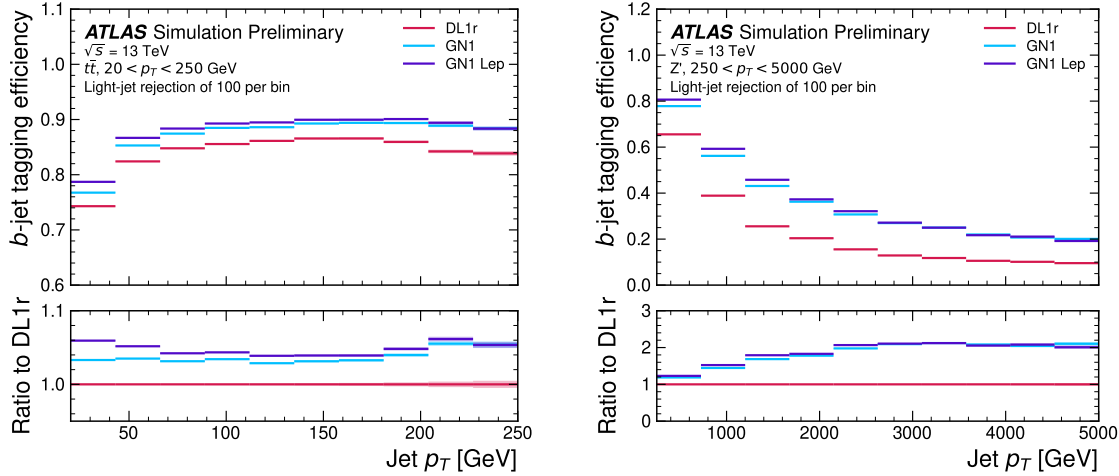


Figure 6.8: The b -jet tagging efficiency for jets in the $t\bar{t}$ sample (left) and jets in the Z' sample (right) as a function of jet p_T with a fixed light-jet rejection of 100 in each bin. A value of $f_c = 0.018$ is used in the calculation of D_b for DL1r and $f_c = 0.05$ is used for GN1 and GN1Lep. GN1 demonstrates improved performance with respect to DL1r accross the p_T range shown. Binomial error bands are denoted by the shaded regions [3].

1700 presents a compelling use case for GN1. As each of the models is trained with three
 1701 output classes, using it as a c -tagging algorithm is trivially analogous to the approach
 1702 used for b -tagging. The model output probabilities are combined into a single score
 1703 D_c , which is defined similarly to Eq. (6.8) as

$$D_c = \log \frac{p_c}{(1 - f_b)p_l + f_b p_b}. \quad (6.9)$$

1704 A value of $f_b = 0.2$ is used for all models, based on the same optimisation procedure
 1705 that was used for the b -tagging use case. Similar to Section 6.5.1, the different
 1706 taggers are compared to one another by scanning through a range of c -jet tagging
 1707 efficiencies and plotting the corresponding b - and light-jet rejection rates, and the
 1708 WPs are defined using jets in the $t\bar{t}$ sample. Standard c -jet tagging efficiency WPs
 1709 used by physics analyses are significantly lower than the b -tagging WPs in order to
 1710 maintain reasonable b - and light-jet rejection rates. This is reflected in the range of
 1711 c -jet tagging efficiencies used in c -tagging plots such as Figs. 6.9 and 6.10. Fig. 6.9
 1712 displays the c -tagging performance of the models on the jets in the $t\bar{t}$ sample. GN1
 1713 is shown to perform significantly better than DL1r. Similar to the b -tagging case,

the b - and light-jet rejection improve most at lower c -jet tagging efficiencies, with the c -jet rejection (light-jet rejection) improving by a factor 2 (1.6) with respect to DL1r at a c -jet tagging efficiency of 25%. GN1Lep again outperforms GN1, though the improvements are more modest than observed for the b -tagging use case, with both the b -jet rejection (light-jet rejection) improving with respect to GN1 by approximately 10% (20%) at the 25% c -jet WP. Fig. 6.10 shows the c -tagging performance on the jets in the Z' sample with $250 < p_T < 5000$ GeV. Both GN1 and GN1Lep perform similarly, improving the b -jet rejection by 60% and the light-jet rejection by a factor of 2 at the 25% c -jet WP.

6.5.3 Ablations

Ablation studies (the removal of certain components of a model in order to study the impact of that component) are carried out to determine the importance of the auxiliary training objectives of GN1 to the overall performance. The “GN1 No Aux” variant retains the primary jet classification objective, but removes both track classification and vertexing auxiliary objectives and correspondingly only minimises the jet classification loss. The “GN1 TC” variant includes the track classification objective but not the vertexing objective. Finally, the “GN1 Vert” includes the vertexing objective, but not the track classification objective.

For jets in both the $t\bar{t}$ and Z' samples, a general trend is observed that the models trained without one or both of the auxiliary objectives results in significantly reduced c - and light-jet rejection when compared with the baseline GN1 model, as shown in Figs. 6.11 and 6.12. For jets in the $t\bar{t}$ sample, the performance of GN1 No Aux is similar to DL1r, while GN1 TC and GN1 Vert perform similarly to each other. For jets in the Z' sample, the GN1 No Aux model shows a clear improvement in c - and light-jet rejection when compared with DL1r at lower b -jet tagging efficiencies. Similar to jets in the $t\bar{t}$ sample, GN1 TC and GN1 Vert perform similarly, and bring large gains in background rejection when compared with GN1 No Aux, but the combination of both auxiliary objectives yields the best performance.

It is notable that the GN1 No Aux model matches or exceeds the performance of DL1r without the need for inputs from the low-level algorithms. This indicates that the performance improvements enabled by the improved neural network architecture used in GN1 appear to be able to compensate for the removal of the low-level

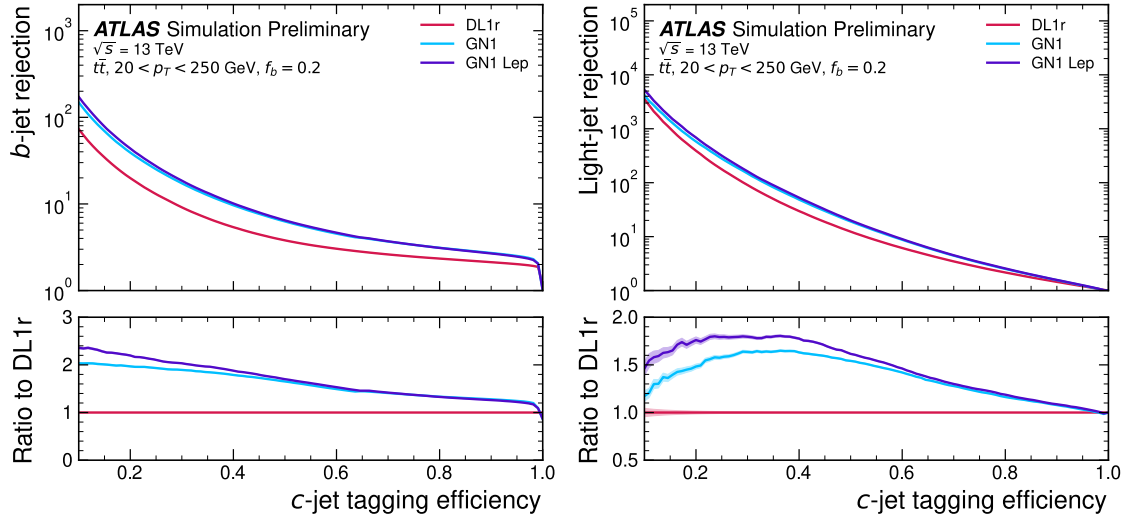


Figure 6.9: The b -jet (left) and light-jet (right) rejections as a function of the c -jet tagging efficiency for $t\bar{t}$ jets with $20 < p_T < 250$ GeV. The ratio to the performance of the DL1r algorithm is shown in the bottom panels. Binomial error bands are denoted by the shaded regions. The x -axis range is chosen to display the c -jet tagging efficiencies usually probed in these regions of phase space [3].

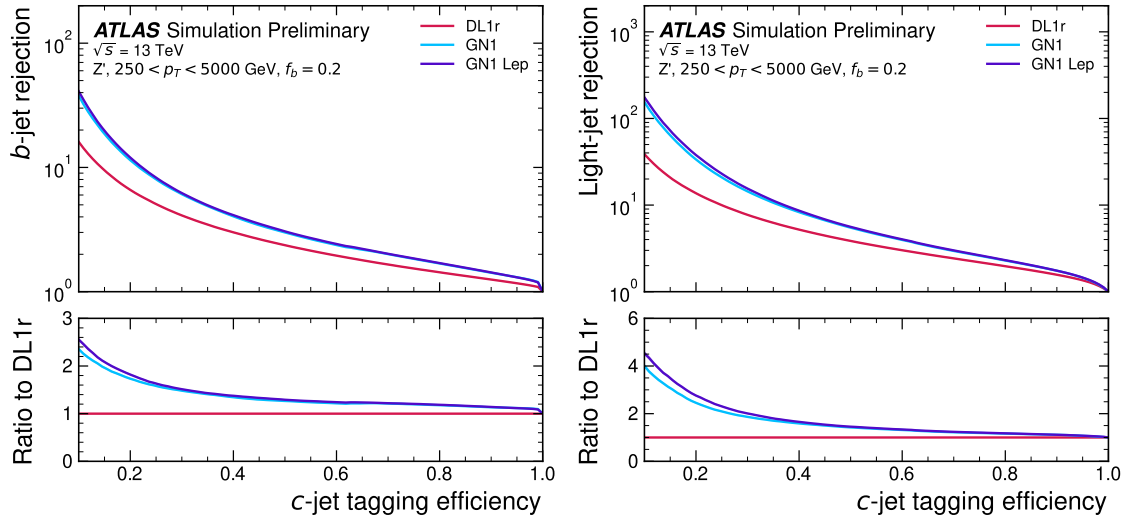


Figure 6.10: The b -jet (left) and light-jet (right) rejections as a function of the c -jet tagging efficiency for Z' jets with $250 < p_T < 5000$ GeV. The ratio to the performance of the DL1r algorithm is shown in the bottom panels. Binomial error bands are denoted by the shaded regions. The x -axis range is chosen to display the c -jet tagging efficiencies usually probed in these regions of phase space [3].

1746 algorithm inputs. The GN1 TC and GN1 Vert variants each similarly outperform
1747 DL1r, demonstrating that both contribute to the overall high performance of the
1748 baseline model. The overall best performing model is the full version of GN1 trained
1749 with both auxiliary objective, demonstrating that the two auxiliary objectives are
1750 complementary.

1751 6.5.4 Inclusion of Low-Level Vertexing Algorithms

1752 As already mentioned, GN1 does not include any inputs from the low-level tagging
1753 algorithms, including the vertexing algorithms SV1 and JetFitter [61]. Since these
1754 algorithms are known to play a key role in contributing to the performance of DL1r,
1755 it was studied whether their inclusion in GN1 could result in further performance
1756 improvements. In a dedicated training of GN1, the SV1 and JetFitter tagger outputs
1757 were added to the GN1 jet classification network as an input, similar to how they
1758 are used in DL1r. These outputs include information on the reconstructed vertices,
1759 including the number of vertices, and the properties of the reconstructed vertices.
1760 In addition, if track was used in the reconstruction of a vertex, a corresponding
1761 index to the vertex was included as a track-level inputs to GN1. These indices were
1762 also used to construct an input feature for the edge classification network used to
1763 identify vertices, which was given a value of one if the track-pair were from a common
1764 reconstructed SV1 or JetFitter vertex, and zero otherwise. The jet classification
1765 performance of this GN1 model was not significantly different to the baseline model,
1766 and in some cases the performance was slightly reduced. It was therefore concluded
1767 that GN1 does not benefit from the inclusion of information from SV1 and JetFitter,
1768 indicating that the model is able to reconstruct the relevant information provided
1769 by these low-level algorithms. The study also demonstrates that the model can
1770 function as a highly performant standalone tagger that does not require (beyond
1771 retraining) any manual optimisation to achieve good performance in a wide range
1772 of phase spaces. A dedicated look at the vertexing performance of GN1 with some
1773 comparisons to SV1 and JetFitter is found in Section 6.5.6

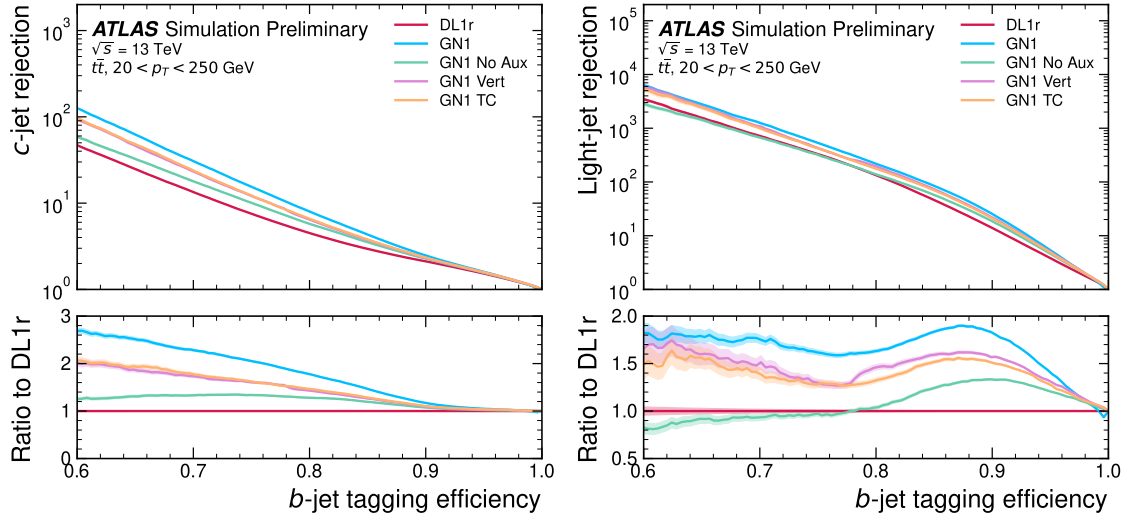


Figure 6.11: The c -jet (left) and light-jet (right) rejections as a function of the b -jet tagging efficiency for $t\bar{t}$ jets with $20 < p_T < 250$ GeV, for the nominal GN1, in addition to configurations where no (GN1 No Aux), only the track classification (GN1 TC) or only the vertexing (GN1 Vert) auxiliary objectives are deployed. The ratio to the performance of the DL1r algorithm is shown in the bottom panels. A value of $f_c = 0.018$ is used in the calculation of D_b for DL1r and $f_c = 0.05$ is used for GN1 [3].

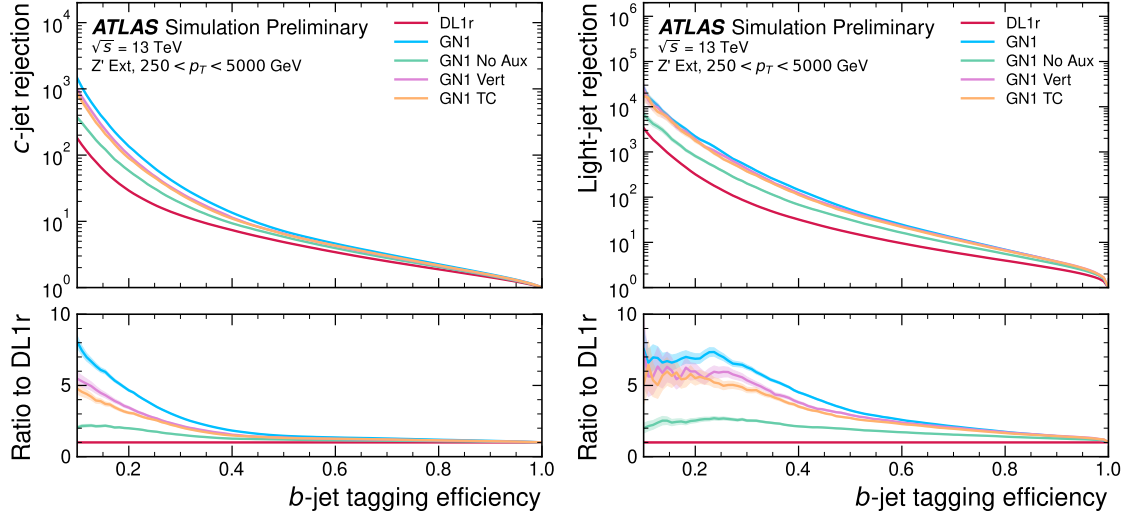


Figure 6.12: The c -jet (left) and light-jet (right) rejections as a function of the b -jet tagging efficiency for Z' jets with $250 < p_T < 5000$ GeV, for the nominal GN1, in addition to configurations where no (GN1 No Aux), only the track classification (GN1 TC) or only the vertexing (GN1 Vert) auxiliary objectives are deployed. The ratio to the performance of the DL1r algorithm is shown in the bottom panels. A value of $f_c = 0.018$ is used in the calculation of D_b for DL1r and $f_c = 0.05$ is used for GN1 [3].

6.5.5 Jet Display Diagrams

The auxiliary training objectives of GN1 allow for improved model interpretability, which is especially important for a monolithic approach as the low level taggers, which provide useful physical insight, are no longer present. Figs. 6.13 and 6.14 provide example comparisons of the true origin and vertexing information compared with the predicted values from GN1, SV1 and JetFitter. Such comparisons can be used to provide an indication that GN1 reconstructs the correct representation of the jet structure, and may also help to identify limitations of the model. In the figures, the tracks in the jet are indexed twice on each of the x - and y -axes, and tracks are grouped into vertices along with other tracks as indicated by common markings in the relevant rows and columns.

In Fig. 6.13, GN1 correctly groups the three primary tracks as having come from the primary vertex. The b -hadron and $b \rightarrow c$ -hadron decay vertices are also correctly predicted, and the origin of the tracks in each is correct. There is a single OtherSecondary track which GN1 incorrectly predicts as having come from pile-up. Meanwhile SV1 (by design) merges the two heavy flavour decay vertices, but incorrectly includes a track from the primary vertex. JetFitter reconstructs two vertices, one which is a combination of two tracks from different truth vertices and two other single track vertices in each of the heavy flavour vertices. GN1 also predicts the flavour of the jet with a high degree of certainty.

Similarly Fig. 6.13 shows that GN1 is also able to relatively accurately predict the origin and vertex information of tracks inside a jet. The pile-up tracks and primary vertex tracks are correctly identified, and the heavy flavour decay tracks are also correctly identified with the exception of one of the b -hadron decay tracks. Again, SV1 merges the two heavy flavour decay vertices along with a track from pile-up, while JetFitter shows signs of being underconstrained by reconstructing two single track vertices, one with a pile-up track and one with a track from a $b \rightarrow c$ -hadron decay. While these examples do not give a complete picture of the performance of GN1, they do show provide a powerful way to visualise and diagnose the behaviour of GN1.

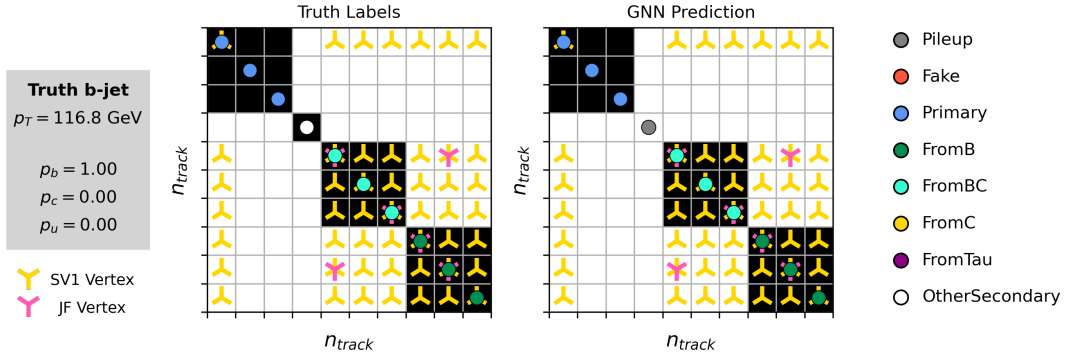


Figure 6.13: A schematic showing the truth track origin and vertex information (left) compared with the predictions from GN1 (right). The diagrams show the truth (left) and predicted (right) structure of a b -jet. The true and predicted origins of the tracks is shown by the coloured circles along the diagonal. The shaded black boxes show the groupings of tracks into different vertices. Vertices reconstructed by SV1 and JetFitter are also marked. Class probabilities p_b , p_c and p_u are rounded to three significant figures. GN1 improves over SV1 and JetFitter by successfully determining the origins and vertex compatibility of all the tracks in the jet with the exception of the truth OtherSecondary track, which is misidentified as pile-up.

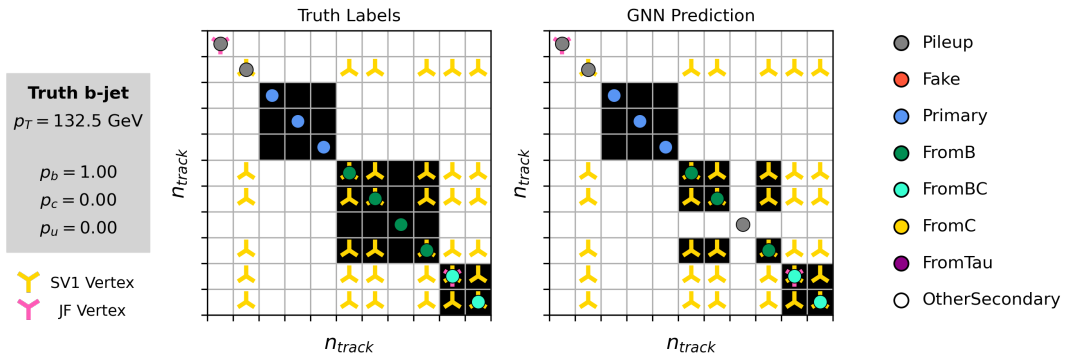


Figure 6.14: A schematic showing the truth track origin and vertex information (left) compared with the predictions from GN1 (right). The diagrams show the truth (left) and predicted (right) structure of a b -jet. The true and predicted origins of the tracks is shown by the coloured circles along the diagonal. The shaded black boxes show the groupings of tracks into different vertices. Vertices reconstructed by SV1 and JetFitter are also marked. Class probabilities p_b , p_c and p_u are rounded to three significant figures. GN1 improves over SV1 and JetFitter by successfully determining the origins and vertex compatibility of all but one tracks in the jet.

1804 6.5.6 Vertexing Performance

1805 From the track-pair vertex prediction, tracks can be partitioned into compatible
1806 groups representing vertices through the use of a deterministed clustering algorithm
1807 (see Ref. [116]). As such, GN1 can perform vertex “finding”, but not vertex “fitting”,
1808 i.e. the reconstruction of a vertex’s properties, which currently still requires the
1809 use of a dedicated vertex fitter. In order to study the performance of the different
1810 vertexing tools, the truth vertex label of the tracks are used.

1811 There are several caveats to a comparison of the vertexing tools which are a result
1812 of the different approaches they take to vertexing. SV1 and JetFitter are designed
1813 to only find secondary vertices in the jet, whereas GN1 is also trained to determine
1814 which tracks in the jet belong to the primary vertex. To account for this the GN1
1815 vertex with the largest number of predicted primary tracks is excluded from the
1816 vertex finding efficiency calculation. While JetFitter and GN1 aim to resolve each
1817 displaced vertex inside the jet, such that secondary vertices from b -hadron decays
1818 are found separately to tertiary vertices from $b \rightarrow c$ decay chains, SV1 by design
1819 attempts to find a single inclusive vertex per jet. This inclusive vertex groups tracks
1820 from the b -hadron decay itself (FromB) and tracks from $b \rightarrow c$ decays (FromBC). In
1821 order to fairly compare the performance of the different tools, both the exclusive and
1822 inclusive vertex finding efficiencies are studied. For the exclusive vertex finding case
1823 JetFitter and GN1 can be directly compared, while a comparison with SV1 is not
1824 possible due to the aforementioned design constraints. The inclusive vertex finding
1825 performance of all three tools can be compared using the procedure outlined below.

1826 The starting point for the secondary vertex finding efficiency in both the exclusive and
1827 inclusive cases is to select truth HF secondary vertices, defined as those containing
1828 only inclusive b -hadron decays. For exclusive HF vertex finding, these truth secondary
1829 HF vertices can be used directly as the denominator for the efficiency calculation.
1830 Meanwhile for the inclusive efficiency all such truth HF secondary vertices in the jet
1831 are merged into a single inclusive target vertex. Correspondingly, for the inclusive
1832 HF vertex finding case, the vertices found by JetFitter are merged into a single
1833 vertex, and the vertices found by GN1 which contain at least one predicted b -hadron
1834 decay track, are also merged. SV1 does not require any vertex merging. Only jets
1835 containing a single b -hadron at truth level are considered.

1836 Next, vertices in the jet found by the different vertexing tools are compared with
 1837 the target truth vertices. The number of correctly and incorrectly assigned tracks is
 1838 computed. In order to call a vertex efficient, it is required to contain at least 65% of
 1839 the tracks in the corresponding truth vertex, and to have a purity of at least 50%.
 1840 Single track vertices are required to have a purity of 100%. Additionally, for GN1
 1841 only, at least one track in the vertex is required to have a predicted heavy flavour
 1842 origin.

1843 Vertex finding efficiencies for b -jets in the $t\bar{t}$ sample are displayed as a function of
 1844 p_T separately for the inclusive and exclusive approaches in Fig. 6.15. For b -jets in
 1845 the $t\bar{t}$ sample with $20 < p_T < 250$ GeV, the exclusive vertex finding efficiency of
 1846 JetFitter and GN1 is relatively flat as a function of p_T . For the truth secondary
 1847 vertices in this p_T region, JetFitter efficiently finds approximately 40% and GN1 finds
 1848 approximately 55%. When finding vertices inclusively the vertex finding efficiency is
 1849 generally higher. An increased dependence on p_T is also visible for JetFitter and SV1.
 1850 As the jet p_T increases from 20 GeV to 100 GeV, the efficiency of JetFitter increases
 1851 from 60% to 65%. In the same range, the efficiency of SV1 increases from 60% to
 1852 75%. GN1 displays less dependence on p_T than JetFitter and SV1, finding upwards
 1853 of 80% of vertices in b -jets in this p_T region. For b -jets with $p_T > 100$ GeV, JetFitter
 1854 finds approximately 65% of vertices, SV1 finds approximately 75% of vertices, and
 1855 GN1 finds approximately 80% of vertices.

1856 Fig. 6.16 compares the exclusive and inclusive HF vertex finding efficiencies for
 1857 b -jets in the Z' sample. The inclusive vertex finding efficiency drops steeply with
 1858 increasing p_T up until $p_T = 3$ TeV. GN1 outperforms SV1 and JetFitter across the p_T
 1859 spectrum. In the first bin, the efficiency of GN1 is 65%, while the efficiencies of SV1
 1860 and JetFitter are around 55%. The efficiency of SV1 drops rapidly to almost zero
 1861 above 3 TeV, while JetFitter and GN1 retain approximately 20% and 30% efficiency
 1862 respectively. For the exclusive HF vertex finding efficiency, JetFitter finds 35% of
 1863 vertices in the first bin, dropping to 20% of vertices above 2 TeV. GN1 finds 55% of
 1864 vertices in the first bin, dropping to 30% above 2 TeV.

1865 While Figs. 6.15 and 6.16 indicate that GN1 is able to successfully find displaced heavy
 1866 flavour vertices in b -jets, it is also important to consider the vertexing performance
 1867 inside light-jets. Light-jets may also contain real displaced vertices due to long lived
 1868 secondary particles and material interactions. These tracks have a truth origin of
 1869 OtherSecondary in the truth labelling scheme enumerated in see Table 5.1. The

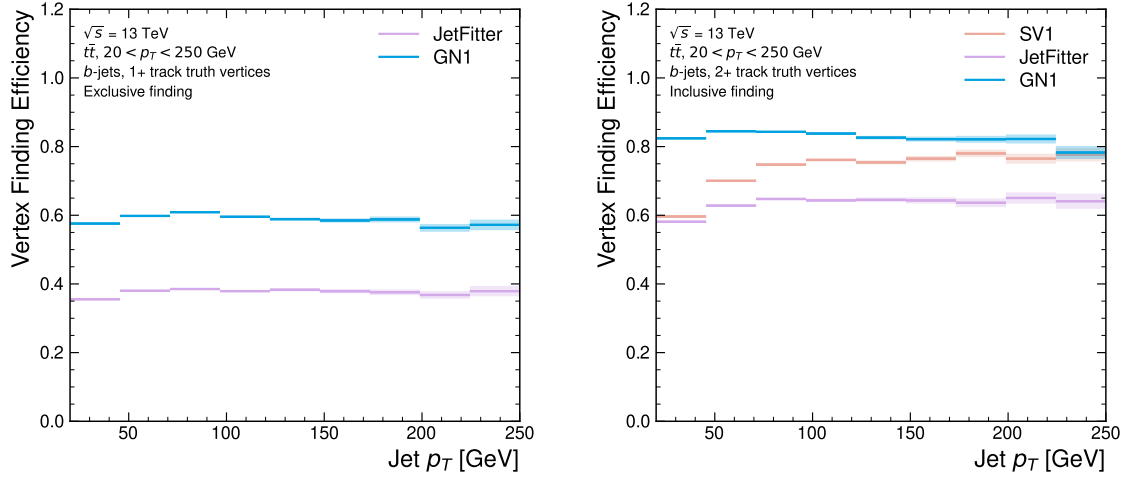


Figure 6.15: Heavy flavour vertex finding efficiency as a function of jet p_T for b -jets in the $t\bar{t}$ sample using the exclusive (left) and inclusive (right) vertex finding approaches. The exclusive vertexing approach includes single track vertices while the inclusive approach requires vertices to contain at least two tracks. Efficient vertex finding requires the recall of at least 65% of the tracks in the truth vertex, and allows no more than 50% of the tracks to be included incorrectly. Binomial error bands are denoted by the shaded regions.

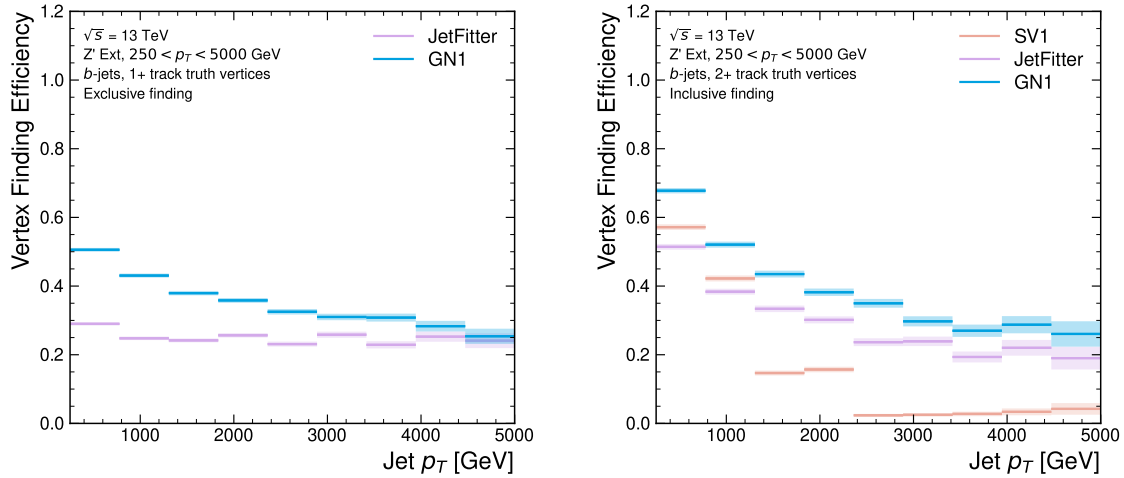


Figure 6.16: Heavy flavour vertex finding efficiency as a function of jet p_T for b -jets in the Z' sample using the exclusive (left) and inclusive (right) vertex finding approaches. The exclusive vertexing approach includes single track vertices while the inclusive approach requires vertices to contain at least two tracks. Efficient vertex finding requires the recall of at least 65% of the tracks in the truth vertex, and allows no more than 50% of the tracks to be included incorrectly. Binomial error bands are denoted by the shaded regions.

efficiency to reconstruct vertices comprised of OtherSecondary tracks can be computed in an analogous way to the heavy flavour vertexing efficiency, which is described above. Figs. 6.17 and 6.18 show the efficiency to reconstruct displaced OtherSecondary vertices in light-jets as a function of p_T for jets in the $t\bar{t}$ sample and jets in the Z' sample respectively. The figures demonstrate that GN1 is able to more effectively find such vertices in light-jets as compared with SV1 and JetFitter. Since the properties of the displaced vertices in light-jets are likely to be significantly different to heavy flavour vertices found in heavy flavour jets, the improved reconstruction of such vertices may help to differentiate between different flavour of jet.

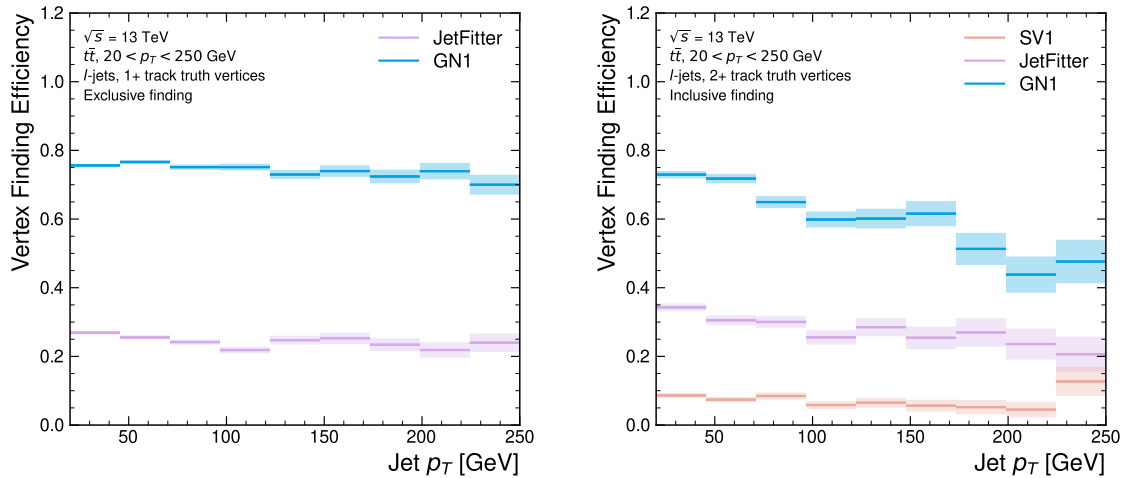


Figure 6.17: Vertex finding efficiency for other secondary decays as a function of jet p_T for light-jets in the $t\bar{t}$ sample using the exclusive (left) and inclusive (right) vertex finding approaches. The exclusive vertexing approach includes single track vertices while the inclusive approach requires vertices to contain at least two tracks. Efficient vertex finding requires the recall of at least 65% of the tracks in the truth vertex, and allows no more than 50% of the tracks to be included incorrectly. Binomial error bands are denoted by the shaded regions.

Collectively, the results in this section demonstrate that GN1 is able to accurately group tracks by their spatial origin in both b -jets and light-jets. The purity of the found vertices was also investigated and was found to be comparable or better than that of SV1 and JetFitter.

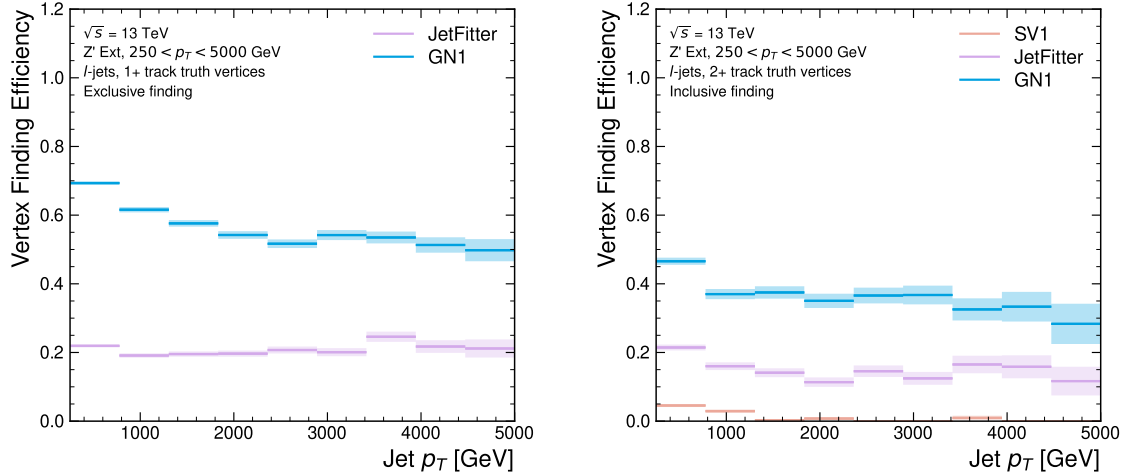


Figure 6.18: Vertex finding efficiency as a function of jet p_T for light-jets in the Z' sample using the exclusive (left) and inclusive (right) vertex finding approaches. The exclusive vertexing approach includes single track vertices while the inclusive approach requires vertices to contain at least two tracks. Efficient vertex finding requires the recall of at least 65% of the tracks in the truth vertex, and allows no more than 50% of the tracks to be included incorrectly. Binomial error bands are denoted by the shaded regions.

1883 6.5.7 Track Classification Performance

1884 One of the two auxiliary training objectives used by GN1 is to predict the truth origin
 1885 of each track associated to the jet. Since the equivalent information is not provided
 1886 by any of the existing flavour tagging tools, a benchmark model used to predict the
 1887 truth origin of each track is trained based on a standard multi-class feed-forward
 1888 classification network. The benchmark model is trained on the same tracks used for
 1889 the baseline GN1 training. The model uses precisely the same concatenated track-
 1890 and-jet inputs as used by GN1, but processes only a single track at a time, meaning
 1891 it cannot take into account the correlations between tracks when determining the
 1892 track origin. The model is made up of five densely connected linear layers with 200
 1893 neurons in each layer. The performance of the model was found to be unsensitive to
 1894 changes in the network structure.

1895 To measure the track classification performance, the area under the curve (AUC) of
 1896 the receiver operating characteristic (ROC) curve is computed for each origin class,
 1897 using a one-versus-all classification approach². The AUCs for the different truth

²One class is taken to be signal and the rest are taken as background, subsequently a binary classification approach is used.

origins are averaged using both an unweighted and a weighted mean. The unweighted mean treats the performance of each class equally, while the weighted mean uses as a weight the relative abundance of tracks of each class. Table 6.3 demonstrates clearly that GN1 outperforms the MLP both at $20 < p_T < 250 \text{ GeV}$ for jets in the $t\bar{t}$ sample and at $250 < p_T < 5000 \text{ GeV}$ for jets in the Z' sample. For example, GN1 can reject 65% of fake tracks in jets in the $t\bar{t}$ sample, while retaining more than 99% of good tracks (i.e. those tracks which are not fake). The GN1 model has two advantages over the MLP which can explain the performance improvement. Firstly, the graph neural network architecture enables the sharing of information between tracks. This is likely to be beneficial since the origins of different tracks within a jet are correlated. Secondly, the jet classification and vertexing objectives may be complementary to the track classification objective, and so the track classification performance is improved by the combined training of complementary objectives.

		AUC		Precision		Recall		F1	
		Mean	Weighted	Mean	Weighted	Mean	Weighted	Mean	Weighted
$t\bar{t}$	MLP	0.87	0.89	0.39	0.71	0.51	0.56	0.36	0.62
	GN1	0.92	0.95	0.51	0.82	0.64	0.70	0.51	0.74
Z'	MLP	0.90	0.94	0.36	0.84	0.47	0.72	0.31	0.76
	GN1	0.94	0.96	0.48	0.88	0.60	0.79	0.48	0.82

Table 6.3: The area under the ROC curves (AUC) for the track classification from GN1, compared to a standard multilayer perceptron (MLP) trained on a per-track basis. The unweighted mean AUC over the origin classes and weighted mean AUC (using as a weight the fraction of tracks from the given origin) is provided. GN1, which uses an architecture that allows track origins to be classified in a conditional manner as discussed in Section 6.4.3, outperforms the MLP model for both $t\bar{t}$ and Z' jets.

Fig. 6.19 shows the track origin classification ROC curves for the different track origins for jets in both the $t\bar{t}$ and Z' samples. In order to improve visual readability of the plot, the curves for the heavy flavour truth origins (FromB, FromBC and FromC) have been combined (weighted by their relative abundance), as have the Primary and OtherSecondary origins. In jets in both the $t\bar{t}$ and Z' samples, the AUC of all the different origin groups exceeds 0.9, representing strong overall classification performance. In both samples fake tracks are the easiest to classify, followed by pile-up tracks. The FromC tracks which are c -hadron decay products, are the hardest

1919 to classify, possibly due to their similarity to both fragmentation tracks and b -hadron
1920 decay tracks, depending on the c -hadron species in question.

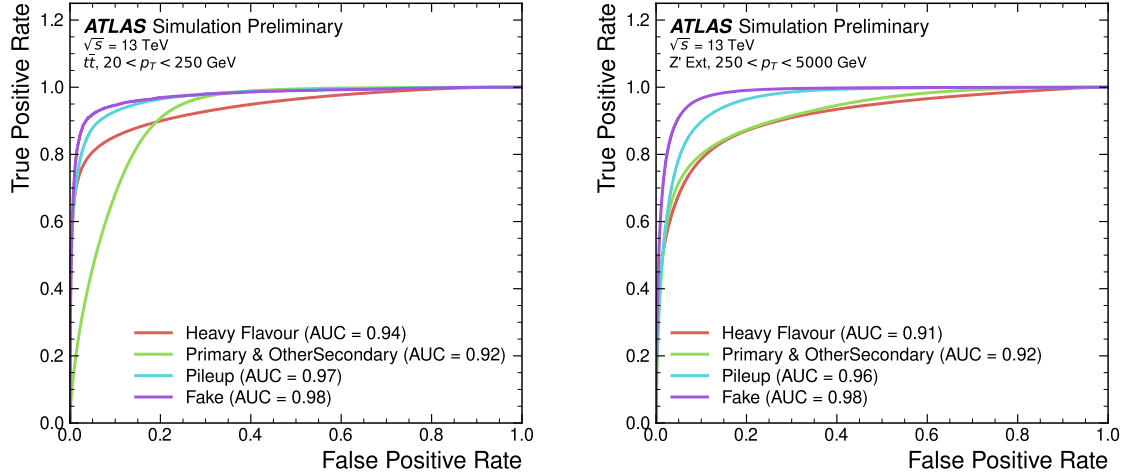


Figure 6.19: ROC curves for the different groups of truth origin labels defined in Table 5.1 for jets in the $t\bar{t}$ sample (left) and jets in the Z' sample (right). The FromB, FromBC and FromC labels have been combined, weighted by their relative abundance, into the Heavy Flavour category, and the Primary and OtherSecondary labels have similarly been combined into a single category. The mean weighted area under the ROC curves (AUC) is similar for both samples [3].

1921 6.5.8 Looser Track Selection

1922 The track selections used to produce the main results are listed in Table 3.2. This
1923 selection includes a cut on the number of shared silicon modules used to reconstruct
1924 the track $N_{\text{shared}}^{\text{Si}}$. This value is calculated as

$$N_{\text{shared}}^{\text{Si}} = N_{\text{shared}}^{\text{Pix}} + N_{\text{shared}}^{\text{SCT}}/2 \quad (6.10)$$

1925 where $N_{\text{shared}}^{\text{Pix}}$ is the number of shared pixel hits and $N_{\text{shared}}^{\text{SCT}}$ is the number of shared
1926 SCT modules on a track. The nominal cut used elsewhere in this thesis is $N_{\text{shared}}^{\text{Si}} < 2$.
1927 As the rate of shared hits is significantly higher for b -hadron decay tracks than for
1928 other tracks, especially at high- p_T , this cut rejects a significant proportion of these
1929 tracks.

1930 Figs. 6.20 and 6.21 show the result of training the GN1 tagger with the full relaxation
1931 of this cut, i.e. allowing tracks with any number of shared hits. The shared hit

1932 requirements applied by the ambiguity solver as part of track reconstruction (see
1933 Section 3.4.1) are still applied. In addition, the maximum allowed value of d_0 is
1934 increased from 3.5 mm to 5.0 mm. The results show that optimisation of the input
1935 track selection can lead to significant improvements in performance over the default
1936 selection. For the jets in the $t\bar{t}$ sample shown in Fig. 6.20, the effect of loosening
1937 the track selection is limited. This is expected due to the lower prevalence of shared
1938 hits at lower transverse momenta. However for jets in the Z' sample as shown in
1939 Fig. 6.21, the light-jet rejection improves with respect to the baseline GN1 model by
1940 30%, while the light-jet rejection improves by 70% at the 50% b -jet WP.

1941 6.6 Other Implementations of GN1

1942 6.6.1 High Level Trigger

1943 The implementation of GN1 described in this chapter has been re-used in several
1944 other contexts, demonstrating its flexibility to easily provide good jet flavour tagging
1945 performance with minimal overhead. The model has been implemented as a b -jet
1946 tagger in the High Level Trigger (HLT) (see Section 3.3.4). The inputs to the model
1947 are the running on precision tracks³ and jet level quantities reconstructed after
1948 primary vertex reconstruction has been performed. Fig. 6.22 shows the performance
1949 of GN1 versus a comparable DL1d model [87], and two versions of DIPS [85], with
1950 EMTopo and PFlow jets (see Section 3.4.3) based on a low-precision region-of-interest
1951 based tracking pass, which is optimised for speed. The trigger implementation of
1952 GN1 improves upon the light-jet rejection of DL1d by 50% at the 60% b -jet WP for
1953 jets in the $t\bar{t}$ sample with $20 < p_T < 250$ GeV.

1954 6.6.2 High Luminosity LHC

1955 The model also demonstrates strong performance for the High Luminosity LHC (HL-
1956 LHC) using the proposed ITk inner tracking detector, as documented in Ref. [127].
1957 Figs. 6.23 and 6.24 are reproduced from Ref. [127]. The results show that GN1

³Precision tracking refers to tracks reconstructed in the trigger using the same reconstruction algorithms as for the offline event reconstruction.

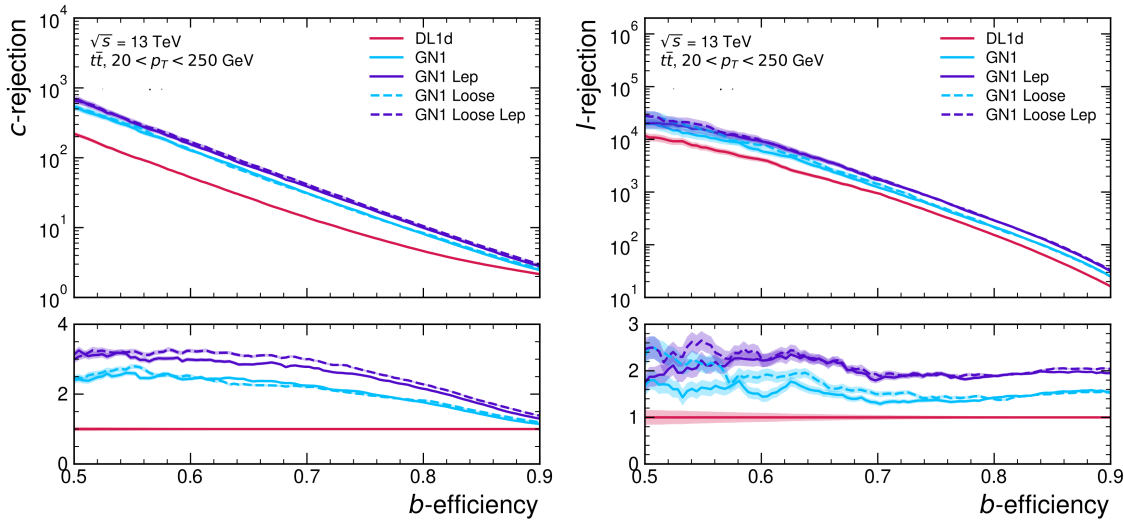


Figure 6.20: The c -jet (left) and light-jet (right) rejections as a function of the b -jet tagging efficiency for $t\bar{t}$ jets with $20 < p_T < 250$ GeV, for the looser track selection trainings of GN1. The ratio to the performance of the DL1d algorithm [87] is shown in the bottom panels. A value of $f_c = 0.018$ is used in the calculation of D_b for DL1d and $f_c = 0.05$ is used for GN1. Binomial error bands are denoted by the shaded regions.

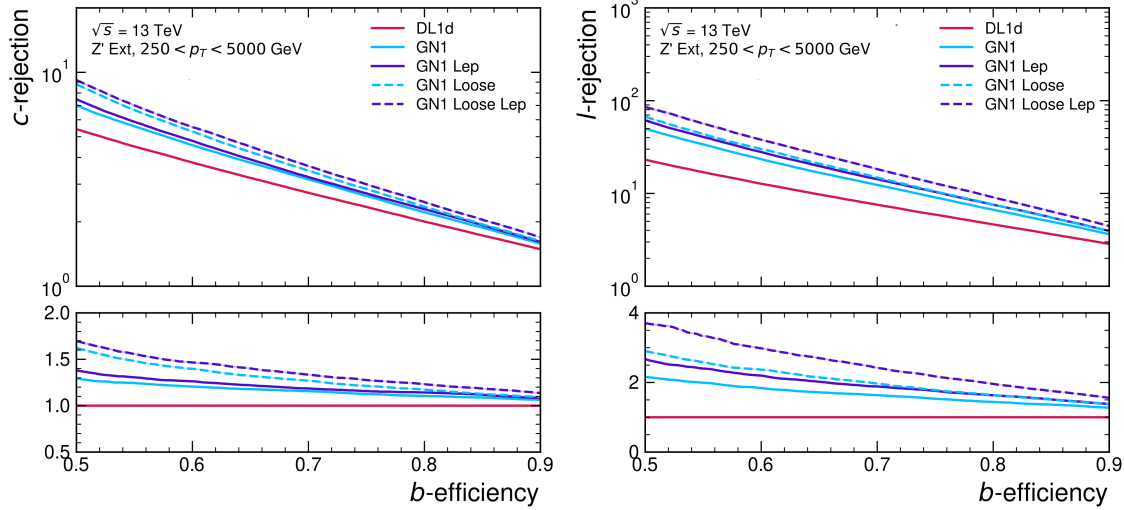


Figure 6.21: The c -jet (left) and light-jet (right) rejections as a function of the b -jet tagging efficiency for Z' jets with $250 < p_T < 5000$ GeV, for the looser track selection trainings of GN1. The ratio to the performance of the DL1d algorithm [87] is shown in the bottom panels. A value of $f_c = 0.018$ is used in the calculation of D_b for DL1d and $f_c = 0.05$ is used for GN1. Binomial error bands are denoted by the shaded regions.

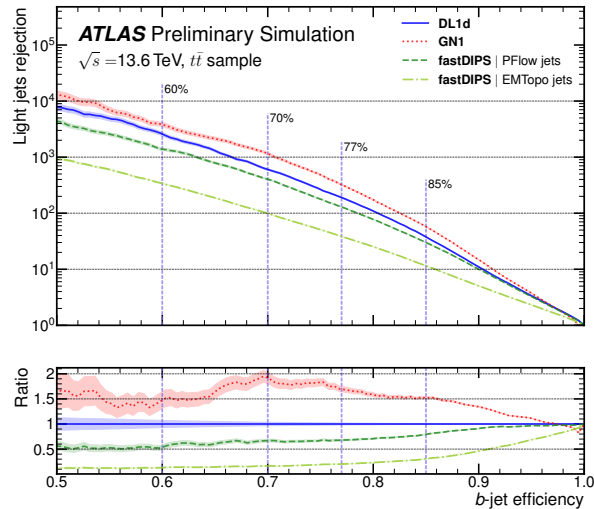


Figure 6.22: The HLT light-jet rejection as a function of the b -jet efficiency jets in the $t\bar{t}$ sample with $20 < p_T < 250 \text{ GeV}$ for events with a centre of mass energy $\sqrt{s} = 13.6 \text{ TeV}$ [126]. The ratio to the performance of the DL1d algorithm [87] is shown in the bottom panels. Binomial error bands are denoted by the shaded regions. The purple vertical dashed lines represent the most common working points used for b -tagging.

1958 outperforms other existing flavour tagging algorithms when trained on an entirely
1959 different detector geometry, the ITk (see Section 3.3.1). When compared with
1960 DL1d [87], GN1 improves on the c -jet rejection (light-jet rejection) by a factor of ~ 2
1961 (~ 2.5) for jets in the $t\bar{t}$ sample at the 60% b -jet WP. Significant improvements in
1962 rejections are also observed for jets in the Z' sample.

1963 6.7 Conclusion

1964 In this chapter a novel jet tagger, GN1, is presented. The model has a graph neural
1965 network architecture and is trained with auxiliary training objectives, which are
1966 shown to improve the performance of the basic model. GN1 significantly improves
1967 flavour tagging performance with respect to DL1r, the current default ATLAS flavour
1968 tagging algorithm, when compared in simulated collisions. GN1 improves c - and
1969 light-jet rejection for jets in the $t\bar{t}$ sample with $20 < p_T < 250$ GeV by factors of
1970 ~ 2.1 and ~ 1.8 respectively at a b -jet tagging efficiency of 70% when compared with
1971 DL1r. For jets in the Z' sample with $250 < p_T < 5000$ GeV, GN1 improves the
1972 c -jet rejection by a factor of ~ 2.8 and light-jet rejection by a factor of ~ 6 for a
1973 comparative b -jet efficiency of 30%.

1974 Previous multivariate flavour tagging algorithms relied on inputs from low-level
1975 tagging algorithms, whereas GN1 needs no such inputs, making it more flexible.
1976 It can be easily fully optimised via a retraining for specific flavour tagging use
1977 cases, as demonstrated with c -tagging and high- p_T b -tagging, without the need for
1978 time-consuming retuning of the low-level tagging algorithms. The model is also
1979 simpler to maintain and study due to the reduction in the number of constituent
1980 components.

1981 GN1 demonstrates improved track classification performance when compared with a
1982 simple per-track MLP. The model is also able to perform vertex finding, and prelimi-
1983 nary studies suggest it outperforms previous manually optimised approaches. The
1984 auxiliary track classification and vertex finding objectives are shown to significantly
1985 contribute to the performance in the jet classification objective, and, along with the
1986 more advanced graph neural network architecture, are directly responsible for the
1987 improvement over DL1r.

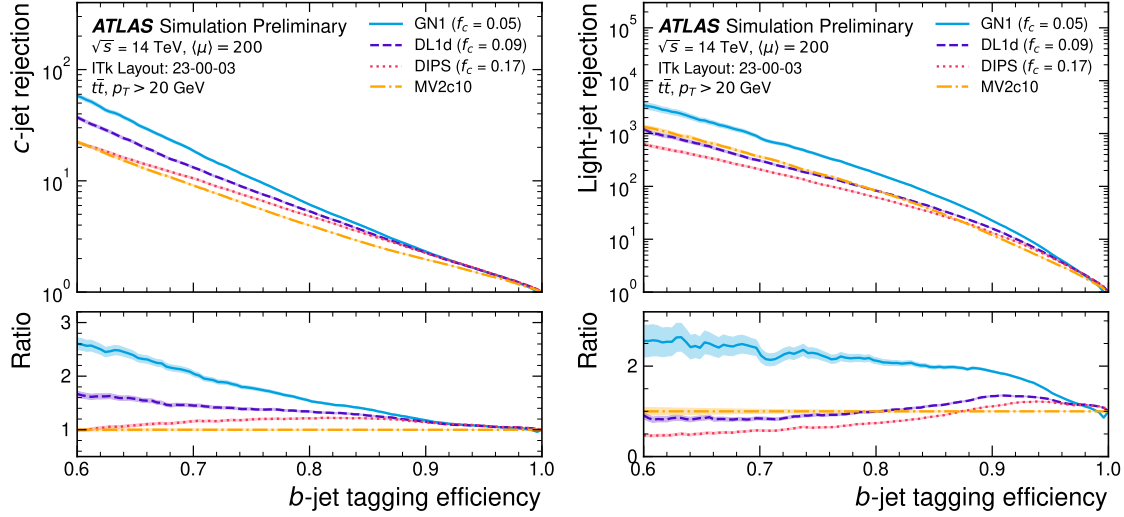


Figure 6.23: The c -jet rejection (left) and light-jet rejection (right) for the upgraded HL-LHC ATLAS detector with $\langle \mu \rangle = 200$ as a function of the b -jet efficiency for jets in the $t\bar{t}$ sample with $20 < p_T < 250$ GeV for events with a centre of mass energy $\sqrt{s} = 14$ TeV [127]. The ratio to the performance of the DL1d algorithm is shown in the bottom panels. Binomial error bands are denoted by the shaded regions. The purple vertical dashed lines represent the most common working points used for b -tagging.

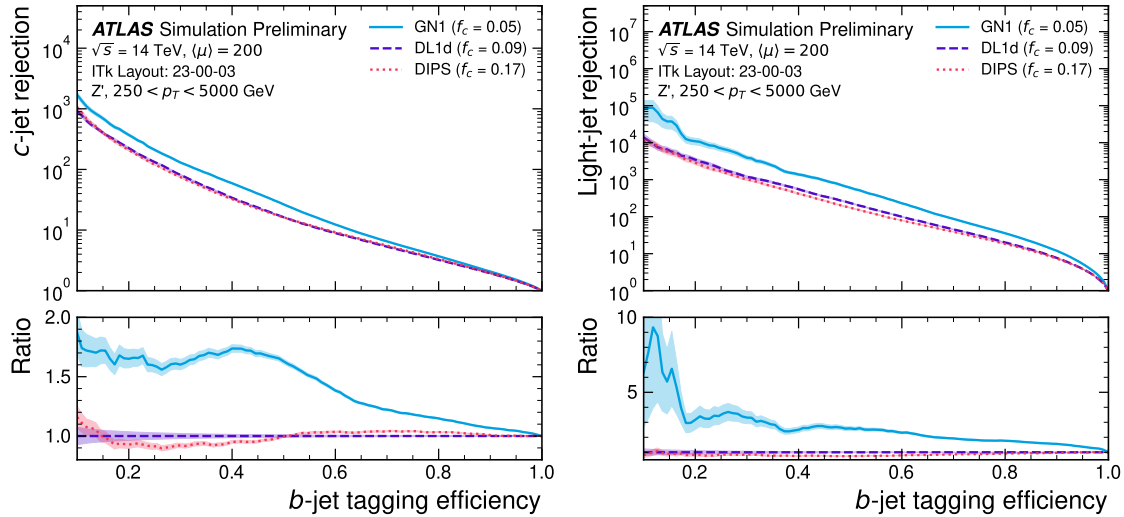


Figure 6.24: The c -jet rejection (left) and light-jet rejection (right) for the upgraded HL-LHC ATLAS detector with $\langle \mu \rangle = 200$ as a function of the b -jet efficiency for jets in the Z' sample with $250 < p_T < 5000$ GeV for events with a centre of mass energy $\sqrt{s} = 14$ TeV [127]. The ratio to the performance of the DL1d algorithm is shown in the bottom panels. Binomial error bands are denoted by the shaded regions.

1988 GN1 has also been shown to perform well for b -tagging in the High Level Trigger,
1989 and in the projected environment for the upgraded High Luminosity LHC. The
1990 performance of the model at high- p_T can be improved by loosening the input track
1991 selection, which increases the number of b -hadron decay tracks that are inputted to
1992 the model.

1993 Preliminary validation of the model demonstrates that the level of discrepancy
1994 between different Monte Carlo event generators is similar to that seen for previous
1995 ATLAS ML based taggers such as DL1r, suggesting that the model has not learnt
1996 additional information that is specific to a single event generator. Initial comparisons
1997 between simulated events and data also show similar levels of agreement as for
1998 previous taggers [128].

1999 Future Work

2000 Further improvements in the b - and c -tagging performance are likely possible with
2001 a more thorough optimisation of the model architecture, and the integration of
2002 additional information from other parts of the ATLAS detector. The addition of
2003 other auxiliary training objectives, such as the prediction of the truth b -hadron decay
2004 radius and transverse momentum and the truth type of input tracks may also yield
2005 additional performance gains.

2006 Although the results demonstrate a significant performance improvement at high- p_T ,
2007 it is also possible that additional studies on further loosening the selection could yield
2008 further improved results. For example the selections on the number of number of
2009 holes and the longitudinal impact parameter could be further relaxed. The maximum
2010 number of tracks provided as input to the model could also be increased from the
2011 default value of 40. In order to validate the change from the default tracking setup,
2012 studies investigating the modelling uncertainties of the additional tracks need to be
2013 carried out.

2014 Given that GN1 exploits the input information in a more sophisticated way than
2015 DL1r, further studies are needed to confirm that the performance gain observed in
2016 these simulated samples is also observed in experimental data. Additional future
2017 work includes the full calibration of the model so it can be used by physics analyses.

2018 The flexible nature of the model means it can also be readily applied to other related
2019 problems outside of standard b - and c -tagging applications, as demonstrated in
2020 Section 6.6. Additional applications for the architecture include $X \rightarrow bb$ and $X \rightarrow cc$
2021 tagging. The model could also be repurposed as a pile-up jet or τ tagger, or general
2022 primary and secondary vertexing tool. Using a vertex fitting algorithm to compare
2023 the reconstructed vertex quantities with those from SV1 and JetFitter is left for
2024 future work.

2025 Chapter 7

2026 Boosted VHbb Analysis

2027 The Higgs boson, first observed by ATLAS and CMS at the LHC in 2012 [14, 15],
2028 is predicted by the standard model to decay primarily to a pair of b -quarks, with
2029 a branching fraction of 0.582 ± 0.007 for $m_H = 125$ GeV [26]. Observation of this
2030 decay mode was reported by ATLAS [79] and CMS [28] in 2018, establishing the
2031 first direct evidence for the Yukawa coupling of the Higgs boson to down-type quarks
2032 (see Section 2.2.2). The $H \rightarrow b\bar{b}$ process is also important for constraining the total
2033 decay width of the Higgs [129].

2034 Whilst the dominant Higgs production mechanism at the LHC is gluon-gluon fusion
2035 as outlined in Section 2.2.3, this mechanism has an overwhelming QCD multijet
2036 background and so overall sensitivity to the Higgs is low. The QCD multijet
2037 background refers to events containing one or more strongly produced jets which
2038 are not the decay product of heavy resonances, for example $g \rightarrow q\bar{q}$. The gluon-
2039 gluon fusion channel contains to leading order only jets in the final state, and
2040 therefore it is extremely difficult to distinguish signal events from the overwhelming
2041 multijet background. The $H \rightarrow b\bar{b}$ observation therefore searched for Higgs bosons
2042 produced in association with a vector boson V (where V can be a W or Z boson)
2043 which subsequently decays leptonically. The leptonic final states allow for leptonic
2044 triggering whilst at the same time significantly reducing the multijet background.

2045 Two full Run 2 dataset analyses were carried out as a follow-up to the $H \rightarrow b\bar{b}$
2046 observation [79]. Similar to the observation, both measured the associated production
2047 of a Higgs with a vector boson, with the Higgs boson decaying to a pair of b -quarks.
2048 The first analysis [130] was focussed on the resolved phase-space, where the Higgs-jet
2049 candidate is reconstructed as two distinct jets with radius parameter $R = 0.4$. The

2050 second analysis [131] was focussed on the boosted phase-space, where the Higgs-jet
 2051 candidate has a sufficiently large transverse momenta such that it can be reconstructed
 2052 as a single jet with a radius parameter of $R = 1.0$. This chapter will focus on the
 2053 latter analysis. The analysis is outlined in Section 7.1. Modelling studies performed
 2054 are detailed in Section 7.2, and the results of the analysis are presented in Section 7.4.
 2055 This analysis has been published in Ref. [131]. Figures and tables from Ref. [131]
 2056 are reproduced here.

2057 7.1 Analysis Overview

2058 The boosted VH , $H \rightarrow b\bar{b}$ analysis is focused on the high transverse momentum
 2059 regime, which has the benefit of being more sensitive to physics beyond the Standard
 2060 Model [132], but the disadvantage of being more challenging due to the increased
 2061 difficulty in the accurate reconstruction of high transverse momentum physics objects
 2062 (discussed in Chapter 4). In order to focus on the high- p_T regime, the reconstructed
 2063 vector boson p_T^V is required to be $p_T^V > 250 \text{ GeV}$ (see Section 7.1.2). Events are
 2064 also split into two p_T^V bins with the first bin covering $250 \text{ GeV} < p_T^V < 400 \text{ GeV}$ and
 2065 the second covering $p_T^V > 400 \text{ GeV}$, which allows the analysis to benefit from the
 2066 improved signal-to-background in the high- p_T regime.

2067 The previous ATLAS analysis in Ref. [79] was primarily sensitive to vector bosons
 2068 with a more modest p_T^V boost in the region of 100–300 GeV. In this regime, the
 2069 Higgs candidate was reconstructed using a pair of jets with radius parameter of
 2070 $R = 0.4$, called small- R jets. However in the high- p_T regime, the decay products
 2071 of the Higgs boson become increasingly collimated and the small- R jets may
 2072 not be individually resolved. In order to enhance the reconstruction of the Higgs
 2073 boson candidate, this analysis uses a large- R jet with radius parameter $R = 1.0$ to
 2074 reconstruct the Higgs boson candidate (see Section 3.4.3). The Higgs candidate is
 2075 required to have exactly two ghost-assciated (see Section 3.4.3) and b -tagged variable-
 2076 radius track-jets. The candidate large- R jet is reconstructed using jet substructure
 2077 techniques, in particular it is trimmed by removing soft and wide-angle components,
 2078 which helps to remove particles from the underlying event and pile-up collisions [133].
 2079 Refer to Section 3.4.3 for more details on jet reconstruction.

2080 On top of the binning in p_T^V , selected events are further categorised into the 0-, 1-
 2081 and 2-lepton channels depending on the number of charged leptons (electrons and
 2082 muons) present in the reconstructed final state (also referred to as the 0L, 1L, and 2L
 2083 channels respectively). The 0-lepton channel targets the $ZH \rightarrow \nu\nu b\bar{b}$ process, the
 2084 1-lepton channel targets $WH \rightarrow \ell\nu b\bar{b}$, and the 2-lepton channel targets $ZH \rightarrow \ell\ell b\bar{b}$,
 2085 where ℓ is an electron or muon and ν is a neutrino. Each channel has a dedicated
 2086 set of selections which are listed in more detail in Section 7.1.3. Events in the 0- and
 2087 1-lepton channels are further split depending on the number of additional small- R
 2088 jets not matched to the Higgs-jet candidate. The high-purity signal region (HP SR)
 2089 has zero such jets, while the low-purity signal region (LP SR) has one or more, and
 2090 therefore absorbs a larger number of background $t\bar{t}$ events. Maintaining a high purity
 2091 signal region is important for the extraction of the signal yield. The 0- and 1-lepton
 2092 channels also make use of a dedicated $t\bar{t}$ control region for jets with one or more
 2093 additional b -tagged small- R jets, described described in Section 7.1.4. A complete
 2094 overview of the different analysis regions is given in Table 7.1.

Channel	Analysis Regions					
	$250 < p_T^V < 400 \text{ GeV}$			$p_T^V \geq 400 \text{ GeV}$		
	0 add. b -track-jets		≥ 1 add. b -track-jets	0 add. b -track-jets		≥ 1 add. b -track-jets
	0 add. small- R jets	≥ 1 add. small- R jets		0 add. small- R jets	≥ 1 add. small- R jets	
0-lepton	HP SR	LP SR	CR	HP SR	LP SR	CR
1-lepton	HP SR	LP SR	CR	HP SR	LP SR	CR
2-lepton	SR			SR		

Table 7.1: Summary of the definitions of the different analysis regions . Signal enriched regions are marked with the label SR. There are regions with relatively large signal purity (HP SR) and with low purity (LP SR). Background enriched regions are marked with the label CR. The shorthand “add” stands for additional small- R jets, i.e. number of small- R jets not matched to the Higgs-jet candidate. The medium and high p_T^V regions are referred to as Mp_T^V and Hp_T^V , respectively [131].

2095 The signal $VH, H \rightarrow b\bar{b}$ yields is extracted from a profile likelihood fit to the large- R
 2096 jet mass over several signal and control analysis regions, which are described in
 2097 Sections 7.1.3 and 7.1.4. The diboson background $VZ, Z \rightarrow b\bar{b}$ yield is simultaneously
 2098 extracted from the fit, and provides a cross check on the signal extraction. The fit

2099 model (described henceforth only as “the fit”) is described in more detail in described
2100 in Section 7.3.

2101 7.1.1 Data & Simulated Samples

2102 Data from centre-of-mass energy $\sqrt{s} = 13$ TeV proton-proton collisions at the LHC
2103 recorded over the course of Run 2 (between 2015 and 2018) were used for the analysis.
2104 The resulting dataset corresponds to a total integrated luminosity of 139 fb^{-1} (see
2105 Fig. 3.4).

2106 An overview of the MC simulated samples used in the analysis is given in Table 7.2.
2107 These samples are used to model the signal and background processes relevant to the
2108 analysis, with the exception of the multijet background which is modelled using a
2109 data-driven technique. Data and simulated events are reconstructed using the same
2110 algorithms, and a reweighting is applied to the simulated events in order to match
2111 the pile-up distribution observed in the data.

2112 7.1.2 Object Reconstruction

2113 The presence of neutrinos in the $WH \rightarrow \ell\nu b\bar{b}$ and $ZH \rightarrow \ell\ell b\bar{b}$ signatures can be
2114 inferred from a momentum imbalance in the transverse plane Section 3.4.5. The
2115 vector boson transverse momentum p_T^V is reconstructed as the missing transverse
2116 energy E_T^{miss} in the 0-lepton channel, as the magnitude of the summed $\mathbf{E}_T^{\text{miss}}$ and
2117 charged-lepton momentum in the 1-lepton channel, and as the transverse momentum
2118 of the 2-lepton system in the 2-lepton channel (see Section 3.4.5).

2119 Electrons and muons are reconstructed as outlined in Section 3.4.4, and following the
2120 approach described in Ref. [79]. Leptons are required to satisfy the selections listed
2121 in Table 7.3. *Baseline* electrons are required to pass the likelihood-based method
2122 described in Section 3.4.4, and *Signal* electron additionally are required to satisfy
2123 a tighter likelihood identification selection. *Baseline* muons are required to pass
2124 the ‘loose’ identification described in Ref. [77], while *signal* muons are required to
2125 pass the ‘medium’ identification working point. All signal leptons are required to
2126 additionally satisfy a $p_T > 27$ GeV selection criteria, except for muons in the 1-lepton
2127 channel where a cut of 25 GeV is used. The number of baseline leptons is used to

Process	ME generator	ME PDF	PS and Hadronisation	UE model tune	Cross-section order
Signal ($m_H = 125$ GeV and $b\bar{b}$ branching fraction set to 58%)					
$gg \rightarrow WH \rightarrow \ell\nu b\bar{b}$	PowHEG-Box v2 [134] + GoSAM [136] + MiNLO [137, 138]	NNPDF3.0NLO (*) [108]	PyTHIA 8.212 [110]	AZNLO [135]	NNLO(QCD) + NLO(EW) [139–145]
$qq \rightarrow ZH \rightarrow \nu\nu b\bar{b}/\ell\ell b\bar{b}$	PowHEG-Box v2 + GoSAM + MiNLO	NNPDF3.0NLO (*)	PyTHIA 8.212	AZNLO	NNLO(QCD) ^(†) + NLO(EW)
$gg \rightarrow ZH \rightarrow \nu\nu b\bar{b}/\ell\ell b\bar{b}$	PowHEG-Box v2	NNPDF3.0NLO (*)	PyTHIA 8.212	AZNLO	NLO + NLL [146–150]
Top quark ($m_t = 172.5$ GeV)					
$t\bar{t}$	PowHEG-Box v2 [134, 151]	NNPDF3.0NLO	PyTHIA 8.230	A14 [111]	NNLO+NNLL [152]
s-channel	PowHEG-Box v2 [134, 153]	NNPDF3.0NLO	PyTHIA 8.230	A14	NLO [154]
t-channel	PowHEG-Box v2 [134, 153]	NNPDF3.0NLO	PyTHIA 8.230	A14	NLO [155]
Wt	PowHEG-Box v2 [134, 156]	NNPDF3.0NLO	PyTHIA 8.230	A14	Approximate NNLO [157]
Vector boson + jets					
$W \rightarrow \ell\nu$	SHERPA 2.2.1 [158–161]	NNPDF3.0NNLO	SHERPA 2.2.1 [162, 163]	Default	NNLO [164]
$Z/\gamma^* \rightarrow \ell\ell$	SHERPA 2.2.1	NNPDF3.0NNLO	SHERPA 2.2.1	Default	NNLO
$Z \rightarrow \nu\nu$	SHERPA 2.2.1	NNPDF3.0NNLO	SHERPA 2.2.1	Default	NNLO
Diboson					
$qq \rightarrow WW$	SHERPA 2.2.1	NNPDF3.0NNLO	SHERPA 2.2.1	Default	NLO
$qq \rightarrow WZ$	SHERPA 2.2.1	NNPDF3.0NNLO	SHERPA 2.2.1	Default	NLO
$qq \rightarrow ZZ$	SHERPA 2.2.1	NNPDF3.0NNLO	SHERPA 2.2.1	Default	NLO
$gg \rightarrow VV$	SHERPA 2.2.2	NNPDF3.0NNLO	SHERPA 2.2.2	Default	NLO

Table 7.2: Signal and background processes with the corresponding generators used for the nominal samples [131]. If not specified, the order of the cross-section calculation refers to the expansion in the strong coupling constant (α_s). (*) The events were generated using the first PDF in the NNPDF3.0NLO set and subsequently reweighted to the PDF4LHC15NLO set [165] using the internal algorithm in POWHEG-BOX v2. (†) The NNLO(QCD)+NLO(EW) cross-section calculation for the $pp \rightarrow ZH$ process already includes the $gg \rightarrow ZH$ contribution. The $gg \rightarrow ZH$ process is normalised using the cross-section for the $pp \rightarrow ZH$ process, after subtracting the $gg \rightarrow ZH$ contribution. An additional scale factor is applied to the $gg \rightarrow VH$ processes as a function of the transverse momentum of the vector boson, to account for electroweak (EW) corrections at NLO. This makes use of the VH differential cross-section computed with HAWK [166, 167].

2128 categorise the event into the 0-, 1- or 2-lepton channels. The 1- and 2-lepton channels
2129 additionally require one signal lepton to be present.

Variable	Electrons	Muons
p_T	$> 7 \text{ GeV}$	
$ \eta $	< 2.47	< 2.7
$s(d_0)$	< 5	< 3
$ z_0 \sin(\theta) $	$< 0.5 \text{ mm}$	

Table 7.3: Selections applied to baseline and signal electrons and muons.

2130 The analysis makes use of large- R and variable-radius small- R track-jets, which
2131 are described in Section 3.4.3. The large- R jets are used to reconstruct the Higgs
2132 boson candidate, while the small- R jets are used for b -tagging and for selection of
2133 the analysis region. The track-jets matched to the Higgs candidate are b -tagged
2134 using the MV2c10 b -tagging algorithm (see Chapter 4). The efficiency of the tagging
2135 algorithm is calibrated to events in data [168–170]. The jet tagging strategy relies
2136 on extensive studies into track-jet b -tagging in boosted topologies [171, 172].

2137 7.1.3 Selection Criteria

2138 An extensive list of selection cuts are applied to each event in order to reject
2139 background events whilst retaining as many signal events as possible. A full list of
2140 selection cuts applied to the different analysis regions is given in Table 7.4, while
2141 some key selections are listed below.

2142 All channels require events with at least one large- R jet with $p_T > 250 \text{ GeV}$
2143 and $|\eta| < 2.0$. The vector boson transverse momentum is also required to satisfy
2144 $p_T^V > 250 \text{ GeV}$. The Higgs candidate is chosen as the highest p_T large- R jet satisfying
2145 these requirements. As mentioned, the candidate large- R jet is required to have
2146 two ghost-assciated and b -tagged variable-radius track-jets. These track-jets are
2147 required to have at least two constituent tracks with $p_T > 500 \text{ MeV}$ and $|\eta| < 2.5$.
2148 The track-jets themselves must satisfy $p_T > 10 \text{ GeV}$ and $|\eta| < 2.5$.

2149 In the 0-lepton channel, trigger selections are applied using an E_T^{miss} trigger with a
2150 luminosity-dependent threshold between 70–110 GeV. In the 1-lepton electron sub-
2151 channel a combination of single electron triggers is used with minimum p_T thresholds
2152 between 24–26 GeV. In the muon sub-channel the same E_T^{miss} trigger as the 0-lepton
2153 channel is used. Since muons are not used for the E_T^{miss} trigger calculations, this
2154 is in effect a p_T requirement on the muon-neutrino system, which in the analysis
2155 phase space is more efficient than a single-muon trigger. The 2-lepton channel uses
2156 the same triggering strategy as the 1-lepton channel. In all channels, the trigger
2157 selections applied are fully efficient for events selected using the full requirements in
2158 Table 7.4.

2159 The combined selections in Table 7.4 result in a signal efficiency ranging from 6–16%
2160 for the WH and ZH processes depending on the channel and p_T^V bin.

2161 7.1.4 Control Regions

2162 The $t\bar{t}$ process presents a major background in the 0- and 1-lepton channels. In these
2163 events, the Higgs candidate is often reconstructed from a correctly tagged b -jet from
2164 the top decay $t \rightarrow Wb$, and an incorrectly tagged c - or light-jet from the subsequent
2165 decay of the W , as shown in Fig. 7.1.

2166 The top quark predominately decays to a W and a b -quark. Hence, the second top
2167 quark from the $t\bar{t}$ pair is also likely to result in a second tagged b -tagged track-jet
2168 outside of the large- R Higgs candidate. To ensure sufficient $t\bar{t}$ rejection, 0- and
2169 1-lepton channel signal regions are defined using a veto on events with b -tagged
2170 track-jets outside the Higgs-jet candidate. These events are used to construct a
2171 control region (CR) which is enriched in $t\bar{t}$ events. The CR is used to constrain the
2172 normalisation of the $t\bar{t}$ background in the fit.

2173 7.1.5 Background Composition

2174 After the selections described in Section 7.1.3 the number of background events
2175 mimicking the VH , $H \rightarrow b\bar{b}$ signal is greatly reduced. However, the number of
2176 background events still greatly outnumbers that of signal events. The background
2177 processes are channel dependent. In the 0-lepton channel the dominant sources of

Selection	0 lepton channel	1 lepton channel	2 leptons channel	
Trigger	E_T^{miss}	E_T^{miss}	e sub-channel	μ sub-channel
Leptons	0 baseline leptons	1 signal lepton	E_T^{miss}	E_T^{miss}
		$p_T > 27 \text{ GeV}$	$p_T > 25 \text{ GeV}$	$p_T > 27 \text{ GeV}$
		no second baseline lepton		≥ 1 signal lepton, $p_T > 27 \text{ GeV}$
				both leptons of the same flavour
				-
				opposite sign muons
E_T^{miss}	$> 250 \text{ GeV}$	$> 50 \text{ GeV}$	-	-
p_T^V			$p_T^V > 250 \text{ GeV}$	-
Large- R jets		at least one large- R jet, $p_T > 250 \text{ GeV}, \eta < 2.0$		
Track-jets		at least two track-jets, $p_T > 10 \text{ GeV}, \eta < 2.5$, matched to the leading large- R jet		
b -tagged jets		leading two track-jets matched to the leading large- R must be b -tagged (MV2c10, 70%)		
m_J			$> 50 \text{ GeV}$	
$\min[\Delta\phi(\mathbf{E}_T^{\text{miss}}, \text{small-}R \text{ jets})]$	$> 30^\circ$		-	
$\Delta\phi(\mathbf{E}_T^{\text{miss}}, H_{\text{cand}})$	$> 120^\circ$		-	
$\Delta\phi(\mathbf{E}_T^{\text{miss}}, \mathbf{E}_{T, \text{trk}}^{\text{miss}})$	$< 90^\circ$		-	
$\Delta y(V, H_{\text{cand}})$	-		$ \Delta y(V, H_{\text{cand}}) < 1.4$	
$m_{\ell\ell}$	-			$66 \text{ GeV} < m_{\ell\ell} < 116 \text{ GeV}$
Lepton p_T imbalance	-			$(p_T^{\ell_1} - p_T^{\ell_2})/p_T^Z < 0.8$

Table 7.4: Event selection requirements for the boosted VH , $H \rightarrow b\bar{b}$ analysis channels and sub-channels [131]. Various channel dependent selections are used to maximise the signal efficiency and reduce the number of background events in each analysis region. The $\min[\Delta\phi(\mathbf{E}_T^{\text{miss}}, \text{small-}R \text{ jets})]$ selection is used to remove jets when the missing transverse momentum $\mathbf{E}_T^{\text{miss}}$ is pointing in the direction of the Higgs candidate, and the $\Delta\phi(\mathbf{E}_T^{\text{miss}}, \mathbf{E}_{T, \text{trk}}^{\text{miss}})$ is used to reject events where the calorimeter missing transverse momentum $\mathbf{E}_T^{\text{miss}}$ is not pointing in the direction of the track-based missing transverse momentum $\mathbf{E}_{T, \text{trk}}^{\text{miss}}$. The $\Delta y(V, H_{\text{cand}})$ quantifies the rapidity difference between the reconstructed vector boson and Higgs candidate.

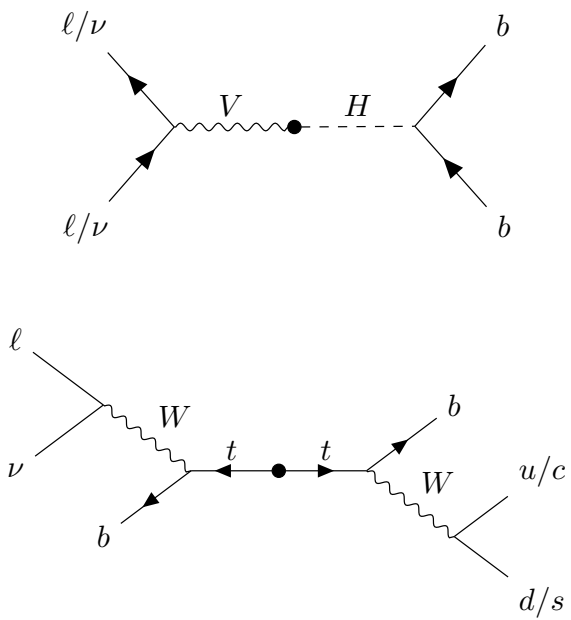


Figure 7.1: Diagrams of the signal process (top) and $t\bar{t}$ background (bottom). Object to the right of centre are reconstructed within the large- R jet. For the $t\bar{t}$ background, the large- R jet contains a mis-tagged c -jet or (less often) a mis-tagged light-jet. The contribution in the 0-lepton channel results from hadronically decaying τ lepton, or a electron or muon which is out of the analysis acceptance.

2178 backgrounds are $Z + \text{jets}$ ($Z \rightarrow \nu\nu$) and $t\bar{t}$, with $W + \text{jets}$ and diboson events being
2179 subdominant. In the event of $W \rightarrow \tau\nu$, and subsequent hadronic decay of the τ or
2180 lack of successful reconstruction/selection of the leptonic decay products, $W + \text{jets}$
2181 can also contribute to the 0-lepton channel. $t\bar{t}$ and $W + \text{jets}$ (with a leptonic decay
2182 of the W as in $W \rightarrow \ell\nu$) are dominant in the 1-lepton channel, while single-top is
2183 subdominant. In the 2-lepton channel, $Z + \text{jets}$ ($Z \rightarrow \ell\ell$) is again dominant followed
2184 by $Z Z$ diboson events.

2185 The diboson background VV consists primarily of WZ and ZZ events in which the
2186 Z decays to a pair of b -quarks. This process very closely matches the signal, with
2187 a resonant peak occurring at $m_Z = 91$ GeV and so is considered as an irreducible
2188 background ($V+b$ -jets is also irreducible).

2189 The $t\bar{t}V$, $t\bar{t}H$ and multijet backgrounds are negligible in the analysis phase space
2190 after the selections have been applied, with the exception of the 1-lepton electron
2191 sub-channel, in which multijet background is not negligible. The multijet background
2192 is made up of events where the isolated leptonic signature has been mimicked by
2193 either a jet or a muon or electron from a semi-leptonic heavy flavour decay, where
2194 the lepton has escaped the jet.

2195 The contributions from the different backgrounds are modelled using Monte Carlo
2196 event generators and the uncertainties associated with these samples are studied in
2197 Section 7.2. The multijet background is modelled using a data-driven technique.

2198 7.2 Systematic Uncertainties & Background 2199 Modelling

2200 Systemic uncertainties are extensively employed to give the fit model enough flexibility
2201 to account for inaccuracies in the various inputs. Two main types of systematic
2202 uncertainty are considered: experimental and modelling. Experimental uncertainties
2203 arise due to the imperfect reconstruction algorithms (in particular the jet recon-
2204 struction and b -tagging algorithms), and due to the imperfect modelling of pile-up
2205 and other effects, as described in Section 7.2.3. Modelling uncertainties arise due
2206 to the imperfections in the Monte-Carlo simulations used to model the signal and
2207 background events. In order to observe a certain process, for example VH , $H \rightarrow b\bar{b}$,

2208 an increase in the number of observed events with respect to the background-only
2209 hypothesis is looked for. The excess is often relatively small against the total number
2210 of background events, and hence accurate modelling of the expected number of
2211 background and signal events is crucial for successfully performing the analysis.
2212 Particular care is paid to the uncertainties on the modelling predictions as discussed
2213 in this section.

2214 Modelling uncertainties are described in detail in the following sections. *Nominal*
2215 samples are used as a reference to which different variations can be compared.
2216 The nominal samples are chosen as the best possible representation of the underlying
2217 physical process. *Alternative* samples are used to understand inaccuracies that may
2218 be present in the nominal samples. Some aspect of the nominal model is varied, and
2219 the discrepancy with respect to the nominal model is quantified. The discrepancy is
2220 used to estimate a systematic uncertainty associated with the model parameter which
2221 was varied. The alternative samples are sometimes obtained via internal weight
2222 variations or parameterisation methods, rather than by re-running the simulation.
2223 This is discussed in more detail in Section 7.2.1.

2224 Modelling studies involving c - and light-jets is hampered by the low number of events
2225 available after the analysis selection is applied, due to the high rejection rates of the
2226 b -tagging algorithm MV2c10. For modelling studies, truth tagging (TT) is therefore
2227 employed to ensure sufficient numbers of jets are available to calculate uncertainties.
2228 TT works by computing a 2-dimensional efficiency map using the jet p_T and η . The
2229 two leading track-jets associated to the large- R jet are weighted based on their p_T
2230 and η using the pre-calculated efficiency map, rather than being required to explicitly
2231 pass the b -tagging requirement.

2232 7.2.1 Implementation of Variations

2233 Modelling variations are implemented in different ways, depending on the associ-
2234 ated uncertainty. Table 7.5 lists the different sources of uncertainty described in
2235 Section 7.2.2 and for each lists the implementation. As production of high-stastic
2236 MC samples is computationally expensive, a technique in state of the art simulation
2237 packages is to store some sources of variation as internal weights, which can be
2238 generated alongside the nominal samples, saving computation time. The nominal

Source of Uncertainty	Implementation
Renormalisation scale (μ_R)	Internal weights
Factorisation scale (μ_F)	Internal weights
PDF set	Internal weights
Parton Shower (PS) models	Alternative samples
Underlying Event (UE) models	Alternative samples
Resummation scale (QSF)	Parameterisation
Merging scale (CKKW)	Parameterisation

Table 7.5: Different sources of uncertainty (i.e. variations in the model) considered for the $V+jets$ background, and the corresponding implementation. For each uncertainty, acceptance and shape uncertainties are derived.

2239 sample then effectively contains information about an ensemble of different samples,
2240 corresponding to different model parameters, which are accessible via reweightings.
2241 When filling histograms for the variations, bins are incremented by the internal
2242 weight of the event associated with the variation in question.

2243 While the inclusion of internal weight variation in MC event generators has decreased
2244 simulation times and increased available statistics, there are in SHERPA 2.2.1 currently
2245 some sources of systematic uncertainty that are unable to be stored as internal weight
2246 variations due to technical limitations. Two examples are the choice of resummation
2247 and merging scales. A method to parameterise the systematic variation using
2248 one sample, and to then apply this parameterisation to another sample, has been
2249 developed by ATLAS [173]. This method was used to derive resummation and
2250 merging uncertainties for the nominal SHERPA 2.2.1 sample, using a previous (lower
2251 statistic) SHERPA 2.1 alternative sample. The resulting uncertainties were studied
2252 and found to be negligible in comparison with systematics from other sources.

2253 7.2.2 Sources of Systematic Modelling Uncertainties

2254 This section briefly describes the different sources of uncertainty in the analysis, and
2255 how each is implemented. For each source of uncertainty, acceptance and shape
2256 uncertainties are derived. Acceptance uncertainties account for the uncertainty in
2257 the overall number of events in each channel, and for the migration of events between

2258 different analysis regions. Meanwhile, shape uncertainties account for differences in
2259 the shapes, but not overall normalisations, of the large- R jet mass.

2260 **QCD Scales**

2261 The $V + \text{jets}$ matrix element calculations contains infrared and ultraviolet divergences.
2262 These are handled by introducing arbitrary parameters corresponding to the renormalisation scale (μ_R) and factorisation scale (μ_F). Physical observables are not
2263 dependent on these parameters when using the infinite perturbation series expansion,
2264 however at some fixed order in QCD a limited dependence is present. To assess the
2265 impact of this, both μ_R and μ_F are independently varied from their nominal values
2266 by factors of 0.5 and 2 to account for higher order corrections to the calculation of
2267 the matrix element used to simulate the process.

2269 **PDF Sets**

2270 Parton distribution functions (PDFs) specify the probability of finding a parton with
2271 a given momentum inside a hadron (in this case, colliding protons). PDFs have
2272 to be derived from data and are a significant source of uncertainty in analyses of
2273 hadronic collision data. There are three sources of PDF uncertainties: the statistical
2274 and systematic errors on the underlying data used to derive the PDFs, the theory
2275 which is used to describe them (which is based on some fixed order perturbative
2276 QCD expansion), and finally the procedure which is used to extract the PDFs from
2277 the data. PDF-related uncertainties were derived following Ref. [165]. This involves
2278 considering 100 PDF replicas which, when combined, form a central value and
2279 associated uncertainty, and also in parallel direct changes to the central values of
2280 PDFs using the MMHT2014 [174] and CT14NLO [175] PDF sets.

2281 **Event Generator**

2282 The choice of parton shower (PS) and underlying event (UE) generators can affect
2283 the analysis outcome. Changing these models modifies several aspects of the event
2284 generation at the same time, such as the accuracy of matrix element predictions and

2285 different approaches to parton showering. This change tends to lead to the largest
2286 discrepancy with respect to the nominal samples.

2287 **Resummation and Merging Scales**

2288 Resummation is a technique used in QCD to help cope with calculations involving
2289 disparate energy scales, and involves the introduction of an associated resummation
2290 scale, the choice of which introduces some systematic uncertainty into the model.
2291 Parton showering models are accurate when simulating low- p_T radiation, however
2292 inaccuracies start to arrive when simulating hard emissions. To combat this, par-
2293 ton showering models utilise more precise matrix element calculations above some
2294 momentum threshold. The choice of threshold, or *merging scale* introduces some
2295 uncertainty into the final result. Resummation (QSF) and merging (CKKW) scale
2296 variations are available for a subset of the SHERPA samples. The number of available
2297 events is significantly lower than the number of events in the nominal sample, and no
2298 statistically significant discrepancy with respect to the nominal samples is observed.
2299 The corresponding uncertainties and therefore neglected.

2300 **7.2.3 Sources of Experimental Uncertainties**

2301 The main experimental uncertainties in the analysis are due to the following sources:

- 2302 • The small- R jet energy scale and resolution, which are informed by in situ
2303 calibration studies and the dependence of the jet energy on the level of pile-
2304 up [68].
- 2305 • The large- R jet energy and mass scales and resolutions. The scales are calibrated
2306 as described in Ref. [72], and an uncertainty of 2% and 20% is applied for the
2307 jet energy and mass resolutions, respectively.
- 2308 • b -tagging uncertainties, which are computed separately for b -, c - and light-flavour
2309 jets as described in the calibration studies in Refs. [168–170]. An additional
2310 extrapolation uncertainty is added to account for jets with transverse momenta
2311 above that which is accessible in the calibration analyses.

- 2312 • Uncertainties associated with the lepton energy and momentum scales, and
2313 reconstruction and identification efficiencies.
- 2314 • Uncertainty on the pile-up models which are used in the simulated samples,
2315 described in Ref. [176].
- 2316 • Uncertainties associated with the reconstruction of the missing transverse energy
2317 E_T^{miss} , which have various sources as described in Ref. [78].

2318 The impact of these uncertainties on the analysis can be found in Table 7.16.

2319 7.2.4 Vector Boson + Jets Modelling

2320 After event selection, the $V+jets$ background is a dominant background in all three
2321 analysis channels as described in Section 7.1.5. The $V+jets$ samples are split into
2322 categories depending on the truth flavour of the track-jets which are ghost-associated
2323 to the large- R jet Higgs candidate. The categories are $V+bb$, $V+bc$, $V+bl$, $V+cc$,
2324 $V+cl$, $V+ll$, and $V+hf$ refers collectively to the categories containing at least one b -
2325 or c -jet. $V+bb$ is dominant generally accounting for 80% of the events, while $V+hf$
2326 accounts for around 90% of the events. The full flavour composition breakdown for
2327 each channel and analaysis region are given in Tables 7.6, 7.8 and 7.9.

2328 In order to access uncertainties associated with the use of MC generators, variations
2329 of the simulation are produced using alternative generators or variation of nominal
2330 generator parameters as described in Section 7.2.1. As described in Section 7.1.1,
2331 the nominal MC event generator used for $V+jets$ events is SHERPA 2.2.1, while
2332 MADGRAPH5_AMC@NLO+PYTHIA8 (which uses a different parton showering
2333 model) is used as an alternative generator.

2334 Modelling systematics can have several impacts, including affecting the overall
2335 normalisation for different processes, the relative acceptances between different
2336 analysis regions (i.e. migrations between HP and LP SRs, between the SR and CR,
2337 and between p_T^V bins), and the shapes of the m_J distributions. Since the fit model
2338 fits only the large- R jet mass m_J to data, all shape uncertainties are estimated with
2339 respect to this observable. Several sources of uncertainty, summarised in Section 7.2.2,
2340 have been assessed.

Sample	Mp_T^V HP SR	Hp_T^V HP SR	Mp_T^V LP SR	Hp_T^V LP SR	Mp_T^V CR	Hp_T^V CR
Wbb	$79.3\% \pm 4.4\%$	$75.0\% \pm 8.6\%$	$77.4\% \pm 2.5\%$	$71.7\% \pm 4.5\%$	$68.0\% \pm 7.6\%$	$63.5\% \pm 14.0\%$
Wbc	$6.6\% \pm 0.9\%$	$3.4\% \pm 1.7\%$	$6.2\% \pm 0.5\%$	$5.3\% \pm 0.9\%$	$14.5\% \pm 3.2\%$	$3.4\% \pm 3.2\%$
Wbl	$3.9\% \pm 0.9\%$	$11.4\% \pm 3.5\%$	$4.5\% \pm 0.5\%$	$8.7\% \pm 1.4\%$	$9.8\% \pm 2.2\%$	$9.1\% \pm 3.8\%$
Wcc	$5.1\% \pm 1.7\%$	$6.8\% \pm 2.4\%$	$7.1\% \pm 1.0\%$	$6.3\% \pm 1.4\%$	$4.2\% \pm 2.4\%$	$12.3\% \pm 7.0\%$
Wcl	$2.3\% \pm 1.4\%$	$2.4\% \pm 2.1\%$	$3.4\% \pm 0.7\%$	$5.2\% \pm 1.5\%$	$2.6\% \pm 1.5\%$	$3.4\% \pm 2.1\%$
Wl	$2.9\% \pm 1.0\%$	$0.9\% \pm 1.6\%$	$1.3\% \pm 0.7\%$	$2.8\% \pm 0.7\%$	$0.9\% \pm 0.6\%$	$8.4\% \pm 5.1\%$
Events	187.5 ± 7.7	38.2 ± 3.1	429.5 ± 10.0	97.8 ± 4.2	33.8 ± 2.5	8.3 ± 1.2

Table 7.6: 0-lepton $W+jets$ nominal sample flavour composition and total event yield [177]. Mp_T^V refers to the medium p_T^V region, and Hp_T^V refers to the high p_T^V region (see Table 7.1).

Sample	Mp_T^V HP SR	Hp_T^V HP SR	Mp_T^V LP SR	Hp_T^V LP SR	Mp_T^V CR	Hp_T^V CR
Wbb	$77.2\% \pm 2.6\%$	$72.4\% \pm 4.3\%$	$77.8\% \pm 1.8\%$	$69.3\% \pm 2.5\%$	$64.6\% \pm 4.9\%$	$53.5\% \pm 6.3\%$
Wbc	$7.4\% \pm 0.7\%$	$7.3\% \pm 1.1\%$	$6.6\% \pm 0.4\%$	$6.3\% \pm 0.6\%$	$13.7\% \pm 1.9\%$	$16.4\% \pm 3.7\%$
Wbl	$4.0\% \pm 0.5\%$	$6.7\% \pm 1.1\%$	$5.1\% \pm 0.3\%$	$8.7\% \pm 0.8\%$	$10.3\% \pm 1.7\%$	$14.6\% \pm 3.0\%$
Wcc	$6.2\% \pm 1.1\%$	$5.5\% \pm 1.7\%$	$6.6\% \pm 0.6\%$	$6.4\% \pm 0.7\%$	$4.5\% \pm 1.7\%$	$9.5\% \pm 3.0\%$
Wcl	$3.6\% \pm 0.8\%$	$4.2\% \pm 1.8\%$	$2.8\% \pm 0.5\%$	$6.2\% \pm 0.8\%$	$4.6\% \pm 1.2\%$	$4.4\% \pm 1.5\%$
Wl	$1.5\% \pm 0.5\%$	$3.9\% \pm 1.3\%$	$1.1\% \pm 0.2\%$	$3.1\% \pm 0.5\%$	$2.3\% \pm 1.2\%$	$1.6\% \pm 0.6\%$
Events	477.1 ± 11.7	147.5 ± 6.4	784.7 ± 12.3	301.8 ± 7.2	68.7 ± 3.5	26.9 ± 2.0

Table 7.7: 1-lepton $W+jets$ nominal sample flavour composition and total event yield [177]. Mp_T^V refers to the medium p_T^V region, and Hp_T^V refers to the high p_T^V region (see Table 7.1).

Channel	Mp_T^V HP SR	Hp_T^V HP SR	Mp_T^V LP SR	Hp_T^V LP SR	Mp_T^V CR	Hp_T^V CR
Zbb	84.56%	81.84%	82.37%	76.06%	66.12%	63.18%
Zbc	6.03%	6.98%	5.80%	7.46%	15.04%	14.30%
Zbl	4.06%	6.55%	3.83%	6.59%	12.66%	12.81%
Zcc	3.68%	3.40%	5.82%	3.75%	3.36%	3.38%
Zcl	1.23%	0.44%	1.47%	3.97%	1.82%	4.95%
Zl	0.44%	0.78%	0.70%	2.16%	1.00%	1.38%
Events	259.91 ± 4.86	66.12 ± 2.04	420.45 ± 5.73	141.97 ± 2.50	43.49 ± 1.73	16.07 ± 0.83

Table 7.8: 0-lepton $Z+jets$ nominal sample flavour composition and total event yield [177]. Mp_T^V refers to the medium p_T^V region, and Hp_T^V refers to the high p_T^V region (see Table 7.1).

Channel	Mp_T^V	Hp_T^V	p_T^V inclusive
Zbb	80.80%	76.95%	79.76%
Zbc	8.10%	6.26%	7.60%
Zbl	4.95%	7.06%	5.52%
Zcc	3.97%	4.46%	4.10%
Zcl	1.61%	3.60%	2.14%
Zll	0.57%	1.68%	0.87%
Events	115.49 ± 2.42	42.42 ± 1.27	157.92 ± 2.73

Table 7.9: 2-lepton $Z+jets$ nominal sample flavour composition and total event yield [177]. Mp_T^V refers to the medium p_T^V region, and Hp_T^V refers to the high p_T^V region (see Table 7.1).

2341 Acceptance Uncertainties

2342 Several different types of acceptance uncertainties have been calculated and im-
 2343 plemented as nuisance parameters in the fit. These account for the uncertainty
 2344 in the overall number of events in each channel, and for the migration of events
 2345 between different analysis regions. The acceptance uncertainties relevant to the
 2346 $V+jets$ processes are summarised below.

- 2347 • **Overall normalisation:** only relevant where normalisation cannot be left
 2348 unconstrained (or “floating”, i.e. determined as part of the fit). The $V+hf$
 2349 component is left floating in the fit, with independent normalisations used for
 2350 $W+hf$ and $Z+hf$. The normalisations are mainly determined by the 1-lepton
 2351 (for $W+hf$) and 2-lepton (for $Z+hf$) regions respectively and then extrapolated
 2352 to the 0-lepton channel. The negligible $V+jets$ backgrounds were constrained to
 2353 their cross-sections in the fit. were constrained to their cross-sections

- **SR-to-CR relative acceptance:** the uncertainty on the relative number of $V+jets$ events in the signal and control regions.
- **HP-to-LP relative acceptance:** the uncertainty on the relative number of $V+jets$ events in the HP and LP SRs.
- **Medium-to-high p_T^V relative acceptance:** the uncertainty on the relative number of $V+jets$ events in the medium and high p_T^V bins.
- **Flavour relative acceptance:** for each flavour $V+xx$, where $xx \in \{bc, bl, cc\}$ the ratio of $V+xx/V+bb$ events is calculated. This corresponds to the uncertainty on the heavy flavour composition of the $V+hf$ background.
- **Channel relative acceptance:** the uncertainty on the relative number of $V+jets$ events between the channels.

The uncertainties arising from the different sources described in Section 7.2.2 are summed in quadrature to give a total uncertainty on each region. A summary of the different acceptance uncertainties that were derived and subsequently applied in the fit are given in Table 7.10. An effort has been made, wherever possible, to harmonise similar uncertainties across different analysis regions and channels.

V+jets Acceptance Uncertainties				
Boson	W		Z	
Channel	0L	1L	0L	2L
Vbb Norm.	30%	-	-	-
SR-to-CR	90% [†]	40% [†]	40%	-
HP-to-LP	18%		18%	-
Medium-to-high p_T^V	30%	10%*	10%	
Channel relative acceptance.	20%	-	16%	-
Vbc/Vbb	30%			
Vbl/Vbb	30%			
Vcc/Vbb	20%			
Vcl Norm.	30%			
VI Norm.	30%			

Table 7.10: $V+jets$ acceptance uncertainties [177]. $W+jets$ SR and CR uncertainties marked with a superscript \dagger are correlated. The 1L $W+jets$ H/M uncertainty marked by * is applied as independent and uncorrelated NPs in both HP and LP signal regions.

2370 Shape Uncertainties

2371 In order to derive shape uncertainties for a given background or signal process,
 2372 normalised distributions of the reconstructed large- R Higgs candidate jet mass m_J
 2373 are compared for the nominal sample and variations. For each variation, the ratio of
 2374 the variation to nominal is calculated, the up and down variations are symmetrised,
 2375 and an analytic function is used to parameterise the ratio. If different analysis regions
 2376 or channels show the same pattern of variation, a common uncertainty is assigned.

2377 An example of a significant source of uncertainty, arising from choice of factorisation
 2378 scale μ_R is shown in Fig. 7.2. The HP SRs in the medium and high p_T^V bins are
 2379 shown for the 0-lepton channel for the $W+hf$ and $Z+hf$ jets. The 0- and 1-lepton
 2380 channels for the $W+hf$ contribution and the 0- and 2-lepton channels for the $Z+jets$
 2381 contribution were found to have compatible shapes in m_J across channels, and so
 2382 were jointly measured. An exponential function $e^{p_0+p_1x} + p_2$ has been fitted to the
 2383 ratio of the normalised distributions. The magnitude of the variation is p_T^V dependent,
 2384 and so separate uncertainties are implemented in the fit for each p_T^V region.

2385 The shape uncertainties for μ_R were derived on the SRs but are also applied to the
 2386 CRs, as the low statistics in the CRs make it difficult to derive dedicated shape
 2387 uncertainties. All the shape uncertainties are fully correlated across regions.

2388 A comparison of the m_J shapes between SHERPA and MADGRAPH is shown in
 2389 Fig. 7.3. The plots are split by process and channel, but merged in SR purity and p_T^V
 2390 bins reflecting similarities between the m_J shapes and variations across these regions.
 2391 Due to the low statistics available for the alternate MADGRAPH sample, and the
 2392 lack of statistically significant variation between the samples, no additional shape
 2393 uncertainty was added to the fit in this case.

2394 The impacts of variations in the factorisation scale μ_F and the choice of PDF set on
 2395 m_J shape were also found to be negligible in comparison with μ_R and are hence no
 2396 additional uncertainty was added to the fit.

2397 7.2.5 Diboson Modelling

2398 The procedure to derive the uncertainties for the diboson background generally
 2399 follows that of $V+jets$.

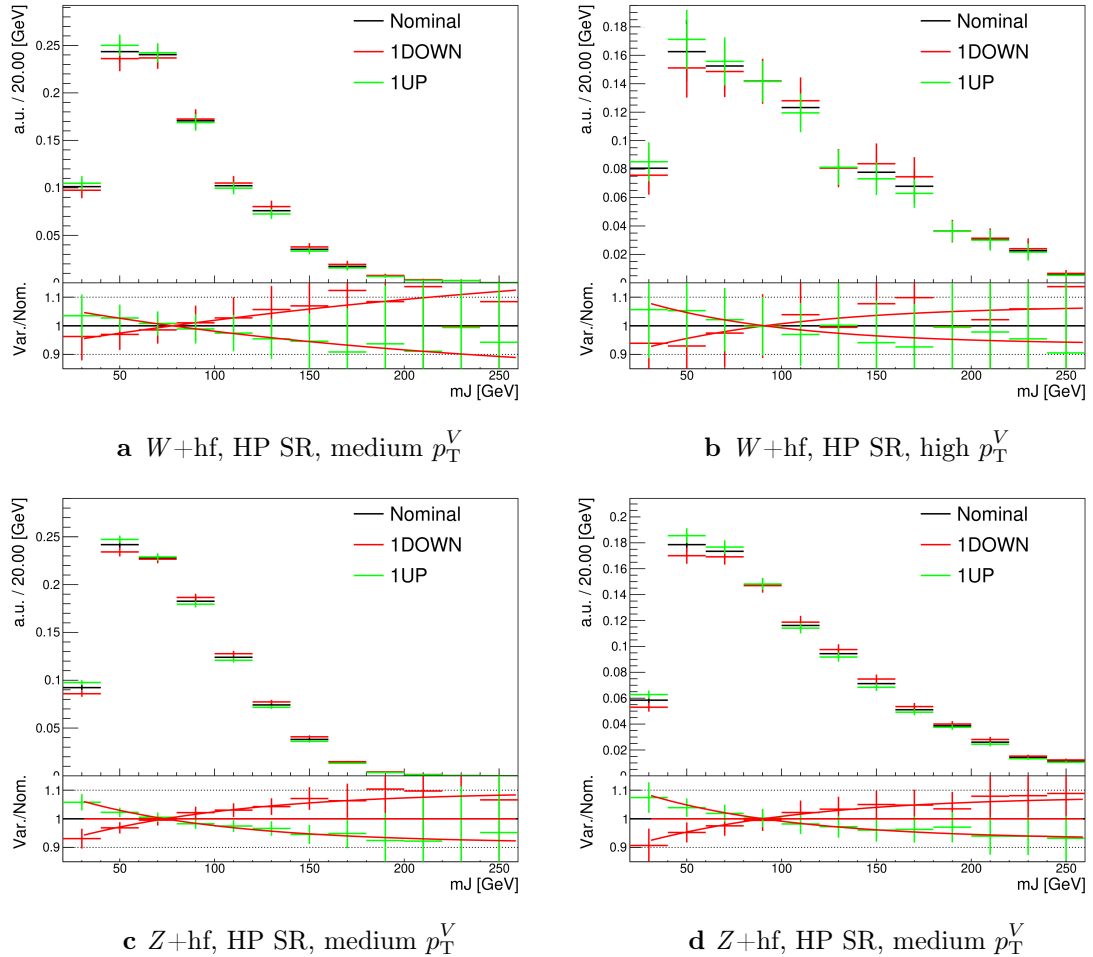


Figure 7.2: Leading large- R jet mass for the Z and $W+\text{hf}$ processes in the HP SR of the 0-lepton channel [177]. The renormalisation scale μ_r has been varied by a factor of 0.5 (1DOWN) and 2 (1UP). An exponential function is fitted to the ratio between the nominal and alternate samples.

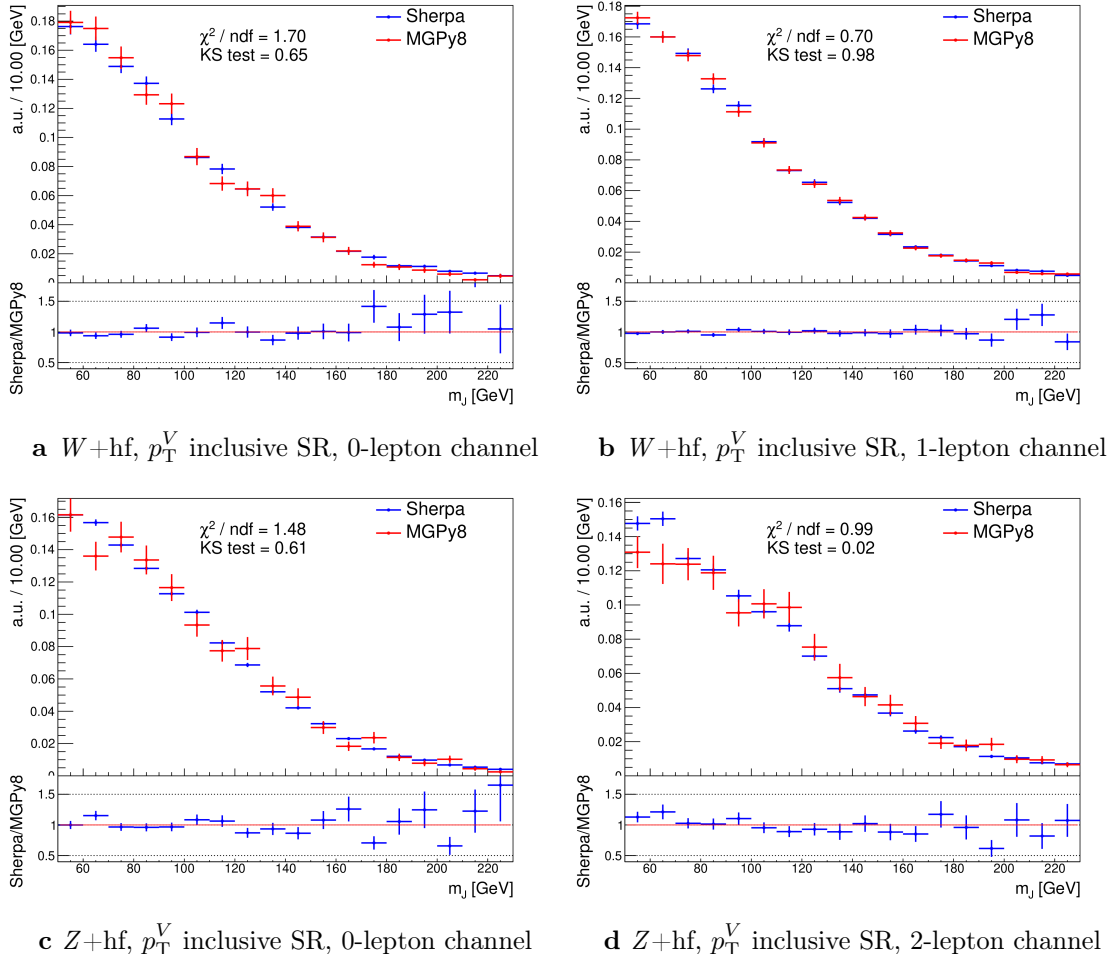


Figure 7.3: Leading large- R jet m_J inclusive in p_T^V for the $V + \text{hf}$ process modelled using both the SHERPA (blue) and MADGRAPH (red) samples [177]. The Kolmogorov-Smirnov test and χ^2/ndf are shown on the plots.

2400 The nominal diboson samples are generated using SHERPA 2.2.1 (except for $gg \rightarrow VV$
2401 which uses SHERPA 2.2.2) with the NNPDF3.0NNLO tune. Alternative samples were
2402 generated using POWHEG interfaced with PYTHIA8, using the AZNLO shower tune
2403 with the CTEQ6L1 PDFs [178]. Unlike SHERPA, POWHEG models the off-shell Z
2404 contribution at NLO.

2405 Acceptance and shape uncertainties are derived in an analogous fashion to $V+jets$
2406 as described below.

2407 Acceptance Uncertainties

2408 Diboson acceptance uncertainties are summarised in Table 7.11. Variations from μ_R ,
2409 μ_F , PDF choice and an alternative generator are considered and are combined via
2410 a sum in quadrature as described in Section 7.2.4. The largest modification to the
2411 nominal acceptance results from the POWHEG+PYTHIA8 alternate sample. Since
2412 the diboson contribution to the $t\bar{t}$ control region is negligible, no SR-to-CR relative
2413 acceptance uncertainty is necessary.

2414 For the WZ contribution, uncertainties are derived using the 1-lepton channel
2415 and applied to all three channels. The 1-lepton channel was used as it has the
2416 largest amount of available statistics. As far as was possible given the limited
2417 statistics available in the other channels, compatibility was checked between the
2418 derived uncertainties and the other channels. An additional 8% channel migration
2419 uncertainty is applied on the WZ 0-lepton channel. For the ZZ contribution, the
2420 normalisation uncertainty is calculated using the 2-lepton channel and applied to all
2421 three channels. The 0- and 1-lepton channels were found to have a similar HP-to-LP
2422 relative acceptance uncertainty of 18%. The 1-lepton medium-to-high p_T^V relative
2423 acceptance is based off the value obtained from the 2-lepton channel, since the
2424 1-lepton channel had an insufficient number of events to estimate the uncertainty
2425 directly. 30% and 18% channel migration uncertainties are applied in the 0- and
2426 1-lepton channels respectively.

2427 Since the contribution from WW is negligible, dedicated studies are not performed,
2428 but a 25% normalisation uncertainty is applied in all the three channels which is
2429 based on the modelling studies performed for the previous analysis [79].

Diboson Acceptance Uncertainties						
Bosons	WZ			ZZ		
Channel	0L	1L	2L	0L	1L	2L
Normalisation	16%			10%		
HP/LP	18%			18%		
High/Medium	10%			6%	18%	
Channel Extrap.	8%	-	-	30%	18%	-

Table 7.11: Diboson acceptance uncertainties [177]. All uncertainties except channel extrapolation uncertainties are fully correlated between ZZ and WZ processes and channels.

2430 Shape Uncertainties

2431 Diboson shape uncertainties are derived in a similar fashion to $V+jets$. Only the
 2432 uncertainties associated with systematic variation of μ_R and the alternate event
 2433 generator have a non-negligible impact on the m_J shape. Variation of μ_R produces
 2434 consistent m_J shape changes across all regions and channels, and hence only a single
 2435 associated uncertainty is derived, shown in Fig. 7.4. A hyperbolic tangent is fitted
 2436 to the symmetrised ratio.

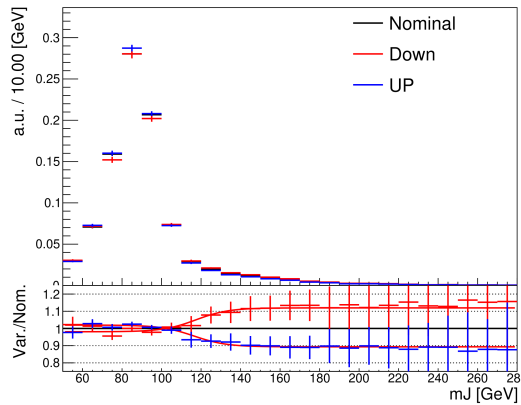


Figure 7.4: Leading large- R jet mass distribution for the WZ and ZZ processes, inclusive across all signal regions and lepton channels [177]. The renormalisation scale μ_R has been varied by a factor of 2 (1up) and 0.5 (1down). The red line shape shows the fitting results of the hyperbolic tangent function.

2437 The comparison between the nominal SHERPA and alternative POWHEG+PYTHIA8
 2438 samples is shown in Fig. 7.5 for the 0- and 1-lepton channels for both the WZ and

2439 ZZ processes. For these channels, the shape of m_J varies in opposite directions
2440 in the LP and HP signal regions. Shapes are similar between p_T^V bins, the 0- and
2441 1-lepton channels and for WZ and ZZ . In order to reduce the effects of statistical
2442 fluctuations on the fit, these regions are merged before deriving the shape uncertainty.
2443 A third order polynomial is fitted to the ratio, and this function transitions to a
2444 constant piecewise function in the high mass region to accurately represent the shape.
2445 Dependence on the event generator was found to be negligible within statistical
2446 uncertainty in the 2-lepton channel, and so no uncertainty was applied. All diboson
2447 shape uncertainties are fully correlated in the fit.

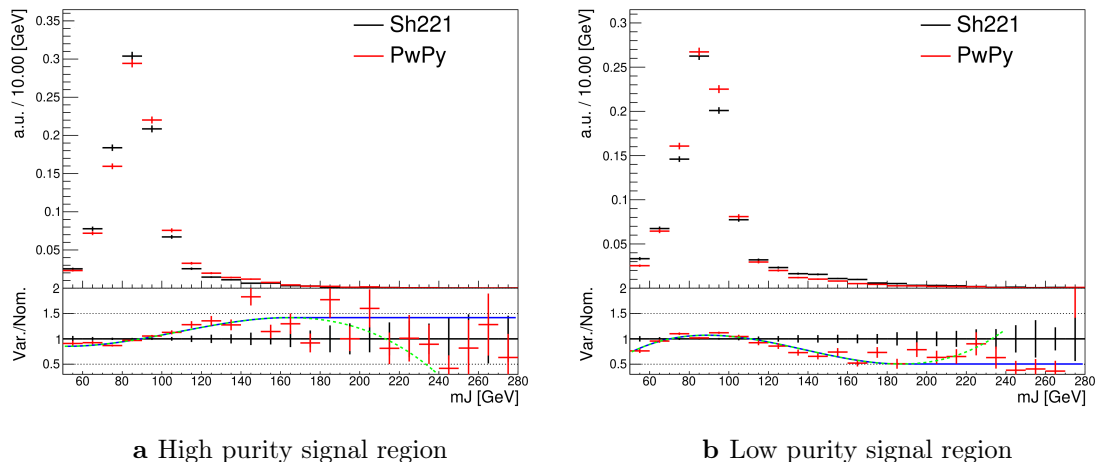


Figure 7.5: The comparison of the shapes of the large- R jet mass m_J between SHERPA (black) and POWHEG+PYTHIA8 (red) samples from WZ and ZZ process in high and low purity signal regions, integrated over p_T^V regions and the 0- and 1-lepton channels [177]. The dashed green line shows the fitted third order polynomial function and the blue lines show the function after a protection is added in the high mass region.

2448 7.2.6 $t\bar{t}$ and single-top Modelling

2449 The main features of the systematic uncertainties on the remaining two modelled
2450 backgrounds, $t\bar{t}$ and single-top, are described below.

2451 The modelling of the $t\bar{t}$ background uses a POWHEG+PYTHIA8 nominal sample.
2452 Two alternate samples were considered: POWHEG+HERWIG7 (providing an alternate
2453 parton shower model) and MADGRAPH5+PYTHIA8.2 (providing an alternate hard
2454 scatter model). Effects of initial and final state radiation (ISR and FSR, respectively)

were assessed using internal weight variations in the nominal sample. Acceptance and shape uncertainties were derived for each of the variations. Of the acceptance uncertainties, the largest contribution is due to the matrix element calculation, with the parton showering model being second. The ISR and FSR acceptance uncertainties were found to be subdominant. For the shape uncertainties, only the ISR and parton showering variations have non-negligible impacts on the m_J shape.

The dominant process contributing to the single-top background is Wt production, relevant for the 0- and 1-lepton channels. The same nominal and alternative samples are used as for the $t\bar{t}$ background. Again, ISR and FSR variations are obtained from internal weight variations in the nominal sample. At higher orders in QCD, diagrams contributing to the Wt production process can also be found in leading-order $t\bar{t}$ production processes. To account for the arising interference effects, the diagram removal (DR) scheme in Ref. [179] was employed for the nominal sample. The uncertainty on the DR scheme was assessed using an alternate sample using a diagram subtraction (DS) method which removes interference at the generator level. The largest sources of acceptance and shape uncertainties were due to this DS-DR variation.

7.2.7 Signal Modelling

The modelling of the systematic uncertainties affecting the signal processes follows the procedure described in Refs. [26, 180, 181]. The $qq \rightarrow VH$ signal samples are generated with POWHEG BOX v2 + GoSAM at next-to-leading order (NLO) accuracy in QCD. An additional $gg \rightarrow ZH$ sample is generated using POWHEG Box v2 at leading order (LO) in QCD. In both cases, the generated events are interfaced with PYTHIA 8 for the parton showering modelling. An alternate HERWIG7 sample is used to assess the uncertainty on the parton showering model. Recommended systematic uncertainties on the signal production cross-sections and $H \rightarrow b\bar{b}$ branching ratio from the LHC Higgs Cross Section Working Group are applied [182, 183]. Acceptance and shape uncertainties arising from missing higher-order QCD and electroweak corrections, PDF uncertainties, renormalisation and factorisation scales, and alternate parton showering model are applied.

2485 7.3 Statistical Treatment

2486 A binned global maximum-profile-likelihood fit of the m_J distribution is performed
 2487 to extract information on the signal, combining all the analysis regions defined
 2488 in Table 7.1. The signal strength $\mu = \sigma/\sigma_{\text{SM}}$ is defined as the ratio between the
 2489 observed and predicted cross-sections, where $\mu = 0$ corresponds to the background-
 2490 only hypothesis and $\mu = 1$ corresponds to the SM prediction. This is a parameter of
 2491 interest (POI) which acts to scale the total number of signal events, and is determined
 2492 during the fit procedure.

2493 The present analysis makes use of two POIs. The first, μ_{VH}^{bb} , is the signal strength
 2494 for the VH , $H \rightarrow b\bar{b}$ process, the primary process under investigation. The diboson
 2495 production strength μ_{VZ}^{bb} for the VZ , $Z \rightarrow b\bar{b}$ process is measured simultaneously and
 2496 provides a validation of the analysis apparatus used for the primary $H \rightarrow b\bar{b}$ measure-
 2497 ment. Alongside the two POIs, the predictive model depends on several parameters
 2498 which are not the primary target of measurement, and represent the systematic
 2499 uncertainties discussed previously. These parameters are called nuisance parameters
 2500 (NPs), collectively referred to as θ . Freely floating background normalisations are
 2501 implemented as NPs and are also extracted during the fitting processes.

2502 7.3.1 Likelihood Function

2503 The statistical setup treats each bin as a Poisson counting experiment and is based on
 2504 the ROOSTATS framework [184]. The combined likelihood over N bins is constructed
 2505 as the product of Poisson probabilities in each bin. Considering the simplified case
 2506 of a single signal strength parameter μ , and neglecting sources of systematic or
 2507 statistical uncertainty, this is given by

$$\mathcal{L}(\mu) = \prod_{i=1}^N \frac{(\mu s_i + b_i)^{n_i}}{n_i!} \exp [-(\mu s_i + b_i)], \quad (7.1)$$

2508 where s_i (b_i) is the expected number of signal (background) events in bin i , and n_i is
 2509 the number of observed data events in bin i .

2510 **Treatment of Uncertainties**

2511 Systematic uncertainties can modify the predicted signal and background yields s_i
2512 and b_i . Each source of systematic uncertainty is taken into account by adding an
2513 additional NP θ_j to the likelihood in the form of a Gaussian cost function. The
2514 combined effect of the NPs is then

$$\mathcal{L}(\theta) = \prod_{j=1}^{N_\theta} \frac{1}{\sqrt{2\pi\sigma_j}} \exp \left[\frac{-(\theta_j - \hat{\theta}_j)^2}{2\sigma_j^2} \right], \quad (7.2)$$

2515 where N_θ is the number of NPs, θ_j is the nominal value of the j th NP, $\hat{\theta}_j$ is the fitted
2516 value, and σ_j is the corresponding associated prior uncertainty on the NP. As the
2517 fitted value $\hat{\theta}_j$ deviates from its nominal value, a cost is introduced. The presence of
2518 NPs modifies the likelihood as

$$\mathcal{L}(\mu) \rightarrow \mathcal{L}(\mu, \theta) = \mathcal{L}(\mu)\mathcal{L}(\theta). \quad (7.3)$$

2519 The predicted signal and background yields are also modified by the presence of the
2520 NPs with

$$s_i \rightarrow s_i(\theta), \quad b_i \rightarrow b_i(\theta). \quad (7.4)$$

2521 For NPs which are left freely floating in the fit, no corresponding Gaussian constraints
2522 are added to the likelihood.

2523 The pull of a NP is defined as the difference between the fitted value $\hat{\theta}_j$ and the
2524 nominal value θ_j , divided by the uncertainty on the NP σ_j . To obtain the uncertainty
2525 on the pull of a NP, the following procedure is used. The Hessian matrix \mathbf{H} is
2526 calculated as

$$\mathbf{H} = \begin{bmatrix} \frac{\partial^2 \mathcal{L}}{\partial \theta_1^2} & \frac{\partial^2 \mathcal{L}}{\partial \theta_1 \partial \theta_2} & \dots & \frac{\partial^2 \mathcal{L}}{\partial \theta_1 \partial \theta_n} \\ \frac{\partial^2 \mathcal{L}}{\partial \theta_2 \partial \theta_1} & \frac{\partial^2 \mathcal{L}}{\partial \theta_2^2} & \dots & \frac{\partial^2 \mathcal{L}}{\partial \theta_2 \partial \theta_n} \\ \vdots & \vdots & \ddots & \vdots \\ \frac{\partial^2 \mathcal{L}}{\partial \theta_n \partial \theta_1} & \frac{\partial^2 \mathcal{L}}{\partial \theta_n \partial \theta_2} & \dots & \frac{\partial^2 \mathcal{L}}{\partial \theta_n^2} \end{bmatrix}. \quad (7.5)$$

2527 Taking the inverse of the Hessian matrix \mathbf{H}^{-1} yields the covariance matrix, from
2528 which the post-fit uncertainties on the different NPs can be extracted. If the post-fit
2529 uncertainty is smaller than the nominal uncertainty, additional information about
2530 the NP has been extracted by the fit, and NP is said to be *constrained*.

2531 The statistical uncertainty on the simulated events is implemented using a dedicated
2532 NP for each bin which can scale the background yield in that bin. Statistical NPs
2533 are also implemented using a Gaussian constraint.

2534 Smoothing and Pruning

2535 To simplify the fit to reduce and improve its robustness, systematic uncertainties
2536 are smoothed and pruned. Smoothing accounts for the large statistical uncertainty
2537 present in some samples that can lead to unphysical fluctuations in the shape
2538 systematics. The smoothing procedure relies on the assumption that the impact of
2539 systematics should be approximately monotonic and correlated between neighbouring
2540 bins.

2541 In addition to smoothing, pruning is the process of removing from the fit those
2542 systematics which only have a very small effect. This improves the stability of the
2543 fit by reducing the number of degrees of freedom. Acceptance uncertainties are
2544 pruned in a given region if they have a variation of less than 0.5%, or if the up and
2545 down variations have the same sign in that region. Shape uncertainties are pruned
2546 in a given region if the deviation in each bin is less than 0.5% in that region. In
2547 addition, acceptance and shape uncertainties are neglected in a given region for any
2548 background which makes up less than 2% of the total background in a given region.

2549 Fit Procedure and Statistical Tests

2550 The best-fit value of μ , denoted $\hat{\mu}$, is obtained via an unconditional maximisation of
 2551 the likelihood. The likelihood is also used to construct a statistical test which can
 2552 confirm or reject the background-only hypothesis. The test statistic q_μ is constructed
 2553 from the profile likelihood ratio,

$$q_\mu = -2 \ln \frac{\mathcal{L}(\mu, \hat{\theta}_\mu)}{\mathcal{L}(\hat{\mu}, \hat{\theta})} \quad (7.6)$$

2554 where $\hat{\mu}$ and $\hat{\theta}$ are chosen to maximise the likelihood \mathcal{L} , and the profile value $\hat{\theta}_\mu$ is
 2555 obtained from a conditional maximisation of the likelihood for a specific choice of
 2556 $\mu = 0$ corresponding to the background-only hypothesis.

2557 The test statistic is used to construct a p -value which is used to probe the background-
 2558 only hypothesis. The p -value is typically reported in terms of the significance Z ,
 2559 defined as the number of standard deviations for a Gaussian Normal distribution
 2560 which will produce a one-sided tail integral equal to the p -value, as in

$$p = \int_Z^\infty \frac{1}{\sqrt{2\pi}} e^{-x^2/2} dx = 1 - \Phi(Z). \quad (7.7)$$

2561 Typically a value of $Z = 3$ constitutes *evidence* of a processes, while $Z = 5$ is required
 2562 for a *discovery*, or observation. Alongside the p -value, the best-fit value of the signal
 2563 strength $\hat{\mu}$ and its corresponding uncertainty are quoted, and compared to their
 2564 expected values.

2565 7.3.2 Background Normalisations

2566 The backgrounds which can be constrained by the fit are left freely floating and
 2567 the corresponding normalisation factors are extracted. Normalisation factors (NF),
 2568 represent the value by which the predicted normalisations are scaled, and are im-
 2569 plemented for the dominant backgrounds ($t\bar{t}$, $Z+hf$, $W+hf$). The NFs are also
 2570 subdivided into different regions of phase-space for $t\bar{t}$, given it is possible to obtain
 2571 a strong constraint in the individual channels. This also removes the need for an
 2572 extrapolation uncertainty.

2573 The normalisations and shapes of all other backgrounds, with the exception of the
2574 multijet background which is estimated using a data driven technique, are initialised
2575 using the nominal samples and the state-of-the art process normalisations, as outlined
2576 in Table 7.2.

2577 **7.3.3 Asimov Dataset & Expected Results**

2578 The Asimov dataset is constructed by replacing the data with the sum of the signal
2579 and background predictions $n_i = s_i + b_i$. A fit to this dataset using the nominal
2580 values of the NPs from the simulation will recover the input values and is useful for
2581 studying the expected result, in addition to constraints on and correlations between
2582 the NPs.

2583 Alternatively, a conditional fit to the Asimov dataset can be performed using values
2584 of the background NPs which are determined from an unconditional fit to data. The
2585 signal NPs and POIs are fixed at their nominal values from the SM simulation. The
2586 result of this fit can be used to calculate expected (median) significances given a
2587 more realistic background model, which can be compared to their observed values,
2588 as is done in Section 7.4.3.

2589 **7.4 Results**

2590 In the present analysis, the two signal strength parameters μ_{VH}^{bb} and μ_{VZ}^{bb} are extracted
2591 from a simultaneous maximisation of the likelihood described in Section 7.3. The
2592 results of the analysis are summarised in this section. The corresponding post-fit
2593 background normalisations are listed in Table 7.12. Post-fit m_J distributions are
2594 shown in Section 7.4.1. The observed signal strengths are given in Section 7.4.3,
2595 along with observed and expected significances. Finally in Section 7.4.4 the impact
2596 of systematic uncertainties on the results is examined.

Process	Normalisation factor
$t\bar{t}$ 0-lepton	0.88 ± 0.10
$t\bar{t}$ 1-lepton	0.83 ± 0.09
$W+\text{hf}$	1.12 ± 0.14
$Z+\text{hf}$	1.32 ± 0.16

Table 7.12: Factors applied to the nominal normalisations of the $t\bar{t}$, $W+\text{hf}$, and $Z+\text{hf}$ backgrounds, as obtained from the likelihood fit [131]. The errors represent the combined statistical and systematic uncertainties.

2597 7.4.1 Post-fit Distributions

2598 In addition to the observed significance and signal strength, it is also necessary to
 2599 study the post-fit m_J distributions to compare level of the agreement between the
 2600 simulation (using the best-fit values of the signal strength $\hat{\mu}$ and the NP $\hat{\theta}$) and the
 2601 data. The best-fit values $\hat{\mu}$ and $\hat{\theta}$ are obtained from an unconditional fit to data over
 2602 all analysis regions. Post-fit m_J distributions are given for the signal regions in the
 2603 0-, 1- and 2-lepton channels in Fig. 7.6. The LP and HP regions are merged for the
 2604 0- and 1-lepton channels for the sake of simplicity. In general there is a good level of
 2605 agreement between the simulation and data, indicating the fit model is performing as
 2606 expected. Fig. 7.7 shows the post-fit plots for the $t\bar{t}$ control regions. Again, a good
 2607 level of agreement is observed given the statistical uncertainties on the distributions.

2608 7.4.2 Post-fit Yields

2609 The post-fit yields resulting from the unconditional fit to data are shown in Table 7.13,
 2610 Table 7.14, and Table 7.15 for the 0-, 1- and 2-lepton channels, respectively.

2611 7.4.3 Observed Signal Strength & Significance

2612 The measured signal strength is computed as the ratio between the measured signal
 2613 yield to the prediction from the SM. The combined result for all three lepton channels
 2614 and all analysis regions is given for μ_{VH}^{bb} in Eq. (7.8), and for μ_{VZ}^{bb} in Eq. (7.9). Both

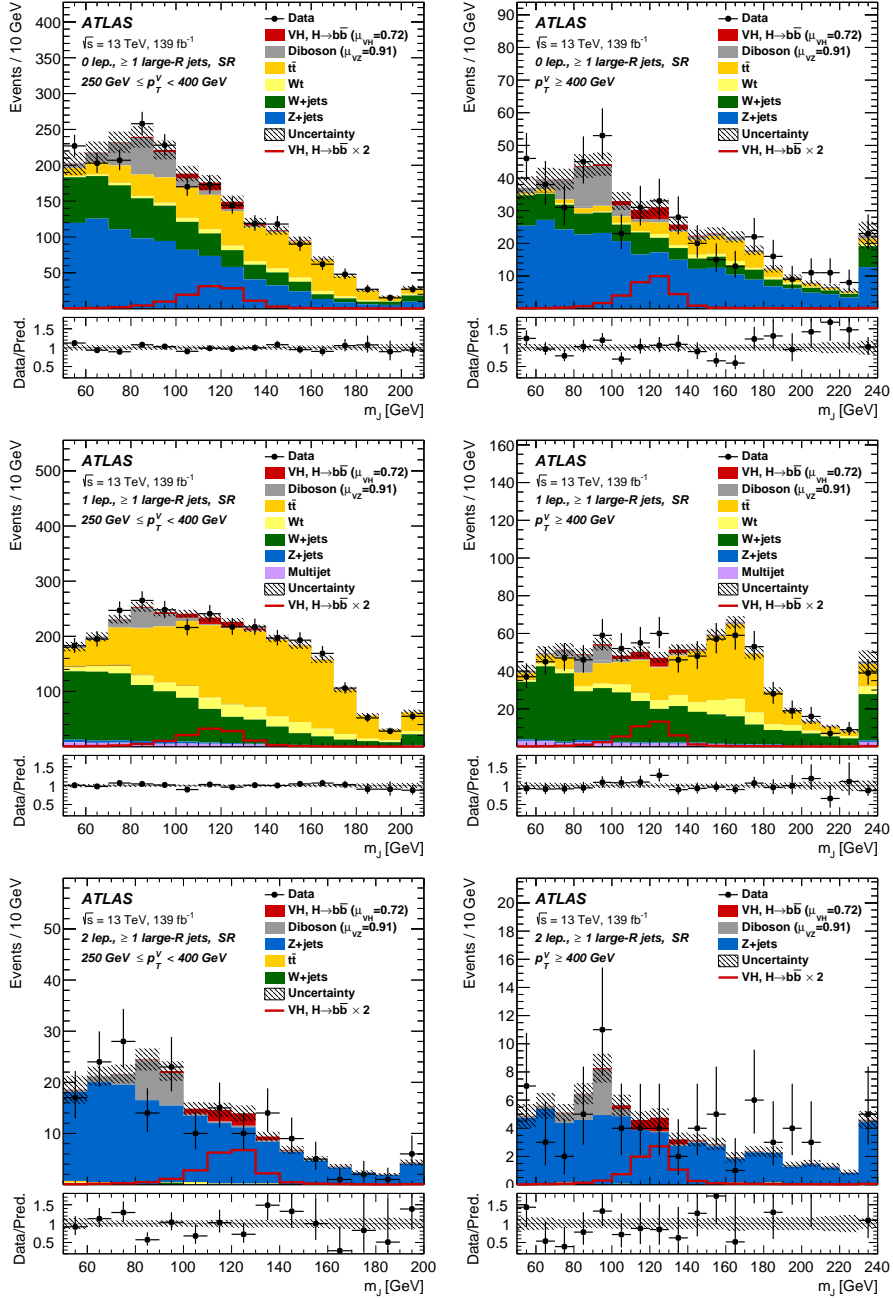


Figure 7.6: The m_J post-fit distributions in (top) the 0-, (middle) 1- and (bottom) 2-lepton SRs for (left) $250 \text{ GeV} < p_T^V < 400 \text{ GeV}$ and (right) $p_T^V \geq 400 \text{ GeV}$. The LP and HP regions are merged for the 0-lepton and 1-lepton channels. The fitted background contributions are shown as filled histograms. The Higgs boson signal ($m_H = 125 \text{ GeV}$) is shown as a filled histogram and is normalised to the signal yield extracted from data ($\mu_{VH}^{bb} = 0.72$), and as an unstacked unfilled histogram, scaled by the SM prediction times a factor of two. The size of the combined on the sum of the fitted signal and background is shown in the hatched band. The highest bin contains the overflow [131].

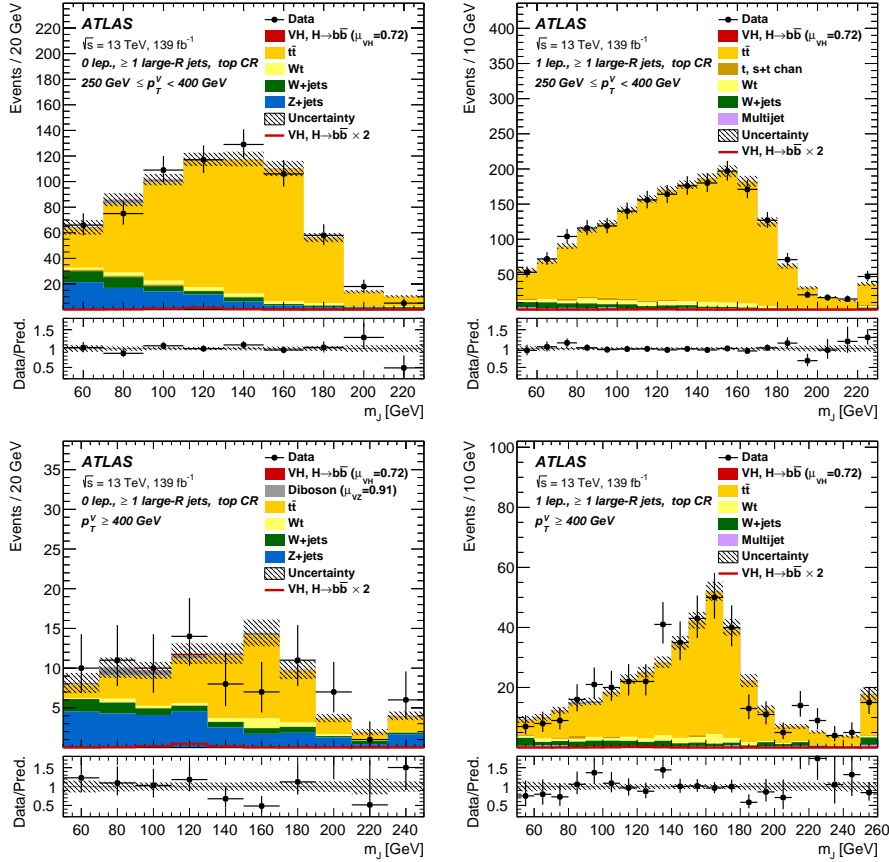


Figure 7.7: The m_J post-fit distributions in the $t\bar{t}$ control region for (top) the 0-lepton channel and the 1-lepton channel for $250 \text{ GeV} < p_T^V < 400 \text{ GeV}$ and (bottom) the 0-lepton channel and the 1-lepton channel for $p_T^V > 400 \text{ GeV}$. The background contributions after the likelihood fit are shown as filled histograms. The Higgs boson signal ($m_h = 125 \text{ GeV}$) is shown as a filled histogram on top of the fitted backgrounds normalised to the signal yield extracted from data ($\mu_{VH}^{bb} = 0.72$), and unstacked as an unfilled histogram, scaled by the SM prediction times a factor of 2. The size of the combined statistical and systematic uncertainty for the sum of the fitted signal and background is indicated by the hatched band. The highest bin in the distributions contains the overflow [131].

Processes	$250 \text{ GeV} < p_T^V \leq 400 \text{ GeV}$			$p_T^V > 400 \text{ GeV}$		
	HP	LP	CR	HP	LP	CR
Signal	21.93±11.17	18.99±9.76	1.05±0.54	5.69±2.88	5.85±3.01	0.33±0.17
W+t	14.70±5.37	45.55±19.44	17.18±8.09	2.03±0.98	8.93±6.33	3.76±2.49
other t+X	0.79±0.03	3.18±0.66	4.51±1.28	-	0.66±0.03	0.11±0.00
$t\bar{t}$	75.19±13.60	423.85±36.12	539.21±31.39	7.54±1.77	38.20±6.75	44.07±7.43
VZ	77.01±17.09	87.70±19.36	6.16±1.56	17.30±4.10	28.77±6.55	2.79±0.72
WW	-	2.15±0.05	0.24±0.01	0.33±0.02	1.80±0.06	-
Whf	100.78±20.01	331.31±59.54	29.97±21.85	20.19±6.24	59.82±17.91	6.61±5.09
Wcl	5.13±2.31	8.44±3.24	0.46±0.01	0.99±0.69	2.77±1.14	0.19±0.07
Wl	5.61±3.93	4.61±2.45	0.16±0.00	1.41±2.06	2.67±1.67	0.57±0.36
Zhf	318.76±35.27	548.71±61.84	76.97±21.47	86.79±10.63	184.99±21.43	25.76±7.43
Zcl	3.97±1.63	6.74±2.68	0.83±0.02	-	6.36±2.73	0.93±0.41
Zl	1.34±0.67	3.61±2.14	0.42±0.01	1.05±0.63	3.68±2.47	0.29±0.16
Data	623	1493	683	146	330	85
Background	603±25	1466±36	676±25	138±9	339±15	85±7

Table 7.13: Post-fit yields in the 0-lepton channel. Combined statistical and systematic uncertainties are shown [177].

Processes	$250 \text{ GeV} < p_T^V \leq 400 \text{ GeV}$			$p_T^V > 400 \text{ GeV}$		
	HP	LP	CR	HP	LP	CR
Signal	24.23±12.34	18.02±9.29	0.88±0.45	7.84±3.96	7.50±3.87	0.39±0.20
W+t	64.35±21.12	159.95±75.14	73.44±29.96	16.40±7.31	53.28±41.74	21.16±15.36
other t+X	1.92±0.48	16.33±0.31	21.89±6.18	0.13±0.01	1.70±0.06	3.95±1.40
$t\bar{t}$	234.76±30.21	1189.51±75.91	1758.08±57.99	50.87±7.34	226.85±23.98	340.61±25.32
VZ	35.94±8.87	56.30±13.98	4.93±1.38	8.63±2.30	20.02±5.29	2.61±0.84
WW	-	6.48±1.63	-	-	4.35±1.32	0.93±0.03
Whf	265.13±27.68	617.81±63.56	59.91±21.90	91.42±11.51	238.81±29.53	26.55±9.84
Wcl	7.33±2.95	13.81±5.65	2.10±0.04	6.23±2.49	10.17±4.09	0.63±0.02
Wl	2.99±1.47	5.66±3.39	0.65±0.01	2.21±1.35	7.67±4.98	0.31±0.01
Zhf	10.16±1.24	24.61±2.46	3.45±0.41	2.12±0.30	6.56±0.79	0.98±0.12
Zcl	0.02±0.00	0.75±0.02	-	-	0.33±0.01	0.02±0.00
Zl	-	0.49±0.01	0.03±0.00	0.30±0.19	0.23±0.01	0.02±0.00
ggWW	-	0.35±0.01	0.27±0.01	0.15±0.02	0.33±0.01	-
MultiJet	17.04±8.87	44.29±22.82	21.78±11.22	7.81±4.50	21.85±12.73	7.86±4.01
Data	668	2161	1946	185	597	410
Background	640±26	2136±44	1947±43	186±11	592±21	406±18

Table 7.14: Post-fit yields in the 1-lepton channel. Combined statistical and systematic uncertainties are shown [177].

Processes	$250 \text{ GeV} < p_T^V \leq 400 \text{ GeV}$	$p_T^V > 400 \text{ GeV}$
	SR	SR
Signal	7.62 ± 3.88	2.79 ± 1.41
W+t	1.28 ± 0.39	-
t̄t	1.64 ± 0.35	0.45 ± 0.10
VZ	19.90 ± 4.86	7.49 ± 2.05
Whf	0.41 ± 0.07	0.07 ± 0.01
Zhf	150.94 ± 12.72	57.15 ± 5.81
Zcl	2.20 ± 0.91	1.80 ± 0.76
Zl	0.94 ± 0.67	1.01 ± 0.67
Data	179	73
Background	177 ± 12	68 ± 6

Table 7.15: Post-fit yields in the 2-lepton channel. Combined statistical and systematic uncertainties are shown [177].

2615 results include a full breakdown of the systematic and statistical uncertainties.

$$\mu_{VH}^{bb} = 0.72^{+0.39}_{-0.36} = 0.72^{+0.29}_{-0.28}(\text{stat.})^{+0.26}_{-0.22}(\text{syst.}) \quad (7.8)$$

2616

$$\mu_{VZ}^{bb} = 0.91^{+0.29}_{-0.23} = 0.91 \pm 0.15(\text{stat.})^{+0.24}_{-0.17}(\text{syst.}) \quad (7.9)$$

2617 The results for μ_{VH}^{bb} and μ_{VZ}^{bb} are consistent with the expectation from the SM. The
 2618 μ_{VH}^{bb} measurement is dominated by statistical uncertainty, while the μ_{VZ}^{bb} measurement
 2619 is dominated by systematic sources of uncertainty. The measured signal strength
 2620 for μ_{VZ}^{bb} corresponds to an observed significance of 2.1 standard deviations, with an
 2621 expected (median) significance given the SM prediction of 2.7 standard deviations.
 2622 The diboson observed (expected) signal strength significance is 5.4 (5.7). These
 2623 results are summarised in Fig. 7.8, which shows the background-subtracted m_J
 2624 distribution. A clear signal excess is visible around the Higgs mass of $m_H = 125 \text{ GeV}$.

2625 Compatability Studies

2626 Alongside the standard 2-POI fit, a (3+1)-POI fit can be performed by splitting μ_{VH}^{bb}
 2627 into three separate POIs, one for each channel. A simultaneous fit to the channel
 2628 specific signal strengths can then be performned, which allows a comparison of the
 2629 contributions from each channel. Fig. 7.9 compares the best-fit signal strengths.
 2630 The 0- and 1-lepton channels show a signal strength which is consistent with the

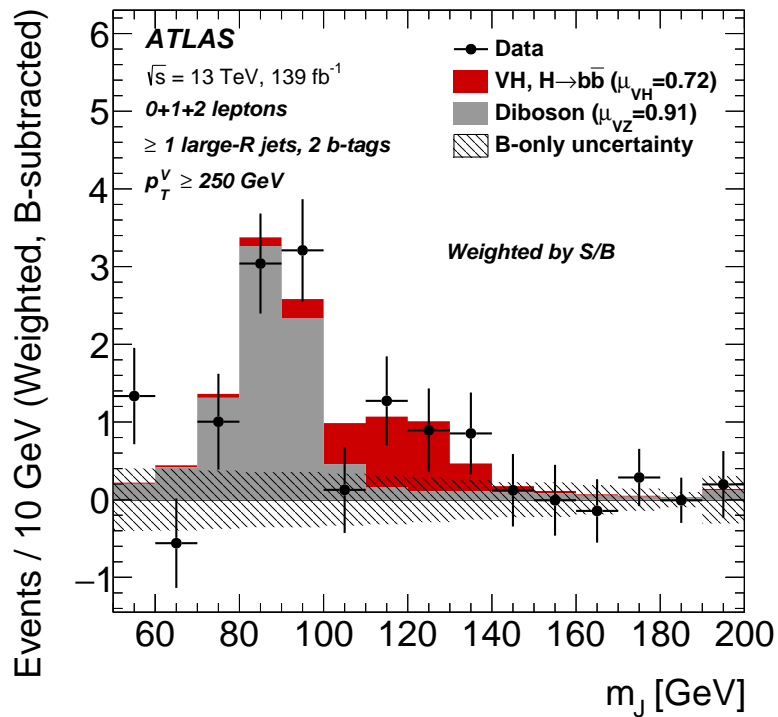


Figure 7.8: m_J distribution in data after subtraction of all backgrounds except for the WZ and ZZ diboson processes. The contributions from all lepton channels and signal regions are summed and weighted by their respective values of the ratio of fitted Higgs boson signal and background yields. The expected contribution of the associated WH and ZH production of a SM Higgs boson with $m_H = 125 \text{ GeV}$ is shown scaled by the measured combined signal strength ($\mu_{VH}^{bb} = 0.72$). The diboson contribution is normalised to its best-fit value of $\mu_{VZ}^{bb} = 0.91$. The size of the combined statistical and systematic uncertainty is indicated by the hatched band. This error band is computed from a full signal-plus-background fit including all the systematic uncertainties defined in Section 7.2, except for the VH/VZ experimental and theory uncertainties [131].

2631 SM prediction, while the 2-lepton channel shows a small deviation within the 1σ
2632 uncertainty. Overall, good compatibility is observed via a χ^2 test with a corresponding
2633 p -value of 49%.

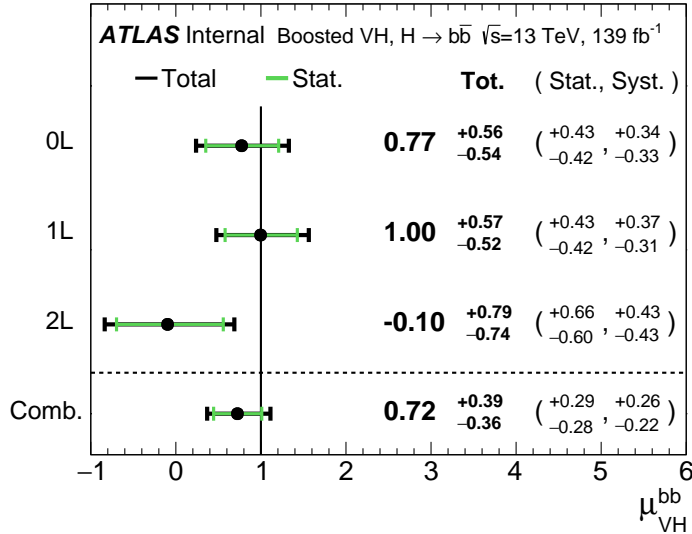


Figure 7.9: Signal strength compatibility test between the (3+1)-POI fit (with the three lepton channels splitted) and the default (1+1)-POI fit. The compatibility of the three channels is evaluated via a χ^2 difference test and results in a p -value of 49% [131].

2634 7.4.4 Impact of Systematics

2635 The impact of systematic uncertainties on the final fitted value $\hat{\mu}^{bb}$ can be studied
2636 using the NP rankings, and the uncertainty breakdown.

2637 Fig. 7.10 shows the NP ranking, which is used to visualise which out of the many
2638 NPs involved in the fit have the largest impact on the sensitivity to the fitted
2639 POI. To obtain the ranking, a likelihood scan is performed for each NP θ_j . First,
2640 an unconditional fit is used to determine $\hat{\theta}_j$. The NP is then fixed to its post-fit
2641 value varied by $\pm 1\sigma$, the fit is repeated and the best-fit value of the POI, $\Delta\hat{\mu}_{VH}^{bb}$, is
2642 calculated, and used to rank the NPs. Also shown in Fig. 7.10 are the pulls and
2643 constraints for the highest ranked NPs.

2644 The experimental uncertainty on the signal large- R jet mass resolution (JMR) has
2645 the largest impact. JMR and jet energy scale (JES) uncertainties also have impacts

2646 for the $V+jets$ background and for the diboson background. The freely-floating
2647 $Z+hf$ normalisation is the second highest ranked NP, and is heavily constrained by
2648 the fit. The VZ POI μ_{VZ}^{bb} is also a significant NP when considering the primary μ_{VH}^{bb}
2649 measurement.

2650 The NP ranking highlights individual NPs which have a large impact on the POI
2651 measurement sensitivity. Complementary information is provided at a higher level
2652 by considering the overall impact of different groups of systematics. The groups
2653 are constructed from NPs which have similar physical origin. The impact of each
2654 group is calculated by running a fit with all the NPs in the given group fixed to their
2655 nominal values. The uncertainty on the POI extracted from this fit is subtracted
2656 in quadrature from the the uncertainty on the POI from the nominal fit, and the
2657 resulting values are provided as the impact for each group. The full breakdown
2658 for the observed impact of uncertainties on the μ_{VH}^{bb} signal strength is provided in
2659 Table 7.16. The total systematic impact is the difference in quadrature between
2660 the nominal uncertainty on μ_{VH}^{bb} and the combined statistical impact. The “data
2661 stat only” group fixes all NPs at their nominal value, while the total statistical
2662 impact fixes all NPs except floating normalisations. The floating normalisations
2663 group fixes only the NPs associated with normalisation which are left floating in
2664 the fit. The uncertainty on μ_{VH}^{bb} is dominated by combined statistical effects (0.28),
2665 although the combined impact of systematics (0.24) is of a comparable size. The
2666 signal largest group is the data stat uncertainty (0.25), demonstrating that the
2667 analysis would benefit from an increased integrated luminosity or improved efficiency
2668 to select signal events (recall from Section 7.1.3 the signal efficiency is in the range of
2669 10%). Of the experimental systematic sources of uncertainty, the dominant impact
2670 is the experimental uncertainties associated with the reconstruction of large- R jets
2671 (0.13). Other experimental sources of uncertainty are small in comparison. Modelling
2672 uncertainties also have a large contribution to the overall systematic uncertainty. The
2673 biggest contribution to the overall uncertainty is the combined statistical uncertainty
2674 on the simulated samples (0.09). Out of the backgrounds, the $W+jets$ and $Z+jets$
2675 have the highest (0.06) and second-highest (0.05) impact respectively.

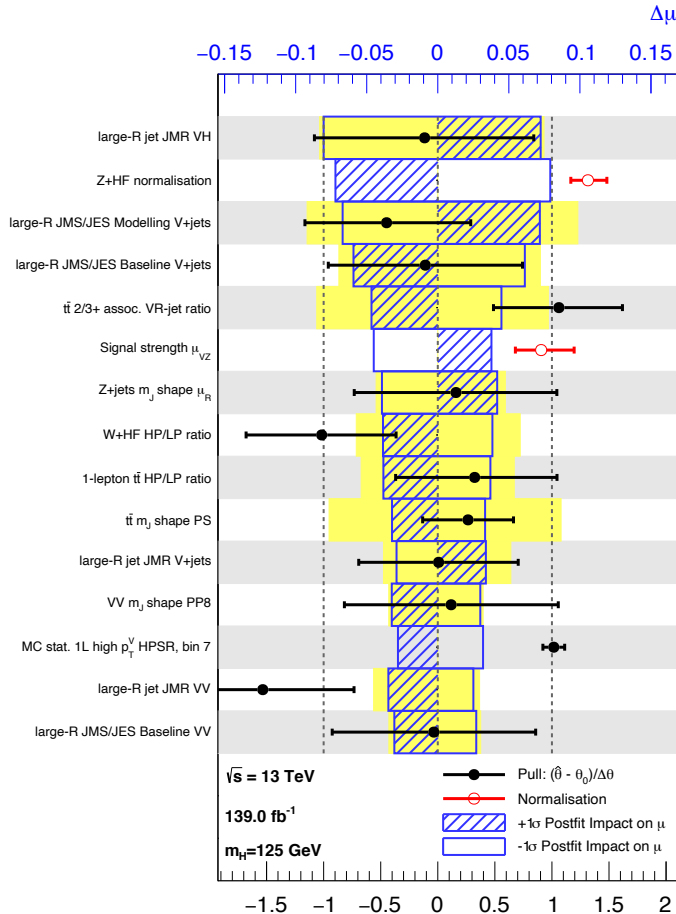


Figure 7.10: Impact of systematic uncertainties on the fitted VH signal-strength parameter $\hat{\mu}_{VH}^{\text{bb}}$ sorted in decreasing order. The boxes show the variations of $\hat{\mu}$, referring to the top x -axis, when fixing the corresponding individual nuisance parameter to its post-fit value modified upwards or downwards by its post-fit uncertainty, i.e. $\hat{\theta} \pm \sigma_{\hat{\theta}}$, and repeating the fit. The impact of up- and down-variations can be distinguished via the dashed and plane box fillings. The yellow boxes show the pre-fit impact (top x -axis) by varying each nuisance parameter by ± 1 . The filled circles show the deviation of the fitted value for each nuisance parameter, $\hat{\theta}$, from their nominal input value θ_0 expressed in standard deviations with respect to their nominal uncertainties $\Delta\theta$ (bottom x -axis). The error bars show the post-fit uncertainties on $\hat{\theta}$ with respect to their nominal uncertainties. The open circles show the fitted values and uncertainties of the normalization parameters that are freely floating in the fit. Pre-fit, these parameters have a value of one [177].

Source of uncertainty	Signed impact	Avg. impact
Total	+0.388 / -0.356	0.372
Statistical	+0.286 / -0.280	0.283
↔ Data stat only	+0.251 / -0.245	0.248
↔ Floating normalisations	+0.096 / -0.092	0.094
Systematic	+0.261 / -0.219	0.240
<hr/>		
Experimental uncertainties		
small-R jets	+0.041 / -0.034	0.038
large-R jets	+0.161 / -0.105	0.133
E_T^{miss}	+0.008 / -0.007	0.007
Leptons	+0.013 / -0.007	0.010
<i>b</i> -tagging	<i>b</i> -jets	+0.028 / -0.004
	<i>c</i> -jets	+0.012 / -0.011
	light-flavour jets	+0.009 / -0.007
	extrapolation	+0.004 / -0.005
Pile-up	+0.001 / -0.002	0.001
Luminosity	+0.019 / -0.007	0.013
<hr/>		
Theoretical and modelling uncertainties		
Signal	+0.073 / -0.026	0.050
Backgrounds	+0.106 / -0.095	0.100
↔ $Z + \text{jets}$	+0.049 / -0.047	0.048
↔ $W + \text{jets}$	+0.059 / -0.056	0.058
↔ $t\bar{t}$	+0.037 / -0.032	0.035
↔ Single top quark	+0.031 / -0.023	0.027
↔ Diboson	+0.034 / -0.029	0.032
↔ Multijet	+0.009 / -0.009	0.009
↔ MC statistical	+0.091 / -0.092	0.092

Table 7.16: Breakdown of the absolute contributions to the uncertainty on the signal strength μ_{VH}^{bb} obtained from the (1+1)-POI fit. The average impact represents the average between the positive and negative uncertainties on μ_{VH}^{bb} . The sum in quadrature of the systematic uncertainties attached to the categories differs from the total systematic uncertainty due to correlations [177].

2676 7.4.5 STXS Interpretation

2677 The Simplified Template Cross Sections (STXS) framework provides a common
2678 categorisation of candidate Higgs boson events according to certain truth-level
2679 properties of the production mode under study [26, 185]. The STXS framework is
2680 designed to be independent of the decay mode of the Higgs boson, and is therefore
2681 well suited to the combination of measurements between different decay channels
2682 and experiments.

2683 The STXS cross sections are independently measured for the ZH and WH production
2684 modes following the approach described in [180]. For each production mode, two
2685 bins in the truth vector boson transverse momentum $p_T^{V,t}$ are considered, $250 \text{ GeV} <$
2686 $p_T^{V,t} < 400 \text{ GeV}$ and $p_T^{V,t} \geq 400 \text{ GeV}$, leading to four independent analysis regions.
2687 Events from the simulated signal samples are categorised into the regions and used
2688 to estimate the expected cross section times branching ratio $\sigma \times B$ in each region,
2689 where

$$B = B(H \rightarrow b\bar{b}) \times B(V \rightarrow \text{leptons}), \quad (7.10)$$

2690 A simultaneous fit of the four cross section times branching ratios is performed.
2691 The uncertainties described in Section 7.2 are reused for the STXS fit, with the
2692 exception of the theoretical uncertainties on the signal cross section and branching
2693 ratios. The result from the fit is shown in Section 7.4.5 and compared with the
2694 expected prediction from the SM. The expected and observed results agree within
2695 the given uncertainties.

2696 7.5 Conclusion

2697 The analysis of the associated production of vector bosons with boosted Higgs bosons
2698 decaying to a pair of b -quarks using large- R jets is presented. The Higgs candidate is
2699 reconstructed as a large- R jet in order to improve sensitivity in the boosted regime
2700 in which the Higgs decay products are significantly collimated. The analysis is
2701 performed using 139 fb^{-1} of proton–proton collision data at $\sqrt{s} = 13 \text{ TeV}$ collected
2702 throughout the duration of Run 2 of the LHC.

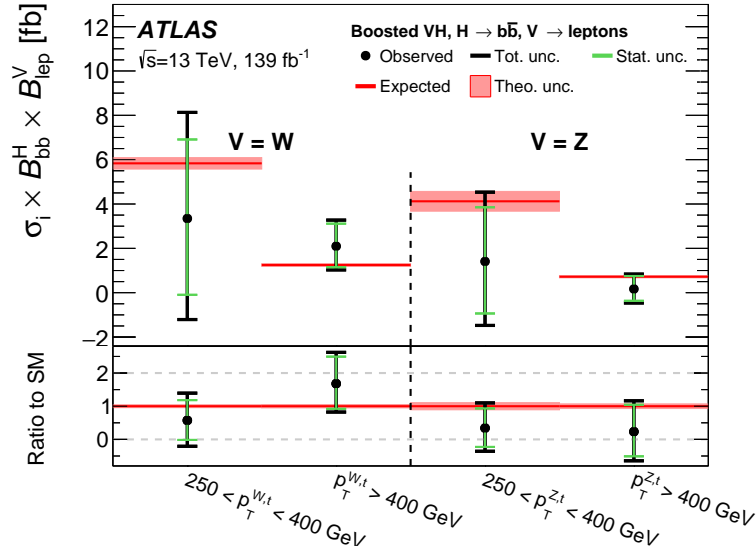


Figure 7.11: Measured VH simplified template cross sections times the $H \rightarrow b\bar{b}$ and $V \rightarrow \text{leptons}$ branching fractions in the medium and high $p_T^{V,t}$ bins [131].

2703 In comparison with the null hypothesis, the Standard Model (SM) VH , $H \rightarrow b\bar{b}$
 2704 process is found to have an observed significance of 2.1 standard deviations, whereas
 2705 the corresponding expected significance is 2.7 standard deviations. The VH , $H \rightarrow b\bar{b}$
 2706 process is measured simultaneously with the diboson VZ , $Z \rightarrow b\bar{b}$ process, which
 2707 provide a cross-check for the main analysis. The observed (expected) significance for
 2708 the diboson process is 5.4 (5.7).

2709 The statistical and systematic sources of uncertainty contribute a similar amount
 2710 to the overall uncertainty on the result. This analysis would therefore likely benefit
 2711 greatly from the improved b -tagging efficiency at high- p_T enabled by GN1 as discussed
 2712 in Chapter 6, due to the associated reduction in statistical uncertainty provided by
 2713 the increased number of events used in the analysis.

2714 The large- R jet mass resolution is found to be the dominant source of systematic
 2715 uncertainty on the μ_{VH}^{bb} measurement. An improved method of reconstructing the
 2716 large- R jet mass, for example by using a machine learning based regression approach,
 2717 possibly as an additional auxiliary task to GN1 (see Chapter 6), would therefore be
 2718 expected to reduce the systematic uncertainty on the μ_{VH}^{bb} measurement.

₂₇₁₉ **Chapter 8**

₂₇₂₀ **Conclusion**

₂₇₂₁ **8.1 Summary**

₂₇₂₂ The current understanding of particle physics contains many unanswered questions,
₂₇₂₃ and improving our understanding of the Standard Model is a promising way to
₂₇₂₄ attempt to answer some of them. One of the key objects which may enhance this
₂₇₂₅ understanding is the Higgs Boson, which was first observed only a decade ago and
₂₇₂₆ remains under intense scrutiny at the LHC. Given it's propensity to decay to heavy
₂₇₂₇ flavour b -quarks, reconstructing and identifying b -jets is of crucial importance to
₂₇₂₈ improving our understanding in this area. As discussed in Chapter 4, this task
₂₇₂₉ becomes increasingly difficult at high transverse momenta.

₂₇₃₀ One of the effects that hampered tracking and b -tagging performance at high- p_T was
₂₇₃₁ identified to be the increased rate of fake tracks. To address this issue, a tools was
₂₇₃₂ developed which was able to successfully identify fake tracks within jets 45% of the
₂₇₃₃ time, with a minimal loss of signal tracks of 1.2%. Removal of such tracks was found
₂₇₃₄ to improve the light-jet mistagging rate of the SV1 and JetFitter algorithms by up
₂₇₃₅ to 20% at high transverse momentum.

₂₇₃₆ A novel approach to b -tagging, GN1 was also developed using a Graph Neural Network
₂₇₃₇ (GNN) architecture. The model is encouraged to learn the topology of the jet through
₂₇₃₈ vertexing and track classification auxiliary tasks. As a single end-to-end trained
₂₇₃₉ model, GN1 simplifies the complexity of the flavour tagging pipeline and is able to
₂₇₄₀ achieve superior performance to the current state-of-the-art algorithms, which rely
₂₇₄₁ on a two-tiered approach. Compared with DL1r, GN1 improves the light-jet rejection

2742 by a factor of ~ 1.8 for jets in the $t\bar{t}$ sample with $20 < p_T < 250 \text{ GeV}$ at the 70%
2743 b -jet WP and by a factor of ~ 6 for jets in the Z' sample with $250 < p_T < 5000 \text{ GeV}$
2744 for a corresponding b -jet efficiency of 30%. GN1 also demonstrates a significant
2745 improvement in the discrimination between b - and c -jets.

2746 The work in this thesis demonstrates that even with suboptimal track reconstruction
2747 in this regime, it is possible to make algorithmic advancements to the flavour tagging
2748 pipeline to improve the identification of b -jets. This work has impacts for any analysis
2749 which relies on the identification of b -jets, including those which are sensitive to the
2750 Higgs Boson.

2751 Analysis of VH , $H \rightarrow b\bar{b}$ events was also carried out with 139 fb^{-1} of Run 2
2752 ATLAS at $\sqrt{s} = 13 \text{ TeV}$. Various background modelling uncertainties were derived
2753 and investigations into the fit model were carried out. The analysis observed a
2754 signal strength of $\mu_{VH}^{bb} = 0.72_{-0.36}^{+0.39} = 0.72_{-0.28}^{+0.29}(\text{stat.})_{-0.22}^{+0.26}(\text{syst.})$ corresponding to an
2755 observed (expected) significance of 2.1σ (2.7σ). The result was validated using a
2756 simultaneous fit to the VZ , $Z \rightarrow b\bar{b}$ process, which acts as a cross check to validate
2757 the primary analysis. The results of the analysis are the most precise measurements
2758 available in the high- p_T for the VH , $H \rightarrow b\bar{b}$ process. The high- p_T region is of
2759 particular interest as it is a region of phase space with good sensitivity to new physics.

2760 8.2 Future Work

2761 Additional algorithmic improvements are likely to yield further improved flavour
2762 tagging performance. Aside from these, large improvements to the flavour tagging
2763 performance will likely be possible if improvements are made to the b -hadron decay
2764 track reconstruction efficiency and accuracy.

2765 At the moment only the tracks from the Inner Detector and kinematic information
2766 about the jet are provided as inputs to the tagging algorithms. In Chapter 6 it
2767 was shown that the addition of a simple track-level variable corresponding to the
2768 ID of the reconstruction lepton to the model improved the performance. However
2769 there is still untapped potential in the form of additional information from the full
2770 parameters of the reconstructed leptons (making full use of the Calorimeters and
2771 Muon Spectrometer), the calorimeter clusters, and even the low level hits. Providing

2772 such additional inputs to the model is likely to complement the information provided
2773 by the tracks and further aid in the improvement of performance.

2774 On the output side, additional auxiliary training objectives may yield improved
2775 performance and also help to add to the explainability of the model. Regression of
2776 jet-level quantities such as the transverse momentum and mass, in addition to the
2777 truth b -hadron decay length are promising regression targets.

2778 The GN1 architecture can also be readily optimised for new use cases and topologies,
2779 as demonstrated by the studies described in Section 6.6. For example, a model
2780 with only hit-level information provided as inputs could be used for a fast trigger
2781 preselection on jets without the need to run the computationally expensive tracking
2782 algorithms. The model could also be repurposed for primary vertexing, or a pile-up
2783 jet tagger. Finally, training a version of GN1 to identify large- R jets would benefit
2784 those analysis investigating such boosted topologies. Ultimately the improved jet
2785 tagging performance enabled by the new algorithm will have a large impact across a
2786 broad spectrum of the ATLAS physics programme.

₂₇₈₇

Bibliography

- ₂₇₈₈ [1] A. Buckley, *A class for typesetting academic theses*, (2010). <http://ctan.tug.org/tex-archive/macros/latex/contrib/heptesis/heptesis.pdf>.
- ₂₇₉₀ [2] J. Shlomi, S. Ganguly, E. Gross, K. Cranmer, Y. Lipman, H. Serviansky et al.,
₂₇₉₁ *Secondary vertex finding in jets with neural networks*, *The European Physical Journal C* **81** (2021) .
- ₂₇₉₃ [3] ATLAS Collaboration, *Graph Neural Network Jet Flavour Tagging with the ATLAS Detector*, ATL-PHYS-PUB-2022-027 (2022).
- ₂₇₉₅ [4] L. Morel, Z. Yao, P. Cladé and S. Guellati-Khélifa, *Determination of the fine-structure constant with an accuracy of 81 parts per trillion*, *Nature* **588** (2020)
₂₇₉₆ pp. 61–65.
- ₂₇₉₈ [5] T. Sailer, V. Debierre, Z. Harman, F. Heiße, C. König, J. Morgner et al.,
₂₇₉₉ *Measurement of the bound-electron g-factor difference in coupled ions*, *Nature* **606**
₂₈₀₀ (2022) pp. 479–483.
- ₂₈₀₁ [6] CDF collaboration, *Observation of top quark production in $\bar{p}p$ collisions*, *Phys. Rev. Lett.* **74** (1995) pp. 2626–2631 [[hep-ex/9503002](#)].
- ₂₈₀₃ [7] D0 collaboration, *Observation of the top quark*, *Phys. Rev. Lett.* **74** (1995)
₂₈₀₄ pp. 2632–2637 [[hep-ex/9503003](#)].
- ₂₈₀₅ [8] S. W. Herb et al., *Observation of a Dimuon Resonance at 9.5-GeV in 400-GeV Proton-Nucleus Collisions*, *Phys. Rev. Lett.* **39** (1977) pp. 252–255.
- ₂₈₀₇ [9] UA1 collaboration, *Experimental Observation of Isolated Large Transverse Energy Electrons with Associated Missing Energy at $\sqrt{s} = 540$ GeV*, *Phys. Lett. B* **122**
₂₈₀₈ (1983) pp. 103–116.
- ₂₈₁₀ [10] DONUT collaboration, *Observation of tau neutrino interactions*, *Phys. Lett. B* **504**
₂₈₁₁ (2001) pp. 218–224 [[hep-ex/0012035](#)].

- 2812 [11] F. Englert and R. Brout, *Broken Symmetry and the Mass of Gauge Vector Mesons*,
2813 *Phys. Rev. Lett.* **13** (1964) pp. 321–323.
- 2814 [12] P. W. Higgs, *Broken Symmetries and the Masses of Gauge Bosons*, *Phys. Rev. Lett.*
2815 **13** (1964) pp. 508–509.
- 2816 [13] G. S. Guralnik, C. R. Hagen and T. W. B. Kibble, *Global Conservation Laws and*
2817 *Massless Particles*, *Phys. Rev. Lett.* **13** (1964) pp. 585–587.
- 2818 [14] ATLAS Collaboration, *Observation of a new particle in the search for the Standard*
2819 *Model Higgs boson with the ATLAS detector at the LHC*, *Phys. Lett. B* **716** (2012)
2820 p. 1 [[1207.7214](#)].
- 2821 [15] CMS Collaboration, *Observation of a new boson at a mass of 125 GeV with the CMS*
2822 *experiment at the LHC*, *Phys. Lett. B* **716** (2012) p. 30 [[1207.7235](#)].
- 2823 [16] Particle Data Group collaboration, *Review of Particle Physics*, *PTEP* **2022** (2022)
2824 p. 083C01.
- 2825 [17] C. N. Yang and R. L. Mills, *Conservation of isotopic spin and isotopic gauge*
2826 *invariance*, *Phys. Rev.* **96** (1954) pp. 191–195.
- 2827 [18] S. L. Glashow, *Partial Symmetries of Weak Interactions*, *Nucl. Phys.* **22** (1961)
2828 pp. 579–588.
- 2829 [19] S. Weinberg, *A Model of Leptons*, *Phys. Rev. Lett.* **19** (1967) pp. 1264–1266.
- 2830 [20] A. Salam, *Weak and Electromagnetic Interactions*, *Proceedings of the 8th Nobel*
2831 *symposium*, Ed. N. Svartholm, Almqvist & Wiksell, 1968, **Conf. Proc. C680519**
2832 (1968) pp. 367–377.
- 2833 [21] T. D. Lee and C. N. Yang, *Question of parity conservation in weak interactions*,
2834 *Phys. Rev.* **104** (1956) pp. 254–258.
- 2835 [22] C. S. Wu, E. Ambler, R. W. Hayward, D. D. Hopper and R. P. Hudson, *Experimental*
2836 *test of parity conservation in beta decay*, *Phys. Rev.* **105** (1957) pp. 1413–1415.
- 2837 [23] R. L. Garwin, L. M. Lederman and M. Weinrich, *Observations of the failure of*
2838 *conservation of parity and charge conjugation in meson decays: the magnetic moment*
2839 *of the free muon*, *Phys. Rev.* **105** (1957) pp. 1415–1417.
- 2840 [24] Y. Nambu, *Quasi-particles and gauge invariance in the theory of superconductivity*,
2841 *Phys. Rev.* **117** (1960) pp. 648–663.

- 2842 [25] J. Goldstone, *Field theories with « superconductor » solutions*, *Il Nuovo Cimento*
2843 (1955-1965) **19** (1961) pp. 154–164.
- 2844 [26] LHC Higgs Cross Section Working Group collaboration, *Handbook of LHC Higgs*
2845 *Cross Sections: 4. Deciphering the Nature of the Higgs Sector*, [1610.07922](#).
- 2846 [27] ATLAS Collaboration, *Observation of $H \rightarrow b\bar{b}$ decays and VH production with the*
2847 *ATLAS detector*, [ATLAS-CONF-2018-036](#) (2018).
- 2848 [28] CMS Collaboration, *Observation of Higgs Boson Decay to Bottom Quarks*, *Phys.*
2849 *Rev. Lett.* **121** (2018) p. 121801 [[1808.08242](#)].
- 2850 [29] L. Evans and P. Bryant, *LHC Machine*, *JINST* **3** (2008) p. S08001.
- 2851 [30] The ALICE Collaboration, *The ALICE experiment at the CERN LHC*, *Journal of*
2852 *Instrumentation* **3** (2008) pp. S08002–S08002.
- 2853 [31] CMS Collaboration, *The CMS experiment at the CERN LHC*, *JINST* **3** (2008)
2854 p. S08004.
- 2855 [32] The LHCb Collaboration, *The LHCb detector at the LHC*, *Journal of*
2856 *Instrumentation* **3** (2008) pp. S08005–S08005.
- 2857 [33] ATLAS Collaboration, *The ATLAS Experiment at the CERN Large Hadron Collider*,
2858 *JINST* **3** (2008) p. S08003.
- 2859 [34] ATLAS Collaboration, *Integrated luminosity summary plots for 2011-2012 data*
2860 *taking*, (2022). <https://twiki.cern.ch/twiki/bin/view/AtlasPublic/LuminosityPublicResults>.
- 2861 [35] ATLAS Collaboration, *Public ATLAS Luminosity Results for Run-2 of the LHC*,
2862 (2022). <https://twiki.cern.ch/twiki/bin/view/AtlasPublic/LuminosityPublicResultsRun2>.
- 2863 [36] CERN, “The accelerator complex.” (2012).
- 2864 [37] G. C. Strong, *On the impact of selected modern deep-learning techniques to the*
2865 *performance and celerity of classification models in an experimental high-energy*
2866 *physics use case*, [2002.01427](#).
- 2867 [38] ATLAS Collaboration, *Atlas track reconstruction – general overview*, (2022).
2868 <https://atlassoftwaredocs.web.cern.ch/trackingTutorial/idoverview/>.
- 2869 [39] ATLAS Collaboration, *Performance of b-jet identification in the ATLAS experiment*,

- 2872 *JINST* **11** (2016) p. P04008 [[1512.01094](#)].
- 2873 [40] ATLAS Collaboration, *Luminosity determination in pp collisions at $\sqrt{s} = 13 \text{ TeV}$ using the ATLAS detector at the LHC*, **ATLAS-CONF-2019-021** (2019).
- 2875 [41] ATLAS Collaboration, *ATLAS Detector and Physics Performance: Technical Design Report, Volume 1*, .
- 2877 [42] for the ATLAS Collaboration collaboration, *Status of the ATLAS Experiment*, Tech. Rep., Geneva (2010). 10.3204/DESY-PROC-2010-04/1.
- 2879 [43] ATLAS Collaboration, *ATLAS Inner Tracker Pixel Detector: Technical Design Report*, ATLAS-TDR-030; CERN-LHCC-2017-021 (2017).
- 2881 [44] ATLAS Collaboration, *ATLAS Inner Tracker Strip Detector: Technical Design Report*, ATLAS-TDR-025; CERN-LHCC-2017-005 (2017).
- 2883 [45] ATLAS Collaboration, *The inner detector*, (2022).
<https://atlas.cern/Discover/Detector/Inner-Detector>.
- 2885 [46] ATLAS Collaboration, *ATLAS Insertable B-Layer: Technical Design Report*, ATLAS-TDR-19; CERN-LHCC-2010-013 (2010).
- 2887 [47] B. Abbott et al., *Production and integration of the ATLAS Insertable B-Layer*, *JINST* **13** (2018) p. T05008 [[1803.00844](#)].
- 2889 [48] ATLAS Collaboration, *Operation and performance of the ATLAS semiconductor tracker*, *JINST* **9** (2014) p. P08009 [[1404.7473](#)].
- 2891 [49] ATLAS Collaboration, *Calorimeter*, (2022).
<https://atlas.cern/Discover/Detector/Calorimeter>.
- 2893 [50] ATLAS Collaboration, *ATLAS Tile Calorimeter: Technical Design Report*, .
- 2894 [51] G. Artoni, *Muon momentum scale and resolution in pp collisions at $\sqrt{s} = 8 \text{ TeV}$ in ATLAS*, Tech. Rep., Geneva (2016). 10.1016/j.nuclphysbps.2015.09.453.
- 2896 [52] ATLAS Collaboration, *Muon spectrometer*, (2022).
<https://atlas.cern/Discover/Detector/Muon-Spectrometer>.
- 2898 [53] ATLAS Collaboration, *Performance of the ATLAS trigger system in 2015*, *Eur. Phys. J. C* **77** (2017) p. 317 [[1611.09661](#)].
- 2900 [54] ATLAS Collaboration, *The ATLAS Collaboration Software and Firmware*, **ATL-SOFT-PUB-2021-001** (2021).

- 2902 [55] T. Cornelissen, M. Elsing, S. Fleischmann, W. Liebig and E. Moyse, *Concepts,*
2903 *Design and Implementation of the ATLAS New Tracking (NEWT)*, .
- 2904 [56] ATLAS Collaboration, *The Optimization of ATLAS Track Reconstruction in Dense*
2905 *Environments*, **ATL-PHYS-PUB-2015-006** (2015).
- 2906 [57] ATLAS Collaboration, *Performance of the ATLAS track reconstruction algorithms in*
2907 *dense environments in LHC Run 2*, *Eur. Phys. J. C* **77** (2017) p. 673 [[1704.07983](#)].
- 2908 [58] ATLAS Collaboration, *A neural network clustering algorithm for the ATLAS silicon*
2909 *pixel detector*, *JINST* **9** (2014) p. P09009 [[1406.7690](#)].
- 2910 [59] R. Jansky, *Truth Seeded Reconstruction for Fast Simulation in the ATLAS*
2911 *Experiment*, .
- 2912 [60] ATLAS Collaboration, *Reconstruction of primary vertices at the ATLAS experiment*
2913 *in Run 1 proton–proton collisions at the LHC*, *Eur. Phys. J. C* **77** (2017) p. 332
2914 [[1611.10235](#)].
- 2915 [61] ATLAS Collaboration, *ATLAS b-jet identification performance and efficiency*
2916 *measurement with $t\bar{t}$ events in pp collisions at $\sqrt{s} = 13$ TeV*, *Eur. Phys. J. C* **79**
2917 (2019) p. 970 [[1907.05120](#)].
- 2918 [62] M. Cacciari, G. P. Salam and G. Soyez, *The anti- k_t jet clustering algorithm*, *JHEP*
2919 **04** (2008) p. 063 [[0802.1189](#)].
- 2920 [63] M. Cacciari, G. P. Salam and G. Soyez, *Fastjet user manual*, *Eur.Phys.J. C* **72** (2012)
2921 p. 1896 [[1111.6097](#)].
- 2922 [64] M. Cacciari, G. P. Salam and G. Soyez, *The Catchment Area of Jets*, *JHEP* **04**
2923 (2008) p. 005 [[0802.1188](#)].
- 2924 [65] ATLAS Collaboration, *Tagging and suppression of pileup jets with the ATLAS*
2925 *detector*, **ATLAS-CONF-2014-018** (2014).
- 2926 [66] ATLAS Collaboration, *Topological cell clustering in the ATLAS calorimeters and its*
2927 *performance in LHC Run 1*, *Eur. Phys. J. C* **77** (2017) p. 490 [[1603.02934](#)].
- 2928 [67] ATLAS Collaboration, *Jet reconstruction and performance using particle flow with*
2929 *the ATLAS Detector*, *Eur. Phys. J. C* **77** (2017) p. 466 [[1703.10485](#)].
- 2930 [68] ATLAS Collaboration, *Jet energy scale measurements and their systematic*
2931 *uncertainties in proton–proton collisions at $\sqrt{s} = 13$ TeV with the ATLAS detector*,
2932 *Phys. Rev. D* **96** (2017) p. 072002 [[1703.09665](#)].

- 2933 [69] J. M. Butterworth, A. R. Davison, M. Rubin and G. P. Salam, *Jet Substructure as a*
2934 *New Higgs Search Channel at the Large Hadron Collider*, *Phys. Rev. Lett.* **100** (2008)
2935 p. 242001 [[0802.2470](#)].
- 2936 [70] ATLAS collaboration, *Measurement of the associated production of a Higgs boson*
2937 *decaying into b-quarks with a vector boson at high transverse momentum in pp*
2938 *collisions at $\sqrt{s} = 13$ TeV with the ATLAS detector*, *Phys. Lett. B* **816** (2021)
2939 p. 136204 [[2008.02508](#)].
- 2940 [71] ATLAS collaboration, *Performance of jet substructure techniques for large-R jets in*
2941 *proton-proton collisions at $\sqrt{s} = 7$ TeV using the ATLAS detector*, *JHEP* **09** (2013)
2942 p. 076 [[1306.4945](#)].
- 2943 [72] ATLAS Collaboration, *In situ calibration of large-radius jet energy and mass in*
2944 *13 TeV proton–proton collisions with the ATLAS detector*, *Eur. Phys. J. C* **79** (2019)
2945 p. 135 [[1807.09477](#)].
- 2946 [73] D. Krohn, J. Thaler and L.-T. Wang, *Jets with Variable R*, *JHEP* **06** (2009) p. 059
2947 [[0903.0392](#)].
- 2948 [74] ATLAS Collaboration, *Variable Radius, Exclusive- k_T , and Center-of-Mass Subjet*
2949 *Reconstruction for $H \rightarrow b\bar{b}$ Tagging in ATLAS*, ATL-PHYS-PUB-2017-010
2950 (2017).
- 2951 [75] ATLAS Collaboration, *Improved electron reconstruction in ATLAS using the*
2952 *Gaussian Sum Filter-based model for bremsstrahlung*, ATLAS-CONF-2012-047 (2012).
- 2953 [76] ATLAS Collaboration, *Electron efficiency measurements with the ATLAS detector*
2954 *using the 2015 LHC proton–proton collision data*, ATLAS-CONF-2016-024 (2016).
- 2955 [77] ATLAS Collaboration, *Muon reconstruction performance of the ATLAS detector in*
2956 *proton–proton collision data at $\sqrt{s} = 13$ TeV*, *Eur. Phys. J. C* **76** (2016) p. 292
2957 [[1603.05598](#)].
- 2958 [78] ATLAS Collaboration, *Performance of missing transverse momentum reconstruction*
2959 *with the ATLAS detector using proton–proton collisions at $\sqrt{s} = 13$ TeV*, *Eur. Phys.*
2960 *J. C* **78** (2018) p. 903 [[1802.08168](#)].
- 2961 [79] ATLAS Collaboration, *Observation of $H \rightarrow b\bar{b}$ decays and VH production with the*
2962 *ATLAS detector*, *Phys. Lett. B* **786** (2018) p. 59 [[1808.08238](#)].
- 2963 [80] ATLAS Collaboration, *Observation of Higgs boson production in association with a*
2964 *top quark pair at the LHC with the ATLAS detector*, *Phys. Lett. B* **784** (2018) p. 173

- 2965 [1806.00425].
- 2966 [81] ATLAS Collaboration, *Search for new resonances in mass distributions of jet pairs*
2967 *using 139fb^{-1} of pp collisions at $\sqrt{s} = 13\text{ TeV}$ with the ATLAS detector*, *JHEP* **03**
2968 (2020) p. 145 [1910.08447].
- 2969 [82] ATLAS Collaboration, *Optimisation and performance studies of the ATLAS*
2970 *b-tagging algorithms for the 2017-18 LHC run*, *ATL-PHYS-PUB-2017-013* (2017).
- 2971 [83] ATLAS Collaboration, *Secondary vertex finding for jet flavour identification with the*
2972 *ATLAS detector*, *ATL-PHYS-PUB-2017-011* (2017).
- 2973 [84] ATLAS Collaboration, *Identification of Jets Containing b-Hadrons with Recurrent*
2974 *Neural Networks at the ATLAS Experiment*, *ATL-PHYS-PUB-2017-003* (2017).
- 2975 [85] ATLAS Collaboration, *Deep Sets based Neural Networks for Impact Parameter*
2976 *Flavour Tagging in ATLAS*, *ATL-PHYS-PUB-2020-014* (2020).
- 2977 [86] ATLAS Collaboration, *Expected performance of the ATLAS b-tagging algorithms in*
2978 *Run-2*, *ATL-PHYS-PUB-2015-022* (2015).
- 2979 [87] ATLAS collaboration, *ATLAS flavour-tagging algorithms for the LHC Run 2 pp*
2980 *collision dataset*, [2211.16345](#).
- 2981 [88] B. R. Webber, *Fragmentation and hadronization*, *Int. J. Mod. Phys. A* **15S1** (2000)
2982 pp. 577–606 [[hep-ph/9912292](#)].
- 2983 [89] Particle Data Group collaboration, *Review of particle physics*, *Phys. Rev. D* **98**
2984 (2018) p. 030001.
- 2985 [90] ATLAS Collaboration, *Comparison of Monte Carlo generator predictions for bottom*
2986 *and charm hadrons in the decays of top quarks and the fragmentation of high p_T jets*,
2987 *ATL-PHYS-PUB-2014-008* (2014).
- 2988 [91] Nazar Bartosik, *Diagram showing the common principle of identification of jets*
2989 *initiated by b-hadron decays*, (2022).
2990 https://en.m.wikipedia.org/wiki/File:B-tagging_diagram.png.
- 2991 [92] ATLAS Collaboration, *Tracking efficiency studies in dense environments*, (2022).
2992 <https://atlas.web.cern.ch/Atlas/GROUPS/PHYSICS/PLOTS/IDTR-2022-03/>.
- 2993 [93] S. Adorni Braccesi Chiassi, *Vector Boson Tagging in the Context of the Search for*
2994 *New Physics in the Fully Hadronic Final State*, Ph.D. thesis, Geneva U., 2021.
2995 10.13097/archive-ouverte/unige:158558.

- 2996 [94] E. Boos, M. Dobbs, W. Giele, I. Hinchliffe, J. Huston, V. Iljin et al., *Generic User*
2997 *Process Interface for Event Generators*, ArXiv High Energy Physics - Phenomenology
2998 *e-prints* (2001) .
- 2999 [95] J. Alwall, A. Ballestrero, P. Bartalini, S. Belov, E. Boos, A. Buckley et al., *A*
3000 *standard format for Les Houches Event Files*, Computer Physics Communications
3001 **176** (2007) pp. 300–304.
- 3002 [96] K. Hornik, M. Stinchcombe and H. White, *Multilayer feedforward networks are*
3003 *universal approximators*, Neural Networks **2** (1989) pp. 359–366.
- 3004 [97] D. E. Rumelhart, G. E. Hinton and R. J. Williams, *Learning representations by*
3005 *back-propagating errors*, nature **323** (1986) pp. 533–536.
- 3006 [98] W. McCulloch and W. Pitts, *A logical calculus of the ideas immanent in nervous*
3007 *activity*, The bulletin of mathematical biophysics **5** (1943) pp. 115–133.
- 3008 [99] J. Hopfield, *Neural networks and physical systems with emergent collective*
3009 *computational abilities*, in *Spin Glass Theory and Beyond: An Introduction to the*
3010 *Replica Method and Its Applications*, pp. 411–415, World Scientific, (1987).
- 3011 [100] A. F. Agarap, *Deep Learning using Rectified Linear Units (ReLU)*, arXiv e-prints
3012 (2018) p. arXiv:1803.08375 [[1803.08375](#)].
- 3013 [101] S. Elfwing, E. Uchibe and K. Doya, *Sigmoid-Weighted Linear Units for Neural*
3014 *Network Function Approximation in Reinforcement Learning*, arXiv e-prints (2017)
3015 p. arXiv:1702.03118 [[1702.03118](#)].
- 3016 [102] Y. A. LeCun, L. Bottou, G. B. Orr and K.-R. Müller, *Efficient backprop*, in *Neural*
3017 *networks: Tricks of the trade*, pp. 9–48, Springer, (2012).
- 3018 [103] D. P. Kingma and J. Ba, *Adam: A Method for Stochastic Optimization*, arXiv
3019 e-prints (2014) p. arXiv:1412.6980 [[1412.6980](#)].
- 3020 [104] P. Nason, *A new method for combining nlo qcd with shower monte carlo algorithms*,
3021 *Journal of High Energy Physics* **2004** (2004) p. 040–040.
- 3022 [105] S. Frixione, G. Ridolfi and P. Nason, *A positive-weight next-to-leading-order monte*
3023 *carlo for heavy flavour hadroproduction*, *Journal of High Energy Physics* **2007** (2007)
3024 p. 126–126.
- 3025 [106] S. Frixione, P. Nason and C. Oleari, *Matching nlo qcd computations with parton*
3026 *shower simulations: the powheg method*, *Journal of High Energy Physics* **2007** (2007)

- 3027 p. 070–070.
- 3028 [107] S. Alioli, P. Nason, C. Oleari and E. Re, *A general framework for implementing nlo*
3029 *calculations in shower monte carlo programs: the powheg box*, *Journal of High Energy*
3030 *Physics* **2010** (2010) .
- 3031 [108] NNPDF collaboration, *Parton distributions for the LHC run II*, *JHEP* **04** (2015)
3032 p. 040 [[1410.8849](#)].
- 3033 [109] ATLAS Collaboration, *Studies on top-quark Monte Carlo modelling for Top2016*,
3034 *ATL-PHYS-PUB-2016-020* (2016).
- 3035 [110] T. Sjöstrand, S. Ask, J. R. Christiansen, R. Corke, N. Desai, P. Ilten et al., *An*
3036 *introduction to PYTHIA 8.2*, *Comput. Phys. Commun.* **191** (2015) p. 159
3037 [[1410.3012](#)].
- 3038 [111] ATLAS Collaboration, *ATLAS Pythia 8 tunes to 7 TeV data*,
3039 *ATL-PHYS-PUB-2014-021* (2014).
- 3040 [112] R. D. Ball et al., *Parton distributions with LHC data*, *Nucl. Phys. B* **867** (2013)
3041 p. 244 [[1207.1303](#)].
- 3042 [113] D. J. Lange, *The EvtGen particle decay simulation package*, *Nucl. Instrum. Meth. A*
3043 **462** (2001) p. 152.
- 3044 [114] ATLAS Collaboration, *The ATLAS Simulation Infrastructure*, *Eur. Phys. J. C* **70**
3045 (2010) p. 823 [[1005.4568](#)].
- 3046 [115] GEANT4 Collaboration, S. Agostinelli et al., *GEANT4 – a simulation toolkit*, *Nucl.*
3047 *Instrum. Meth. A* **506** (2003) p. 250.
- 3048 [116] H. Serviansky, N. Segol, J. Shlomi, K. Cranmer, E. Gross, H. Maron et al.,
3049 *Set2Graph: Learning Graphs From Sets*, *arXiv e-prints* (2020) p. arXiv:2002.08772
3050 [[2002.08772](#)].
- 3051 [117] P. W. Battaglia, J. B. Hamrick, V. Bapst, A. Sanchez-Gonzalez, V. Zambaldi,
3052 M. Malinowski et al., *Relational inductive biases, deep learning, and graph networks*,
3053 *arXiv e-prints* (2018) p. arXiv:1806.01261 [[1806.01261](#)].
- 3054 [118] M. Zaheer, S. Kottur, S. Ravanbakhsh, B. Poczos, R. Salakhutdinov and A. Smola,
3055 *Deep Sets*, *arXiv e-prints* (2017) p. arXiv:1703.06114 [[1703.06114](#)].
- 3056 [119] ATLAS Collaboration, *Muon reconstruction performance in early $\sqrt{s} = 13$ TeV data*,
3057 *ATL-PHYS-PUB-2015-037* (2015).

- 3058 [120] ATLAS Collaboration, *Electron reconstruction and identification in the ATLAS*
3059 *experiment using the 2015 and 2016 LHC proton–proton collision data at*
3060 $\sqrt{s} = 13\text{ TeV}$, *Eur. Phys. J. C* **79** (2019) p. 639 [[1902.04655](#)].
- 3061 [121] D. Hwang, J. Park, S. Kwon, K.-M. Kim, J.-W. Ha and H. J. Kim, *Self-supervised*
3062 *Auxiliary Learning with Meta-paths for Heterogeneous Graphs*, arXiv e-prints (2020)
3063 p. arXiv:2007.08294 [[2007.08294](#)].
- 3064 [122] S. Brody, U. Alon and E. Yahav, *How Attentive are Graph Attention Networks?*,
3065 arXiv e-prints (2021) p. arXiv:2105.14491 [[2105.14491](#)].
- 3066 [123] A. Vaswani, N. Shazeer, N. Parmar, J. Uszkoreit, L. Jones, A. N. Gomez et al.,
3067 *Attention Is All You Need*, arXiv e-prints (2017) p. arXiv:1706.03762 [[1706.03762](#)].
- 3068 [124] D. P. Kingma and J. Ba, *Adam: A Method for Stochastic Optimization*, arXiv
3069 e-prints (2014) p. arXiv:1412.6980 [[1412.6980](#)].
- 3070 [125] J. Bai, F. Lu, K. Zhang et al., *ONNX: Open neural network exchange*, (2019).
3071 <https://github.com/onnx/onnx>.
- 3072 [126] ATLAS Collaboration, *Performance of Run 3 HLT b-tagging with fast tracking,*
3073 *Public b-Jet Trigger Plots for Collision Data*, (2022).
3074 [https://twiki.cern.ch/twiki/bin/view/AtlasPublic/
3075 BJetTriggerPublicResults#Performance_of_Run_3_HLT_b_taggi](https://twiki.cern.ch/twiki/bin/view/AtlasPublic/BJetTriggerPublicResults#Performance_of_Run_3_HLT_b_taggi).
- 3076 [127] ATLAS Collaboration, *Neural Network Jet Flavour Tagging with the Upgraded*
3077 *ATLAS Inner Tracker Detector at the High-Luminosity LHC*,
3078 **ATL-PHYS-PUB-2022-047** (2022).
- 3079 [128] ATLAS Collaboration, *Jet flavour tagging with gn1 and dl1d. generator dependence,*
3080 *run 2 and run 3 data agreement studies*, (2023).
3081 <https://atlas.web.cern.ch/Atlas/GROUPS/PHYSICS/PLLOTS/FTAG-2023-01/>.
- 3082 [129] R. Lafaye, T. Plehn, M. Rauch, D. Zerwas and M. Duhrssen, *Measuring the Higgs*
3083 *Sector*, *JHEP* **08** (2009) p. 009 [[0904.3866](#)].
- 3084 [130] ATLAS Collaboration, *Measurements of WH and ZH production in the $H \rightarrow b\bar{b}$*
3085 *decay channel in pp collisions at 13 TeV with the ATLAS detector*, *Eur. Phys. J. C*
3086 **81** (2021) p. 178 [[2007.02873](#)].
- 3087 [131] ATLAS Collaboration, *Measurement of the associated production of a Higgs boson*
3088 *decaying into b-quarks with a vector boson at high transverse momentum in pp*
3089 *collisions at $\sqrt{s} = 13\text{ TeV}$ with the ATLAS detector*, *Phys. Lett. B* **816** (2021)

- 3090 p. 136204 [[2008.02508](#)].
- 3091 [132] K. Mimasu, V. Sanz and C. Williams, *Higher order QCD predictions for associated*
3092 *Higgs production with anomalous couplings to gauge bosons*, *JHEP* **08** (2016) p. 039
3093 [[1512.02572](#)].
- 3094 [133] ATLAS Collaboration, *Performance of jet substructure techniques for large- R jets in*
3095 *proton–proton collisions at $\sqrt{s} = 7$ TeV using the ATLAS detector*, *JHEP* **09** (2013)
3096 p. 076 [[1306.4945](#)].
- 3097 [134] S. Alioli, P. Nason, C. Oleari and E. Re, *A general framework for implementing NLO*
3098 *calculations in shower Monte Carlo programs: the POWHEG BOX*, *JHEP* **06** (2010)
3099 p. 043 [[1002.2581](#)].
- 3100 [135] ATLAS collaboration, *Measurement of the Z/γ^* boson transverse momentum*
3101 *distribution in pp collisions at $\sqrt{s} = 7$ TeV with the ATLAS detector*, *JHEP* **09**
3102 (2014) p. 145 [[1406.3660](#)].
- 3103 [136] G. Cullen, N. Greiner, G. Heinrich, G. Luisoni, P. Mastrolia, G. Ossola et al.,
3104 *Automated one-loop calculations with GoSam*, *Eur. Phys. J. C* **72** (2012) p. 1889
3105 [[1111.2034](#)].
- 3106 [137] K. Hamilton, P. Nason and G. Zanderighi, *MINLO: multi-scale improved NLO*,
3107 *JHEP* **10** (2012) p. 155 [[1206.3572](#)].
- 3108 [138] G. Luisoni, P. Nason, C. Oleari and F. Tramontano, *$HW^\pm/HZ + 0$ and 1 jet at*
3109 *NLO with the POWHEG BOX interfaced to GoSam and their merging within*
3110 *MiNLO*, *JHEP* **10** (2013) p. 083 [[1306.2542](#)].
- 3111 [139] M. L. Ciccolini, S. Dittmaier and M. Krämer, *Electroweak radiative corrections to*
3112 *associated WH and ZH production at hadron colliders*, *Phys. Rev. D* **68** (2003)
3113 p. 073003 [[hep-ph/0306234](#)].
- 3114 [140] O. Brein, A. Djouadi and R. Harlander, *NNLO QCD corrections to the*
3115 *Higgs-strahlung processes at hadron colliders*, *Phys. Lett. B* **579** (2004) pp. 149–156
3116 [[hep-ph/0307206](#)].
- 3117 [141] G. Ferrera, M. Grazzini and F. Tramontano, *Associated Higgs-W-Boson Production*
3118 *at Hadron Colliders: a Fully Exclusive QCD Calculation at NNLO*, *Phys. Rev. Lett.*
3119 **107** (2011) p. 152003 [[1107.1164](#)].
- 3120 [142] O. Brein, R. V. Harlander, M. Wiesemann and T. Zirke, *Top-quark mediated effects*
3121 *in hadronic Higgs-Strahlung*, *Eur. Phys. J. C* **72** (2012) p. 1868 [[1111.0761](#)].

- 3122 [143] G. Ferrera, M. Grazzini and F. Tramontano, *Higher-order QCD effects for associated*
3123 *WH production and decay at the LHC*, *JHEP* **04** (2014) p. 039 [[1312.1669](#)].
- 3124 [144] G. Ferrera, M. Grazzini and F. Tramontano, *Associated ZH production at hadron*
3125 *colliders: The fully differential NNLO QCD calculation*, *Phys. Lett. B* **740** (2015)
3126 pp. 51–55 [[1407.4747](#)].
- 3127 [145] J. M. Campbell, R. K. Ellis and C. Williams, *Associated production of a Higgs boson*
3128 *at NNLO*, *JHEP* **06** (2016) p. 179 [[1601.00658](#)].
- 3129 [146] L. Altenkamp, S. Dittmaier, R. V. Harlander, H. Rzehak and T. J. E. Zirke,
3130 *Gluon-induced Higgs-strahlung at next-to-leading order QCD*, *JHEP* **02** (2013) p. 078
3131 [[1211.5015](#)].
- 3132 [147] B. Hespel, F. Maltoni and E. Vryonidou, *Higgs and Z boson associated production via*
3133 *gluon fusion in the SM and the 2HDM*, *JHEP* **06** (2015) p. 065 [[1503.01656](#)].
- 3134 [148] R. V. Harlander, A. Kulesza, V. Theeuwes and T. Zirke, *Soft gluon resummation for*
3135 *gluon-induced Higgs Strahlung*, *JHEP* **11** (2014) p. 082 [[1410.0217](#)].
- 3136 [149] R. V. Harlander, S. Liebler and T. Zirke, *Higgs Strahlung at the Large Hadron*
3137 *Collider in the 2-Higgs-doublet model*, *JHEP* **02** (2014) p. 023 [[1307.8122](#)].
- 3138 [150] O. Brein, R. V. Harlander and T. J. E. Zirke, *vh@nnlo – Higgs Strahlung at hadron*
3139 *colliders*, *Comput. Phys. Commun.* **184** (2013) pp. 998–1003 [[1210.5347](#)].
- 3140 [151] S. Frixione, G. Ridolfi and P. Nason, *A positive-weight next-to-leading-order Monte*
3141 *Carlo for heavy flavour hadroproduction*, *JHEP* **09** (2007) p. 126 [[0707.3088](#)].
- 3142 [152] M. Czakon and A. Mitov, *Top++: A program for the calculation of the top-pair*
3143 *cross-section at hadron colliders*, *Comput. Phys. Commun.* **185** (2014) p. 2930
3144 [[1112.5675](#)].
- 3145 [153] S. Alioli, P. Nason, C. Oleari and E. Re, *NLO single-top production matched with*
3146 *shower in POWHEG: s- and t-channel contributions*, *JHEP* **09** (2009) p. 111
3147 [[0907.4076](#)].
- 3148 [154] N. Kidonakis, *Next-to-next-to-leading logarithm resummation for s-channel single top*
3149 *quark production*, *Phys. Rev. D* **81** (2010) p. 054028 [[1001.5034](#)].
- 3150 [155] N. Kidonakis, *Next-to-next-to-leading-order collinear and soft gluon corrections for*
3151 *t-channel single top quark production*, *Phys. Rev. D* **83** (2011) p. 091503 [[1103.2792](#)].
- 3152 [156] E. Re, *Single-top Wt-channel production matched with parton showers using the*

- 3153 *POWHEG method*, *Eur. Phys. J. C* **71** (2011) p. 1547 [[1009.2450](#)].
- 3154 [157] N. Kidonakis, *Two-loop soft anomalous dimensions for single top quark associated production with a W^- or H^-* , *Phys. Rev. D* **82** (2010) p. 054018 [[1005.4451](#)].
- 3155
- 3156 [158] T. Gleisberg, S. Höche, F. Krauss, M. Schönherr, S. Schumann, F. Siegert et al., *Event generation with SHERPA 1.1*, *JHEP* **02** (2009) p. 007 [[0811.4622](#)].
- 3157
- 3158 [159] E. Bothmann et al., *Event generation with Sherpa 2.2*, *SciPost Phys.* **7** (2019) p. 034 [[1905.09127](#)].
- 3159
- 3160 [160] F. Cascioli, P. Maierhöfer and S. Pozzorini, *Scattering Amplitudes with Open Loops*, *Phys. Rev. Lett.* **108** (2012) p. 111601 [[1111.5206](#)].
- 3161
- 3162 [161] T. Gleisberg and S. Höche, *Comix, a new matrix element generator*, *JHEP* **12** (2008) p. 039 [[0808.3674](#)].
- 3163
- 3164 [162] S. Schumann and F. Krauss, *A parton shower algorithm based on Catani–Seymour dipole factorisation*, *JHEP* **03** (2008) p. 038 [[0709.1027](#)].
- 3165
- 3166 [163] S. Höche, F. Krauss, M. Schönherr and F. Siegert, *QCD matrix elements + parton showers. The NLO case*, *JHEP* **04** (2013) p. 027 [[1207.5030](#)].
- 3167
- 3168 [164] S. Catani, L. Cieri, G. Ferrera, D. de Florian and M. Grazzini, *Vector Boson Production at Hadron Colliders: a Fully Exclusive QCD Calculation at NNLO*, *Phys. Rev. Lett.* **103** (2009) p. 082001 [[0903.2120](#)].
- 3169
- 3170
- 3171 [165] J. Butterworth et al., *PDF4LHC recommendations for LHC Run II*, *J. Phys. G* **43** (2016) p. 023001 [[1510.03865](#)].
- 3172
- 3173 [166] A. Denner, S. Dittmaier, S. Kallweit and A. Mück, *Electroweak corrections to Higgs-strahlung off W/Z bosons at the Tevatron and the LHC with Hawk*, *JHEP* **03** (2012) p. 075 [[1112.5142](#)].
- 3174
- 3175
- 3176 [167] A. Denner, S. Dittmaier, S. Kallweit and A. Mück, *HAWK 2.0: A Monte Carlo program for Higgs production in vector-boson fusion and Higgs strahlung at hadron colliders*, *Comput. Phys. Commun.* **195** (2015) pp. 161–171 [[1412.5390](#)].
- 3177
- 3178
- 3179 [168] ATLAS Collaboration, *Measurements of b -jet tagging efficiency with the ATLAS detector using $t\bar{t}$ events at $\sqrt{s} = 13$ TeV*, *JHEP* **08** (2018) p. 089 [[1805.01845](#)].
- 3180
- 3181 [169] ATLAS Collaboration, *Calibration of light-flavour b -jet mistagging rates using ATLAS proton–proton collision data at $\sqrt{s} = 13$ TeV*, *ATLAS-CONF-2018-006* (2018).
- 3182
- 3183

- 3184 [170] ATLAS Collaboration, *Measurement of b -tagging efficiency of c -jets in $t\bar{t}$ events using*
- 3185 a likelihood approach with the ATLAS detector, **ATLAS-CONF-2018-001** (2018).
- 3186 [171] ATLAS Collaboration, *Flavor Tagging with Track-Jets in Boosted Topologies with the*
- 3187 *ATLAS Detector*, **ATL-PHYS-PUB-2014-013** (2014).
- 3188 [172] ATLAS Collaboration, *Identification of boosted Higgs bosons decaying into b -quark*
- 3189 *pairs with the ATLAS detector at 13 TeV*, *Eur. Phys. J. C* **79** (2019) p. 836
- 3190 [[1906.11005](#)].
- 3191 [173] J. K. Anders and M. D'Onofrio, *V+Jets theoretical uncertainties estimation via a*
- 3192 *parameterisation method*, Tech. Rep. ATL-COM-PHYS-2016-044, Geneva (2016).
- 3193 [174] L. A. Harland-Lang, A. D. Martin, P. Motylinski and R. S. Thorne, *Parton*
- 3194 *distributions in the LHC era: MMHT 2014 PDFs*, *Eur. Phys. J. C* **75** (2015) p. 204
- 3195 [[1412.3989](#)].
- 3196 [175] S. Dulat, T.-J. Hou, J. Gao, M. Guzzi, J. Huston, P. Nadolsky et al., *New parton*
- 3197 *distribution functions from a global analysis of quantum chromodynamics*, *Phys. Rev.*
- 3198 **D93** (2016) p. 033006 [[1506.07443](#)].
- 3199 [176] ATLAS Collaboration, *Measurement of the Inelastic Proton–Proton Cross Section at*
- 3200 *$\sqrt{s} = 13$ TeV with the ATLAS Detector at the LHC*, *Phys. Rev. Lett.* **117** (2016)
- 3201 p. 182002 [[1606.02625](#)].
- 3202 [177] ATLAS Collaboration, *Search for the Standard Model Higgs boson produced in*
- 3203 *association with a vector boson and decaying to a pair of b -quarks using large- R jets*,
- 3204 **ATL-COM-PHYS-2019-1125** (2019).
- 3205 [178] J. Pumplin et al., *New generation of parton distributions with uncertainties from*
- 3206 *global qcd analysis*, *JHEP* **07** (2002) p. 012 [[0201195](#)].
- 3207 [179] S. Frixione, E. Laenen, P. Motylinski, C. White and B. R. Webber, *Single-top*
- 3208 *hadroproduction in association with a W boson*, *JHEP* **07** (2008) p. 029 [[0805.3067](#)].
- 3209 [180] ATLAS Collaboration, *Measurement of VH , $H \rightarrow b\bar{b}$ production as a function of the*
- 3210 *vector-boson transverse momentum in 13 TeV pp collisions with the ATLAS detector*,
- 3211 *JHEP* **05** (2019) p. 141 [[1903.04618](#)].
- 3212 [181] ATLAS Collaboration, *Evidence for the $H \rightarrow b\bar{b}$ decay with the ATLAS detector*,
- 3213 *JHEP* **12** (2017) p. 024 [[1708.03299](#)].
- 3214 [182] LHC Higgs Cross Section Working Group, S. Dittmaier, C. Mariotti, G. Passarino

- 3215 and R. Tanaka (Eds.), *Handbook of LHC Higgs Cross Sections: 2. Differential*
- 3216 *Distributions*, [CERN-2012-002](#) (2012) [[1201.3084](#)].
- 3217 [183] LHC Higgs Cross Section Working Group, *Handbook of LHC Higgs Cross Sections: 3.*
- 3218 *Higgs Properties*, [CERN-2013-004](#) (2013) [[1307.1347](#)].
- 3219 [184] L. Moneta, K. Belasco, K. Cranmer, S. Kreiss, A. Lazzaro, D. Piparo et al., *The*
- 3220 *roostats project*, *arXiv preprint arXiv:1009.1003* (2010) .
- 3221 [185] J. R. Andersen et al., *Les Houches 2015: Physics at TeV Colliders Standard Model*
- 3222 *Working Group Report*, in *9th Les Houches Workshop on Physics at TeV Colliders*
- 3223 (*PhysTeV 2015*) *Les Houches, France, June 1-19, 2015*, 2016, [1605.04692](#).

3224 List of figures

<small>3225</small>	2.1	The Higgs potential $V(\phi)$ of the complex scalar field singlet $\phi = \phi_1 + i\phi_2$, with a choice of $\mu^2 < 0$ leading to a continuous degeneracy in the true vacuum states. A false vacuum is present at the origin.	<small>3226</small> 21
<small>3228</small>	2.2	Higgs boson production cross sections as a function of Higgs mass (m_H) at $\sqrt{s} = 13$ TeV [26]. Uncertainties are shown in the shaded bands. At $m_H = 125$ GeV, Higgs boson production is dominated by gluon-gluon fussion, vector boson fusion, associated production with vector bosons, and top quark fusion.	<small>3229</small> 26
<small>3233</small>	2.3	Diagrams for the four main Higgs boson production modes at the LHC for a Higgs mass $m_H = 125$ GeV at a centre of mass energy $\sqrt{s} = 13$ TeV.	<small>3234</small> 26
<small>3235</small>	2.4	Higgs boson branching ratios as a function of Higgs mass (m_H) at $\sqrt{s} = 13$ TeV [26]. Uncertainties are shown in the shaded bands. At $m_H = 125$ GeV, the Higgs predominantly decays to a pair of b -quarks, around 58% of the time. The leading subdominant decay mode is to a pair of W bosons.	<small>3236</small> 27
<small>3239</small>	3.1	An overview of the CERN accelerator complex [36]. The LHC is fed by a series of accelerators starting with Linac2 (or Linac4 from 2020). Next are the Proton Synchrotron Booster, the Proton Synchrotron, and finally the Super Proton Synchrotron which injects protons into the LHC.	<small>3240</small> 30
<small>3243</small>	3.2	The coordinate system used at the ATLAS detector, showing the locations of the four main experiments located at various points around the LHC. The 3-vector momentum $\mathbf{p} = (p_x, p_y, p_z)$ is shown by the red arrow. Reproduced from Ref. [37].	<small>3244</small> 31
<small>3245</small>			<small>3246</small>

3247	3.3 The track parameterisation used at the ATLAS detector. Five coordinates $(d_0, z_0, \phi, \theta, q/p)$ are specified, defined at the track's point of closest approach to the nominal interaction point at the origin of the coordinate system. The figure shows the three-momentum \mathbf{p} and the transverse momentum p_T (defined in Eq. (3.2)). The basis vectors e_x , e_y and e_z are also shown. Reproduced from Ref. [38].	33
3253	3.4 Delivered, recorded, and usable integrated luminosity as a function of time over the course of Run 2 [35]. A total of 139 fb^{-1} of collision data is labelled as good for physics, meaning all sub-detector systems were operating nominally.	35
3257	3.5 Average pile-up profiles measured by ATLAS during Run 2 [35].	35
3258	3.6 A 3D model of the entire ATLAS detector [42]. Cutouts to the centre of the detector reveal the different subdetectors which are arranged in concentric layers around the nominal interaction point.	36
3261	3.7 A 3D model of the ATLAS ID showing the pixel, SCT and TRT subdetectors [45].	37
3263	3.8 A cross-sectional view of the ATLAS ID, with the radii of the different barrel layers shown [38].	38
3265	3.9 A schematic cross-sectional view of the ATLAS IBL [46].	39
3266	3.10 The ATLAS calorimeters [49]. The ECal uses LAr-based detectors, while the HCal uses mainly scintillating tile detectors. In the forward region the HCal also includes the LAr hadronic endcaps.	41
3269	3.11 The ATLAS muon spectrometer [52].	43
3270	3.12 Particles (left) which have enough separation will leave charge depositions which are resolved into separate clusters. Sufficiently close particles (right) can lead to merged clusters. Their combined energy deposits are recon- structed as a single merged cluster [57].	47
3274	3.13 A sketch of electron reconstruction using the ATLAS detector [76]. Electron reconstruction makes use of the entire ID and the calorimeters.	52

3276	4.1 An overview of different high and low level taggers used in ATLAS.	
3277	The low level taggers are IPxD, SV1 and JetFitter, and RNNIP and DIPS	
3278	[61, 83–85]. The outputs of these taggers are fed into the high level taggers	
3279	DL1, DL1r and DL1d [82, 87].	55
3280	4.2 The truth b -hadron decay radius L_{xy} as a function of truth transverse	
3281	momentum p_T for reconstructed b -jets in Z' events. Error bars show the	
3282	standard deviation. The pixel layers are shown in dashed horizontal lines.	57
3283	4.3 Diagram of a typical b -jet (blue) which has been produced in an event	
3284	alongside two light jets (grey) [91]. The b -hadron has travelled a significant	
3285	distance (pink dashed line) from the primary interaction point (pink dot)	
3286	before its decay. The large transverse impact parameter d_0 is a characteristic	
3287	property of the trajectories of b -hadron decay products.	58
3288	4.4 At lower p_T (left) the decay length of the b -hadron is on average reduced, and	
3289	the decay tracks are less collimated. At higher p_T (right) the b -hadron decay	
3290	length increases and the resulting decay tracks are more collimated and have	
3291	less distance over which to diverge before reaching detector elements. As a	
3292	result, the ID may be unable to resolve charged depositions from different	
3293	particles, resulting merged clusters.	59
3294	4.5 b -hadron decay track reconstruction efficiency as a function of truth b -hadron	
3295	p_T [92]. Nominal track reconstruction is shown in black, while the track	
3296	reconstruction efficiency for track candidates (i.e. the pre-ambiguity solver	
3297	efficiency) is shown in green. For high- p_T b -hadrons, the ambiguity solver	
3298	is overly aggressive in its removal of b -hadron decay tracks. Suggestions for	
3299	the improvement of the track reconstruction efficiency in this regime by the	
3300	loosening of cuts in the ambiguity solver are shown in blue and red.	60
3301	4.6 Hit multiplicities on the IBL (left) and the pixel layers (right) as a function	
3302	of the p_T of the reconstructed track for tracks in jets in a Z' sample at	
3303	$\sqrt{s} = 13$ TeV. Tracks from the weak decay of the b -hadron are shown in red,	
3304	while fragmentation tracks (which are prompt) are in blue. Baseline tracks	
3305	are those produced in the standard reconstruction described in Section 3.4.1,	
3306	while pseudotrack represent the ideal performance of the ATLAS detector	
3307	and are described in Section 3.4.1.	61

3308	4.7 The fraction of IBL (left) and B-layer (right) hits which are shared on 3309 <i>b</i> -hadron decay tracks as a function of the production radius of the <i>b</i> -hadron 3310 decay product for tracks in jets in a Z' sample at $\sqrt{s} = 13$ TeV. Pseudotacks 3311 represent the ideal performance given the ATLAS detector, see Section 3.4.1.	63
3312	4.8 The average number of good (left) and wrong (right) IBL hits as a function 3313 of <i>b</i> -hadron p_T for tracks using baseline tracking (black) and the modified 3314 version of the outlier removal procedure (red).	65
3315	4.9 (left) <i>b</i> -hadron decay track d_0 pulls ($d_0/s(d_0)$) for baseline and modified 3316 GX2F tracks. (right) The absolute value of the d_0 pull as a function of the 3317 truth <i>b</i> -hadron transverse momentum.	66
3318	5.1 A diagram displaying the logical flow of a single neuron with three inputs 3319 x_i^j . Each input is multiplied by a weight θ_j , and the resulting values are 3320 summed. A bias term θ_0 is added, and the result z is passed to an activation 3321 function. Each neuron can be thought of as a logistic regression model.	70
3322	5.2 The output of several common choices for the activation function $g(z)$ of 3323 an artificial neuron. The input z is the output of the dot product between 3324 the activation and the weights, plus a bias term.	71
3325	5.3 Rate of fake tracks as a function of jet transverse momentum (left) and 3326 $\Delta R(\text{track}, \text{jet})$ (right) for jets in the Z' sample. The rate of fake tracks 3327 increases significantly as a function of p_T , and also increases as the distance 3328 to the jet axis decreases.	74
3329	5.4 The light-jet efficiency of the low level tagger SV1 for jets in the Z' sample 3330 with $250 < p_T < 5000$ GeV, as a function of <i>b</i> -jet efficiency. The nominal 3331 tracking setup (black) is shown alongside the case where fake tracks which 3332 are not from the decay of a <i>b</i> -hadron are removed. The light-jet efficiency 3333 is decreased, demonstrating that the presence of fake tracks is detrimental 3334 to the algorithm performance.	75

3335	5.5 (left) Normalised histograms of the fake track classification model output 3336 separated for signal and fake tracks, and further separated by those tracks 3337 which are from the decay of a b -hadron. (right) The ROC curve for all 3338 tracks (solid line) and tracks from the decay of a b -hadron (dashed line). 3339 The plots show tracks in the combined $t\bar{t}$ and Z' testing sample. The model 3340 is able to successfully discriminate between signal and fake tracks, and 3341 shows a very similar performance when looking specifically at tracks from 3342 the decay of a b -hadron.	79
3343	5.6 (left) Normalised histogram of the b -hadron track identification model 3344 output separated for tracks from the decay of a b -hadron and tracks from 3345 other sources. The two groups are further separated into those tracks which 3346 are fake. (right) The ROC curve for all tracks (solid line). The plots show 3347 tracks in the combined $t\bar{t}$ and Z' testing sample.	81
3348	5.7 The effect of applying the fake track identification algorithm together with 3349 the b -hadron decay track identification on the jet tagging performance of 3350 SV1 for jets in the Z' sample with $250 \text{ GeV} < p_T < 400 \text{ GeV}$ (left) and 3351 $400 \text{ GeV} < p_T < 1 \text{ TeV}$ (right). The nominal SV1 light-jet rejection (black) 3352 is compared to two working points of fake track removal, labelled “A” (red) 3353 and “B” (orange), which represent two different 2D working points of the 3354 track classification tools. Removal of fake tracks based on truth information 3355 is shown by the green curves.	82
3356	6.1 Comparison of the existing flavour tagging scheme (left) and GN1 (right). 3357 The existing approach utilises low-level algorithms (shown in blue), the 3358 outputs of which are fed into a high-level algorithm (DL1r). Instead 3359 of being used to guide the design of the manually optimised algorithms, 3360 additional truth information from the simulation is now being used as 3361 auxiliary training targets for GN1. The solid lines represent reconstructed 3362 information, whereas the dashed lines represent truth information [3]. . .	85
3363	6.2 The flow of information through a graph neural network layer for (left) a full 3364 implementation of the layer and (right) a deep sets model [118]. Reproduced 3365 from Ref. [117].	88

3366	6.3 The inputs to GN1 are the two jet features ($n_{\text{jf}} = 2$), and an array of 3367 n_{tracks} , where each track is described by 21 track features ($n_{\text{tf}} = 21$). The 3368 jet features are copied for each of the tracks, and the combined jet-track 3369 vectors of length 23 form the inputs of GN1 [3].	93
3370	6.4 The network architecture of GN1. Inputs are fed into a per-track initialisation 3371 network, which outputs an initial latent representation of each track. 3372 These representations are then used to populate the node features of a 3373 fully connected graph network. After the graph network, the resulting node 3374 representations are used to predict the jet flavour, the track origins, and 3375 the track-pair vertex compatibility [3].	93
3376	6.5 Comparison between the DL1r and GN1 b -tagging discriminant D_b for jets 3377 in the $t\bar{t}$ sample. The 85% WP and the 60% WP are marked by the solid 3378 (dashed) lines for GN1 (DL1r), representing respectively the loosest and 3379 tightest WPs typically used by analyses. A value of $f_c = 0.018$ is used in the 3380 calculation of D_b for DL1r and $f_c = 0.05$ is used for GN1. The distributions 3381 of the different jet flavours have been normalised to unity area [3].	98
3382	6.6 The c -jet (left) and light-jet (right) rejections as a function of the b -jet 3383 tagging efficiency for jets in the $t\bar{t}$ sample with $20 < p_{\text{T}} < 250 \text{ GeV}$. The 3384 ratio with respect to the performance of the DL1r algorithm is shown in 3385 the bottom panels. A value of $f_c = 0.018$ is used in the calculation of D_b 3386 for DL1r and $f_c = 0.05$ is used for GN1 and GN1Lep. Binomial error bands 3387 are denoted by the shaded regions. The x -axis range is chosen to display 3388 the b -jet tagging efficiencies usually probed in these regions of phase space [3].	101
3389	6.7 The c -jet (left) and light-jet (right) rejections as a function of the b -jet 3390 tagging efficiency for jets in the Z' sample with $250 < p_{\text{T}} < 5000 \text{ GeV}$. The 3391 ratio with respect to the performance of the DL1r algorithm is shown in 3392 the bottom panels. A value of $f_c = 0.018$ is used in the calculation of D_b 3393 for DL1r and $f_c = 0.05$ is used for GN1 and GN1Lep. Binomial error bands 3394 are denoted by the shaded regions. The x -axis range is chosen to display 3395 the b -jet tagging efficiencies usually probed in these regions of phase space [3].	101

3396 6.8 The b -jet tagging efficiency for jets in the $t\bar{t}$ sample (left) and jets in the Z' sample (right) as a function of jet p_T with a fixed light-jet rejection of 100 in each bin. A value of $f_c = 0.018$ is used in the calculation of D_b for DL1r and $f_c = 0.05$ is used for GN1 and GN1Lep. GN1 demonstrates improved performance with respect to DL1r across the p_T range shown. Binomial error bands are denoted by the shaded regions [3].	102
3402 6.9 The b -jet (left) and light-jet (right) rejections as a function of the c -jet tagging efficiency for $t\bar{t}$ jets with $20 < p_T < 250$ GeV. The ratio to the performance of the DL1r algorithm is shown in the bottom panels. Binomial error bands are denoted by the shaded regions. The x -axis range is chosen to display the c -jet tagging efficiencies usually probed in these regions of phase space [3].	104
3408 6.10 The b -jet (left) and light-jet (right) rejections as a function of the c -jet tagging efficiency for Z' jets with $250 < p_T < 5000$ GeV. The ratio to the performance of the DL1r algorithm is shown in the bottom panels. Binomial error bands are denoted by the shaded regions. The x -axis range is chosen to display the c -jet tagging efficiencies usually probed in these regions of phase space [3].	104
3414 6.11 The c -jet (left) and light-jet (right) rejections as a function of the b -jet tagging efficiency for $t\bar{t}$ jets with $20 < p_T < 250$ GeV, for the nominal GN1, in addition to configurations where no (GN1 No Aux), only the track classification (GN1 TC) or only the vertexing (GN1 Vert) auxiliary objectives are deployed. The ratio to the performance of the DL1r algorithm is shown in the bottom panels. A value of $f_c = 0.018$ is used in the calculation of D_b for DL1r and $f_c = 0.05$ is used for GN1 [3].	106
3421 6.12 The c -jet (left) and light-jet (right) rejections as a function of the b -jet tagging efficiency for Z' jets with $250 < p_T < 5000$ GeV, for the nominal GN1, in addition to configurations where no (GN1 No Aux), only the track classification (GN1 TC) or only the vertexing (GN1 Vert) auxiliary objectives are deployed. The ratio to the performance of the DL1r algorithm is shown in the bottom panels. A value of $f_c = 0.018$ is used in the calculation of D_b for DL1r and $f_c = 0.05$ is used for GN1 [3].	106

3428	6.13 A schematic showing the truth track origin and vertex information (left) compared with the predictions from GN1 (right). The diagrams show the truth (left) and predicted (right) structure of a b -jet. The true and predicted origins of the tracks is shown by the coloured circles along the diagonal. The shaded black boxes show the groupings of tracks into different vertices. Vertices reconstructed by SV1 and JetFitter are also marked. Class probabilities p_b , p_c and p_u are rounded to three significant figures. GN1 improves over SV1 and JetFitter by successfully determining the origins and vertex compatibility of all the tracks in the jet with the exception of the truth OtherSecondary track, which is misidentified as pile-up.	108
3438	6.14 A schematic showing the truth track origin and vertex information (left) compared with the predictions from GN1 (right). The diagrams show the truth (left) and predicted (right) structure of a b -jet. The true and predicted origins of the tracks is shown by the coloured circles along the diagonal. The shaded black boxes show the groupings of tracks into different vertices. Vertices reconstructed by SV1 and JetFitter are also marked. Class probabilities p_b , p_c and p_u are rounded to three significant figures. GN1 improves over SV1 and JetFitter by successfully determining the origins and vertex compatibility of all but one tracks in the jet.	108
3447	6.15 Heavy flavour vertex finding efficiency as a function of jet p_T for b -jets in the $t\bar{t}$ sample using the exclusive (left) and inclusive (right) vertex finding approaches. The exclusive vertexing approach includes single track vertices while the inclusive approach requires vertices to contain at least two tracks. Efficient vertex finding requires the recall of at least 65% of the tracks in the truth vertex, and allows no more than 50% of the tracks to be included incorrectly. Binomial error bands are denoted by the shaded regions. . .	111
3454	6.16 Heavy flavour vertex finding efficiency as a function of jet p_T for b -jets in the Z' sample using the exclusive (left) and inclusive (right) vertex finding approaches. The exclusive vertexing approach includes single track vertices while the inclusive approach requires vertices to contain at least two tracks. Efficient vertex finding requires the recall of at least 65% of the tracks in the truth vertex, and allows no more than 50% of the tracks to be included incorrectly. Binomial error bands are denoted by the shaded regions. . .	111

3461	6.17 Vertex finding efficiency for other secondary decays as a function of jet p_T for light-jets in the $t\bar{t}$ sample using the exclusive (left) and inclusive (right) vertex finding approaches. The exclusive vertexing approach includes single track vertices while the inclusive approach requires vertices to contain at least two tracks. Efficient vertex finding requires the recall of at least 65% of the tracks in the truth vertex, and allows no more than 50% of the tracks to be included incorrectly. Binomial error bands are denoted by the shaded regions.	112
3462		
3463		
3464		
3465		
3466		
3467		
3468		
3469	6.18 Vertex finding efficiency as a function of jet p_T for light-jets in the Z' sample using the exclusive (left) and inclusive (right) vertex finding approaches. The exclusive vertexing approach includes single track vertices while the inclusive approach requires vertices to contain at least two tracks. Efficient vertex finding requires the recall of at least 65% of the tracks in the truth vertex, and allows no more than 50% of the tracks to be included incorrectly. Binomial error bands are denoted by the shaded regions.	113
3470		
3471		
3472		
3473		
3474		
3475		
3476	6.19 ROC curves for the different groups of truth origin labels defined in Table 5.1 for jets in the $t\bar{t}$ sample (left) and jets in the Z' sample (right). The FromB, FromBC and FromC labels have been combined, weighted by their relative abundance, into the Heavy Flavour category, and the Primary and OtherSecondary labels have similarly been combined into a single category. The mean weighted area under the ROC curves (AUC) is similar for both samples [3].	115
3477		
3478		
3479		
3480		
3481		
3482		
3483	6.20 The c -jet (left) and light-jet (right) rejections as a function of the b -jet tagging efficiency for $t\bar{t}$ jets with $20 < p_T < 250$ GeV, for the looser track selection trainings of GN1. The ratio to the performance of the DL1d algorithm [87] is shown in the bottom panels. A value of $f_c = 0.018$ is used in the calculation of D_b for DL1d and $f_c = 0.05$ is used for GN1. Binomial error bands are denoted by the shaded regions.	117
3484		
3485		
3486		
3487		
3488		
3489	6.21 The c -jet (left) and light-jet (right) rejections as a function of the b -jet tagging efficiency for Z' jets with $250 < p_T < 5000$ GeV, for the looser track selection trainings of GN1. The ratio to the performance of the DL1d algorithm [87] is shown in the bottom panels. A value of $f_c = 0.018$ is used in the calculation of D_b for DL1d and $f_c = 0.05$ is used for GN1. Binomial error bands are denoted by the shaded regions.	117
3490		
3491		
3492		
3493		
3494		

3495	6.22 The HLT light-jet rejection as a function of the b -jet efficiency jets in the $t\bar{t}$ sample with $20 < p_T < 250$ GeV for events with a centre of mass energy $\sqrt{s} = 13.6$ TeV [126]. The ratio to the performance of the DL1d algorithm [87] is shown in the bottom panels. Binomial error bands are denoted by the shaded regions. The purple vertical dashed lines represent the most common working points used for b-tagging.	118
3501	6.23 The c -jet rejection (left) and light-jet rejection (right) for the upgraded HL-LHC ATLAS detector with $\langle \mu \rangle = 200$ as a function of the b -jet efficiency for jets in the $t\bar{t}$ sample with $20 < p_T < 250$ GeV for events with a centre of mass energy $\sqrt{s} = 14$ TeV [127]. The ratio to the performance of the DL1d algorithm is shown in the bottom panels. Binomial error bands are denoted by the shaded regions. The purple vertical dashed lines represent the most common working points used for b-tagging.	120
3508	6.24 The c -jet rejection (left) and light-jet rejection (right) for the upgraded HL-LHC ATLAS detector with $\langle \mu \rangle = 200$ as a function of the b -jet efficiency for jets in the Z' sample with $250 < p_T < 5000$ GeV for events with a centre of mass energy $\sqrt{s} = 14$ TeV [127]. The ratio to the performance of the DL1d algorithm is shown in the bottom panels. Binomial error bands are denoted by the shaded regions.	120
3514	7.1 Diagrams of the signal process (top) and $t\bar{t}$ background (bottom). Object to the right of centre are reconstructed within the large- R jet. For the $t\bar{t}$ background, the large- R jet contains a mis-tagged c -jet or (less often) a mis-tagged light-jet. The contribution in the 0-lepton channel results from hadronically decaying τ lepton, or a electron or muon which is out of the analysis acceptance.	131
3520	7.2 Leading large- R jet mass for the Z and $W+hf$ processes in the HP SR of the 0-lepton channel [177]. The renormalisation scale μ_r has been varied by a factor of 0.5 (1DOWN) and 2 (1UP). An exponential function is fitted to the ratio between the nominal and alternate samples.	142
3524	7.3 Leading large- R jet m_J inclusive in p_T^V for the $V+hf$ process modelled using both the SHERPA (blue) and MADGRAPH (red) samples [177]. The Kolmogorov-Smirnov test and χ^2/ndf are shown on the plots.	143

3527	7.4 Leading large- R jet mass distribution for the WZ and ZZ processes, inclusive across all signal regions and lepton channels [177]. The renormalisation scale μ_R has been varied by a factor of 2 (1up) and 0.5 (1down). The red line shape shows the fitting results of the hyperbolic tangent function.	145
3531	7.5 The comparison of the shapes of the large- R jet mass m_J between SHERPA (black) and POWHEG+PYTHIA8 (red) samples from WZ and ZZ process in high and low purity signal regions, integrated over p_T^V regions and the 0- and 1-lepton channels [177]. The dashed green line shows the fitted third order polynomial function and the blue lines show the function after a protection is added in the high mass region.	146
3537	7.6 The m_J post-fit distributions in (top) the 0-, (middle) 1- and (bottom) 2-lepton SRs for (left) $250 \text{ GeV} < p_T^V < 400 \text{ GeV}$ and (right) $p_T^V \geq 400 \text{ GeV}$. The LP and HP regions are merged for the 0-lepton and 1-lepton channels. The fitted background contributions are shown as filled histograms. The Higgs boson signal ($m_H = 125 \text{ GeV}$) is shown as a filled histogram and is normalised to the signal yield extracted from data ($\mu_{VH}^{bb} = 0.72$), and as an unstacked unfilled histogram, scaled by the SM prediction times a factor of two. The size of the combined on the sum of the fitted signal and background is shown in the hatched band. The highest bin contains the overflow [131].	154
3547	7.7 The m_J post-fit distributions in the $t\bar{t}$ control region for (top) the 0-lepton channel and the 1-lepton channel for $250 \text{ GeV} < p_T^V < 400 \text{ GeV}$ and (bottom) the 0-lepton channel and the 1-lepton channel for $p_T^V > 400 \text{ GeV}$. The background contributions after the likelihood fit are shown as filled histograms. The Higgs boson signal ($m_h = 125 \text{ GeV}$) is shown as a filled histogram on top of the fitted backgrounds normalised to the signal yield extracted from data ($\mu_{VH}^{bb} = 0.72$), and unstacked as an unfilled histogram, scaled by the SM prediction times a factor of 2. The size of the combined statistical and systematic uncertainty for the sum of the fitted signal and background is indicated by the hatched band. The highest bin in the distributions contains the overflow [131].	155

3590 List of tables

<small>3591</small>	2.1 The fermions of the SM [16]. Three generations of particles are present. <small>3592</small> Also present (unlisted) are the antiparticles, which are identical to the <small>3593</small> particles up to a reversed charge sign.	15
<small>3594</small>	2.2 The bosons of the SM [16]. The photon, weak bosons and gluons are gauge <small>3595</small> bosons arising from gauge symmetries, and carry the four fundamental forces <small>3596</small> of the SM. The recently discovered Higgs boson is the only fundamental <small>3597</small> scalar particle in the SM.	16
<small>3598</small>	3.1 Overview of the different LHC runs [34, 35]. The average number of interactions per bunch-crossing is denoted as $\langle \mu \rangle$ (see Section 3.2.3), and is here averaged over the entire run. The luminosity is the peak instantaneous luminosity. Numbers for Run 3 are preliminary and are only provided to give an indication of expected performance.	29
<small>3603</small>	3.2 Quality selections applied to tracks, where d_0 is the transverse IP of the track, z_0 is the longitudinal IP with respect to the PV and θ is the track polar angle (see Section 3.2.2 for the IP definitions). Silicon hits are hits on the pixel and SCT layers. Shared hits are hits used on multiple tracks which have not been classified as split by the cluster-splitting neural networks [57]. A hole is a missing hit, where one is expected, on a layer between two other hits on a track.	46

3610	5.1 Truth origins which are used to categorise the physical process that led to the production of a track. Tracks are matched to charged particles using the truth-matching probability [57]. A truth-matching probability of less than 0.75 indicates that reconstructed track parameters are likely to be mismeasured and may not correspond to the trajectory of a single charged particle. The “OtherSecondary” origin includes tracks from photon conversions, K_S^0 and Λ^0 decays, and hadronic interactions.	74
3617	5.2 Input features to the fake track classification NN. Basic jet kinematics, along with information about the reconstructed track parameters and constituent hits are used. Shared hits, are hits used on multiple tracks which have not been classified as split by the cluster-splitting neural networks [57], while split hits are hits used by multiple tracks which have been identified as merged, and therefore split.	77
3623	5.3 Hyperparameter for the track classification model	78
3624	5.4 Good and fake track selection efficiencies for the combined $t\bar{t}$ and Z' samples. Two working points are defined, cutting on the NN output at 0.06 and 0.12.	80
3626	5.5 Cut values for the fake and b -hadron decay track MVAs for the two defined working points. Working point “B” cuts more aggressively on the MVA outputs than WP “A”, removing more fake tracks but resulting in an increased loss of signal tracks (which here are all b -hadron decay tracks).	81
3630	6.1 Input features to the GN1 model. Basic jet kinematics, along with information about the reconstructed track parameters and constituent hits are used. Shared hits, are hits used on multiple tracks which have not been classified as split by the cluster-splitting neural networks [57], while split hits are hits used on multiple tracks which have been identified as merged. A hole is a missing hit, where one is expected, on a layer between two other hits on a track. The track leptonID is an additional input to the GN1Lep model [3].	90
3637	6.2 A summary of GN1’s different classification networks used for the various training objectives, adapted from Ref. [3]. The hidden layers column contains a list specifying the number of neurons in each layer. ReLU activation is used through the network [100].	95

3641 6.3 The area under the ROC curves (AUC) for the track classification from
3642 GN1, compared to a standard multilayer perceptron (MLP) trained on a
3643 per-track basis. The unweighted mean AUC over the origin classes and
3644 weighted mean AUC (using as a weight the fraction of tracks from the
3645 given origin) is provided. GN1, which uses an architecture that allows track
3646 origins to be classified in a conditional manner as discussed in Section 6.4.3,
3647 outperforms the MLP model for both $t\bar{t}$ and Z' jets. 114

3648 7.1 Summary of the definitions of the different analysis regions . Signal enriched
3649 regions are marked with the label SR. There are regions with relatively
3650 large signal purity (HP SR) and with low purity (LP SR). Background
3651 enriched regions are marked with the label CR. The shorthand “add” stands
3652 for additional small- R jets, i.e. number of small- R jets not matched to the
3653 Higgs-jet candidate. The medium and high p_T^V regions are referred to as
3654 Mp_T^V and Hp_T^V , respectively [131]. 125

3655 7.2 Signal and background processes with the corresponding generators used for the
3656 nominal samples [131]. If not specified, the order of the cross-section calculation
3657 refers to the expansion in the strong coupling constant (α_s). (★) The events
3658 were generated using the first PDF in the NNPDF3.0NLO set and subsequently
3659 reweighted to the PDF4LHC15NLO set [165] using the internal algorithm in
3660 PowHEG-Box v2. (†) The NNLO(QCD)+NLO(EW) cross-section calculation for
3661 the $pp \rightarrow ZH$ process already includes the $gg \rightarrow ZH$ contribution. The $qq \rightarrow ZH$
3662 process is normalised using the cross-section for the $pp \rightarrow ZH$ process, after
3663 subtracting the $gg \rightarrow ZH$ contribution. An additional scale factor is applied to
3664 the $qq \rightarrow VH$ processes as a function of the transverse momentum of the vector
3665 boson, to account for electroweak (EW) corrections at NLO. This makes use of
3666 the VH differential cross-section computed with HAWK [166, 167]. 127

3667 7.3 Selections applied to baseline and signal electrons and muons. 128

3668	7.4 Event selection requirements for the boosted VH , $H \rightarrow b\bar{b}$ analysis channels and sub-channels [131]. Various channel dependent selections are used to maximise the signal efficiency and reduce the number of background events in each analysis region. The $\min[\Delta\phi(\mathbf{E}_T^{\text{miss}}, \text{small-}R \text{ jets})]$ selection is used to remove jets when the missing transverse momentum $\mathbf{E}_T^{\text{miss}}$ is pointing in the direction of the Higgs candidate, and the $\Delta\phi(\mathbf{E}_T^{\text{miss}}, \mathbf{E}_{T, \text{trk}})$ is used to reject events where the calorimeter missing transverse momentum $\mathbf{E}_T^{\text{miss}}$ is not pointing in the direction of the track-based missing transverse momentum $\mathbf{E}_{T, \text{trk}}^{\text{miss}}$. The $\Delta y(V, H_{\text{cand}})$ quantifies the rapidity difference between the reconstructed vector boson and Higgs candidate.	130
3678	7.5 Different sources of uncertainty (i.e. variations in the model) considered for the $V + \text{jets}$ background, and the corresponding implementation. For each uncertainty, acceptance and shape uncertainties are derived.	134
3681	7.6 0-lepton $W + \text{jets}$ nominal sample flavour composition and total event yield [177]. Mp_T^V refers to the medium p_T^V region, and Hp_T^V refers to the high p_T^V region (see Table 7.1).	138
3684	7.7 1-lepton $W + \text{jets}$ nominal sample flavour composition and total event yield [177]. Mp_T^V refers to the medium p_T^V region, and Hp_T^V refers to the high p_T^V region (see Table 7.1).	138
3687	7.8 0-lepton $Z + \text{jets}$ nominal sample flavour composition and total event yield [177]. Mp_T^V refers to the medium p_T^V region, and Hp_T^V refers to the high p_T^V region (see Table 7.1).	139
3690	7.9 2-lepton $Z + \text{jets}$ nominal sample flavour composition and total event yield [177]. Mp_T^V refers to the medium p_T^V region, and Hp_T^V refers to the high p_T^V region (see Table 7.1).	139
3693	7.10 $V + \text{jets}$ acceptance uncertainties [177]. $W + \text{jets}$ SR and CR uncertainties marked with a superscript † are correlated. The 1L $W + \text{jets}$ H/M uncertainty marked by * is applied as independent and uncorrelated NPs in both HP and LP signal regions.	140
3697	7.11 Diboson acceptance uncertainties [177]. All uncertainties except channel extrapolation uncertainties are fully correlated between ZZ and WZ processes and channels.	145

3700	7.12 Factors applied to the nominal normalisations of the $t\bar{t}$, $W+\text{hf}$, and $Z+\text{hf}$ backgrounds, as obtained from the likelihood fit [131]. The errors represent the combined statistical and systematic uncertainties.	153
3703	7.13 Post-fit yields in the 0-lepton channel. Combined statistical and systematic uncertainties are shown [177].	156
3705	7.14 Post-fit yields in the 1-lepton channel. Combined statistical and systematic uncertainties are shown [177].	156
3707	7.15 Post-fit yields in the 2-lepton channel. Combined statistical and systematic uncertainties are shown [177].	157
3709	7.16 Breakdown of the absolute contributions to the uncertainty on the signal strength μ_{VH}^{bb} obtained from the (1+1)-POI fit. The average impact represents the average between the positive and negative uncertainties on μ_{VH}^{bb} . The sum in quadrature of the systematic uncertainties attached to the categories differs from the total systematic uncertainty due to correlations [177].	162
3714		